

**Parametric Studies and Data Development of Two-  
dimensional Cellular Structures and Crystals at  
Different Length Scales**

**Cong Tang**

**A thesis submitted in partial fulfilment of the  
requirement of the Liverpool John Moores University  
for the degree of Doctor of Philosophy**

**School of Engineering, Technology and Maritime  
Operations, Liverpool John Moores University**

**July 2020**

---

## ACKNOWLEDGEMENTS

I would like to express my sincere gratitude and special thanks to my supervisors, Dr. Lisa Li, Dr Gylnn Rothwell and Prof. James Ren who have provided guidance, advice and encouragement during this research study.

Many other academic, secretarial and technical members of staff have facilitated the realisation of this thesis and I express my gratitude to all of them. I would like to thank Mr. Clive Eyre, Mr. Anthony Dunmore, Mr. Steve Gotts and Mr. Barker Tom for their invaluable technical support with the sample manufacturing process, sensor and data logging design and material testing.

I would like to take this opportunity to thank my group mates, Dr. Andrew Norbury, Mr. Al-Badani, Khaled, Dr. Shudong Li, Mr. Vince Zevallos Herencia for their friendship and sharing their experience. I also would like to thank the academics and fellow PhD students I have met and worked with as part of researcher exchange programs (Prof. Yunche Wang, National Cheng Kung University (Taiwan); Dr Prof. Dr. Anurak Prasatkhetrarn (University of Phayao, Thailand); Dr. Farazila Binti Yusof, University of Malaya). I am also grateful for the help from my friends, who gave me help in many ways and shared a great time in my studies and life at Liverpool John Moores University.

I am grateful to LJMU for providing the facilities for the research. I am also grateful to the colleagues from the Auxetic Materials Conference 2018&19 for many insightful suggestion and advices.

Finally, my sincere thanks go to my family and my wife Ms Xiaochun Zhan for sustained encouragement, and continuous and unselfish love and support during my Ph.D. study.

Cong (Victor) Tang

---

## **Declaration**

I declare that this thesis has been composed solely by myself and that it has not been submitted, in whole or in part, in any previous application for a degree. Except where states otherwise by reference or acknowledgment, the work presented is entirely my own.

Cong Tang

July 2020

---

# Table of Contents

ACKNOWLEDGEMENTS .....	2
Declaration .....	3
Table of Contents .....	4
List of Symbols .....	8
List of Abbreviations.....	10
List of Figures .....	11
ABSTRACT.....	18
List of Publications and External Reports.....	20
CHAPTER ONE .....	22
INTRODUCTION .....	22
1.1 Introduction.....	23
1.2 Aims and Objectives .....	27
1.3 Outline of the thesis .....	28
CHAPTER TWO .....	31
BACKGROUND AND LITERATURE REVIEW .....	31
2.1 Introduction.....	32
2.2 Poisson’s ratio and measurements.....	33
2.3 Materials property data and Poisson’s ratios of different materials. .....	38
2.4 Mechanisms of auxetic structures at different length scales.....	42
2.5 Regular honeycomb structure, FE modelling and key deformation stages.....	47
2.6 Experimental and numerical research in auxetic structures.....	54
2.7 Different materials models in finite element modelling .....	57
2.8 Application of Python scripts in structure /material modelling and data analysis.....	61
2.9 Modelling at different scales and data development.....	72
2.10 Main issues and challenges.....	78
CHAPTER THREE.....	81
EXPERIMENTALS, NUMERICAL MODELLING AND DATA ANALYSIS	

---

PROGRAMS.....	81
3.1 Introduction and main research works .....	82
3.2 FE modelling and structures. ....	85
3.3 Materials studios .....	89
3.4 Python program and key developments in the work.....	90
CHAPTER FOUR.....	92
NUMERICAL STUDY ON AUXETIC STRUCTURE .....	92
4.1 Introduction and main research works .....	93
4.2 Program development in Abaqus for building different structures.....	97
4.3 Deformation of missing rib models in tension.....	109
4.3.1. FE modelling of auxetic structures in tension and comparison with analytical and experimental data.....	109
4.3.2 Effect of sample size effect on the Poisson’s ratio and stability of auxeticity.....	115
4.3.3 Effect of beam angles and the beam length ratio on the Poisson’s ratio and auxeticity.....	117
4.4 Deformation mechanism of missing rib models under compression .....	123
4.4.1 Structures, Experimental and Modelling Approaches.....	123
4.4.2 Deformation of normal missing rib structures with a beam angle of 90 (MS-90).....	127
4.4.3 Deformation of missing rib structures with different beam angles.....	131
4.4.4 Deformation of the mixed structures and Poisson’s ratio under compression .....	133
4.4.5 Effect of the sample size on the initial contact and Poisson’ ratio .....	137
4.5 FE modelling of self-similar hierarchical honeycombs .....	140
4.5.1 Self-similar hierarchical structures. ....	140
4.5.2 Deformation of self-similar hierarchical honeycomb and FE model validation.....	142
4.6 Modelling and analysis of cell area changes of regular, missing ribs and self-similar hierarchical honeycomb structure under compression	

---

and tension. ....	149
4.6.1 Area calculation program development and structures .....	149
4.6.2 Area calculation approach .....	150
4.6.3 Area calculation in finite element modelling and python program .....	154
4.6.4 Typical area changes of different cellular structures under tension or compression.....	159
4.7 Discussion .....	165
4.7.1 Effect of modelling approach and sample size/stiffness ratio/Poisson's ratio on auxeticity of missing rib structure .....	165
4.7.2 Effect of different modelling approaches and mesh sensitivity .....	169
4.7.3 Factors affecting the area analysis with different approaches and use of the program in random structures generation .....	177
4.7.4 Development of mixed structures of regular shapes/patterns with targeted Poisson's ratios and other targeted properties. ....	182
4.7.5 Development of random auxetic structures.....	184
CHAPTER FIVE.....	190
NUMERICAL STUDY ON DIFFERENT CRYSTAL STRUCTURES....	190
5.1 Introduction and main research works .....	191
5.2 The main process and data in first principle calculation of ground state properties .....	193
5.3 Calculation of anisotropic parameters and monocarbides .....	196
5.3.1 Computational Method and data integration.....	197
5.3.2 Elastic constants and ground elastic properties.....	201
5.3.3 Directional anisotropy data of elastic properties based on 3D surface construction and plane projection.....	207
5.4 GUI for building crystal structure and systematic study of ground properties, anisotropy, Poisson's ratios of large number of carbides	213
5.4.1 Data for crystals structure .....	213
5.4.2 GUI for calculating ground state mechanical properties...	215
5.4.3 Typical materials (carbides) used, Poisson's ratio and anisotropy data analysis .....	217

---

5.5 Discussion .....	220
5.5.1. Correlation between the Poisson’s ratio and other properties. .....	220
5.5.2 Effect of temperature on the Poisson’s ratio and anisotropy data of simple monocarbides.....	223
5.5.3 Use of Material Studio in studying other material properties and processes.....	230
5.5.4 Link between properties at crystal and Poisson’s ratio of materials at different scales .....	235
CHAPTER SIX .....	240
CONCLUSIONS AND FUTURE WORK.....	240
6.1 Summary .....	241
6.2 Recommendations for further works.....	243
Reference: .....	244

---

## List of Symbols

$\mu_i$  &  $\alpha_i$ : Material constants in hyperelastic material model

$\gamma$ : Shear strain

$D_x$ : Deformation in the transverse direction

$D_Y$ : Deformation in the loading direction

$J^{el}$ : Elastic volume ratio

$\bar{I}_1$ : First deviatoric strain invariants

$\bar{\lambda}_i$ : Principal stretches

$a$ : Dimension of the chamber

$A_{comp}$ : Percent anisotropy in compressibility

$A_{Shear}$ : Percent anisotropy in shear

$A_U$ : Universal elastic anisotropic index

$B$ : Left Cauchy-Green strain tensor

$b$ : Radius of the cylindrical indenter

$C_1$  &  $C_2$ : material constants in hyperelastic material model

$C_{10}$  &  $D_1$ : Temperature-dependent material parameters in hyperelastic material model

$C_{ij}$ : Stiffness tensor

$E$ : Young's Modulus

$E_{slab}$ : Total energy of the slab

$E_{surf}$ : Surface energy

$E_{total}$ : Calculated total energy

$G$ : Shear modulus

$I_1$ : First invariant of the unimodular component

$I_2$ : Second invariant of the unimodular component

$K$ : Bulk modulus

$K$ : Strength coefficient in the material model for elastic-plastic materials

$l_1, l_2$  &  $l_3$ : Directional cosines in spherical coordinate system

$n$ : Strain hardening exponent

---

$S_{ij}$ : Compliance tensor

U: Strain energy potential

$\nu$ : Poisson's ratio

W: Strain energy

$\epsilon_x$ : transverse strain (Lateral strain)

$\epsilon_y$ : Loading strain (axial strain)

$\sigma$ : Stress

---

## List of Abbreviations

ANN: Artificial neural network  
APIs: Application programming interfaces  
CASTEP: Cambridge Serial Total Energy Package  
CCD: Charge-coupled device  
CLI: Command line interface  
DFT: Density Functional Theory  
DOFs: Degree of freedom  
FDIC: Fluorescent digital image correlation  
FEA: Finite element analysis  
FEM: Finite element modelling  
GGA: Generalized gradient approximation  
GUI: Graphical User Interface  
HF: Heron's formula  
MR: Missing Rib  
MS: Mixed structure  
OpenCV: Open-source computer Vision Library  
ORR: Oxygen reduction reaction  
PAW: Projector augmented plane wave  
PBC: Periodic boundary conditions  
PBE: Perdew-Burke-Ernzerhof function  
PIP: point in polygon  
RSG: Really Simple GUI  
RVE: Representative Volume Elements  
SM: Shoelace Method  
TPE: Thermoplastic elastomer

---

## List of Figures

- Figure 1.1** Typical missing rib (a) and self-similar hierarchical structures.
- Figure 2.1** The deformation of a sample under tension or compression and definition of the Poisson's ratio of a material.
- Figure 2.2** Different approaches of testing and analysis of Poisson's ratio.
- Figure 2.3** Schematics showing the different behaviour of Non-auxetic and Auxetic materials in tension and compression.
- Figure 2.4** Poisson's ratio of different material groups and its link with bulk and shear modulus.
- Figure 2.5** Deformation of auxetic materials under different loading conditions and applications.
- Figure 2.6** Manufacturing processes of hexagonal cell type honeycomb core.
- Figure 2.7** FE models and typical results of a laterally loaded honeycomb.
- Figure 2.8** Comparison of measured and calculated force-displacement responses of a honey-comb specimen and calculated collapse configuration.
- Figure 2.9** FE modelling of honeycomb with different dimensions.
- Figure 2.10** Typical data showing the effect of honeycomb cell geometry on compressive response of Kagome (at two different orientations) and Square lattice.
- Figure 2.11** Different stress strain curves for linear elastic, elastic-plastic materials (metal and plastics) and hyperelastic material behaviours.
- Figure 2.12** Testing methods for defining material parameters used in Abaqus (a) and typical data of different stress strain curves of Rubber in different type of tests.
- Figure 2.13** ABAQUS CAE Plug-in toolkit, used by [Winker et al., \(2005\)](#) to generate gear models.
- Figure 2.14** Typical simulation system for modelling large H-beam hot rolling process.
- Figure 2.15** Typical Abaqus Plug-in showing the main functions and parameter used to study the effect of the negative Poisson's ratio matrix on the indentation resistance.

---

**Figure 2.16** The computation flow to estimate the effective elastic properties based on representative volume element (RVE) approach.

**Figure 2.17** Typical boundary conditions of a representative volume element model and deformed shapes. ( $u_1$  is strain in 'x' direction,  $u_2$  is strain in the 'y' direction).

**Figure 2.18** Key structure of an ABAQUS plugin tool for periodic RVE homogenisation and the node sorting process.

**Figure 2.19** Combination of python and FE modelling in studying random lattice structures.

**Figure 2.20** Different research approaches as shown by the growth of publications involving Poisson's ratio.

**Figure 2.21** Use of materials simulation data with machine learning to analyse the distribution of Poisson's ratio and Auxeticity in Zeolite system.

**Figure 3.1** Overall research structure and key approach.

**Figure 3.2** Some typical 3D printed Auxetic samples.

**Figure 3.3** Abaqus working flow and application of python in different parts.

**Figure 3.4** Typical case of Abaqus Plug-in graphical user interface (GUI) of missing rib parametric modelling.

**Figure 4.2.1** A Plugin GUI for building a regular Honeycomb (a); and typical example (b).

**Figure 4.2.2** Typical simple input GUI for building missing rib auxetic models of different angles and beam lengths in Abaqus.

**Figure 4.2.3** Key procedures to build a 1<sup>st</sup> order self-similar hierarchical honeycomb.

**Figure 4.2.3** Key procedures to build a 1<sup>st</sup> order self-similar hierarchical honeycomb.

**Figure 4.2.4** GUI for building Voronoi random cellular structure.

**Figure 4.2.5** Main process and data in building random cellular structures based the Voronoi approach.

**Figure 4.2.6** Typical structures studied.

**Figure 4.3.1** Centrosymmetric (a & c) and Axisymmetric (b & d) missing rib models in the FE analysis.

**Figure 4.3.2** Mesh, boundary and loading conditions of FE models of missing rib

---

models in tension.

**Figure 4.3.3** Deformed shape and lateral displacement field of the auxetic samples in tension. (a) 4-4 Centrosymmetric model; (b) 4-4 Centrosymmetric model.

**Figure 4.3.4** Comparison between the Poisson's ratio from FE modelling, analytical and experiments of the two missing rib models.

**Figure 4.3.5** Structures with different cell numbers used to study the sample size effect.

**Figure 4.3.6** Models and deformed patterns of auxetic structures at 20% load strain with different beam angles.

**Figure 4.3.7** Poisson's ratio and its stability over different strain level for missing rib auxetic structures with different beam angles.

**Figure 4.3.8** Data showing the effect of the beam angles on the Poisson's ratio and critical strain for auxeticity.

**Figure 4.3.9** Single cell of missing rib models with different beam length ratio ( $L1/L2$ ).

**Figure 4.3.10** Figures showing the effect of the beam length ratio on deformation patterns of missing rib structures.

**Figure 4.3.11** Data showing the effect of beam length ratio on the Poisson's ratio and its stability.

**Figure 4.3.12** The effect of the beam length ratio on the Poisson's ratio and critical strain for stable auxeticity.

**Figure 4.4.1** Typical structures studied. (a) Missing rib auxetic structure (90-degree beam angle). (b) Missing rib auxetic structure (60-degree beam angle). (c) Typical structure of wider samples. (d) Typical structure of larger superstructure.

**Figure 4.4.1** Typical models of studied in Oblique side 3D view.

**Figure 4.3.3** The load and boundary conditions in the finite element model. using a regular missing model MR-90 (4-4) as an example.

**Figure 4.4.4** Numerical and experiment stress-strain data and deformation of MR-90(4-4) sample.

**Figure 4.4.5** Comparison between numerical and testing data of MR-90 (7-3) sample

---

**Figure 4.4.6** Comparison between numerical and published force-displacement data (MR-90 (7-3) sample)

**Figure 4.4.7** Simulation and experiment results of structures with different beam angles.

**Figure 4.4.8** Typical mixed structures studied. (a) the design concept of mixed structures (MS) (b) 4-4 model of Mixed structure (MS-1). (c) 4-4 model of Mixed structure 2 (MS-2), (d) 10-10 model of Mixed structure 1 (MS-1) (e) 10-10 model of Mixed structure 2 (MS-2).

**Figure 4.4.9** Numerical and experimental data of normal missing rib (i) and mixed structures: MS-1(ii)&MS-2(iii).

**Figure 4.4.10** Stress-strain, Poisson's ratio and deformed shape of the mixed structures.

**Figure 4.4.11** Initial corner edge-wall contact position and deformed shapes (U1: Lateral displacement).

**Figure 4.4.12** Poisson's ratio vs Eng. strain of normal missing rib structure and mixed structures.

**Figure 4.5.1** Regular honeycomb (a) and 1<sup>st</sup> order self-similar hierarchical honeycomb (b) structures.

**Figure 4.5.2** Second order self-similar hierarchical honeycomb. (2D and 3D view).

**Figure 4.5.3** FE models of regular and self-similar hierarchical honeycomb structure under compression and deformation patterns.

**Figure 4.5.4** Comparison between FE model predicted deformation pattern and published data of self-similar hierarchical structure.

**Figure 4.5.5** Comparison between FE model predicted deformation pattern and Poisson's ratio of self-similar hierarchical structures with published data.

**Figure 4.5.6** Result with a 3D printed sample showing negative Poisson's ratio behaviour.

**Figure 4.5.7** Deformation of higher order self-similar Hierarchical honeycomb structures showing negative Poisson's ratio behaviour.

**Figure 4.5.8** FE Poisson's ratio vs. axial strain for different order hierarchical honeycomb (S=0.3 L=10).

**Figure 4.5.9** Effect of repeating cell numbers (a) on the Poisson's ratio (S=0.3

---

L=10)

**Figure 4.6.1** Point-in-polygon (PIP) algorithm to calculate the area of an enclosed polygon of points  $P_1$ - $P_7$ .

**Figure 4.6.2** Diagram showing the point-in-polygon (PIP) approach to calculate the area of Convex and Concave polygons.

**Figure 4.6.3** The area partition of undeformed and deformed hexagonal cells of regular honeycomb model based on the nodes on the edge.

**Table 4.6.1** Key stages and operations of the program for calculating the area of cellular structures under in-plane tension or compression.

**Figure 4.6.4** Typical structures used in the deformation and area changes analysis.

**Figure 4.6.5** Area changes of the single cell models for different structures (regular honeycomb and missing rib modeling tension or under compression).

**Figure 4.6.6** Area changes of the cells in the missing rib model under compression/tension.

**Figure 4.6.7** Area changes of the cells in the regular honeycomb model under compression and tension.

**Figure 4.6. 8** Cell area change of self-similar hierarchical honeycomb under compression.

**Figure 4.7.1** Effect of element number per beam on Engineering stress and Poisson's ratio at 10% Engineer strain. (Beam length = 10 mm, the beam angle = 90-degree,  $E=22\text{MPa}$ )

**Figure 4.7.2** Effect of mesh size of on the Poisson's ratio of a 1<sup>st</sup> order self-similar hierarchical model

**Figure 4.7.3** Solid cube FE model and regular honeycomb model used to evaluate the effectiveness of representative volume element (RVE) approach with periodical boundary conditions in predicting the Poisson's ratio.

**Figure 4.7.4** RVE models with periodical boundary conditions (PBC) of normal missing rib structure of different sizes.

**Figure 4.7.5** Comparison of the Poisson's ratio of normal missing ribs structure (beam angle 90 degree) from the RVE modelling with periodical boundary conditions and different sample sizes (4-4, 10-10, 20-20) simulated with full load conditions.

---

**Figure 4.7.6** Area calculation with different methods and validation against a cell with known area.

**Figure 4.7.7** Cases for which the Shoelace Method has a limitation to deal with when calculating the polygon area.

**Figure 4.7.8** Typical random structures produced by the Voronoi method and the area data.

**Figure 4.7. 9** Finite element model of mixed structure with alternating cell angles in the rows and columns. Mixed structure-3 (MS-3).

**Figure 4.7.10** The deformation of mixed structure (MS-3) determined from different sample sizes and RVE models.

**Figure 4.7.11** Flow chart showing the overall structure of the program for identify structures with a negative Poisson's a ratio over different strains.

**Table 4.7.12** Main steps and key operation of the program for generating and searching random structures with auxetic behaviours.

**Figure 4.7.13** Abaqus GUI for producing random structures.

**Figure 4.7.14** Main steps in building the random structures.

**Figure 4.7.15** Typical auxetic structures predicted.

**Figure 5.2.1** Typical operation in Materials studio to predict the ground state properties,

**Figure 5.2.2** Flow chart show to show data and key procedure in molecular dynamic simulation data analysis/ property calculation.

**Figure 5.3.1** The crystal structure of TiC, VC and NbC

**Figure 5.3.2** Effects of the cut-off energy and K-point on finial energy and elastic stiffness constants of Titanium carbide. (lattice parameter 4.35\*4.35\*4.35, Space group: Fm-3m)

**Figure 5.3.3** Main programs integrating materials studio data, property and anisotropy analysis.

**Figure 5.3.4** Predicted elastic properties and Vicker's hardness of the carbides.

**Figure 5.3.5** Anisotropy index data of the carbides.

**Figure 5.3.6** Euler angles and geometrical reference frame.

**Figure5.3.7** Surface construction and plane projection of bulk modulus of the carbides

---

**Figure 5.3.8** Surface construction and plane projection of Young's modulus of the carbides

**Figure 5.3.9** Surface construction and plane projection of shear modulus of the carbides

**Figure 5.3.10** Surface construction and plane projection of Poisson's ratio of the carbides

**Figure 5.3.11** Anisotropy in elastic properties ( $E, G, \nu$ ) based on the ratio between maximum and minimum property value (Max/Min).

**Figure 5.4.1** GUI of crystallography and main data.

**Figure 5.4.2** GUI for property and anisotropy calculation and visualisation.

**Figure 5.4.3** Typical crystal structures of selected carbides.

**Figure 5.4.5** Variation in Poisson's ratio universal anisotropy index.

**Figure 5.5.1** Correlation between the Poisson's ratio and  $K/G$  and maximum and minimum Poisson's ratio.

**Figure 5.5.2** Comparison of the elastic constant  $C_{11}$  of TiC from this work and published simulation data and experimental data.

**Figure 5.5.3** Typical elastic property data of TiC at different temperatures in comparison with published data.

**Figure 5.5.4** Typical elastic property data of VC at different temperatures in comparison with published data.

**Figure 5.5.5** The Cell volume change and elastic property change with different Temperature.

**Figure 5.5.6** Temperature effects on the elastic modulus of NbC.

**Figure 5.5.7** Temperature effect on the Anisotropy of NbC.

**Figure 5.5.8** The crystal structure of Ferrite with different plane and Calculation of the surface energy of Ferrite

**Figure 5.5.9** Crystal geometries of reactants, transition states, and products for oxygen reduction reaction (ORR) of boron nitride nano-sheets ( $\text{OOH} + \text{H}^+ + \text{e}^- \rightarrow 2\text{OH}$ )

**Figure 5.5.11** Crystal structure of Be<sub>2</sub>C and hexagonal dodecahedron

---

## ABSTRACT

The work presented in the thesis is focused on developing effective data-led simulation approaches for studying the behaviour and properties of auxetic structures and crystals with a particular focus on the Poisson's ratio, auxeticity and anisotropy. Python based parametric programs are developed and integrated with Finite element modelling (Abaqus) and ab initio quantum mechanical programs (Materials Studio CASTEP) for structure development and data processing.

A range of auxetic structures have been studied including missing rib structures in tension, missing rib and mixed cellular structures in compression and self-similar hierarchical structures in compression. A Python program is also developed for calculating and tracking of the area changes for cellular structures under compression and tension loads. The use of Python programs in developing Voronoi random structures and random structures with auxetic behaviors is also presented. The models are used to establish the effect of key dimensional parameters on the deformation process, Poisson's ratio and stability of auxeticity. The results show that the area analysis is effective in studying the changes in cell shape and area; the areas of the missing rib and honeycomb cell follows a more uniform cell deformation trend in tension than in compression. The area changes of the missing rib model under compression reflect the main deformation stages including the corner edge-cell wall contact. The work shows that deformation and instability auxeticity of normal missing rib structure and mixed structures are associated with the corner edge wall contact. The mixed model showed different beam-wall contact patterns, which contributes to the much higher critical strain of stable auxeticity and overall shape stability.

The work with ab initio quantum mechanical program (Materials Studio CASTEP) is focused on developing a Python-based data system for

---

systematic crystal structure processing and establishing the link between crystal structures and key ground state properties of crystals based on first principle calculations with Materials Studio. A range of ground state properties (e.g., elastic constants ( $C_{ij}$ ), bulk modulus (K), Young's modulus (E), shear modulus (G), Poisson's ratio ( $\nu$ ), etc.) have been studied with a particular focus on the Poisson's ratio and anisotropy. The correlation between the ground state elastic parameters and other properties are analysed. Some typical results on key engineering carbides including simple cubic systems (TiC, VC and NbC) are presented together with the mathematical operation to calculate the K, E, G,  $\nu$ . 3D surface constructions of the ground state parameters including anisotropic features are presented with an integrated program. The Python graphical user interface developed is effective for systematic calculation and visualization of the key structures, properties and anisotropy features. The relationship between maxima and minima of Poisson's ratio and the anisotropy index of a range of carbides showed a good agreement with the other published data based on a large quantity of data. Some compounds with low or negative Poisson's ratio were identified and detailed structures and properties data are given. The data highlighted the source of uncertainty in Poisson's ratio and the link between property data. The Data for structures with Negative Poisson's ratio is briefly presented and analysed including links between the auxetic crystal structure and some macro lattice structure with auxetic behaviors. The procedure for modelling surface energy, oxygen reduction reaction (ORR), crystals with doping elements and the effect of temperatures are also presented and showed a good agreement with published works. Future use of the framework developed, and main research focuses in both FE modelling and ab initio quantum mechanical simulation are discussed.

---

## List of Publications and External Reports

**C. Tang**, J. Guo, B. Li., A. Kostenevich, L. Wang, G. Rothwell and J. Ren, First Principle Calculation and Data Analysis of Anisotropy in Elastic Properties of Cubic MonoCarbides TiC, VC and NbC; *The 15th Global Congress on Manufacturing and Management*, April 2021, Liverpool (Accepted)

**C. Tang**, L. Li L, L. Wang, VZ. Herencia and XJ Ren, Numerical and Experimental Studies on the Deformation of Missing-Rib and Mixed Structures under Compression, *Physica Status Solidi B: Basic Solid-State Physics*, 2020. DOI: 10.1002/pssb.202000150

XJ. Ren (Keynote), **C. Tang**, J. Guo, L. Li and G. Rothwell, Data driven research for environmentally friendly complex material systems, *5th International Conference on Green Materials and Environmental Engineering (GMEE2019)*, Guangzhou, December 2019

X.J. Ren, **C. Tang**, J. Guo, L. Li and G. Rothwell, (Invited Talk), Data Based Approach for Analysing Negative Poisson's Ratio Systems with Different Scales, *11th International Conference on Auxetics and Related Systems with "Negative" characteristics*, Sept 2019, Poznan, Poland.

J. Guo, **C. Tang**, G. Rothwell, L. Li, YC. Wang, Q. Yang, X J. Ren. 2019. Welding of High Entropy Alloys A Review, *Entropy*, 21. DOI: 10.3390/e21040431.

K. Al-Badani, E. Elmshawet, **C. Tang**, T. Kaid, L. Li, J. Liu, J. Wang, and XJ. Ren., 2019, Investigating the Effect of TIG Welding on the Surface Roughness of the Welded Closure of Thin Stainless-Steel Tubes, *Journal of IOP Conference Series: Materials Science and Engineering (MSE)*. pp1-7.

K. Al-Badani, **C. Tang**, T. Kaid, Li. Lisa, D. Allanson and XJ Ren., Experimental and Numerical Studies of Droplet Formation of Different Material Systems, 6th International Conference on Nanomanufacturing, *NanoMan2018*, 04-06 July 2018, Brunel University London, UK, pp1-8.

K. Al-Badani, **C. Tang**, S. Li, T. Kaid, E. Elmshawet, Y. Gu, L. Li, G.

---

Rothwell, and XJ. Ren, Numerical Modelling of Materials with Embedded System in an Elastic Matrix in Contact with Solid and Liquid Impactors, *9th International Conference and 14th International Workshop on Auxetics and Related Systems with "Negative" characteristics*, Sheffield, UK - 10th to 13th September 2018.

**C. Tang**, First principle modelling of carbides, Ferrite and interfaces; *Presentation at University of Malaya*, 2019.

**C. Tang**, 2018, 2019, Numerical Modelling and prediction of auxetic structures. Faculty Research Week, LJMU.

J. Ren and **C. Tang**, Use of Materials Studios CASTEP in modelling carbides and interfaces. EU RISE Project (*i-weld*), First Year Report and Tutorial for the mid-term workshop.

**Papers in Process:**

First principle calculation of the effect of temperature effects on the anisotropy in carbides and lattice mismatch (In preparation for Crystals) (Ren XJ, **Tang C**, Guo J, Li B and Rothwell G)

Design and numerical modelling on the deformation of mixed auxetic structures (**Tang C**, Li B and Rothwell G and Ren XJ)

---

# **CHAPTER ONE**

## **INTRODUCTION**

---

## 1.1 Introduction

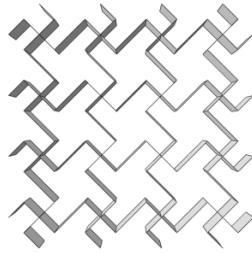
Poisson's ratio is an important material property reflecting the ratio between the lateral strain and axial strain when the material is under tension or compression loads. Most conventional materials have a positive Poisson's ratio, the material exhibits shrinking in the lateral direction in tension and expanding under compression. Auxetic (also called a negative Poisson's ratio material) are a relatively new group of materials, exhibiting lateral expansion when being stretched and shrinking when being compressed (Gaspar et al., 2005; Mousanezhad et al., 2015). Their unique properties opened a window towards a wide range of potential applications in biomedical applications, sport, and engineering applications such as membrane filters with variable permeability, personal protective equipment (e.g., shin pad, etc.) and smart implant (Sanami et al., 2014; Darwish and Aslam, 2014; Mousanezhad et al., 2015). There are many mechanisms/structures that have been identified or developed to generate negative Poisson's ratio behaviours, such as missing rib structure, re-entrant structures, self-similar hierarchical honeycombs, chiral structures, rotating rigid/semi-rigid units, and angle ply laminates (Kolpakov, 1985; Gibson, 1982; Grima et al., 2012; Brely et al., 2015; Prawoto and Alias, 2015; Ho et al., 2016; Lake, 2017). These established structures have opened the possibility of developing material systems with designed Poisson's ratio suitable for different applications. Auxetic behaviours may exist at different scales at macrolevel as well as atomic and microlevels (Lake, 2017) and the understanding of Poisson's ratio and auxeticity with other features such as anisotropy of crystals is gaining more and more research attention with the support of large-scale data from physical-based modelling such as first principle calculations (Farhadizadeh et al., 2017). A detailed understanding of the deformation modes under different loading modes or strain levels and systematic data for establishing the effects of key design parameters on the material behaviour at different scales are very important.

---

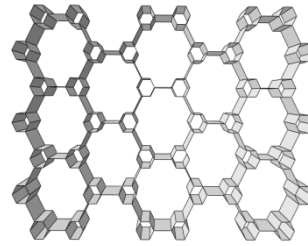
The development in numerical modelling (e.g., finite element modelling (FEM) and physical modelling (molecular and atomic) has improved the understanding of structure-property relationships of many materials. It has offered an opportunity in materials development linked to Poisson's ratio and auxeticity with systematic tools. As a flexible open-source program, Python program integrated with numerical modelling could provide an important tool for both research and development in auxetic materials, applications, and related areas. Python plug-in with graphical user interface (GUI) for modelling the auxetic structures in model building, simulation and data analysis will make the numerical modelling much more efficient. Such a program will also help test the effect of factors such as sample size, lattice patterns as well as establishing the effects of the key design or materials parameters. This is particularly relevant to the missing rib (MR) auxetic models and self-similar Hierarchical honeycombs. MR auxetic structures have attracted much research attention recently (Figure 1.1a). (Remennikov et al., 2019; Koudelka et al., 2016; Gaspar et al., 2009; Adorna et al., 2018; Farrugia et al., 2018; Jiang et al., 2019; Mizzi et al., 2018; Mizzi et al., 2020). The structure was initially developed mainly for tension models (Gaspar and Ren et al 2005, but recently, many of the applications are intended for under in-plane compression loads (Remennikov et al., 2019). It is important to establish a detailed understanding on the deformation process, in particular the contact between the edges and cell walls at high strains for normal missing rib and mixed structures. The edge-cell wall is a unique feature of missing rib models, which could significantly influence the mechanical behaviours and the stability of cell and samples. Mixed structures of regular auxetic structure or random structures could offer opportunities to further enhance the freedom in structures design. It is important to establish the detailed deformation mechanisms, properties, and stabilities. The hierarchical structures (Figure 1.1b) can undergo different deformation modes, resulting in different shapes and Poisson's ratios at different compressive levels (Haghpanah et al., 2013). This gives more options for materials design and development. A parametric program to build the structures and simulate its deformation would help to establish its deformation mechanism and the effect of key dimensional parameters such as the order of hierarchical levels, and the ratio between the edge length of the hexagons

---

at different levels.



(a) A typical 4-4 lattice pattern structure of missing rib structure.



(b) Self-similar hierarchical structure.

**Figure 1.1** Typical missing rib (a) and self-similar hierarchical structures.

The ground state properties of crystals (e.g., bulk modulus ( $K$ ), Young's modulus ( $E$ ), shear modulus ( $G$ ) and Poisson's ratio) are important property data for design, materials selection and processing. Most of the crystals at small scales are anisotropy, their properties are different over different crystalline planes or direction. Some of these anisotropies can be established through experimental testing, but in some cases, it is difficult to establish the full distribution of the anisotropy. This is particularly complicated for the Poisson' ratio. For example, the Young's modulus can be defined based on one direction, but the way Poisson's ratio is defined make it more to represent the anisotropy. In addition, recent work shows that many crystal structures can exhibit negative Poisson's ratio in some directions (Lake, 2017). It is important to establish these features and include the information associated with anisotropy such a range of the properties and potential auxeticity for the data of material groups, which may provide useful information for understanding the properties and manufacturing processes. For example, for developing the data system for stainless steels, there are many precipitated phases such as carbides ( $TiC$ ,  $NbC$ ,  $VC$ ) or nitrides ( $TiN$ ) in stainless steels or welded structures, these precipitates are very small in size, some properties of which could not be physically tested. But their structural, properties and anisotropy data may not only affect the mechanical properties but also influence the grain structure formation in manufacturing and treatment process. For example, many carbides can act as the nucleation agent for

---

metallic phases (Ferrite, Austenite) or more complex carbides such as  $M(\text{Fe}, \text{Cr})_7\text{C}_3$  carbides. So, developing detailed data for these compounds is essential. First principle calculation is increasingly used in predicting crystal structure, electronic, physical, and elastic properties of materials. Materials Studio is a complete modelling and simulation environment to predict and understand the relationships of a material's atomic and molecular structure with its properties and behaviour. First principle calculation is a method to calculate physical properties which based on the principle of quantum mechanics. Typical relevant data from first principles calculation covers elastic constants, physical properties, thermal properties, interface between different phases, electrochemical oxygen reduction reaction, corrosion, etc. (Sun et al., 2010; Cuppari et al., 2016; Wen et al., 2018). The computerised calculation process and subsequent large data analysis could generate a detailed source of materials data for establishing more detailed understanding of material parameters and their correlations. For analysis of mechanical properties, the prediction of the elastic properties involves the mathematical approximation combining the Voigt, Reuss and Hill bounds of bulk and shear moduli (Voigt, 1928; Hill, 1929; Reuss, 1929). In addition, the data from first principle calculation and subsequent analysis also provide the means to estimate the properties such as Vickers hardness based on the ground state elastic parameters/properties (Chen et al., 2011; Tian et al., 2012). As materials informatics is increasingly being applied in engineering analyses and design of complex materials systems, data from physical modelling also offers new opportunities in further understanding of the correlation between different sets of properties with more details. In addition, by integrating first principle calculation with data analysis, it is possible to establish data for enhancing the visualization of the difference of properties in different crystal planes or directions, which could be a useful tool for training use. The data from both macro and molecular level are increasingly providing information through different scales. This is an important future direction.

---

## 1.2 Aims and Objectives

This work aims to develop an effective framework integrating Python based programming with Finite element (FE) modelling for studying the deformation of auxetic structures and *ab initio* quantum mechanical calculations/First principle calculation (Materials Studio CASTEP) for establishing detailed data anisotropy of ground state structural and mechanical properties.

The main objectives are:

- To develop a parametric numerical modelling approach for simulating deformation of two key auxetic structures (missing rib and self-similar honeycombs) and establish the effects of key dimensional parameters.
- To develop an effective approach to measure and monitor the dynamic cell area change during in-plane deformation and correlate the cell area changes with the key deformation stages of regular honeycomb and auxetic structures.
- To evaluate the effects of mixed structures of missing rib models and random structures on the Poisson's ratio and the stability of auxeticity
- To establish an effective modelling approach for developing data and visualisation of the ground state structural, mechanical properties data and anisotropy in single crystal compound and establish the link between Poisson's ratio and anisotropy parameters.

---

## 1.3 Outline of the thesis

In Chapter 2, the key concepts associated with Poisson's ratio and auxeticity and their effects on material behaviours in different loading conditions is reviewed together with research methods. Materials property data together with approaches for representing nonlinear mechanics and strain energy functions of materials in finite element modelling are presented. Main related research works and mechanisms of auxetic structures at different length scales are reviewed. The deformation of cellular structure under different loading conditions/orientation is reviewed with a particular focus on the main deformation stages and effective modelling approaches. Application and development of Python scripts in integrated structure/material modelling, key focuses, and different approaches are outlined. Recent works in modelling crystal structures and data of ground state properties are briefly reviewed, the potential use of the data in material research and development is highlighted. Challenges and significance of developing effective modelling at different scales and systematic data are reviewed and discussed.

Chapter 3 outline the main research works including the parametric numerical modelling of missing rib and self-similar hierarchical structures, 3D printed samples and programs used in first principles calculation of the ground state properties. The focus of the parametric program development is explained with reference to key data in finite element modelling with Abaqus. The main process and functions of Materials studio CASTEP is introduced. The key feature of the Python program and its feature used in this work is described together with its use in image processing and area measurement.

Chapter 4 presents the work on parametric modelling of the deformation of different auxetic structures under tension and compression loading using Abaqus. Part of the focus is on the development of Python based numerical models of typical auxetic structures. The models are used to investigate their deformation behaviours and establish the effect of key dimensional parameters on the deformation process, Poisson's ratio and stability of

---

auxeticity. Python program is integrated with the FE models used to automate building models of different structures and to calculate/analyse key parameters and results. A range of auxetic structures has been developed with a particular focus on missing rib models in tension, missing rib and mixed cellular structures in compression, self-similar hierarchical structures in compression, calculation and tracking of the area changes for cellular structures under compression and tension loads. The discussion covered the key affecting factors on cellular materials deformation, the stability of Poisson's ratios, and the design of the random structures with auxeticity.

Chapter 5 summarizes the main work and key results on developing data for analysing the data and link between crystal structures and key ground state properties of crystals based first principle calculation with Materials studios. The main parts of a Graphical User Interface for processing the data and properties is briefly explained. Some typical results on key engineering carbides including simple cubic systems (TiC, VC and NbC) are presented together with an explanation of the mathematical operation to calculate the K, E, G,  $\nu$  and function for 3D surface constructions of the ground state parameters including anisotropic features. The structure of a Python Graphical User Interface developed for systematic calculation and visualization of the key structures, properties and anisotropy features is explained in detail. The structure and properties of a range of carbides were analysed with a particular focus on the link between the range of Poisson's ratios and anisotropy parameters. In the discussion section, the key factor affecting the accuracy and efficiency of first principle calculation when dealing with data of different material system is outlined. The uncertainty in Poisson's ratio and the link between property data is discussed. The Data for structures with Negative Poisson's ratio is briefly presented and analysed including link between the atomic structure and some macro structure with auxetic behaviours. Some typical data when evaluating the use of materials studio in simulating other properties and processes is also briefly presented and discussed including surface energy, oxygen reduction reaction (ORR), structures with doping elements and the effect of temperatures. The overall

---

use of the system and future work in data development is also discussed.

In Chapter 6, overall conclusions are given, and future work is recommended.

---

**CHAPTER TWO**

**BACKGROUND AND**

**LITERATURE REVIEW**

---

## 2.1 Introduction

In this chapter, the key concept of Poisson's ratio and measurement method with different loading conditions are reviewed. The materials property data and Poisson's ratios of different materials are presented. A review of mechanisms of auxetic structures at different length scales is investigated. The deformation of the regular honeycomb structure in finite element modelling with different key deformation stages is reviewed. The different material models in finite element modelling are presented. The application and development of Python scripts in structure integrating and key focus outlined. The recent work on modelling at different scales and data development is presented. Challenges and significance of developing effective modelling at different scales and systematic data are reviewed and discussed.

---

## 2.2 Poisson's ratio and measurements.

Poisson's ratio is an important material property. It is expressed by the negative value of the ratio between the transversal strain and axial strain when the material is being stretched (Figure 2.1). The Poisson's ratio is determined by the ratio of the transverse strain and axial strain (loading direction) (Equations 1-3).

$$\nu = -\frac{\epsilon_x}{\epsilon_y} \quad (2.1)$$

$$\epsilon_x = \frac{\Delta x}{x_0} \quad (2.2)$$

$$\epsilon_y = \frac{\Delta y}{y_0} \quad (2.3)$$

Where  $\nu$  is Poisson ratio,  $\epsilon_x$  is transverse strain (lateral direction) and  $\epsilon_y$  is strain at the loading direction,  $\Delta x$  is deformation in the transverse direction;  $x_0$  is the original width (diameter for a round cross-section).  $\Delta y$  is the deformation in the loading direction,  $y_0$  is the original length of the sample in the loading direction.

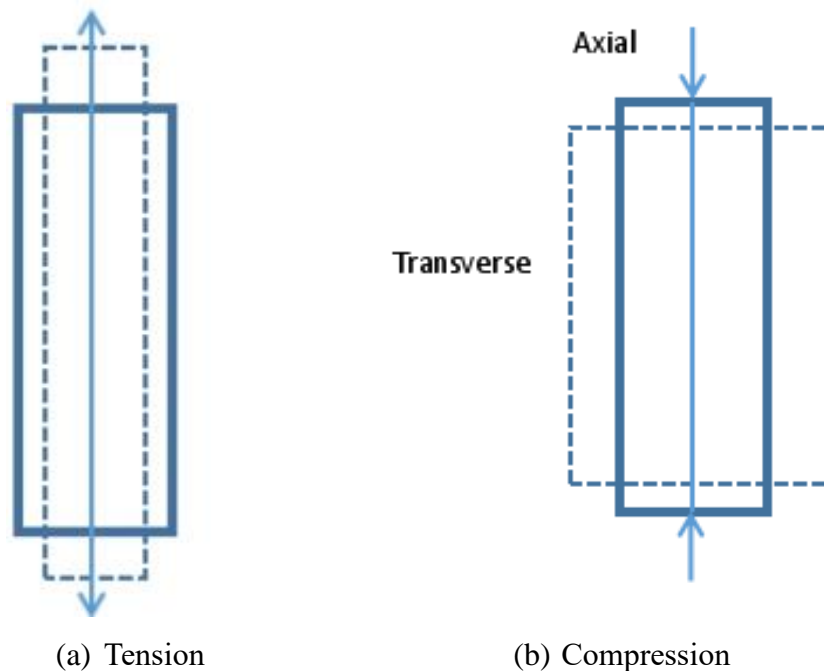


**Figure 2.1** The deformation of a sample under tension or compression.

For an isotropic linear elastic, this leads to the following notation of Hooke's law,

$$\begin{bmatrix} \varepsilon_{xx} \\ \varepsilon_{yy} \\ \varepsilon_{zz} \\ \gamma_{yz} \\ \gamma_{zx} \\ \gamma_{xy} \end{bmatrix} = \begin{bmatrix} \frac{1}{E} & -\frac{\nu}{E} & -\frac{\nu}{E} & 0 & 0 & 0 \\ -\frac{\nu}{E} & \frac{1}{E} & -\frac{\nu}{E} & 0 & 0 & 0 \\ -\frac{\nu}{E} & -\frac{\nu}{E} & \frac{1}{E} & 0 & 0 & 0 \\ 0 & 0 & 0 & \frac{1}{G} & 0 & 0 \\ 0 & 0 & 0 & 0 & \frac{1}{G} & 0 \\ 0 & 0 & 0 & 0 & 0 & \frac{1}{G} \end{bmatrix} = \begin{bmatrix} \sigma_{xx} \\ \sigma_{yy} \\ \sigma_{zz} \\ \sigma_{yz} \\ \sigma_{zx} \\ \sigma_{xy} \end{bmatrix} \quad (2.4)$$

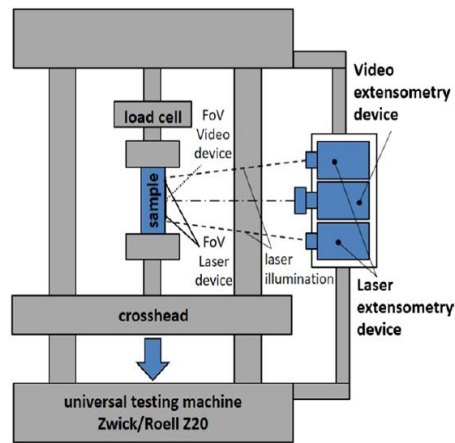
Where E is the Young's Modulus,  $\nu$  is the Poisson's ratio and G is the shear modulus.

There are many different testing methods used to measure the Poisson's ratios such as contact-extensometers, non-video extensometers, video imaging correlation, full field strain correlation (Kumpenza et al., 2018). Figure 2.2a shows a typical contact extensometer, in which the deformation of the sample is monitored by the relative movement between two pins/edges in a tight contact with the sample surface (also called a clip-on). Both the axial displacement (loading direction) and lateral deformation of the sample is measured, then the axial and lateral strain is determined and used to measure the Poisson's ratio following equations (1-3). Figure 2.2b shows the set-up of typical non-contact methods with laser extensometer and video extensometer (Kumpenza et al., 2018). A video extensometer is a non-contact measurement device, in which the relative displacement between the two markers are monitored. It is a convenient method where it is impractical to use a feeler arm or contact extensometer. The monitoring of the sample deformation can be performed based on laser, which can perform measurements of the displacement or strain on materials with clean surface. In the test, the specimen surface is normally illuminated with a laser and the reflections from the specimen surface are then received by a CCD (charge-coupled device) camera. One significant advantage of a laser extensometer lies in the fact that markers to the specimen is not completely necessary, this makes the testing much easier. Figure 2.2c is a typical example of full field mapping method (Wen et al., 2019). In this work, fluorescent digital image correlation (FDIC)

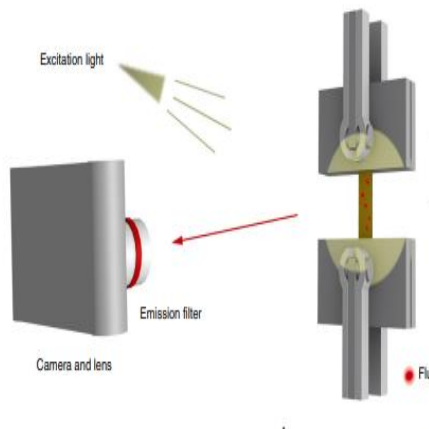
is used to measure the in-plane deformation of a film specimen. The process works by tracking speckle pattern in the reference and the deformed images during the loading process. This normally requires a computer algorithm to match the points based on the pixel/grey scales (Hu et al., 2017). The digital image correlation technique allows measurement of the full-field displacements with sub-pixel accuracy. A precondition is that speckle patterns are formed using Fluorescent particles to track movement of material points in the film under deformation.



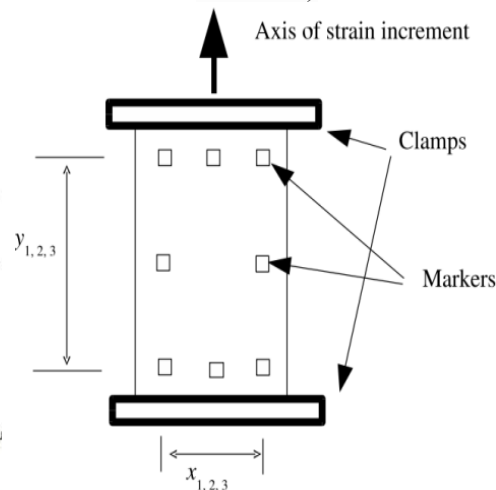
(a) Contact extensometer  
<https://www.epsilontech.com/products/transverse-and-diametral-extensometer-model-3575/>



(b) Non-contact measurement. The laser extensometry and video extensometry system. (Kumpenza et al., 2018)



(c) Full field mapping method  
 (Wen et al., 2019)



(d) Marker position for testing the in-plane Poisson's ratio. (Gaspar and Ren et al., 2005)

**Figure 2.2** Different approaches of testing and analysis of Poisson's ratio.

---

For the video-based method, normally, special reflective markers or markers made of pens that distinguishes the marker from the specimen base colour and texture in the captured image are required. The distances between these markers are constantly tracked in the captured video in the captured image, while the specimen under test is stretched or compressed. Calculation can be done easily with the photo if an object (such as a ruler/scale or a feature with known dimensions) is in the photo taken in similar conditions, at both axial and lateral direction. For Poisson's ratio measurement, the position of the markers could affect the measurement results directly. For 2D material such as a sheet or mesh or honeycomb, the marks could be placed close to the edge of the sample rather than using the markers on the edge to avoid the boundary effect. A typical setting used by [Gaspar and Ren et al \(2005\)](#) shown in Figure 2.2d is widely used. The set-up was used to measure the Poisson's ratio of several thin auxetic honeycombs with positive or negative Poisson's ratios. In the test, the samples (e.g., honeycomb, meshes, thin sheet) were clamped at both ends and subjected to a strain along one axis, three pairs of markers were used in both longitudinal and lateral directions, located approximately at 1/4; 1/2 and 3/4 of the length and width. The sample under strain was imaged and digitized. The changes of the separation between the markers in the two directions (longitudinal and lateral) were measured from the digitized images and the axial strains were calculated. With the development of imaging technologies, this approach is becoming very popular. The image can be done with CCD, optical cameras or other imaging equipment. Increasingly, mobile phones are being used to capture images in materials testing ([Chen et al., 2017](#); [Yelleswarapu et al., 2019](#)). In this approach, smart phones are used to capture images in a much more flexible way, then the image is correlated by frame by frame. For example, in the work by [Chen et al \(2017\)](#), the contour of a pendent droplet is captured by a smart phone, then an algorithm is used to calculate the contour and calculate the surface tension. This is particularly convenient for materials such as foams or materials under complex/non homogenous in-plane or out-of-plane deformations. For cellular materials, the regular connection points could naturally form points for measurement. The development of an imaging analysis program is also relevant to the Poisson's

---

ratio measurement. Instead of expensive specialized image analysis software, many other image analysis methods (such as ImageJ ([Sheffield, 2007](#)), Potrace ([Selinger, 2003](#))) can be used to either measure the deformation from images under different strains, and/or tracking the distance between markers on the sample being tested. These will provide more data for materials testing and analysis of Poisson's ratio, the measurement of which is more complicated than other materials properties such as Young's Modulus. The Young's Modulus can be measured by recording the force and displacement, then converting the force into stress and displacement into strain.

---

## 2.3 Materials property data and Poisson's ratios of different materials.

Poisson's ratio is one of the most important material parameters, and it influences the mechanics of materials and many other functional properties (Evans, 1991). This is evident in the key mechanic formula when the material is under both well-defined loading conditions (compression, tension, and shear) and non-standard loading conditions (such as indentation, bending etc.). When a material is under plane stress conditions (very thin sample), the stress in the thickness direction is zero. The shear modulus  $G$ , which is the indication of the resistance of the material to shear loading, is related to Young's modulus ( $E$ ) and the Poisson's ratio by the following equation:

$$G = \frac{E}{2(1+\nu)} \quad (2.5)$$

For a free block of the material that is in stable equilibrium, the elastic modulus  $E$  and shear modulus  $G$  must be positive, therefore the Poisson's ratio must be equal to or larger than  $> -1$ . (Lakes and Witt, 2002). The bulk modulus, the relative change in the volume of a body due to a compression or tensile stress acting uniformly over its surface, is linked to the Poisson's ratio and Young's modulus of the substance by

$$K = \frac{E}{3(1-2\nu)} \quad (2.6)$$

As  $K$  is a physical property, the bulk modulus  $K$  has to be a positive value, so  $0 < \nu < 0.5$  (Lake and Witt, 2002). So, for a material to be stable, the rule is  $-1 < \nu < 0.5$ .

The Poisson's ratio also affects the deformation when the material is under complex loading. For example, for localized loading such as indentation, where an indenter is pressed into a material, the effect of the Poisson's' ratio is dependent on the indenter shapes. The analytical solution (Equation 2.7) for flat-ended cylindrical indentation on a homogeneous material is (Aw et al., 2015).

---

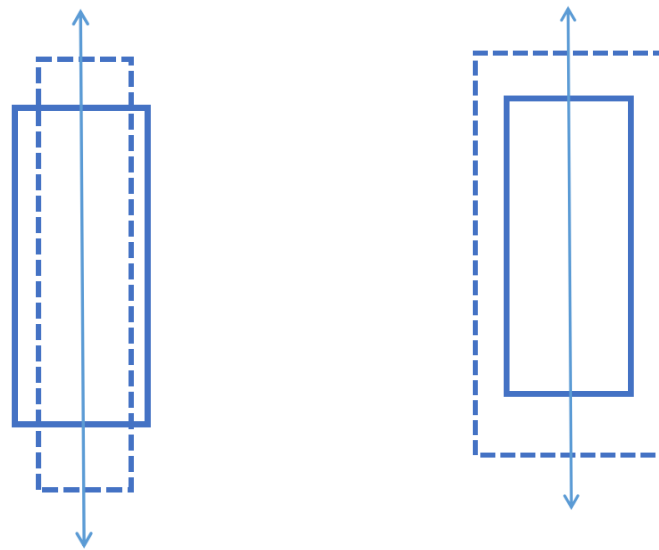

$$P = \frac{2bE\Delta}{(1-\nu^2)} \quad (2.7)$$

Where ‘P’ is the load on the indenter, ‘b’ is the radius of the cylindrical indenter; ‘E’ is the Young’s Modulus of the matrix. ‘ν’ is the Poisson’s ratio of the matrix. ‘Δ’ is the displacement of the indenter. For indentation of a thin membrane, the analytical solution force-displacement is represented by [Aw et al \(2015\)](#).

$$\Delta = f(\nu)a\left(\frac{p}{Eat}\right)^{\frac{1}{3}} \quad (2.8)$$

In equation (2.8), ‘a’ is the dimension of the chamber supporting a thin membrane; p is the load on the indenter and t is the sample thickness. These equations show the Poisson’s ratio has a complex influence on the material behaviour. Other works also show that the Poisson’s ratio could influence the materials deformation, for example thin sheet embedded in an elastic matrix ([Li et al, 2017](#)), liquid droplet impact onto soft materials ([Al-Badani, 2020](#)). For material properties such as Young’s Modulus or shear modulus, their value is always positive. But the values for Poisson’s ratio could be positive or negative. As shown in Figure 2.3, for a positive Poisson’s ratio, the material shrinks upon being stretched, and gets expand when being compressed, while with a negative Poisson’s ratio materials, the materials expand when being stretched. The material shrinks when being pressed. The finding of negative Poisson’s ratio material (also termed Auxetic materials, which is derived from the Greek word αὐξητικός (auxetikos) which means "that which tends to increase") has its root in the word αὐξησης, or *auxesis*, meaning "increase" (noun) ([Evans and Alderson, 2000](#)). Auxetic materials are attracting significant attention from researchers from different fields ([Gaspar et al., 2005](#); [Mousanezhad et al., 2015](#)). Apart from its unique mechanical behaviours, Poisson’s ratio can also affect many functional properties, for example, the wave propagation ([Ungureanu et al., 2015](#)). Ungureanu reported that wave propagation through a class of mechanical metamaterials opens unprecedented avenues in seismic wave protection based on spectral properties of auxetic-like metamaterials. The elastic parameters of these

metamaterials like the bulk and shear moduli, the mass density, and even the Poisson's ratio, can exhibit negative values. Numerical data showed that there is a big difference in behaviour between the propagation of seismic waves through a homogeneous isotropic elastic medium (concrete) and an auxetic-like metamaterial plate. This novel class of seismic metamaterials opens band gaps at frequencies compatible with seismic waves when they are designed appropriately, what makes them interesting candidates for seismic isolation structures.



(a) Deformation of a Non-auxetic material in tension. (b) Deformation of an auxetic material in tension.

**Figure 2.3** Schematics showing the different behaviour of Non-auxetic and Auxetic Materials in tension and compression.

Figure 2.4 shows the Poisson's ratio of different material groups, its effect on bulk and shear moduli. The data shows that most materials have a positive Poisson's ratio. For example, metals (e.g., steel, copper, aluminum) have a Poisson's ratio between 0.2-0.3; ceramics have a Poisson's ratio range 0.1-0.2, while the Poisson's ratio for polymers varies from 0.3 (for engineering plastics) to 0.5 for rubber or gels (representing in-compressibility, i.e., no volume change when deformed). Concrete and bone have a relatively low Poisson's ratio. It has been known for a long time that Cork has a very low Poisson's ratio, which makes it ideal for application as a wine bottle stopper, being easier to put in and out due to the low lateral deformation. Some

representative groups with auxetic behaviours relevant to engineering include carbon nano tubes sheets (Scarpa et al., 2010; Baimova et al., 2017), re-entrant foams (Spagnoli et al., 2015; Duncan et al., 2018), laminates (Lim et al., 2009; Milton et al., 1992), and colloidal crystals (Tretiakov et al., 2014). The honeycomb quoted in the figure 2.4 is a designed honeycomb with a low in-plane Poisson's ratio (Grima et al., 2010). Regular honeycomb (with a cell wall of 120 degree) has a Poisson's ratio close to 1 (Hoffman, 1958; Papka and Kyriakiudes, 1994). The figure also shows that the Poisson's ratio is loosely correlated to the ratio between the shear modulus (G) and the bulk modulus (K) but follows a different trend at different G/K ranges.

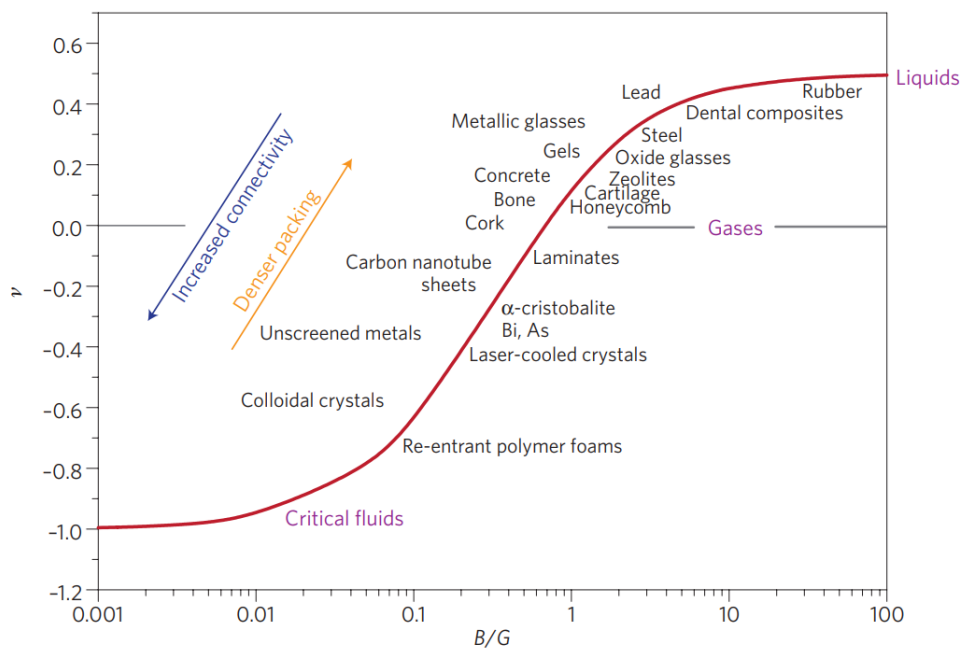


**Figure 2.4** Poisson's ratio of different material groups and its link with bulk and shear modulus. (Greaves et al., 2013)

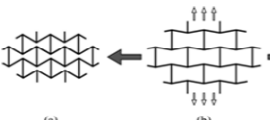
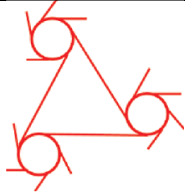
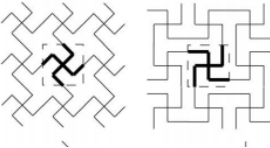
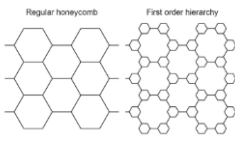
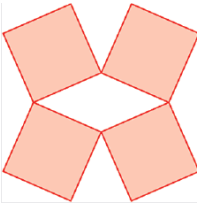
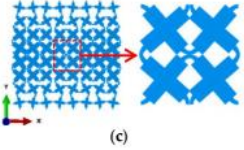
---

## 2.4 Mechanisms of auxetic structures at different length scales.

The factors influencing the Poisson's ratio of a material have been the topics of intensive research and development, in which many different investigative approaches were being used including theoretical, experimental and more recently computational, evident from a recent review and several other review papers (Greaves et al, 2012; Lakes, 2017, Duncan et al, 2018). Analytical works involve mechanical analysis of the deformation, movement/rotation of beam or cell walls under simplified loading conditions (Gaspar and Ren, 2005; Lake, 2017). The computation works involve both numerical modelling and molecular simulation (Yao et al., 2016; Mizzi et al., 2018). Many factors may affect the Poisson's ratio and the auxeticity, among which geometry at different scales are the main factors (Selvadurai, 2009; Mitschke et al., 2016). The research and development work has established many different mechanisms which may lead to auxetic behaviours, which has opened up more opportunities to develop negative Poisson's ratio materials at different length scales (Riccardi and Montanari, 2004; Selvadurai, 2009; Shariatmadari, English and Rothwell, 2010; Sissler et al., 2013; Wafai et al., 2015; Yu et al., 2008). Table 2.1 lists some selected structures with auxetic behaviours. In the re-entrant structure (Table 2.1a), one of the points for a regular hexagonal auxetic is pointed inwards. When a tensile force is applied in the horizontal direction, the ribs move outward and the structure expands in a vertical direction giving rise to auxetic behaviour. In other words, in a Re-entrant honeycomb cell, bendable ligaments give rise to a negative Poisson's ratio. The extent of the auxetic behaviour depends on the length of horizontal rib, length of inclined rib, thickness and depth of ribs, and angle of inclined rib with the vertical axis. As shown in the chiral structure (Table 2.1b), the six ligaments are attached tangentially to each rigid ring, when a load is applied in one direction, it causes the rotation of rings which gives rise to auxetic behaviour in the transverse direction. Chiral honeycombs display the auxetic effect for both in-plane and bending loads, which is achieved by arranging the cylinders on the base of a re-entrant structure (Rad et al., 2014). In the missing

rib model (Table 2.1c), the model is based on a network of ribs with bi-axial symmetry, and the “auxetic” form is a similar network but with a proportion of cell ribs removed (Smith et al., 2000). The auxetic behaviour is obtained by selective removal of ribs from hexagonal structure without changes in the internal angles. The Hierarchical honeycomb structure (Table 2.1d) involves replacing the varieties of a regular hexagonal lattice with smaller hexagons. This can be repeated to different levels by repeating the operation of replacing the varieties and forming a hierarchy of different orders (e.g., 1st, 2nd, 3rd). The origin of this behaviour is linked to the added hexagonal features within the hierarchical structure which make the instabilities occur at smaller compressive strains compared to the original non-hierarchical structure leading to auxetic behaviour (Mousanezhad et al., 2015). The rotating rigid/semi-rigid units (Table 2.1e) are formed by connecting straight ligaments (ribs) to central nodes which may be circles or rectangles or other geometrical forms (Grima et al., 2012). Table 2.1f is a buckling of connecting model. There are also other models which have been covered by several reviews (Duncan et al., 2019; Lake, 2017)

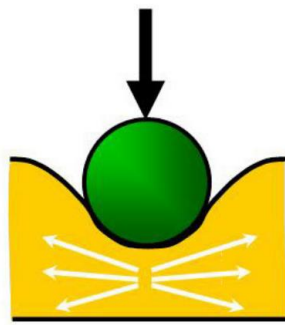
**Table 2.1 Typical mechanisms of structure with auxetic behaviours.**

Mechanism/ principles	Typical Structure	Mechanism/ principles	Typical Structure
(a) Re-entrant structures (Gibson et al., 1982)		(b) Chiral structures (Grima et al., 2008b)	
(c) Missing Rib (Gaspar et al., 2005)		(d) Hierarchical honeycomb (Mousanezhad et al., 2015)	
(e) Rotating units (Grima et al., 2006)		(f) Buckling of connecting (Cabras and Brun, 2014)	

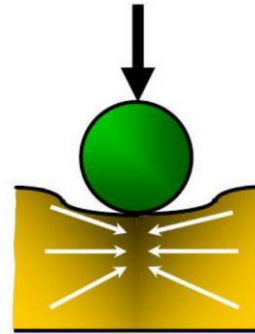
---

The negative Poisson's ratio could change the material behaviour in different loading conditions. Their unique properties opened a window towards a wide range of applications such as the design of novel fasteners, biomedical applications, energy-absorbing devices, acoustic dampers, membrane filters with variable permeability, personal protective equipment (e.g. shin pad, etc.) and smart implant (Sanami et al, 2014; Darwish and Aslam., 2014; Mousanezhad et al., 2015; Aw et al., 2015; Lake, 2017; Duncan et al., 2018). From the natural definition of the material, the material expands under tension, this could lead to applications such as novel bandage, seat belt (Sanami et al., 2014). For application such as novel bandage or seat belt, as the materials are getting wider rather than thinner under tension, this could avoid the loss of shape and maintain uniform pressure. Under indentation the material with a negative Poisson's ratio tends to move in rather than move away from under the indenter (Figure 2.5 a &b). Negative Poisson's ratio also affects the doming of structure, which is relevant to applications such as helmet (Mir et al., 2014; Lake, 2017; Duncan et al., 2018). Doming is caused by axial (due to loading) and lateral (due to Poisson's ratio) extension on the upper surface combined with equivalent contractions on the lower surface. Negative Poisson's ratio materials will contract laterally on the upper surface and expand laterally on the lower surface. The auxetic materials have a natural tendency in bending to form dome-shaped doubly curved (synclastic) surfaces (in Figure 2.5c&d), unlike conventional materials which tend to form saddle-shaped surfaces (Mir et al., 2014). Figure 2.5 (e&f) shows the sample used in application of auxetic in filtering applications. Figure 2.5 (e) is a conventional structure design, Figure 2.5 (f) is an auxetic structure. The work used small-sized glass beads initially resting on the membrane then stretched the sample and observed the opening of the cells (Alderson et al., 2000) The work showed that the auxetic sample opens more to allow the beads to pass through the membranes. The work also modelled the pore-opening properties of both types of membranes, and the observed behaviour for the auxetic membrane is consistent with the model. For more complex filtering applications, the filter needs to release particles/components with selected dimensions because of the enlargement of its unit cells when swollen by a

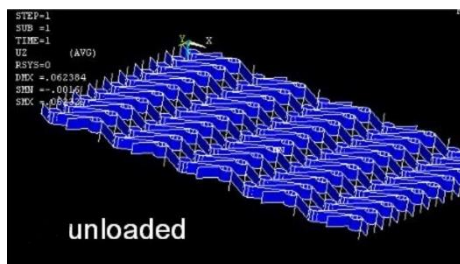
liquid. Conversely, auxetic porous filters could absorb liquids at higher volume than conventional porous materials (Scarpa et al., 2020).



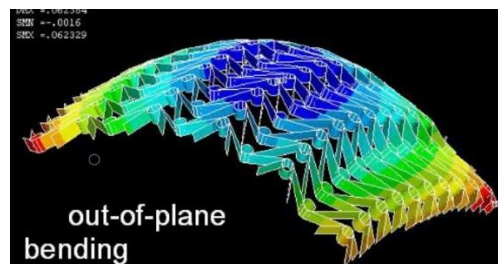
(a) Deformation of a non-auxetic material under the indentation of a spherical indenter. (Sanami et al., 2014)



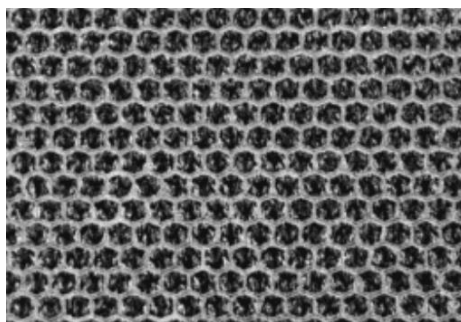
(b) Deformation of an auxetic material under the indentation of a spherical indenter. (Sanami et al., 2014)



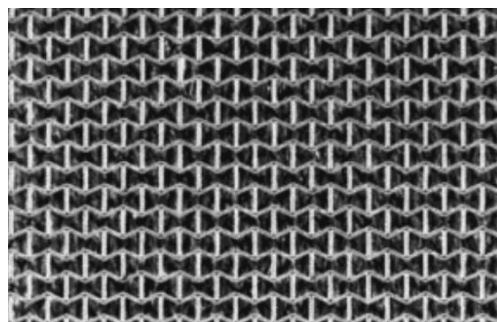
(c) Underformed FE modelling of Chiral Arrowhead Honeycomb In bending (Sanami et al., 2014).



(d) Deformed FE modelling of Chiral Arrowhead Honeycomb in bending (Sanami et al., 2014).



(e) Polymeric conventional honeycomb membrane. (Alderson et al., 2000)



(f) Polymeric re-entrant honeycomb membrane. (Alderson et al., 2000)

**Figure 2.5** Deformation of auxetic materials under different loading conditions and applications.

---

Different forms of auxetic materials such as Polymer foams, Honeycomb, Tubes, Fibres, Shell/Membranes and spheres can be produced (Liu et al, 2010; Mir et al., 2014; Lake, 2017; Ren et al., 2018). These developments in research methods and techniques, wide ranges of mechanism discovery and establishment, manufacturing methods (both conventional and 3D printing) have greatly enhanced the understanding of Poisson's ratio, auxeticity. and potential applications. The work on auxeticity has also opened up many design ideas and brought new direction and requirements for modelling and development of data systems of which previously Poisson's ratio was not a main focus. One major area is in cellular structures as an active development area both in design and applications. The structure, deformation mechanic and main Auxetics structures are to be briefly introduced in the next section in comparison with research into conventional honeycomb structures with a particular focus on structure and their effect on the deformation process.

---

## 2.5 Regular honeycomb structure, FE modelling and key deformation stages.

The properties of a cellular structure are controlled by the structure, material and manufacturing process. The most common one is the regular honeycomb structure, which has a basic cell of hexagonal shape with 120-degree wall angle, normally the length of the beam is much bigger than the thickness of the shell. Honeycomb is manufactured via the expansion process and the corrugation process as shown in Figure 2.6 (Tian, 2012; Kaman et al., 2010; Rebhi et al., 2016). The in-plane and out of plane deformation of honeycomb has been subject of many studies. (Papka and Kyriakides, 1994; Wilbert et al., 2011; Soroohan et al., 2016; Ajdari et al., 2011). One particular focus of these works is the deformation stages of the cellular structures. Wilbert et al (2011) studied a lateral compressive response of hexagonal honeycomb panels from the initial elastic regime to a fully crushed state. Figure 2.7a shows the mesh used and loading conditions. The work used shell elements and the load is applied from the top (out of plane direction). The work used the nonlinear FE code ABAQUS using S4 shell elements, which is a fully integrated 4-node element that allows for finite membrane strains. As shown in Figure 2.7b the nonlinear deformation is associated with initial elastic buckling, then inelastic collapse leads to the localization occurring at a higher load. It is also reported by the authors that imperfections also influence the collapse stress. As shown in the figure 2.7, an imperfection reduced the stress to reach the collapse stage. Figure 2.7c&d shows the full deformation stages. As shown in Figure 2.7c, the numerical model is able to predict the trend of the full deformation process and all the main stages as indicated by the numbers (0-9). As shown in Figure 2.7d, the crushing involves contact between folds of adjacent cell walls as well as self-contact. In the FE model, contact was assigned for both sides of the cell walls (Abaqus “all exterior” parameter). This process ensures that contact occurs at the actual surface of the walls since shell elements was used. The calculated crushing response is shown to resemble measured deformation reasonably well and the average crushing stress can be captured with a

reasonable accuracy (Wilbert et al, 2011).

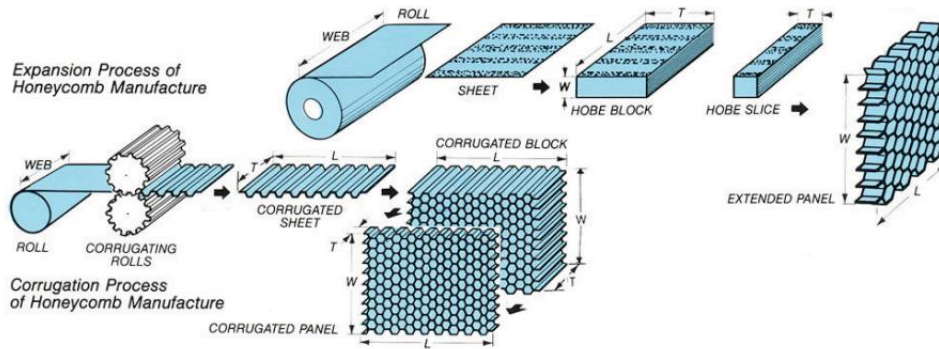
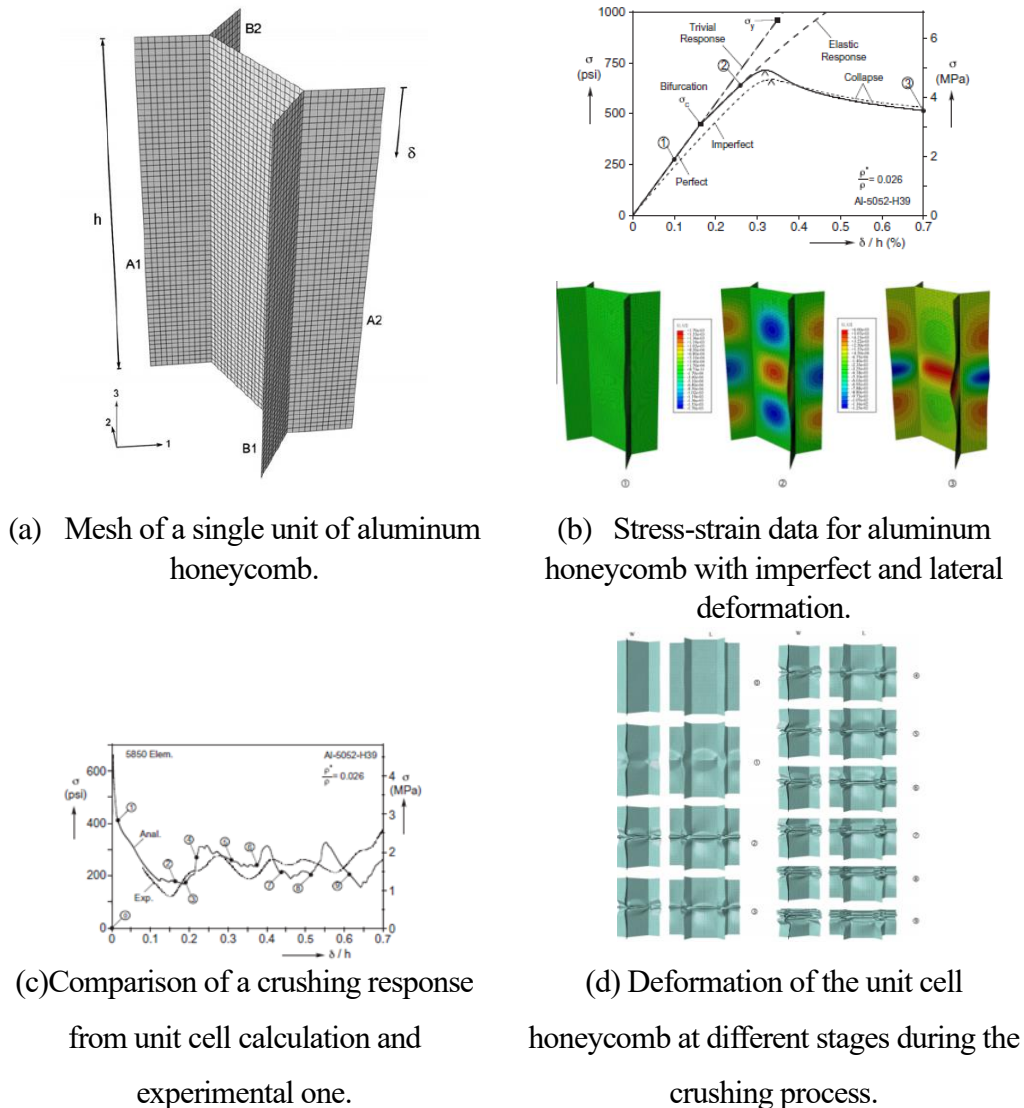


**Figure 2.6** Manufacturing processes of hexagonal cell type honeycomb core (Tian., 2012).



(a) Mesh of a single unit of aluminum honeycomb.

(b) Stress-strain data for aluminum honeycomb with imperfect and lateral deformation.

(c) Comparison of a crushing response from unit cell calculation and experimental one.

(d) Deformation of the unit cell honeycomb at different stages during the crushing process.

**Figure 2.7** FE models and typical results of a laterally loaded honeycomb. (Wilbert et al., 2011)

---

Papka and Kyriakides (1994) presented a systematic study on In-plane compressive response and crushing of honeycomb combining experiment and mechanical analysis. A typical result comparing the analysis and experimental data is shown in Figure 2.8a. In the experiments, an in-plane compression was applied on an aluminium (AI-5052-H39) honeycomb specimen along the direction of the members with double wall thickness (as the corrugated sheets are bonded together to form corrugated blocks in the manufacturing process as shown in Figure 2.6). In the work, a test specimen with a 9-6 lattice was compressed from a displacement controlled, quasi-static experiment ("strain" rate of  $2.6 \times 10^{-3} \text{ s}^{-1}$ ). The specimen has a periodic microstructure, as shown in the figure, the effective stress-strain data exhibits a relatively sharp initial rise to a load maximum, then followed by a load plateau, then a sharp rise in load is followed. The stress is calculated by reactive force divided by the cross-sectional area perpendicular to the loading direction. The strain is displacement divided by the original height. As shown in Figure 2.8b, the material deforms essentially in a uniform fashion (stable) for the first part of stress-strain curve (Stage (1). Then the deformation starts to become highly confined after the load maximum, it localizes to one row of cells, the cells collapse (accompanied by dropping overall load) until the walls of each cell come into contact. Once the cell walls are in contact, the deformation is spread to the adjacent/next rows. As it is done with displacement-control, this way of deformation (i.e., row by row collapse) continued, there are relatively limited changes in the load/stress. After the whole specimen is collapsed, all the cells are in contact (densification), the load starts to increase more stiffly/sharply. These simulated key stages showed a reasonable agreement with experiment images.

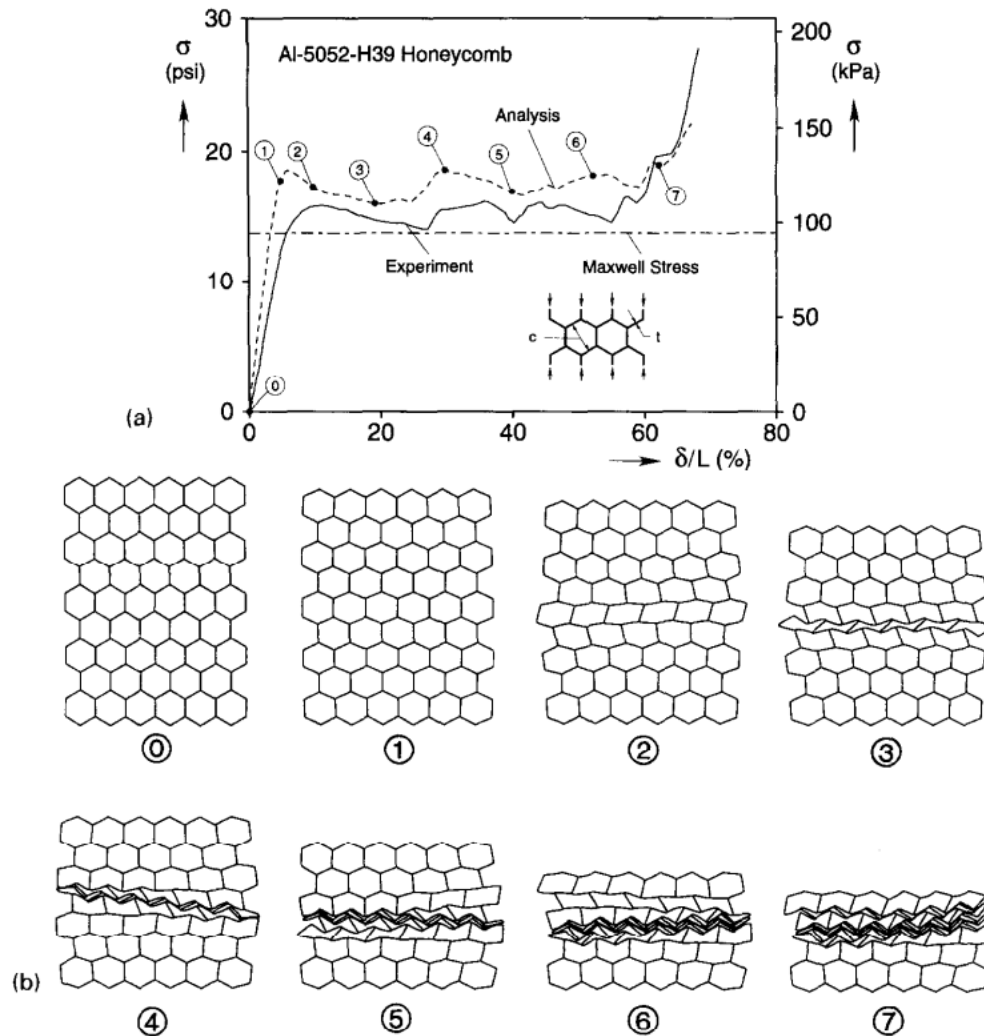
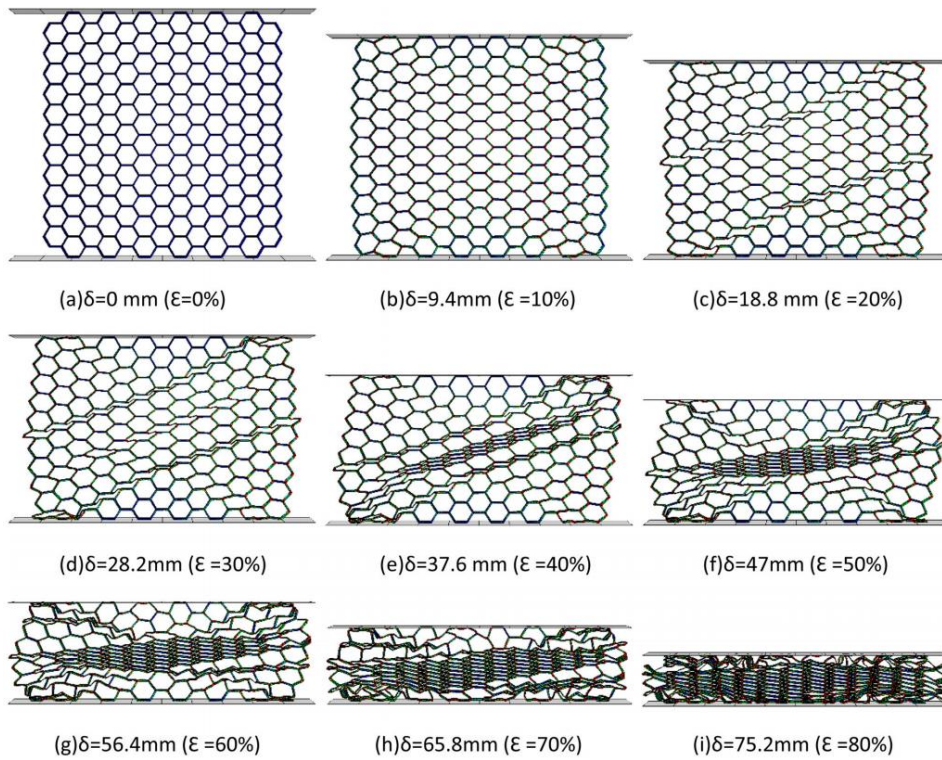


**Figure 2.8** Comparison of measured and calculated force-displacement responses of a honey-comb specimen and calculated collapse configuration. (Papka and Kyriakides, 1994)

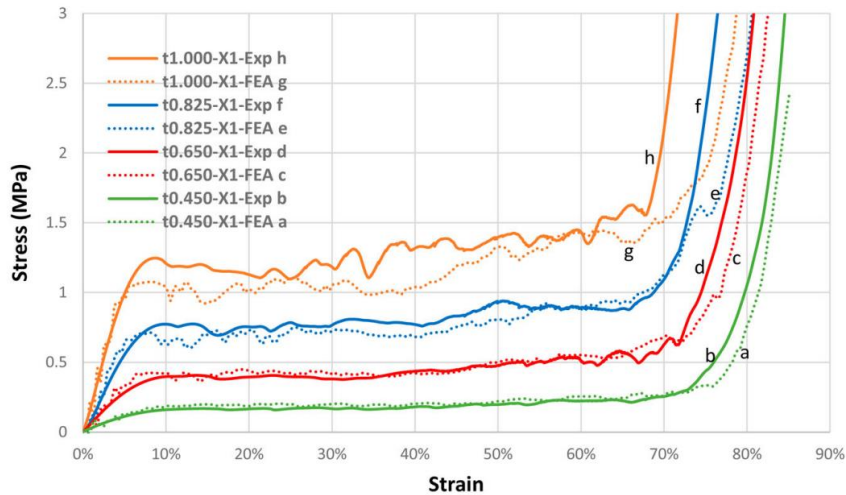
The loading of hexagonal honeycomb has also been studied by experimental and numerical modelling. (Ajdari et al., 2011; Baumgart et al., 2018). Ajdari et al (2011) used dynamic explicit solver with general frictionless contact available in ABAQUS to simulate the in-plane dynamic response of the honeycombs under impact and crushing. In the work, the general contact option available in ABAQUS was used, the geometrical model was extruded normal to its cross section to create three dimensional models of honeycomb. The model was meshed with 4-node shell elements and plane strain condition was imposed on the model by constraining the out of plane degrees of

---

freedom along the edges of the cell walls. A mesh sensitivity analysis was carried out to ensure that the results are not sensitive to the mesh size. The work tested many different loading rates and established a deformation map for regular honeycomb structures subjected to dynamic crushing depending on the crushing rate and honeycomb relative density of the structure. A recent work ([Habib et al., 2017](#)) studied the in-plane energy absorption of 3D printed polymeric honeycombs. The material properties of Nylon 12 were used in finite element analysis (FEA) simulations. The deformation of 3D printed plastic samples was established, and the typical deformation mode and data are shown in Figure 2.9. Figure 2.9a shows the deformation stages of FEA honeycomb structure under quasi-static compression. Figure 2.9b shows the effect of the wall/shell thickness on the deformation and stress level. The honeycomb structures become unstable at around 10% strain, and reach densification at around 70%. The overall stress-strain curve shape is similar, but the stress is higher for a thicker shell. The critical strain for reaching the densification stage for a thinner shell is slightly higher. In general, the FE modelling is able to predict the force-displacement data with shell element. Many papers have also studied different shapes and mixed structures such as triangle, square, diamond, ([Ren et al., 2010](#); [Habib et al., 2017](#); [Langrand et al., 2017](#)). For example, in a recent work, [Baumgart et al \(2018\)](#) studied the effect of honeycomb cell geometry on compressive properties through Finite element analysis and experimental verification. In the work, FE shell mode was used to establish the deformation of Kagome lattices at two different loading directions and square lattice. A typical set of data is shown in Figure 2.10. The Kagome lattices are described as intersecting webs of corner-sharing triangles or an ordered sequence of hexagons and triangles. As shown in Figure 2.10a, the pattern of deformation is clearly different. The Kagome lattice is much more stable than the square lattice, the square lattice has clearly lost its shape stability. The FE modelling is able to establish the difference in the deformation stages and pattern as well as force-displacement data between these structures. These works on modelling and experiments have laid a good foundation for modelling auxetic and mixed structures.



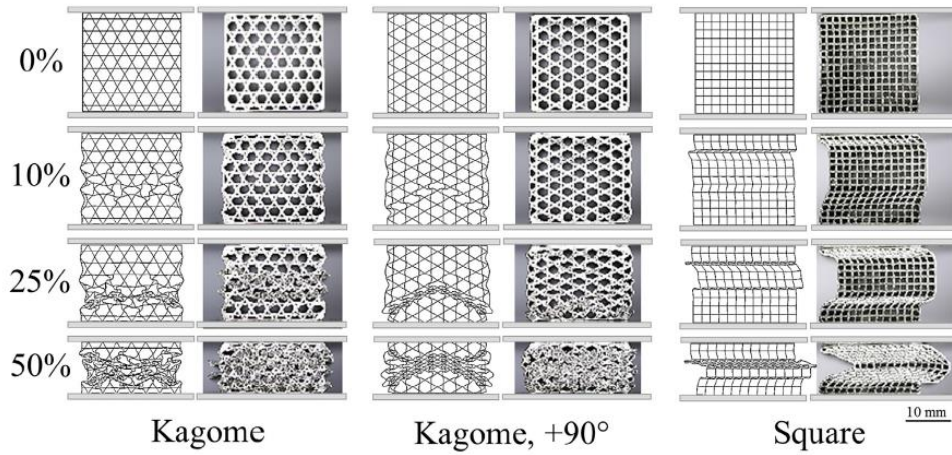
(a) Sequential screen shots of a honeycomb specimen of  $t = 0.450$  mm under quasi-static compression simulation in direction X1 using ABAQUS/Explicit



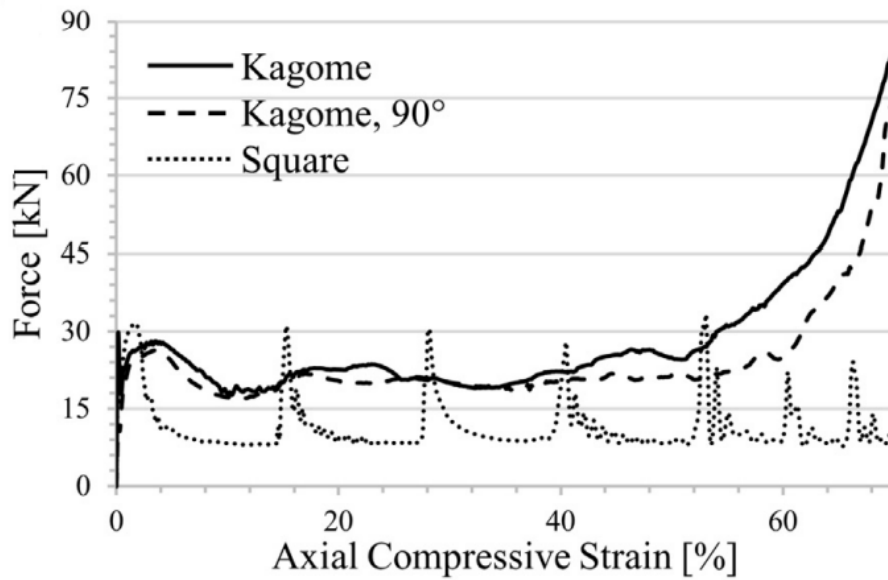
(b) Comparing experimental and numerical stress–strain diagrams when the honeycombs compressed in X1 direction

**Figure 2.9** FE modelling of honeycomb with different dimensions.

(Habib et al., 2017).



(a) Different structure and Deformation of lattice at different strains.



(b) Force displacement data of a Kagome (at two different orientations) and Square lattice.

**Figure 2.10** Typical data showing the effect of honeycomb cell geometry on compressive response of Kagome (at two different orientations) and Square lattice. (Aumgart et al., 2018)

---

## 2.6 Experimental and numerical research in auxetic structures.

The deformation of porous materials under a compression load over large strains is more complex than simple uniaxial tension loading. The deformation of different auxetic structures under compression has been increasingly studied (Bertoldi, 2018; Yang et al., 2018; Cui et al., 2018; Dong et al., 2019; Hedayati et al., 2018; Wang et al., 2018; Remennikov et al., 2019; Hanifpour et al., 2017; Tanaka et al., 2016; Meena and Singamneni, 2019) such as negative Poisson's convex-concave foams (Cui et al., 2018); re-entrant unit cell (Dong et al., 2019; Hedayati et al., 2018; Wang et al., 2018; Remennikov et al., 2019); disordered auxetic metamaterials (Hanifpour et al., 2017); cellular structures (Tanaka et al., 2016); arrowhead structures (Yang et al., 2018) and missing rib auxetic structures (Meena and Singamneni, 2019; Smith et al., 2000; Gaspar et al., 2003; Adorna et al., 2018; Farrugia et al., 2018; Jiang et al., 2019; Koudelka et al., 2016; Remennikov et al., 2019). Yang et al (2018) studied the behaviour of auxetic structures under compression using both static model and dynamic model. The results showed that auxetic materials could be effective in reducing the shock forces. The properties such as stiffness, Poisson's ratio, and efficiency in shock absorption were found to be dependent on the structure and material combination. Dong et al (2019) studied the compressive mechanical properties of the metallic auxetic re-entrant honeycomb. The work found that the modelling results are affected by the number of cells used in the finite element model. Wang et al (2018) compared the characterization of composite three-dimensional re-entrant auxetic cellular structures made from carbon fibre reinforced polymer and single materials. The composite 3D re-entrant auxetic structure showed the potential to significantly increase the specific stiffness of the structure. Remennikov et al (2019) studied the quasi-static compression and drop hammer impact tests of sandwich panel design with re-entrant honeycomb design. The results suggest that sandwich panels with a re-entrant honeycomb core have a strong potential for lightweight impact-

---

resistant protective systems. Apart from research on single mechanism structures, several works have been reported exploring the use of mixed structures which combined auxetics materials with different mechanisms (Cabras and Brun, 2014; Fozdar et al., 2011; Hedayati et al., 2018; Hu et al., 2019; Meena and Singamneni, 2019; Nika and Constantinescu, 2018; Streck et al., 2017; Yang et al., 2015). All these have opened up opportunities in design materials with auxetic structures.

In all these cases, the use of auxetic structures showed significant potential benefits on the functional performances such as improved impact energy, resistance, and acoustic properties (Lakes, 2017; Ren et al., 2018). The work also shows that the influence of auxeticity could be highly structure and materials dependent. Factors such as sample size may directly affect the material deformation and stability of the key properties (e.g. auxeticity) for some structures. This is an important issue for design and manufacture of auxetics structures or mixed-structure systems (Jiang et al., 2019). Furthermore, if the auxeticity effect is induced by instability in porous materials and lattice structures (Babae et al., 2013; Shim et al., 2013; Duncan et al., 2018; Zhang et al., 2015), the instability at cell level may cause loss of symmetric structures at a macroscale, thus directly influencing the shape of deformation process of the cell and the samples. Missing rib auxetic structure is one of the most active research topics. (Smith et al., 2000; Gaspar, Smith and Evans, 2003; Gaspar et al., 2015; Adorna et al., 2018; Farrugia et al., 2018; Jiang et al., 2019; Koudelka et al., 2016; Remennikov et al., 2019). The basic structure (as shown in the previous section (Table 2.1 (c)), consists of both vertical and horizontal columns that potentially could lead to auxetic behaviours pending on the angles and beam lengths (Gaspar et al., 2005). The original model developed has been expanded to some new structures. Soman and Chen (2013) discussed the use of missing rib structure in projection printing of three-dimensional tissue scaffolds with tunable Poisson's ratio. In the work by Koudelka et al (2016), the compressive properties of missing rib structure made by acrylic material were studied. Remennikov et al (2019) reported a recent work on using 3D printed missing rib structures for protective systems. Farrugia et al (2018) studied the different deformation

---

mechanisms leading to auxetic behaviour in missing rib structures. A parametric analysis using finite element analysis revealed that two mechanisms can act, one involving the bending of the ligament and the other the bending of the crossed ligaments. The results indicate that the former leads to a more negative Poisson's ratio than the latter. [Zhu et al \(2020\)](#) reported a recent work on enhanced hexa-missing rib auxetics for achieving targeted constant negative Poisson's ratio and in-plane isotropy at finite deformation. These works show that it is important to establish a detailed understanding on the deformation process, in particular the contact between the edges and cell walls at high strains for both normal missing rib models and mixed structures, which are relevant to the mechanical behaviours and the stability of samples. Mixed structures (missing rib model with different angles or mixtures of missing rib model with other structures) could offer opportunities to further enhance the freedom in structures design.

---

## 2.7 Different materials models in finite element modelling

Apart from an effective modelling method, the properties of the solid material in building the foam or cellular material are also important for understanding the performance of cellular structures. This includes density, thermal conductivity, stiffness, yielding. The materials can have different materials models to describe their stress strain curves, which can influence the linear and nonlinear behaviour of cellular structure (such as the initial linear part, the buckling, instability, and the densification process as shown in Figure 2.7, 2.8, 2.9). Many materials have been used such as steel, stainless, Titanium, Plastic, Rubber ([Duncan et al., 2018](#); [Lekesiz et al., 2017](#); [Kolken and Zadpoor, 2017](#)) in developing cellular structures, these materials need to be simulated in different material models ([Abaqus Manual Version 2017](#)).

Figure 2.11 shows schematically the main type of stress strain relationships of materials, this is relevant to modelling the solid of the beam or wall materials used in building the cellular. Figure 2.11a is linear elastic, Figure 2.11b is elastic plastic, Figure 2.11c is hyperelastic or hyper foam. As shown in Figure 2.11a, for an elastic material, the stress is proportional to the strain and the strain is recoverable if the stress is removed, i.e., the specimen returns to its original dimensions. This occurs in the initial linear region of the stress-strain curve of plastics, rubber, flexible foams (open cell foam). The linear material behaviours can be represented by the slope of the stress-strain (i.e.,  $E$ ) for an isotropic material. But for an anisotropic material, the stiffness may be affected by the Young's modulus in different directions.

Figure 2.11b shows a typical stress-strain curve of elastic-plastic material (such as steel and plastics), Nylon. The engineering stress and strain, denoted as  $\sigma_e$  and  $\varepsilon_e$  respectively, are determined from the measured load and material deformation against the original specimen cross-sectional area. In the elastic portion of the curve, many materials obey Hooke's law; stress is proportional to strain with the constant of proportionality being the modulus of elasticity or Young's modulus is defined as the ratio of the stress over the

strain.

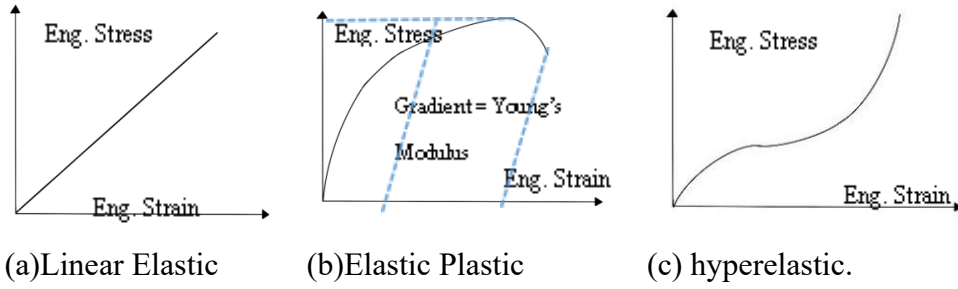


**Figure 2.11** Different stress strain curves for linear elastic, elastic-plastic materials (metal and plastics) and hyperelastic material behaviours.

The plastic behaviour is normally described by the three-parameter power-hardening rule commonly used as:

$$\sigma = \sigma_y + K\epsilon^n \quad (2.10)$$

where ' $\sigma_y$ ' represents the yield stress, ' $\epsilon$ ' represents the plastic strain, ' $K$ ' represents the strength coefficient and ' $n$ ' represents the strain hardening exponent. In Abaqus, the input of plastic properties is the plastic stress and strain data in a tabular form ([Abaqus 2017 User's Manual](#)).

For hyperelastic behaviour as shown in Figure 2.11(c), the initial part is close to a linear relationship, then the stress reaches the plateau stage showing limited change with increasing strain. Many different function/materials models have been developed to describe different materials ([Abaqus 2017 User's Manual](#)). Mooney-Rivlin model in terms of strain energy can be used for rubber. Equation 2.11 is the initial proposed linear form of strain energy functions as:

$$W = C_1(C_1 - 3) + C_2(C_2 - 3) \quad (2.11)$$

In the equation,  $C_1$  and  $C_2$  are constants  $I_1$  and  $I_2$  are the first and the second invariant of the unimodular component of the left Cauchy–Green deformation tensor:

$$\bar{I}_1 = J^{-2/3} I_1; I_1 = \lambda_1^2 + \lambda_2^2 + \lambda_3^2; J = \det(F) \quad (2.12)$$

$$\bar{I}_2 = J^{-4/3} I_2; I_2 = \lambda_1^2 \lambda_2^2 + \lambda_2^2 \lambda_3^2 + \lambda_3^2 \lambda_1^2 \quad (2.13)$$

---

The Mooney-Rivlin material was originally developed for rubber, but it is applicable to many incompressible rubber-like materials. This equation gives a marginally better fit to some of the experimental data of rubber than pure elastic models with suitable choices of  $C_1$  and  $C_2$ .

### **Neo-Hookean form model**

The form of the neo-Hookean strain energy potential is given by

$$U = C_{10}(\bar{I}_1 - 3) + \frac{1}{D_1}(J^{el} - 1)^2 \quad (2.14)$$

where  $C_{10}$  and  $D_1$  are temperature-dependent material parameters,  $\bar{I}_1$  is the first deviatoric strain invariants;  $J^{el}$  is the elastic volume ratio.

### **Ogden form models**

This model is used to describe the non-linear stress-strain behaviours of complex materials such as rubbers, polymers and biological tissue.

Equation 2.15 shows the shear modulus and bulk modulus for small strains based on the Ogden form (Ogden et al., 2004)

$$\mu_0 = \sum_{i=1}^N \mu_i, K_0 = K_1 \quad (2.15)$$

$U$  is a function of the principal values  $b_1, b_2, b_3$  of  $\mathbf{B}$ .

$$U = \sum_n (\mu_n / \alpha_n) (b_1^{\alpha_n} + b_2^{\alpha_n} + b_3^{\alpha_n} - 3) \quad (2.16)$$

Where  $\mu_n$  is constants, and  $\alpha_n$  is not necessarily integers and may be positive or negative.  $\mathbf{B}$  is left Cauchy-Green strain tensor,

$$\mathbf{B} = \mathbf{F}\mathbf{F}^T \quad (2.17)$$

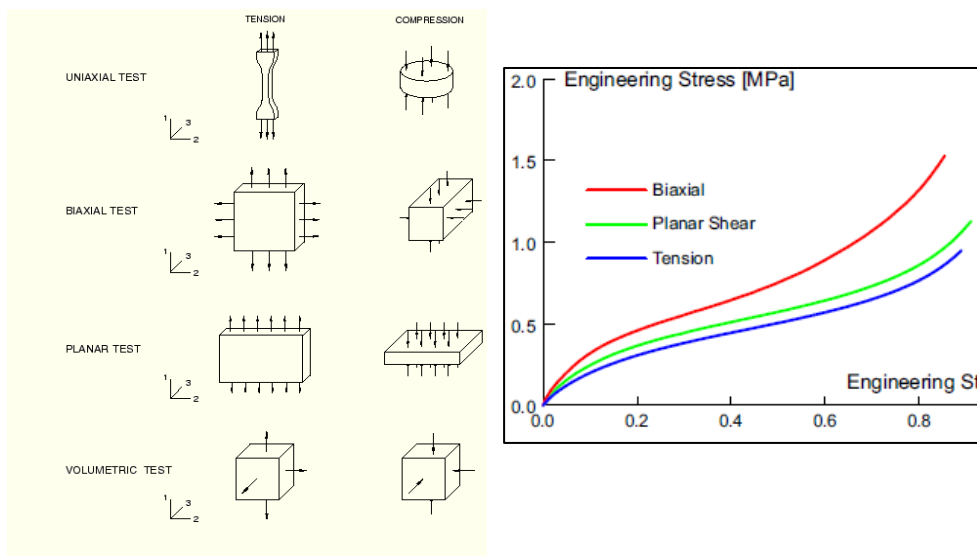
and  $b_1, b_2, b_3$  are principal values of  $\mathbf{B}$ .

The general form of the Ogden strain energy potential is shown in Equation 2.18

$$U = \sum_{i=1}^N \frac{2\mu_i}{\alpha_i^2} (\bar{\lambda}_1^{\alpha_i} + \bar{\lambda}_2^{\alpha_i} + \bar{\lambda}_3^{\alpha_i} - 3) + \sum_{i=1}^N \frac{1}{D_i} (J^{el} - 1)^{2i} \quad (2.18)$$

Where  $\bar{\lambda}_i$  are the principal stretches;  $\mu$  and  $\alpha_i$  is a material constant; and  $D_i$  are temperature-dependent material parameters (ABAQUS user Manual

2017). There are several parameters in the Ogden model, so a complex testing approach is required to determine these parameters. Normally, tests with different stress strain condition need to be performed, then the parameters can be determined by a curve fitting process. Some tests are shown in Figure 2.12. In a modelling process, the test data of different forms can be input in the materials module in Abaqus then the program will work out the parameters through fitting the curves and then identify the materials parameters which give the best overall match to the data.



(a) Deformation modes of various experimental tests for defining material parameters (*ABAQUS User Manual 6.14*).

(b) Typical stress strain curves of rubber materials under different testing models (*“White paper – Nonlinear finite element analysis of elastomers”, MSC Software Corporation.*)

**Figure 2.12** Testing methods for defining material parameters used in Abaqus (a) and typical data of different stress strain curves of Rubber from different type of tests (b).

---

## **2.8 Application of Python scripts in structure /material modelling and data analysis.**

As shown in the sections above, FE modelling is an important method for studying the deformation of cellular materials. A range of modelling software has been used by various researchers. For example, Abaqus, Ansys, LS-DYNA, Solidwork and Hyperwork. Among which, Abaqus is the most widely used. A useful research tool to aid the development of an analysis is to develop a Python-based program linked with Abaqus for model development and data analysis. Python's open-source pedigree is a major advantage over other programs, it is becoming increasingly popular and is aided by a large user and developer base in industry as well as the sciences. Python is a modern, interpreted, object-oriented, open-source language used in different kinds of software engineering. Python language is interpreted, development is much easier, and a compiler and linker are not needed thus saving time and resources. Python code is more robust, and less brittle supported by modern data structures and the object-oriented nature of the language. The developer can take advantage of different open-source Python packages. These cover works in visualization, numerical libraries, interconnection with compiled and other languages, memory caching, web services, mobile and desktop graphical user interface programming, and others. There are some disadvantages of Python. For example, pure Python code runs much more slowly than compiled code, and the number of scientific libraries is relatively limited compared to Fortran.

Python is used in image analysis, ([Gostick et al., 2019](#); [Putanowicz, 2015](#)). One active application area of Python is developing Plug-in with numerical simulation such as Abaqus, which can be used for parametric model building as well developing systematic data for analysis or in structure optimization, which is relevant to the modelling of cellular structures including studying Poisson's ratio and auxetic structures. Plug-in has been used in design. For engineering applications, Python is used in conjunction with other engineering software to create a Graphical User Interface (GUI). Creating a

---

GUI *via* a plug-in allows the user to input all analysis information in an intuitive way. The information input by the user through the plug-in will automatically configure both the subroutines and the model itself so that an analysis can be performed, using a single procedure, allowing much of the required data to be input using a simple text file rather than changes to the code itself. This automation removes many of the sources of error, whilst at the same time providing a more convenient and faster way. Finite Element package ABAQUS/CAE has an application called GUI Toolkit, which has been widely used in parametric research studies. Design process and optimization have been important area in early work on Python ([Nesládek et al., 2016](#); [Li et al., 2015](#)). For example, [Winkler et al \(2005\)](#) created plug-ins to generate spur and worm gear models as shown in Figure 2.13. This paper reported a method of parametrically modelling spur and worm gears with spur or helical gear teeth. The program considered assembly deviations such as centre distance error or shaft angle error and defining standard load cases to be analysed and evaluated using the finite element package Abaqus. In more recent works, [Li et al \(2015\)](#) developed a plug-in for FE modelling of large H-beam hot rolling in ABAQUS. The program consists of thermal analysis and elastic-plastic properties. It also included embedding re-meshing algorithm and subroutines. The key design component and function is shown in Figure 2.14. The plug-in covered Roller modelling interface, pre-processing interface, Abaqus kernel and post-process. The model building and extracting simulation results during post-processing can be automatically performed. The re-meshing algorithm and the information transfer method of the clearance between two passes are synthetically used to ensure the continuous simulation of multi-pass hot rolling process and improve the accuracy of simulation results. The system allows the automatic input of the dimensional data (Figure 2.14b) and materials properties (Figure 2.14c) including density, thermal, mechanical, etc. The integrated system is effective in collecting all the key data as well as the real-time detection of internal information for H-beam and deformable roller in the rolling process, which is difficult to be realized.

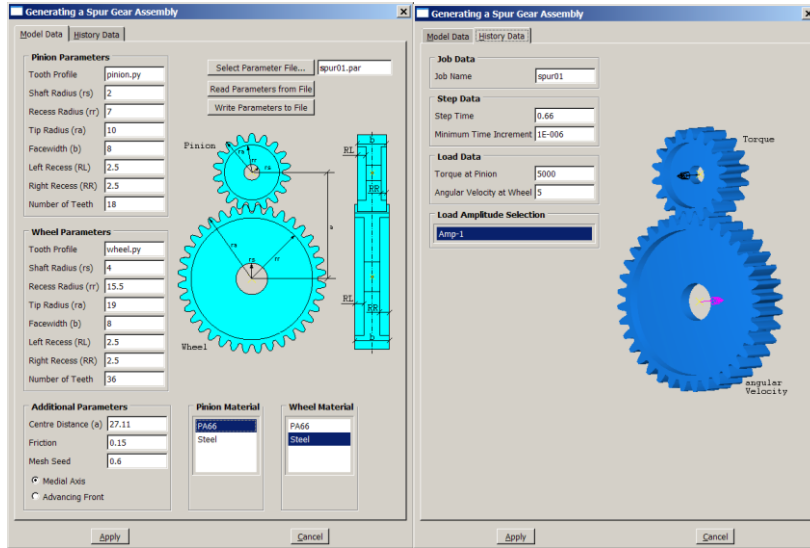
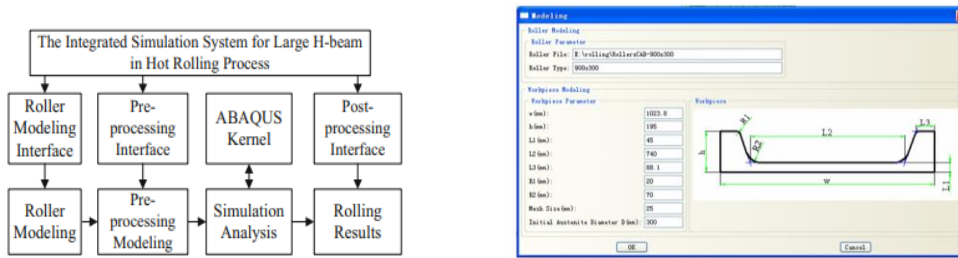
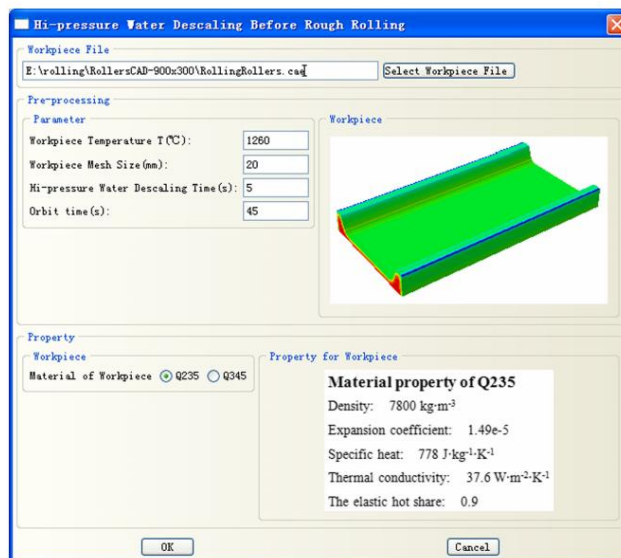


Figure 2.13 ABAQUS CAE Plug-in toolkit, used by Winker et al., (2005) to generate gear models.



(a) The overall structure of the (b) Modelling dialog box. integrated simulation system.



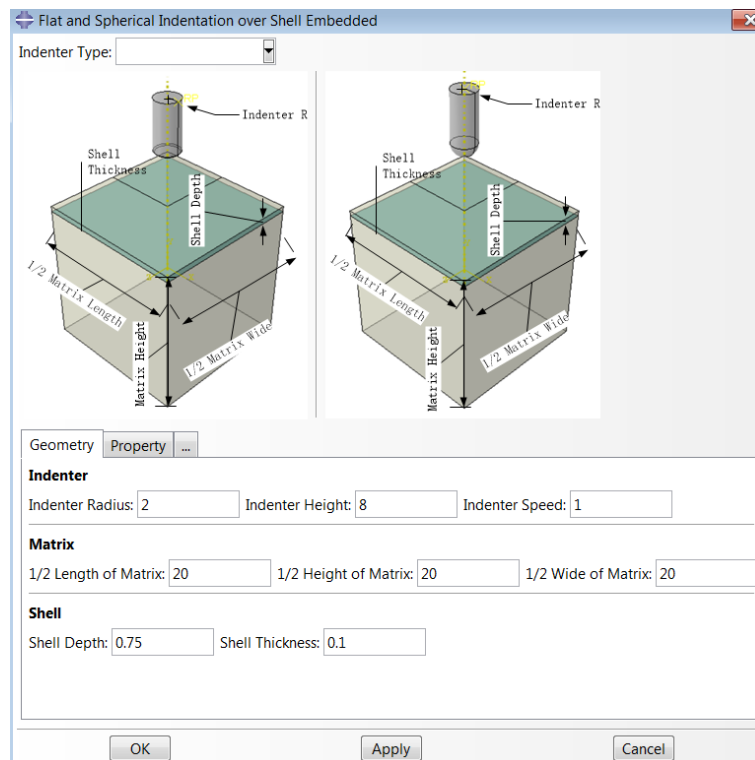
(c) The dialog box of the high-pressure water descaling before the rough rolling

Figure 2.14 Typical simulation system for large H-beam hot rolling. (Li, 2015)

---

Li et al (2018) developed a Python based Abaqus plug-in to systematically study the effect of shell depth and Poisson's ratio of the matrix on the indentation resistance based on a dynamic FE model. Figure 2.15 shows the main factors considered when designing the user interface for modelling indentation of an embedded shell within an elastic matrix. The program allows users to select indenter shapes (Flat-ended, spherical, etc.), the position of the indenter (Indenter height) at the original position and indenter speed (at the original position). The user can input the position of the embedded shell (of different thickness) in the matrix. One feature of the user interface is the selection of indenter shape through a Really Simple GUI (RSG) window. Another key issue is the partition of the embedment and interaction between the matrix and embedment. Partition is needed in thin embedment modelling so that the high-quality hex mesh can be applied to achieve a more efficient model. The model has been successfully used in studying the effect of auxeticity of the matrix on the indentation resistance, which shows that an auxetic matrix could enhance the indentation resistance (Li et al., 2018). Recently, the model was extended to study the effect of the negative Poisson's ratio on the interaction between water droplets during impact (Al-Badani, 2020). In the work, the indenter is replaced by a liquid droplet (the coordinates were taken from Ansys Fluent simulation), impacting onto materials of different Young's Modulus, the reaction force and spreading of the liquid on the surface were simulated. Plug-in is also widely used in welding process, for example Nguyen et al (2017) reported the use of a parametric Python program for Predicting Temperature in a Fillet Weld T-Joint used in Welding Simulation; Parmar 2016 (2016) reported a work of simulation of a Multi-Pass Dissimilar Metal Nozzle to Pipe Weld Using Abaqus 2D Weld GUI and Comparison with Measurements. Norbury (2017) also used Plug-in to study the mechanical and thermal performance of sheathed thermocouples. Python is also increasing in developing tools for the multiscale modelling including structure generation (Das et al., 2018; Barrett et al., 2018; Malians et al., 2016; Omairey et al., 2018; Riaño and Joliff, 2019; Nguyen et al., 2017; Parmar et al., 2016). Das et al (2018) reported work on modelling drag and

heat transfer closures for realistic numerically generated random open-cell solid foams using an immersed boundary method; Barrett et al (2018) reported a work on automated procedure for geometry creation and finite element mesh generation: Application to explicit grain structure models and machining distortion; Riaño et al (2018) reported an Abaqus™ plug-in for the geometry generation of Representative Volume Elements (RVE) with randomly distributed fibres and interphases; Malians et al (2016) reported a work on random lattice structures modelling of their mechanical response and effective properties. An RVE can be used to obtain homogenized material properties from a smaller scale model considering the structure details, then use the properties in a macro scale model. This can avoid the problem with meshing a large system. Obtaining homogenized properties involves performing an analysis from which the homogenized properties can be determined as well as post processing to calculate the homogenized material properties (Omairey et al., 2018).



**Figure 2.15** Typical Abaqus Plug-in showing the main functions and parameters used to study the effect of the negative Poisson's ratio matrix on the indentation resistance. (Li, 2018)

---

One typical application of Python based program with RVE is to determine the effective properties of materials with non-homogeneous structures, such as composite. The process involves building FE models considering the microstructure, then estimating an effective material parameter, which can represent the behaviour of the materials based on stress-strain data, energy, etc. The effective property data can be isotropic data ( $E, G, \nu$ ) or *highly anisotropic* i.e. (full property matrix data in materials module for simulation). For example, when the homogenization method is applied to fibre reinforced composites, the RVE is modelled as a homogeneous orthotropic medium with certain effective properties that describe the average material properties of the composite (Bensoussan et al., 1979). The effective Macro stress and macrostrain data of the materials can be obtained by averaging the stress and strain tensor over the volume of the RVE in order to describe the macroscopically homogeneous medium. Figure 2.16 shows the data flow of a python program for estimating the effective materials properties. The first stage is building an FE model based on the real structure and materials properties for each constituent (e.g., in the case the fibre and matrix will have different properties), the periodical boundary condition is applied. As shown in the figure 2.16, the key data such as stress, strain and strain energy ( $U$ ) stored in the heterogeneous RVE of the volume  $V_{RVE}$  can be calculated the stiffness tensor ( $C_{ij}$ ), which can then be used to determine the compliance tensor ( $S_{ij}$ ) as the inverse of the stiffness tensor ( $C_{ij}$ ). The properties such as directional Young's modulus ( $E_{ij}$ ) and Poisson's ratio ( $\nu_{ij}$ ) can be derived. Both the  $C_{ij}$  data or the ( $E_{ij}, \nu_{ij}$ ) data can be used as inputs in the FE modelling.

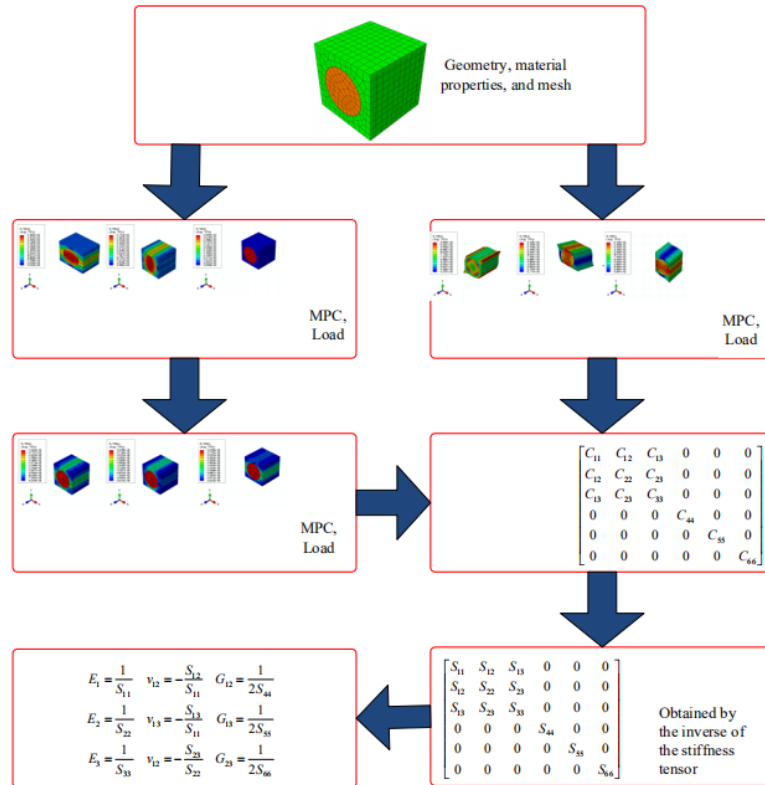
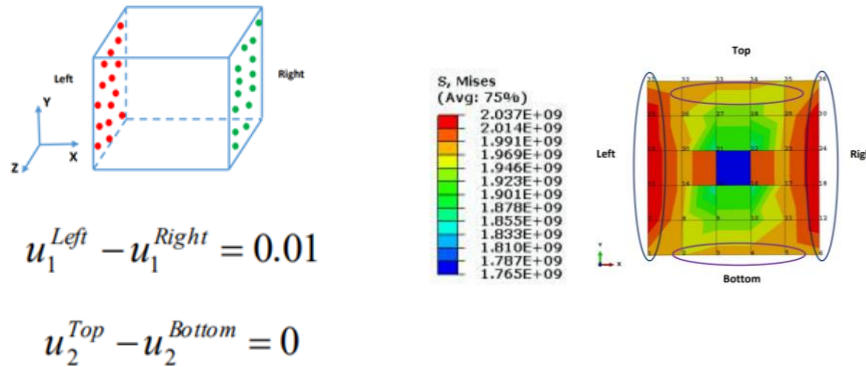


**Figure 2.16** The computation flow to estimate the effective elastic properties based on representative volume element (RVE) approach. (Wu et al., 2014)

Periodic boundary conditions (PBC) are a set of boundary conditions that can be used to simulate a large system (i.e., bulk material) simply by modelling a finite representative volume element (RVE). Periodic boundary conditions are commonly applied in molecular dynamics, dislocation dynamics and materials modelling to eliminate the existence of surface and avoid a huge number of molecules or large size of simulation box (Wu and Owino, 2014). A simple case is Applying Periodic Boundary Conditions in Finite Element Analysis as shown in Figure 2.17 (Wu and Owino, 2014). Figure 2.17a is a 3D cube element, in the model, a strain is applied to left-right direction, while the relative displacement between the top and bottom face is determined through the equation. In this case, the relative strain/ displacement of the top and bottom surface is set to be the '0', in other words, the two surfaces will move in the same way in the  $u_2$  (or  $y$  axis direction). Figure 2.17b shows the stress distribution, the equation  $(U_2^{Top} - U_2^{Bottom} = 0)$  will ensure that the  $u_2$  for nodes on the top 31-36 is identical to that of 1-6, respectively. This reflects in

the situation that the material is sample fraction in a larger sample.

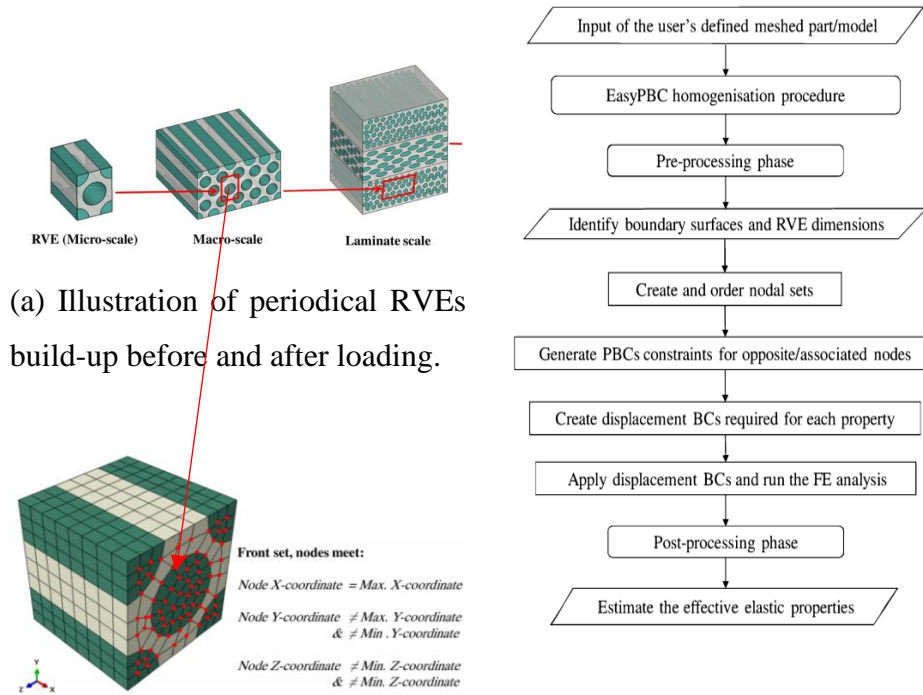


(a) A 3D RVE with nodes on left and right-side surfaces (b) A 1×1 RVE model and stress contour with strain controlled PBC

**Figure 2.17** Typical boundary conditions of a representative volume element model and deformed shapes. ( $u_1$  is strain in ‘x’ direction,  $u_2$  is strain in the ‘y’ direction). (Wu et al., 2014)

One key work for multiscale modelling is setting the boundary conditions (identify the corresponding nodes and apply the equation), in particular the use of periodic boundary is particular useful for multiscale modelling of materials at small scales. (Meza et al., 2017; Omairey et al., 2018). A typical example of ABAQUS plug-in tool for periodic RVE homogenization is shown in Figure 2.18 (Omairey et al., 2018). In the theory of composite materials, the representative elementary volume (also called the representative volume element (RVE) or the unit cell) is the smallest volume over which a measurement can be made that will yield a value representative of the structures of the materials (Gitman et al., 2007). As shown in Figure 2.18a, the RVE shall be selected/modelled such that duplicating it provides sufficient accuracy of representing the material’s larger scales. During the RVE homogenization process, the imposition of uniform strains on a microscale RVE to compute the effective elastic properties was carried out (Figure 2.18b. The program is developed in Python (EasyPBC) and worked as an ABAQUS CAE plug-in developed to estimate the homogenised effective elastic properties of user created periodic representative volume element (RVE), all within ABAQUS without the need to use third-party software. As shown in the flowchart in Figure 2.18c, the first phase

determines RVE's geometrical dimensions, identifies boundary surfaces, creates nodal sets, creates node-to-node constraint equations, and applies the required displacement boundary conditions. Whereas the post-processing phase handles stress-strain calculations, and other operations related to estimating.



estimates the effective elastic properties. Whereas the post-processing phase handles stress-strain calculations, and other operations related to estimating.

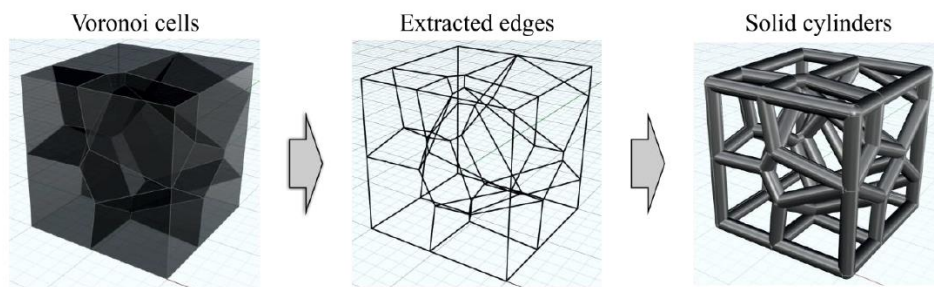
**Figure 2.18** Key structure of an ABAQUS plug-in tool for periodic RVE homogenisation and the node sorting process. (Omairey et al., 2018).

As shown in the flow chart in Figure 2.18c, two key stages are “the create and order node set” and “generate PBCs constraints for opposite /associated nodes”. This involves complex operation/programming with internal ABAQUS environments after the model is meshed. In this process, the nodes are sorted into an order on the paired surfaces, the equation can be set for

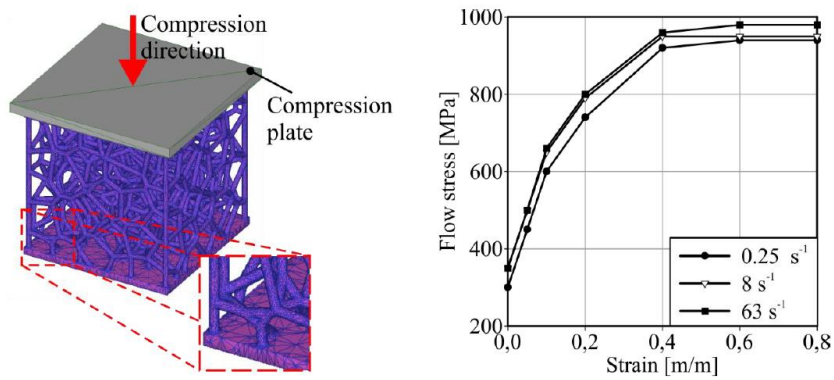
---

corresponding nodes. This is similar to the operation on the nodes in Figure 2.17 (e.g., 1 to 31) but much more complicated in processing in order to facilitate the linking of nodal degrees of freedom of the nodes. To achieve this, for each node in associated sets/pairs, the code identifies its corresponding node in the opposite set when the coordinate difference between the two nodes is smaller than a specified mapping accuracy. The default value of mapping accuracy was set as 1E-7 mm in the program. When the difference in each component of the coordinate (in the x,y, z directions separately) is within this limit, the program will assume the mesh structure is nearly identical on opposite sides of the RVE. From the original code, this value can be adjusted depending on the mapping accuracy required by the user.

For porous structures, this could be more complicated due to contact. Figure 2.19 shows a typical example of combined structure generation and FE modelling considering the contacts. (Maliens et al., 2016). The key stages in the solid modelling procedure are shown in Figure 2.19a including Voronoi cells, then extracted edges and solid model. Voronoi tessellation (or Voronoi diagram) is based on a space partitioning method to create polyhedral in 2D or 3D geometry. In this procedure, several random space points will be generated randomly then linked to a 3D Voronoi structure. With the automatic structure building procedure, it is able to generate CAD geometry with controllable structural parameters, such as porosity, cell number and strut thickness, then transfer to FE modelling in Deform 3D FEA software. A typical example of Figure 2.19b shows the deformation and stress strains. The stress is the force divided by the overall area perpendicular to the loading direction. The program is able to evaluate the effect of materials properties and loading rate as well as identify the initial contacting point. This is a good example, showing that integrating structure generation and FE modelling is a useful development. With such a program, many different structures and properties can be produced.



(a) The modelling procedure to solid



(b) Developed FEA model and applied rate dependent material properties for stainless steel 304.

**Figure 2.19** Combination of Python and FE modelling in studying random lattice structures. (Malians et al. 2016)

---

## 2.9 Modelling at different scales and data development

As shown in early sections (Figure 2.20) computer modelling is an important part in materials data development. Molecular simulation is a very active area analysing materials/compound in different forms. It allows the analysis of fundamental materials parameters and provides guidance in materials design, and applications. Materials Studio (<https://www.3dsbiovia.com/products/collaborative-science/biovia-materials-studio/>) is one of the most widely used software (Xie et al., 2015; Guo et al., 2016; Yang et al., 2009; Benyelloul and Aourag, 2013). Materials Studio is a simulation software that can be run on a computer by ACCELRTS for researchers in the field of materials science and structural chemistry. Materials Studio offers validated, efficient, and user-friendly quantum mechanical applications based on Density Functional Theory (DFT), hybrid QM/MM and semi-empirical methods. Quantum mechanical methods yield accurate thermodynamic, kinetic, and structural results, providing an efficient adjunct to experiment. (<https://www.3dsbiovia.com/products/collaborative-science/biovia-materials-studio/quantum-catalysis-software.html>). DFT is a computational quantum mechanical modelling method used in physics, chemistry and materials science to investigate the electronic structure (or nuclear structure) (principally the ground state) of many-body systems, in particular atoms, molecules, and the condensed phases. Using this theory, the properties of a multi-electron system can be determined by using functionals, i.e., functions of another function. In the case of DFT, these are functionals of the spatially dependent electron density. DFT is among the most popular and versatile methods available in condensed-matter physics, computational physics, and computational chemistry ([https://en.wikipedia.org/wiki/Density\\_functional\\_theory](https://en.wikipedia.org/wiki/Density_functional_theory)). The DFT is an effective approach to compute the electronic structure of matter and its application ranges from atoms, molecules and solids to nuclei and quantum and classical fluids. (Bultinck and Carbó-Dorca, 2005). Materials Studio

supports a variety of operating platforms (for example Linux, Windows) to enable researchers in materials science to establish three-dimensional molecular models and analyse in-depth inorganic crystals, organic crystals, polymers, and amorphous materials (Xie et al., 2015) more easily. Materials Studio software enables every researcher to achieve world-class material simulation level. The content of the simulation includes the most important topics in the fields of materials science and chemical research, such as organic matter, polymers, catalysts, crystallography, solid chemistry, power diffraction, and material characteristics (Hall et al., 2008).

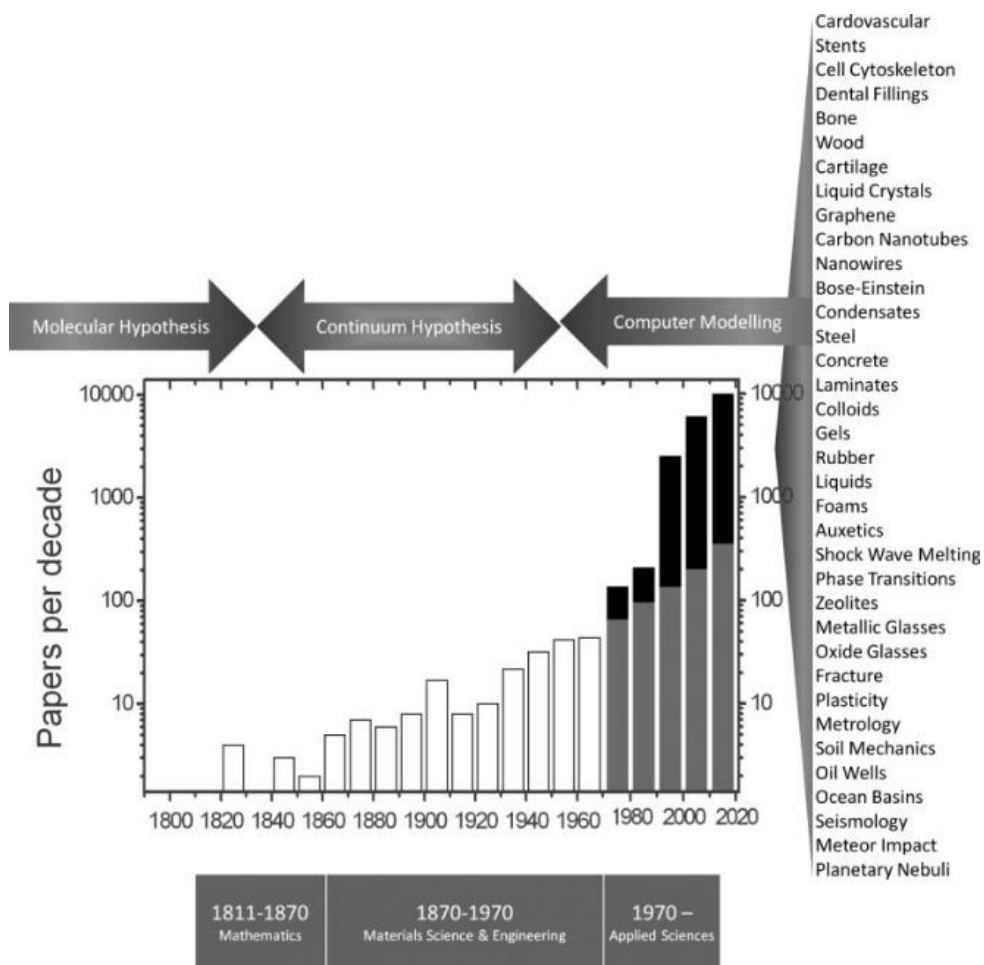


**Figure 2.20** Different research approaches as shown by the growth of publications involving Poisson's ratio. (Greaves et al., 2013). The white, grey and black bar mean different published statistics sources.

One active area is in materials data and materials discovery. Typical application includes property polymer modelling (Chenoweth et al., 2005),

---

reaction prediction (He et al., 2018), physical property calculation (Guo et al., 2016; Shi et al., 2011; Liu et al., 2014; Chong et al., 2017), and X-ray diffraction simulation (Guo et al., 2016; Yang et al., 2009). The most used is the first-principles calculation simulation package CASTEP which is a calculation module in the Materials Studio software package. The CASTEP is an acronym for Cambridge Sequential Total Energy Package and is a quantum mechanics program based on first principles. It is a powerful tool that uses plane wave pseudopotential basis sets combined with density functional theory to study and design the physical properties of materials. CASTEP is mainly used in the calculation of solid-solid related properties in solid physics. (Clark et al., 2005). In recent years, more and more researchers have used CASTEP for the simulation prediction, calculation, and synthesis of chemical substances, which has improved the efficiency of chemical research and reduced the research time, thus making CASTEP more widely used. Yang et.al (Yang et al., 2009) calculated elastic properties and hardness of TiC and TiN. The elastic constant of results is close to experiment data. Benyelloul and Aourag (Benyelloul and Aourag, 2013) calculated the elastic constant of face centred cubic austenitic stainless steel. The CASTEP code page is used to run mechanical simulation by efficient strain–stress method of generalized gradient approximation (GGA). And an artificial neural network (ANN) is also used in propagation algorithm training of correlation between the elastic properties and composition. The three different elastic constants  $c_{11}$ ,  $c_{12}$  and  $c_{44}$  were employed as outputs. Elastic constants obtained from ANN models were compared with those obtained from quantum mechanical simulation and with those reported in the literature. The prediction results obtained by the two methods showed a reasonable agreement. Guo et al (2016) calculated the local electron work function, surface energy, adhesive force, modulus and deformation of ferrite and austenite phases in a duplex stainless steel by CASTEP. The results are matched well with experiment data and the work function modulus and adhesive force of austenite is higher than ferrite. The mechanism behind was explained by first-principles calculation. The results show that the difference in properties between austenite and ferrite is intrinsically related to their

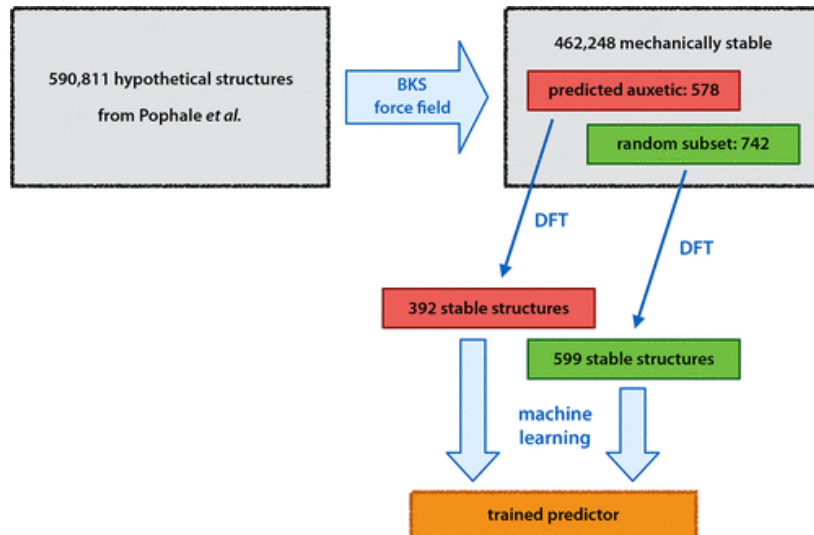
---

electronic work functions. [Liu et al \(2014\)](#) used first-principles calculations to study the lattice parameters, stability, mechanical properties, and anisotropic sound velocity of hexagonal and orthogonal diamond Cr<sub>7</sub>C<sub>3</sub>. The cohesive energy and enthalpy of formation of these compounds indicate that they have a thermodynamically stable structure. The stress-strain method and Voigt-Reuss-Hill were used to approximate the elastic constant and mechanical modulus of these compounds. In addition, the sound velocity anisotropy and mechanical anisotropy of Hexa-Cr<sub>7</sub>C<sub>3</sub> and adjacent Cr<sub>7</sub>C<sub>3</sub> were also studied. [Tokmakova \(2005\)](#) studied the direction of the Poisson's ratio with extreme values in the direction of the cubic diagonal extension in the crystal, and the corresponding lateral strain on the orthogonal cubic diagonal and cubic axis are considered. A stereo projection of Poisson's ratio of a group of natural lenses with cubic, hexagonal, and single-slope symmetry was calculated. From these stereoscopic projections, the Poisson's ratio of any possible tensile and lateral strain directions in the crystal was calculated, and the directions of the tensile and lateral strain with the extreme value of Poisson's ratio were obtained. It reveals crystals with bulging behaviour. The directions of the tensile direction and the lateral strain direction (with negative values of Poisson's ratio) were determined. One important conclusion is that stretching of material with negative Poisson's ratio leads to an unexpected transverse expansion. Stretching of anisotropic material can cause expansion in one direction and contraction in another direction

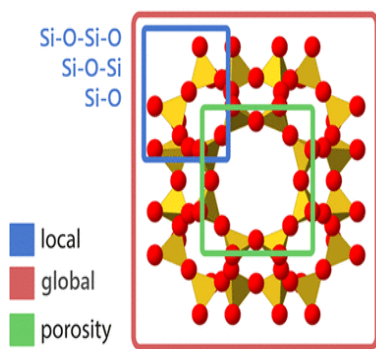
In recent work, physical simulation has been used in material data development as well as materials discoveries including auxetic materials. In materials data development, a large amount of modelling is conducted automatically for a particular materials group through materials mining and discoveries ([Dagdelen et al., 2017](#)). The work by [Dagdelen et al \(2017\)](#) reported a large-scale work to accelerate the discovery of materials with target properties, such as auxetics, by using high-throughput computations and open databases. As part of the materials data development, the Poisson's ratios were derived from the calculated elastic tensor of each material in this reduced set of compounds. And compounds with special properties including

---

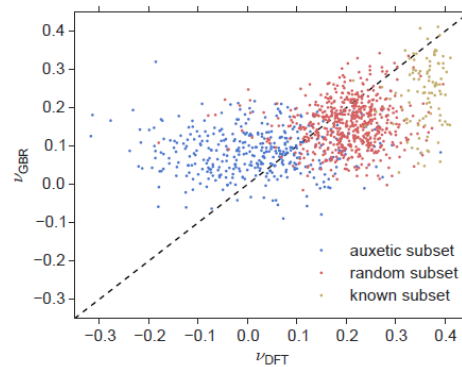
negative Poisson's ratio are identified. The characterization of the mechanical properties of crystalline materials is nowadays considered a routine computational task in DFT calculations (Gaillac et al., 2020). The framework of the work and key results is shown in Figure 2.21. The work combined materials simulation and supervised machine learning to investigate the materials parameters, error range and the effect of machine learning on the efficiency (time saving) in property prediction. As shown in the figure, the work used data generated in molecular simulation to generate data, then used the data to predict the materials with different positive or negative Poisson's ratio. As illustrated in Figure 2.21b, the descriptors are used as entries in the machine learning process. The program scanned through a large number of structures to identify if the structure is stable based on the energy. The work used supervised training, the main principle is to create a predictor by training an algorithm on two sets of variables in the training data set: some simple geometric descriptors of each material, obtained at low computational cost, and the required property that one wants to predict (calculated at a higher level of theory). The trained machine learning algorithms, as implemented in the scikit-learn Python library to create three predictors based on regression methods, targeting the average, minimum, and maximum values of the directional Poisson's ratio, the work is able to identify potential Auxetic structures (as shown in Figure 2.21c).



(a) Description of the modelling strategy and different zeolite subsets used in the present work. BKS: a Beest–Kramer–van Santen (BKS) potential.



(b) Summary of the descriptors used as entries in the machine learning process classified in local properties, global properties, and porosity-related properties.



(c) Data used in machine learning to predict potential structure with negative Poisson's ratios.  $v_{DFT}$  is calculated Poisson's ratio.  $v_{GBR}$  is parameter of GBR method.

**Figure 2.21** Use of materials simulation data with machine learning to analyse the distribution of Poisson's ratio and Auxeticity in Zeolite system. (Gaillac et al., 2020)

---

## 2.10 Main issues and challenges.

The development in numerical modelling and physical modelling has improved the understanding of structure-property relationships of many materials. It has offered an opportunity in materials development linked to Poisson's ratio and auxeticity. There are some key issues that need to be addressed:

One is the development of a Python-based program integrated with numerical modelling which could provide an important tool for both research and development in auxetic materials, applications, and related areas. Python plug-in for modelling these structures including automatic model building and data analysis will make the FE modelling much more efficient. Such a program will also help test the effect of factors such as sample size, lattice patterns as well as establishing the effects of the key design or materials parameters. This is particularly relevant to the missing rib (MR) auxetic models. MR auxetic structures have attracted much research attention recently. ([Remennikov et al., 2019](#); [Koudelka et al., 2016](#); [Gaspar et al., 2019](#); [Adorna et al., 2018](#); [Farrugia et al., 2018](#); [Jiang et al., 2019](#); [Mizzi et al., 2018](#); [Mizzi et al., 2020](#)). Many of the applications are intended for application under in-plane compression loads, and it is important to establish a detailed understanding of the deformation process, in particular, the contact between the edges and cell walls at high strains for normal MR, which are directly relevant to the mechanical behaviours and the stability of the cell and overall sample deformation. Many of the applications are intended for application under compression loads, it is important to establish a detailed understanding on the deformation process, in particular the contact between the edges and cell walls at high strains for normal missing rib and mixed structures, which are relevant to the mechanical behaviours and the stability of cell and samples. Mixed structures with MR models could offer opportunities to further enhance the freedom in structures design. It is important to establish the detailed deformation mechanisms, properties, and stabilities. For the hierarchical structures, the structure can undergo different deformation modes

---

and result in different shapes ([Haghpanah et al., 2013](#)). This gives more options for materials design and development.

First principle calculation is increasingly used in predicting crystal structure, electronic, physical, and elastic properties of ceramics (e.g., carbides, nitrides, and multicomponent carbides). First principle calculation is a method to calculate physical properties directly from basic physical quantities (such as the mass and charge, and coulomb force of an electron, etc.) based on the principle of quantum mechanics. It naturally links multidisciplinary research areas and data in physics, chemistry, materials, and processing. Typical relevant data from first principles calculation covers elastic constants, physical properties, thermal properties, interface between different phases, electrochemical oxygen reduction reaction, corrosion, etc. ([Sun et al., 2010](#); [Cuppari et al., 2016](#); [Wen et al., 2018](#)). The computerised calculation process and subsequent large data analysis generate a rich source of materials data for establishing more detailed understanding of material parameters and their correlations. For analysis of mechanical properties, the prediction of the elastic properties involves the mathematical approximation combining the Voigt, Reuss and Hill bounds of bulk and shear moduli ([Voigt, 1928](#); [Hill, 1952](#); [Reuss, 1929](#)). In addition, the data from first principle calculation and subsequent analysis also provide the means to estimate the properties such as Vickers hardness based on the ground state elastic parameters/properties ([Chen et al., 2011](#); [Tian et al., 2012](#)). As materials informatics is increasingly being used in engineering analyses and design of complex materials systems, data from physical modelling also offers new opportunities in further understanding of the correlation between different sets of properties with more details. It provides a mean to establish systematic data of the key elastic properties bulk modulus (K), Young's modulus (E), shear modulus (G), as well as the Poisson's ratio. In addition, by integrating first principle calculation with data analysis, it is possible to establish data for enhancing the understanding and visualization of the difference of properties in different crystal planes or directions. The systematic data in anisotropy is often challenging, or in some cases very difficult, to be established through pure

---

experimental means for secondary particles in steel and welded structures. With the development of modelling at both macro and crystal structure or molecular levels, the data from both levels are increasingly providing information through different scales, this is an important future direction.

---

**CHAPTER THREE**  
**EXPERIMENTALS,**  
**NUMERICAL MODELLING**  
**AND DATA ANALYSIS**  
**PROGRAMS**

---

## 3.1 Introduction and main research works

Figure 3.1 shows the overall research structure and key approach. The main research work of experiment, numerical modelling and data analysis program is shown in table 3.1. The material characterisation is focused on measuring the key material parameters and calibration procedures related to auxetic behaviour. This includes using a 3D printed experiment sample, set-up procedures and comparison with numerical data. Details of the work are presented in section 4.3-4.5. The experiment data is helping to validate the accuracy and reliability of the numerical study. The parametric numerical modelling investigated the modelling parameter effect on two auxetic structures - missing rib structure and self-similar hierarchical honeycomb structure. The different modelling parameters including beam length, beam angle and lattice pattern are evaluated for the effect on Poisson's ratio. During the parametric study, a large number of simulations are investigated. Hence, a Python based Abaqus plug-in is developed to improve the effectiveness and efficiency of the numerical study. In the self-similar hierarchical honeycomb structure, the modelling is much more complete than in the missing rib structure especially in the high order model. A Python program is developed to build parametric self-similar hierarchical honeycomb by multiple nested loops.

A Computational quantum chemistry Analysis software, Materials Studio V2017, is used for crystal structure modelling and calculating elastic stiffness constant  $C_{ij}$ , the elastic stiffness constant and its inversion value, elastic compliance constant  $S_{ij}$ , are used to calculate ground state property included bulk modulus, Young's modulus, Shear modulus, Poisson's ratio and anisotropy of those ground state properties. To visualize the anisotropy of ground state properties, a Python program is developed to plot 3D surface construction and 2D plane projection. 12 carbides are selected to study the relation between anisotropy index and ground state property. Three crystal structures with negative Poisson's ratio are investigated.

---

**Table 3.1 Main Research Works**

**Parametric study of Missing Rib structure (Chapter 4)**

- Development of Python program for parametric modelling of missing rib structures
- Comparison between numerical model, published data and experiment data.
- Evaluation of effect of beam length, beam angle, lattice pattern number on Poisson's ratio.
- Development of mixed structure and initial contact under compression.

**Parametric study of self-similar hierarchical honeycomb structure**

- Development of Python program for parametric modelling of self-similar hierarchical honeycomb structure.
- Comparison between numerical model, published data and experiment data.
- Evaluation of effect of order number, beam length between higher and lower order and lattice pattern number on Poisson's ratio.

**Discussion**

- Evaluation of effect of different modelling approaches and sample size of auxeticity
- Development of complex beam shapes and patterns with Voronoi and new random approach
- Comparison of different approaches for evaluating the accuracy and feasibility of area calculation
- Factors affecting the area analysis, comparison with other approaches and use in other fields.

**Numerical study on different crystal structures (Chapter 5)**

- Numerical modelling and calculation of elastic stiffness constant.
- Calculation of anisotropic parameters of different carbides.
- Graphical user interface of ground state property calculation and Visualization
- Correlation between the ground state properties and anisotropy data.

**Discussion**

- Correlation between the Poisson's ratio and other properties.
- Crystal structure with Negative Poisson's ratio.
- Evaluation of effect of temperature on ground state property.
- Evaluation of other properties from Materials Studio

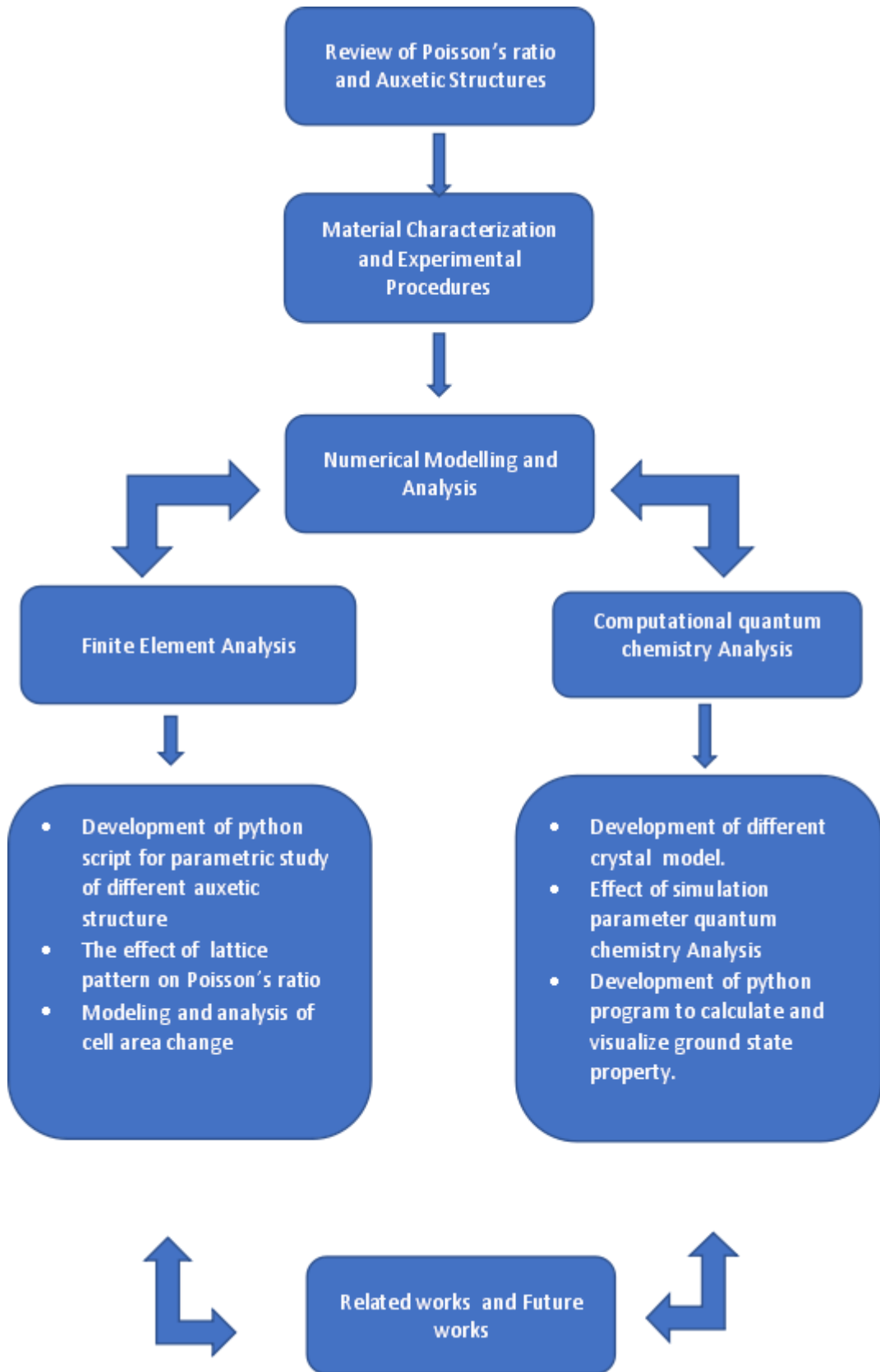
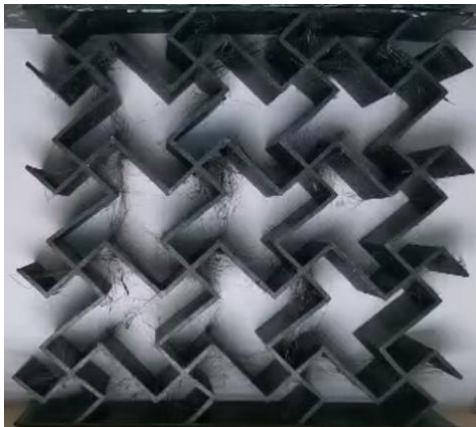


**Figure 3.1** Overall research structure and key approach

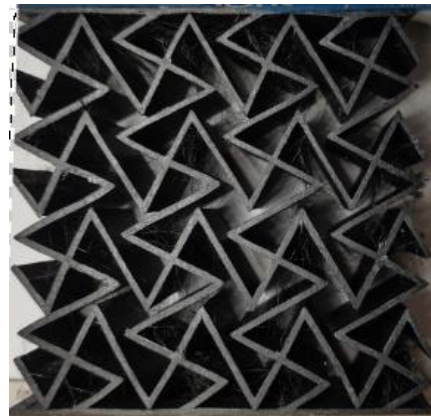
---

## 3.2 FE modelling and structures.

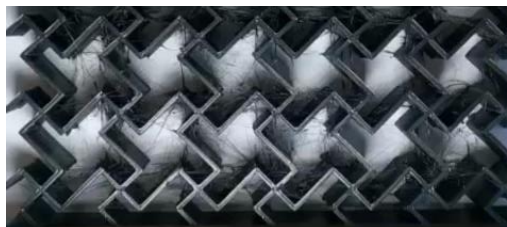
The Finite Element modelling and parametric program development is focused on auxetic structures and related systems, including the missing rib models and self-similar hierarchical structures. The deformation of the structures under compression and tension is investigated. Some typical examples produced by 3D printing to assess the FE modelling and structure development are shown in Figure 3.2. The 3D printing was conducted on a Prusa I3 Mk2 3D printer. The main material used in 3D printing is Thermoplastic elastomer (TPE) plastics (supplied by Verbatim). TPE is a class of copolymers or a physical mix of polymers. The Young's Modulus is 22 MPa and the Poisson's ratio is 0.3. The property was checked by Shore D hardness tests and a MT2000 micro bending tests (Deben Vertical 3/4 Point Bending Stage).



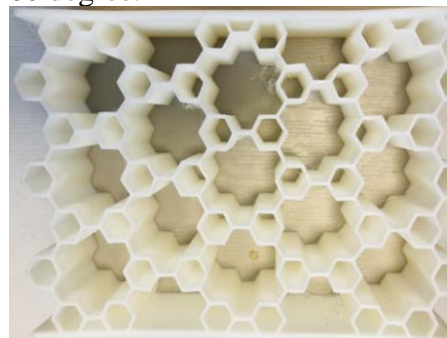
(a) Missing rib with a beam angle 90 degree.



(b) Missing rib with a beam angle 60 degree.



(c) Wider sample (7-3 lattice pattern)



(d) Self similar hierarchical structure

**Figure 3.2** Some typical 3D printed Auxetic samples.

The FE modelling is performed using ABAQUS (version 2017), which is a general finite element simulation package (Abaqus User’s Manual 2017). The ABAQUS scripting interface is an object-based program library, embedded in the scripting language Python, and provides a set of application programming interfaces (APIs) to operate ABAQUS/CAE to achieve modelling/post-processing functions. The programming uses Python syntax to write scripts. In the secondary development of ABAQUS, the pre-processing modelling and post-processing analysis can be achieved through kernel (Python) scripts, and an Abaqus plug-in through the graphical user interface can be created through GUI scripts (PYQT5) to interact with users. Figure 3.3. shows Abaqus working flow and Python application. The user can set a simulation setting though Abaqus Graphical User Interface (GUI), command line interface (CLI), Python script and Python Plug-in. Those operations are sent to Python interpreter to process Abaqus input file(.inp) and Abaqus input file is sent to Abaqus solver to solve the case. The result of simulation is storage in the ODB file. Then Python can be used to collect the data from the ODB file and post-processing the data. In addition to research and development works, the use of parametric programs and GUI make it easier to generate systematically and manage large quantities of data with different formats (numerical, image, animation, etc.) which can be used for research and training.

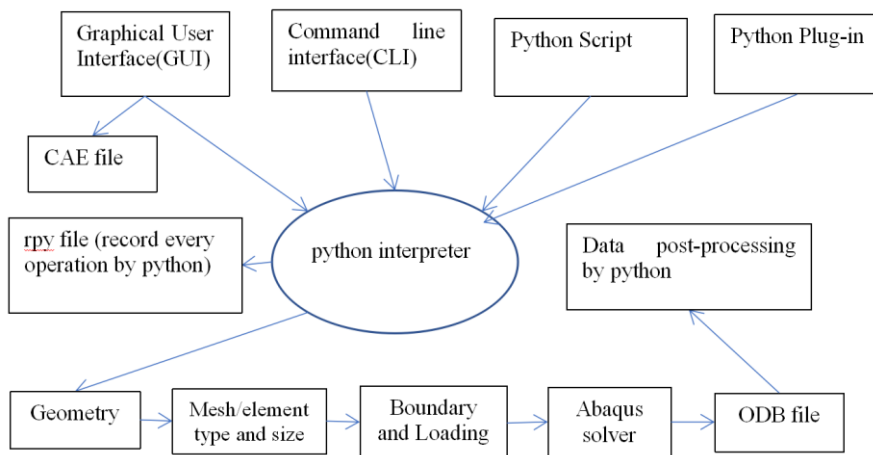


**Figure 3.3** Abaqus working flow and application of Python in different

---

parts. (Zhang et al., 2016)

Python programs and GUI scripts are used to create new graphical user interfaces for simulating known auxetic structures and identifying new structures with auxeticity. In this work, the Abaqus Graphical user interface (GUI) Toolkit is used to Create a new GUI module, which is a grouping of similar functionality. A GUI toolkit is also used which contains more specific functionality that may be used by one or more GUI modules. The parametric functions can be used to control many factors in the geometry, loading, boundary, meshing, choice of solution models, selection of static or dynamics approaches. It can also be used in post-process, to combine data, calculation of specific data which is not readily available. For example, Poisson's ratio of a structure is not readily available, so a program function is implemented to track the axial and lateral displacement of the sample edge, then calculate the strain to determine the Poisson's ratio-strain data. Main numerical works include modelling the deformation of the structures under compression and the tension load with a particular focus on the deformation modes, Poisson's ratios and auxeticity (negative Poisson's ratio). The Python script and Abaqus plug-in presented in this thesis included Missing Rib parametric models (section 4.2 and 4.4), self-similar hierarchical honeycomb parametric modelling (section 4.2 and 4.5), area calculation from ODB (section 4.6), random structure modelling (section 4.7). Limited work has also been performed on other structures such as regular honeycombs for validation and comparison purposes. Figure 3.4 shows a typical case of GUI used in this thesis. The GUI is built by RSG dialogue builder, which is one of the inbuilt tools in Abaqus, the dimensions of which can be automatically changed through user input. The variables include the beam length, beam thickness, lattice pattern (the way the unit cell is repeated to form a large sample) and other parameters.

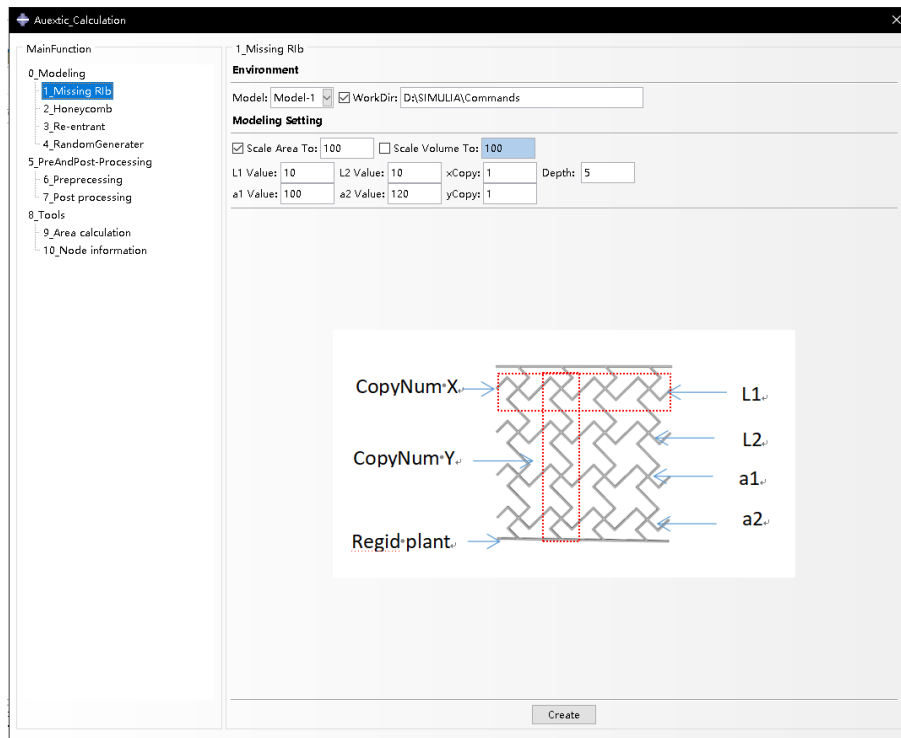


**Figure 3.4** Typical case of Abaqus Plug-in graphical user interface (GUI) of missing rib parametric modelling.

---

### 3.3 Materials studios

The molecular simulation was performed in Materials Studio 2017. Materials Studio is developed by BIOVIA (formerly Accelrys) for computational chemistry, bioinformatics, cheminformatics, molecular dynamics simulation, and quantum mechanics (Farhadizadeh et al., 2017). The main components of the materials studio used in this work is CASTEP (Cambridge Serial Total Energy Package), which is widely used to predict electronic, optical, and structural properties for lattice parameters of single crystals or molecules. CASTEP ([www.castep.org](http://www.castep.org)) is a leading code for calculating the properties of materials from first principle calculations. Using density functional theory (Bao et al., 2019), it can simulate a wide range of properties of materials proprieties including energetics, structure at the atomic level, vibrational properties, electronic response properties etc. In the simulation, the main inputs are atomic number and crystal structure, which can determine the structure and the properties of the materials. The focus of this work is to develop a Python program to process the CASTEP simulation results from crystal geometry optimisation and properties (mainly energy and elastic constants) to systematically calculate the bulk modulus, young's modulus, shear modulus and Poisson's ratios, hardness and establish data reflecting the anisotropic features of the key properties. Other work also covered such areas as surface energy of crystals and effect of temperature on the ground state properties, anisotropy, and Poisson's ratio, including crystals with auxetic behaviours. The program is used for systematic research as well as visualization of the anisotropy in 3D surface and 2D plane projections. A range of materials has been involved with the focus on analysis of some key monocarbides (TiC, NbC and VC), and some crystals with auxetic behaviours.

---

## 3.4 Python program and key developments in the work

Python program is becoming more and more important in materials and data led research. Python is a widely used interpreted, advanced programming, and general-purpose programming language. The design philosophy of Python emphasizes the readability and concise syntax of the code. Python has wide applications such as Artificial intelligence, machine learning, big data, robots, and graphic design applications, etc. Compared to other programming languages (C, C++, or Java), Python has a lot of advantages such as large standard libraries. Several extensive libraries are used in this thesis such as NumPy, Panda, scikit-learn, etc; Python is easy to use, Python allows developers to express ideas with less code which is easier to program especially for Programmers from other fields. And the libraries and clean object-oriented designs also increase two to tenfold the programmer's productivity while using languages like Java, VB, Perl, C, C++, and Python has powerful control capabilities as it calls directly through C, C++, or Java via Python. Python also processes XML and other mark-up languages as it can run on all modern operating systems through the same byte code. An open source Voronoi library based on C++ language is written to a Dynamic link library file(.pyd) which can directly call this to generate Voronoi structure in this work.

Apart from the use of Python integrated with FE modelling and processing data from materials studio simulations, Python is also used in image analysis for some relevant functions, such as the area analysis and the measurement of Poisson's ratio also related to image analysis. In the early stage of the work, an OpenCV program (OpenCVopencv.org) and ImageJ (<https://imagej.nih.gov/ij/>) is used to assess the accuracy of the area program developed. ImageJ can display, edit, analyse, process, save and print 8-bit, 16-bit and 32-bit images. It can read a wide range of image formats including TIFF, GIF, JPEG, BMP, DICOM, etc. It supports "stacks", a series of images

---

that share a single window. OpenCV refers to Open-Source Computer Vision Library, which is a cross-platform computer vision library. OpenCV can be used to develop real-time image processing, computer vision, and pattern recognition programs. Two programs developed in this work used OpenCV, one program is Poisson's ratio calculation from experiment videos, in which the program automatically tracks the distance between markers and calculates the Poisson's ratio. The program of Poisson's ratio calculation from experiment video can track the key measurement points by colour differences. This provides additional data for cross checking the Poisson's ratio measurement as a comparison to the frame-to-frame analysis. OpenCV is also evaluated for area measurement in the early stage of the work as a comparison to the main area calculation program based on coordinates of each cellular cell integrated in Abaqus. Details are to be presented in Sections 4.6 and 4.7.

---

**CHAPTER FOUR**

**NUMERICAL STUDY ON**

**AUXETIC STRUCTURE**

---

## 4.1 Introduction and main research works

As listed in Table 4.1, this chapter details the work on simulation of different auxetic structures under tension and compression loading using Abaqus. The work will concentrate on the development of Python based numerical models of typical auxetic structures. The models are used to investigate their deformation behaviours and establish the effect of key dimensional parameters on the deformation process, Poisson's ratio, and stability of auxeticity. Python program is integrated with the FE models used to automatically build models of different structure and to calculate/analyse key parameters and results. A range of auxetic structures has been developed, this chapter will be focused on missing rib models in tension (section 4.3), missing rib and mixed cellular structures in compression (section 4.4), self-similar hierarchical structures in compression (section 4.5), calculation and tracking of the area changes for cellular structures under compression and tension loads. The approach is also used to establish the key affecting factors on cellular materials deformation, the stability of Poisson's ratios, and the prediction of the structures for the targeted property (4.7 Discussion).

As listed in Table 4.1, section 4.2 introduces the main structure and functions of the Abaqus program and Graphical user interface (GUI) developed and used for building auxetic and related structures. The input of the Python program for building different structures is explained. Section 4.3 reports the FE models and typical results for missing rib (MR) structures under uniaxial tensions. The numerical results are compared to analytical solution and experimental data. The effect of sample sizes and cell numbers on the Poisson's ratio are studied based on the parametric FE models. Models with different beam angles are developed and the effect of the beam angles on the deformation modes, Poisson's ratio and auxeticity is presented. The effect of the ratio of the beam length is also studied and data is established systematically. Apart from the data for Poisson's ratios with different beam angle and length ratios, the stability of the Poisson's ratio of missing rib models and the critical strain levels for stable auxeticity is also established

---

based on systematic data.

Section 4.4 described experimental and numerical modelling of missing rib structures under in-plane compression. Parametric numerical models have been developed and correlated to testing data on structures of different beam angles, sample sizes/aspect ratios. The modelling results are also compared to other published experimental data of a different material. The key edge-wall contact stages in samples of different sizes and their effects on the structure deformation were investigated and analysed. The deformation of auxetic structures with different beam angles is established with a particular focus on the corner edge-wall contact and the deformed shapes at the full contact stage under compression. The deformation of mixed structures with alternating columns of different directions are studied experimentally and numerically; the Poisson's ratio and its stability are established. The influence of corner-edge and beam wall contacts on the overall structural deformation, critical strain range for auxeticity and stability of the structures is discussed. Section 4.5 presents the parametric program for modelling self-similar hierarchical honeycombs and typical results, including the deformation of self-similar honeycombs with different orders, effect of cell numbers and the ratio between the edge length of different ordered structures.

Section 4.6 presents a work in calculating the areas of individual cells in different cellular structures under loads in Abaqus. The approach used in area calculation and the function of the Python program is introduced. The area calculation program integrated with Abaqus models is presented and the key functional operation of the program is briefly introduced. Some typical data of cell area changes in regular and auxetics honeycomb structures is presented and analysed, and the results are correlated to the influence of the negative Poisson's ratio behaviours.

Section 4.7 discussed the effect of key results from the FE modelling of the missing rib models and key factors (such as beam angles, samples sizes, etc.) influencing the Poisson's ratio, deformation modes and areas changes. The effect of different modelling approaches and mesh sensitivity in different structures are also analysed, supported by selected data. The use of periodic boundary conditions is described, and the results are compared to data based

on full boundary/loading conditions presented in the main sections. Factors affecting the area analysis with different approaches and use of the program in random structures generation is also presented. The Development of mixed structures of regular shapes/patterns with a targeted Poisson's ratio and other targeted properties is discussed and a new approach in developing random structures with more freedom to produce structures with auxetic behaviour is presented and key results presented and its advantage in producing auxetic structures over other methods (e.g., Voronoi method) is outlined. The use of data systems for future works for user interface is also outlined.

**Table 4.1 Main Research Works**

Python based parametric Finite Element models and Abaqus plug-in GUI for building different cellular structures and typical structures studied in this work
<p><b>FE modelling of the deformation of missing rib models in tension</b></p> <ul style="list-style-type: none"> <li>➤ FE modelling of auxetic structures in tension and comparison with analytical and experimental data</li> <li>➤ Effect of sample size on the Poisson's ratio and stability of auxeticity</li> <li>➤ Effect of beam angles and the beam length ratio on the Poisson's ratio and auxeticity</li> </ul>
<p><b>Deformation mechanism of missing rib models under compression</b></p> <ul style="list-style-type: none"> <li>➤ Main deformation stages and contact formation of regular missing rib structures with a beam angle of 90.</li> <li>➤ Deformation and Poisson's ratio of missing rib structures with different beam angles.</li> <li>➤ Deformation of the mixed structures and Poisson's ratio under compression</li> <li>➤ Effect of the sample size on the initial contact and Poisson' ratio of missing rib structures</li> </ul>
<b>FE modelling of Hierarchical honeycomb.</b>

- Parametric program for building self-similar hierarchical structure FE models and approaches used for studying Poisson's ratio and auxeticity.
- Deformation of self-similar hierarchical honeycomb of different hierarchical orders
- The effect of the beam length ratios between hexagons at different structural levels on the auxetic deformation. .

**Modelling and analysis of cell area changes of regular and auxetic honeycomb.**

- Area calculation program development and integration with FE modelling.
- Typical data showing the cell area changes of regular honeycomb, missing rib structures and self-similar hierarchical structure in single cell model and multiple cell models.
- 

**Discussion.**

- Main factors influencing the deformation stages and Poisson's ratio of auxetic structures
- Use of parametric modelling in assessing the influence of different modelling approaches and mesh sizes
- Comparison between different area calculation and program approaches and typical use of the area calculation in 2D random Voronoi structure generation.
- Development of mixed structures of regular shapes/patterns of auxetic structures
- Development of more complex beam shapes and patterns
- Use of data system and user interface and future works

---

## 4.2 Program development in Abaqus for building different structures.

This section mainly introduces the main structure and functions of the Python program and graphical user interface (GUI) developed to build regular honeycombs, missing rib structures, self-similar hierarchical honeycomb structures, random cellular structures, and mixed structures. Detailed FE modelling for each structure will be presented in the results and discussion sections 4.3-4.7.

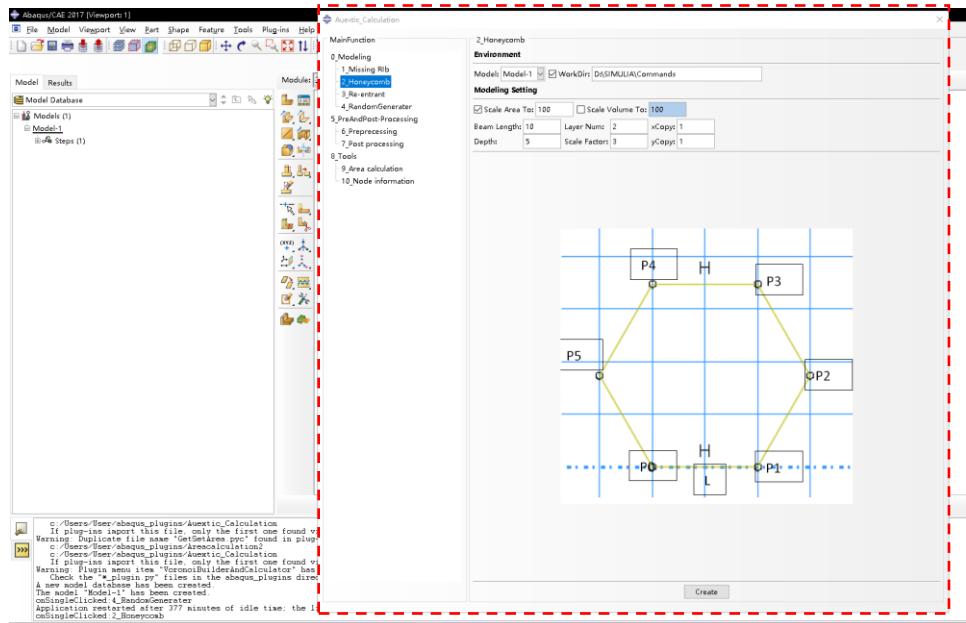
Parametric modelling-based approach is an effective research method, in which the key dimensional/materials variables can be parameterized, so it can be changed systematically. Abaqus provides Python language interface for secondary development users. Parametric modelling can be integrated into any of the main stages of finite element simulation including pre-processing/modelling building, simulation, post-processing, and data analysis ([Abaqus User's Manual 2017](#)). As outlined in the literature review, there are many structures with auxetic behaviours, which are of different patterns, so a program to automatically build the structures is an important starting point for research and development on auxetic cellular structures. A parametric program in building the structures will also provide a structured framework to develop more complex functions/programs relevant to Poisson's ratio and auxetic behaviours. It will also provide systematic data for establishing the effect of key design or material parameters such as sample size, cell size, mixed structures, etc.

### **Regular Honeycomb Structure**

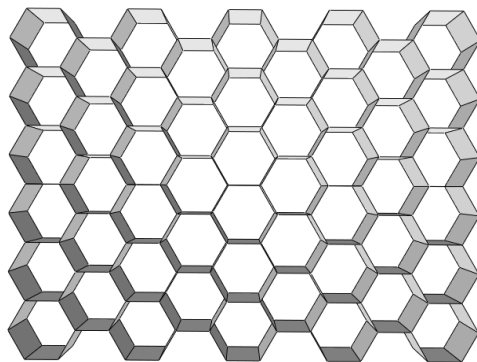
Figure 4.2.1 shows a simple GUI for regular honeycomb. It is mainly developed to assess the structure building process and validate the modelling approaches, as regular honeycomb has been widely studied experimentally and numerically ([Papka and Kyriakides, 1994](#)). The main GUI is shown in Figure 4.2.1. The main window of the GUI is highlighted with a red-dotted line box. The key functions of an ABAQUS CAE window are also shown for

---

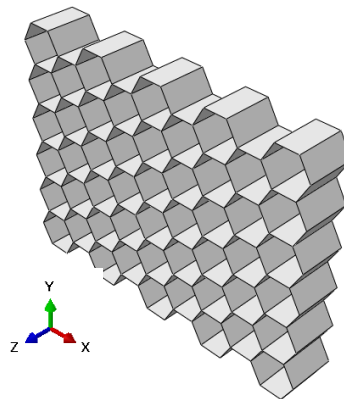
the processing. The program can build the structures automatically based on input of the length of the beam, number of cells in the horizontal and vertical direction. The building program starts from a single cell. The points were generated through a loop operation start from p0 to P5 (Figure 4.2.1a). Then the single cell is repeated based on the cell numbers designed by the user (xCopy and yCopy). The dimension of the honeycomb model shown in Figure 4.2.1 is adapted from published work by [Papka and Kyriakides \(1994\)](#). The program is able to provide efficient data for validation of the model building process as well as evaluating different modelling approaches, meshing etc. It also provides detail on the deformation process. Regular honeycomb also has a detailed analytic solution on the deformation and forces, which is important for validating the modelling approaches.



(a) The GUI of regular honeycomb Plug-in.



(b) A typical shell model build by Plug-In. (XY In-plane)



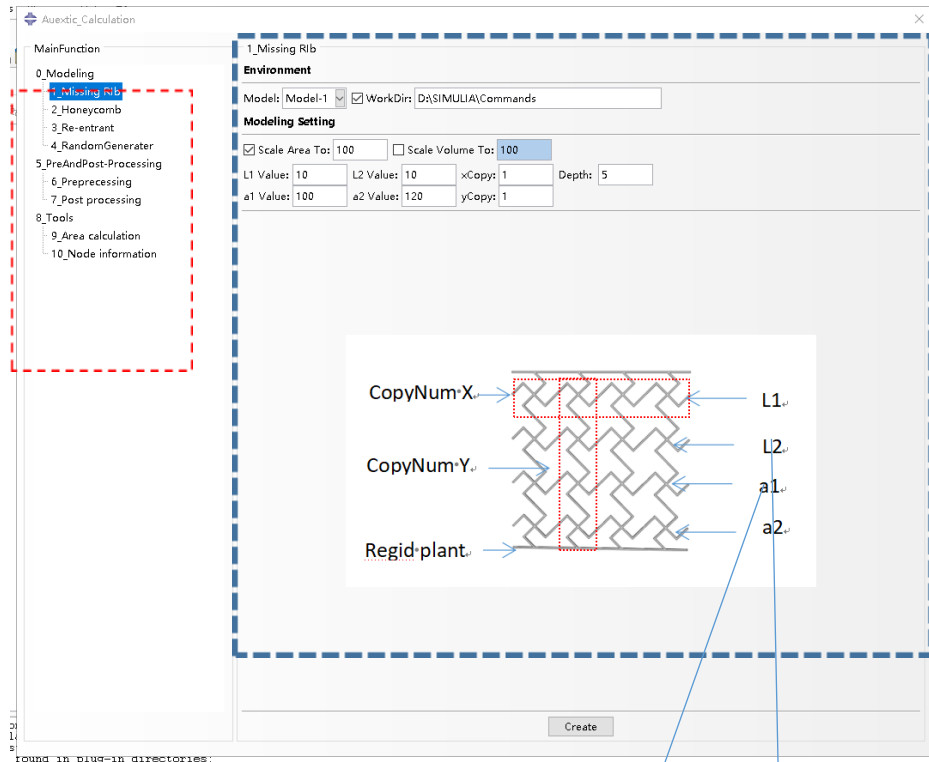
(c) Oblique view of the model showing the (out-of-plane dimension or extrusion depth)

**Figure 4.2.1** A Plug-in GUI for building a regular Honeycomb (a); and typical example (b). The dimension and lattice pattern are adapted from [Papka and Kyriakides \(1994\)](#) for validation purposes.

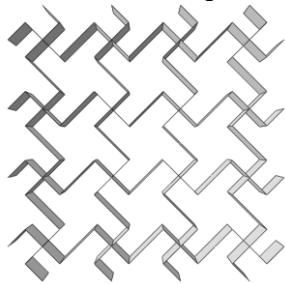
---

## **Missing Rib Auxetic Structure**

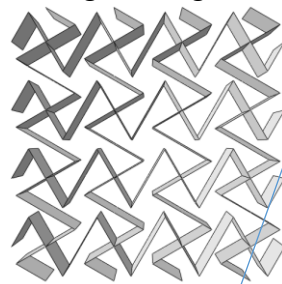
Figure 4.2.2 shows the structure of the missing rib auxetic model, which is the main focus of this work. The original model is proposed by [Smith et al \(2000\)](#) then later developed by [Gaspar and Ren et al \(2005\)](#). The missing rib structure and related system has attracted many research works in different forms. As shown in GUI, the initial input can be geometric inputs such as the length of the Beams ( $L_1$ ,  $L_2$ ), the angles between the beams ( $a_1$  and  $a_2$ ), the number of the repeating units, CopyNumX and CopyNumY, which is the repeating number of columns in the horizontal direction and the vertical directions, respectively. Depth refers to the out-of-plane extrusion depth ( $Z$  direction). The size of the sample can also be modified by two special scaling functions design. One is Scale area; one is for Scale Volume. These functions can further change the size of the structures to different aspect ratios, size and density. These are useful functions for quantitatively comparing structures to ensure they have the comparable dimensions or area or density. Similar to the missing rib models, other structures and more complex structures are also developed, as illustrated by the modules such as re-entrant structure, randomly generated cellular structures and mixed structures between missing rib and other structures (Figure4.2.3). Details of which will be presented in each individual section, including the modelling approach and key results in sections 4.3-4.7.



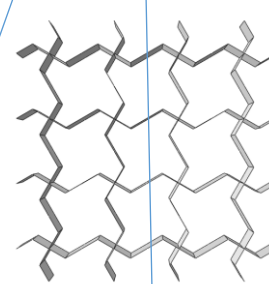
(a) Main input for building missing rib structures.



(b) A typical lattice structure.



(c) A typical 4-4 lattice pattern structure with a beam angle ( $a_1$ ,  $a_2$ ) of 60.



(d) Typical 4-4 lattice pattern structure with different beam length ratio ( $L_1/L_2$ ).

**Figure 4.2.2** Typical simple input GUI for building missing rib auxetic models of different angles ( $a_1$ ,  $a_2$ ) and beam lengths ( $L_1$ ,  $L_2$ ) in Abaqus.

---

### **Self-similar hierarchical honeycomb**

A self-similar hierarchical honeycomb is generated based on a regular hexagonal honeycomb structure. The modification consists of replacing each three-beam joint with a small hexagon, aligned parallel to the original honeycomb. The key procedures for building the hierarchical structures in this work is illustrated in Figure 4.2.3. It involves building the unit cell first then repeating the units and positioning them in a corresponding position. A loop operation is used to create the 6 points for the first hexagon edge points as shown in Figure 4.5.2a. In step 2, the vertices are replaced by a smaller hexagon, which is built with the replaced vertices at the centre point. A ratio between higher order hexagon edge length and lower order hexagon edge length is defined to control the size of the higher order hexagon in the program ( $d_2/d_1$  in Figure 4.2.3b), which is designated as ‘S’) following the approaches conventionally used (Mousanezhad et al., 2015; Zhang et al., 2016). The thickness of the beam is kept as the same between the hexagons of different orders. The parametric program can change the ratio, the thickness, and properties.

As shown in the Figure, the key process for the self-similar Table 4.5.1 shows the code in setting the input parameters. One key parameter is S, which is used to control the size of the higher order hexagon in the program ( $d_2/d_1$  in Figure 4.2.3). The dimensions are based on the edge length of the original hexagon, then the size of the smaller hexagon is controlled by the S value assigned. The remaining are mainly geometrical operations when building the unit cell. Then the number of repeating units are controlled by ‘xNum’ and ‘yNum’. Table 4.5.2 illustrates the code of generating the nodes. It is based on a Loop operation when replacing the original vertices by the smaller hexagon. When generate the repeating structures (i.e., based on ‘xNum’ and ‘yNum’), a rotation operation is required to ensure that all the edges and points are aligned properly.

**Table 4.2.1** Main input for building self-similar hierarchical structures

wd1= 'F:/temp'	# Abaqus work director
-----	
#Model parameter	
lengths = [10]	#Beam length of lowest order Beam
widths = [50]	#Extruded depth
scarps = [3]	#Ratio between higher beam length and lower beam
length66666666	
roots = [2]	#The order number of self-similar hierarchical honeycomb
igsName = 'Hierarchicalhoneycomb'	#Model name
xNum = 3	#Cell number in X direction (lateral)
yNum = 3	# Cell number in Y direction (Vertical)
shellThick = 1	#Shell thickness
-----	
#Materials properties for the solid material	
elastic = 1.7	#Young's modulus
poisonRatio = 0.3	#Poisson's ratio
density = 1e-9	#Density
havePlastic = 0	# Elastic or Perfect elastic plastic (0= Elastic,1= Perfect
elastic plastic)	
plasticStress = 10	#Yield stress
fraction = 0.2	#Fraction Coefficient
-----	
#Mesh and boundary condition	
meshSize = 1	#Global mesh size
loadStrain = 0.3	#Maximum load strain
loadTime = 1	#Total load time
-----	
#Post Processing	
numIntervals=100	# Number of output animation frames
figureOutputVals = ['Mises','U1','U2']	# Image output parameters,
optional:'Mises','U','U1','U2','U3'	
figureOutputAngs = ['Iso','Front']	# Image output angle, optional:'
Iso','Front','Left','Right','Top','Bottom'	
aviOutputVals = ['Mises','U1','U2']	# Animation output parameters
aviOutputAngs = ['Iso','Front']	# Animation output angle
aviRate = 2	# Animation frame rate

**Table 4.2.2** Codes for building the structure based on the midpoint approaches.

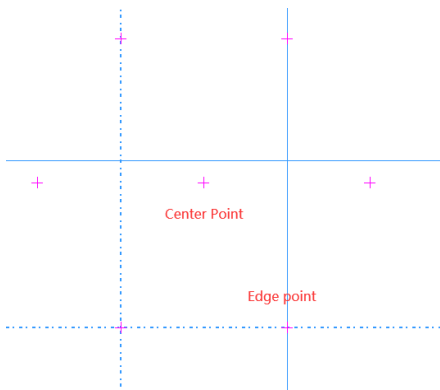
def getLevelLines(self,cent,d,edgelen):	# Nested function, used to get the edge
information under the current level	
if d==edgelen:	# Determine whether the current is the lowest order
hexagon or not	
points = []	
for i in range(6):	#Cycle to calculate six corner points of hexagon
x = cent[0]+d*sin(i*pi/3.0)	#X coordinate of corner point
y = cent[1]+d*cos(i*pi/3.0)	# Y coordinate of corner point
points.append([x,y])	# Storage point information
if i>0:	
self.lines.append([points[i-1],points[i]])	#Store line segment information
self.lines.append([points[-1],points[0]])	
elif d>edgelen:	# Next order cycle judgment
d <sub>r</sub> = d*cos(pi/6.0)	# Distance from center to side
ang = atan(edgelen/2.0/d <sub>r</sub> )	# Angle between edges
d <sub>cen</sub> = sqrt(d <sub>r</sub> **2+edgelen**2/4.0)	# Beam actual radius
newD = d/float(self.scarp)	# New hexagon beam length in the next order
newEdgelen = newD-(d-edgelen-2*newD)	# New actual beam length in the next order
for i in range(6):	# Loop to obtain line data, and solve the next
order at each corner	
x = cent[0]+d*sin(i*pi/3.0)	# X coordinate of center point
y = cent[1]+d*cos(i*pi/3.0)	# Y coordinate of center point
x1 = cent[0]+d <sub>cen</sub> *sin(i*pi/3.0+pi/6.0+ang)	# X coordinate of left point of actual beam
y1 = cent[1]+d <sub>cen</sub> *cos(i*pi/3.0+pi/6.0+ang)	# Y coordinate of left point of actual beam
x2 = cent[0]+d <sub>cen</sub> *sin(i*pi/3.0+pi/6.0-ang)	# X coordinate of right point of actual beam

```

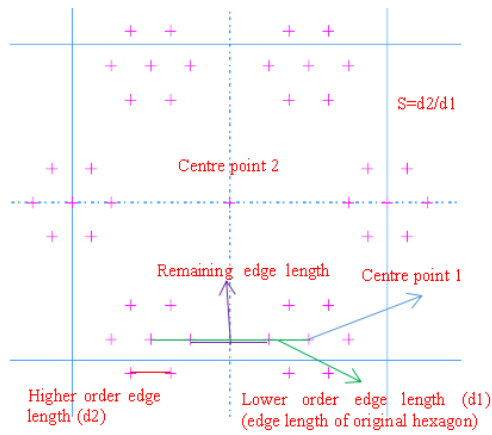
y2 = cent[1]+dcen*cos(i*pi/3.0+pi/6.0-ang) # Y coordinate of right point of actual beam
self.lines.append([[x1,y1],[x2,y2]])
self.getLevelLines([x,y],newD,newEdgelen)

def lineRotate(self,lines,angle): # Rotation function
    newlines = []
    theta = angle/180.0*pi
    for line in lines:
        newline = []
        for node in line:
            newline.append([node[0]*cos(theta)+node[1]*sin(theta),
                node[1]*cos(theta)-node[0]*sin(theta)]) # Two-dimensional coordinate
        transformation formula
        newlines.append(newline)
    return newlines

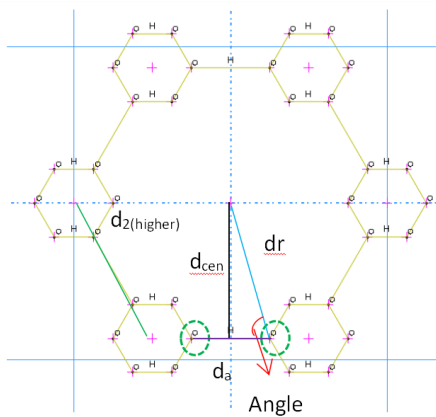
```



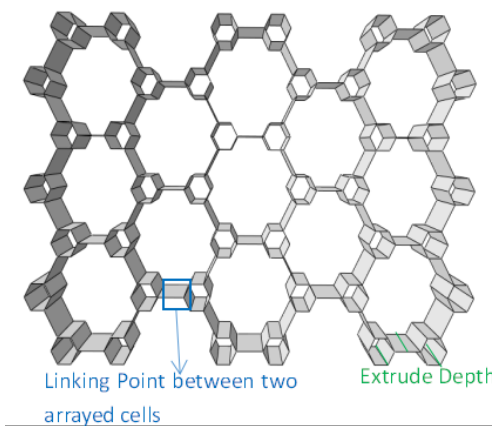
Step-1, drawing the edge points for a single regular hexagon.



(b) Step-2, Drawing edge points for the higher order hexagon.



(c) Step-3, Link the points to form a single Cell of hierarchical honeycomb.



(d) Step-4, Repeat the unit cell to form an array of the structures and extrude the 2D structure to form a cellular hierarchical honeycomb structure.

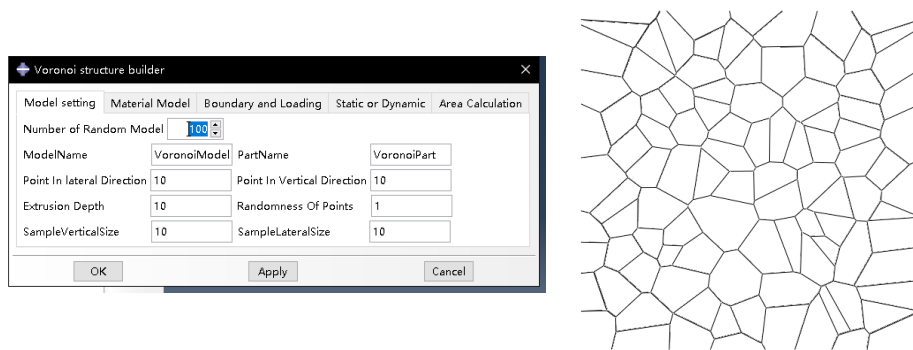
**Figure 4.2.3** Key procedures to build a 1<sup>st</sup> order self-similar hierarchical honeycomb.

---

### **Voronoi random structure**

Apart from the structures with auxetic behaviours, limited work was also conducted on random structures based on the Voronoi approach. Figure 4.2.4 shows the GUI for generating random Voronoi structures. The Voronoi diagram is a partition of a plane into regions call Voronoi cells. In the simplest case, these objects are just finitely many points in the plane (called seeds, sites, or generators). For each seed there is a corresponding region consisting of all points of the plane closer to that seed than to any other. To do this, individual seed points are positioned across the surface and the Voronoi algorithm is used to partition the surface into individual cells, separating each seed point from its neighbour with a cell wall positioned halfway between the two seed points (Alsayednoor and Harrison, 2016). In this work, a python program is built to generate the 2D Voronoi shell structure, the two-dimensional Voronoi polygon information is generated by Vorop++ which is an open sourced Voronoi algorithm library.

As shown in Figure 4.2.5, the first step of the program is generating the grid from random point, the grid size is the model overall size divided by the axial grid number (Step 1). The third step is randomly picking the grid point by control randomness (control size regularity of the cells) (Step 2). Then Step 3 and Step 4 are connecting the random point to a triangle and reconnecting the midpoint of the triangle beam to a Voronoi 2D sketch. These processes are operated by Vorop++ library (<https://www.nuget.org/packages/voroplusplus/>). In step 5 the sketch is extruded to a cellular structure by controlling the extrusion depth for further FE modelling.



(a) GUI for building random cellular (b)Typical random structure.

**Figure 4.2.4** GUI for building Voronoi random cellular structure.

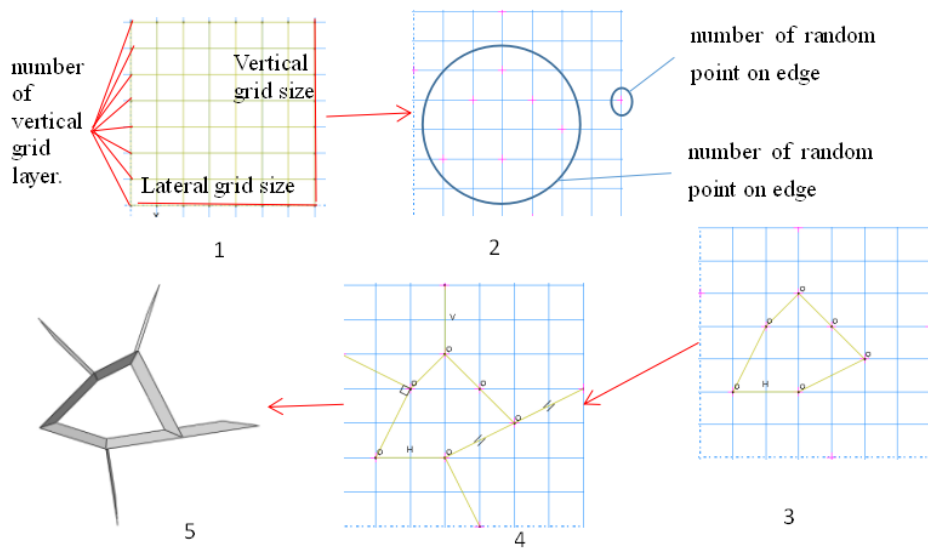
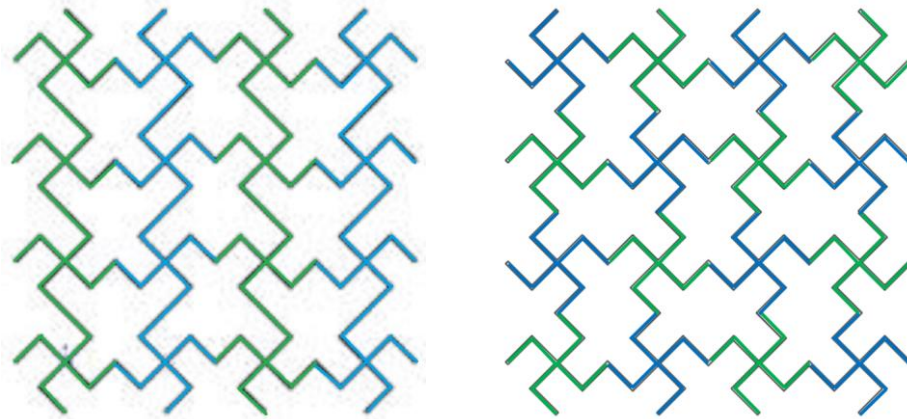


**Figure 4.2.5** Main process and data in building random cellular structures based on the Voronoi approach.

---

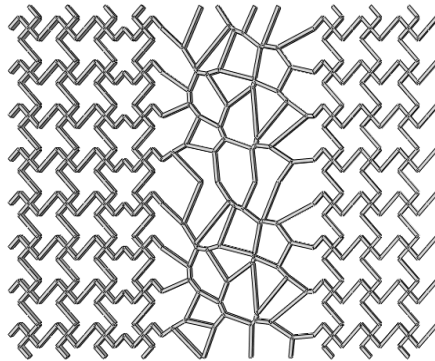
### Mixed Structures

Like the missing rib models, other mixed structures are also developed to study their effect on the Poisson's ratios. Some typical examples are shown in Figure 4.2.6. Figure 4.2.6a is a mixed structure formed by missing rib models with alternating columns of opposite angles. Figure 4.2.6b is a mixed structure of alternating orientation at both row and column. Figure 4.2.6c shows a structure between regular and random structures.



(a) A typical mixed Missing Rib structures with alternating columns.

(b) A typical mixed missing rib structures with alternating rows and columns.



(c) Mixed random and regular structure.

**Figure 4.2.6** Typical structures studied in this section.

The Python-based program is integrated in Abaqus for finite element analysis. As explained in the section above, it can generate different structures including missing rib structures of different beam angles, length ratio, etc. The program for the self-similar honeycomb can be used to automatically

---

produce structures of different hierarchical orders as well with different length scales by altering the S values (Figure 4.2.3). The Python program in itself can be used as a stand-alone program for designing the structures. Details of finite element modelling will be presented in each individual section, including the modelling approach and key results in section 4.3-4.7 together with details of the meshing, boundary/loading conditions in Finite element models and typical results focused on the Poisson's ratio and auxeticity.

---

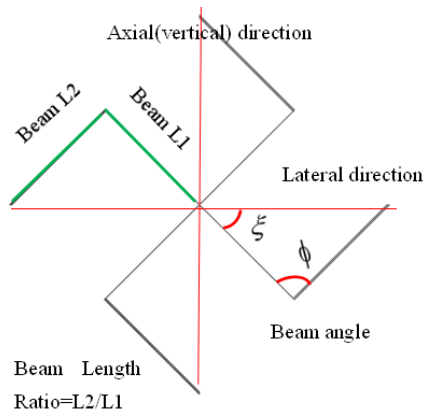
## 4.3 Deformation of missing rib models in tension.

This section reports on the FE models and typical results for missing rib (MR) structures under uniaxial tensions. The numerical results are compared to analytical solutions and experimental data. The effect of sample sizes and cell numbers on the Poisson's ratio are studied based on a parametric FE model. Models with different beam angles are developed and the effect of the beam angles on the deformation modes and Poisson's ratio is presented. The effect of the ratio of the beam length is also studied and systematic data is established. Apart from the data for Poisson's ratios with different beam angles and length ratios, the stability of the Poisson's ratio of MR models and the critical strain levels for stable auxeticity is established based on systematic data.

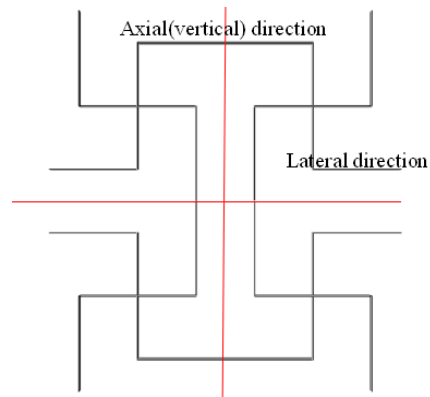
### 4.3.1. FE modelling of auxetic structures in tension and comparison with analytical and experimental data

Figure 4.3.1 shows models of two typical honeycomb structures. Figure 4.3.1a is a unit cell designated as the centrosymmetric missing rib model, and Figure 4.3.1b is a unit cell designated as the axisymmetric missing rib model, which has the same dimensions as Figure 4.3.1a but at a different orientation. Typical larger models consisting of a lattice pattern of 4x4 (axial x transverse direction) units are shown in Figures 4.3.1c&d. For the model presented, the beam length is 10mm, beam thickness is 1mm. As shown in Figures 4.3.1a there are four main geometrical variables where 'L1', 'L2' are the length of the first and second-line segment,  $\phi$  is the angle between 'L1' and 'L2',  $\zeta$  is the angle of between 'L1' and adjacent side of 'L1'. Figure 4.3.2 shows the mesh, boundary and loading conditions of FE models. The FE model is built with ABAQUS. The extrusion depth of the shell is 10mm for the model presented. The shell element is used with the thickness of shells set at 1 mm. There are 5 integration points through the thickness. Mesh sensitivity has been performed to determine an accurate result with optimum computational resource used. As shown in Figure 4.3.2c&d, the displacement is applied on the top of the model with the left and right sides being free to move. An ENCASTRE condition is applied on the fixed end of the structures with all the

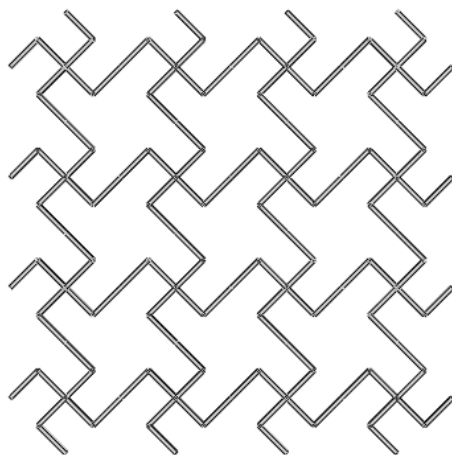
degrees of freedom (DOFs) set as zero. The resultant axial and lateral displacements are used in the calculation of the transverse strain and the Poisson's ratio. The lateral displacement is based on the displacement of the points at the edge. The materials property used is  $E=22$  MPa and  $\nu=0.3$  in the simulation.



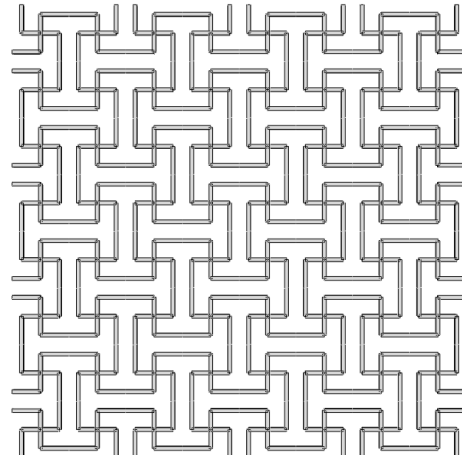
(a) Structure with a Centrosymmetric missing rib model. (shell thickness=1mm)



(b) Structure with an Axisymmetric missing rib model. (shell thickness=1mm)

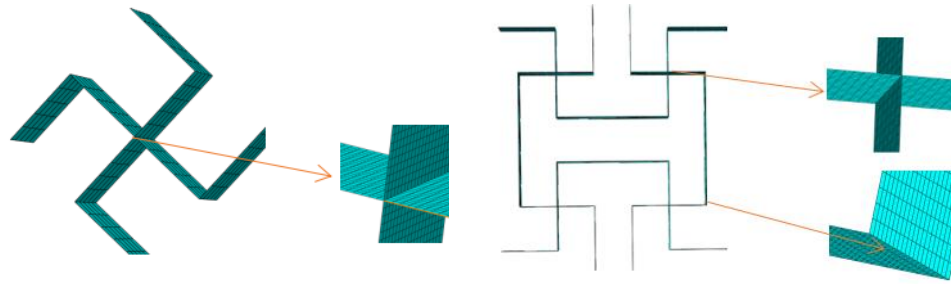


(c) Centrosymmetric missing rib honeycomb. (lattice pattern:4-4)



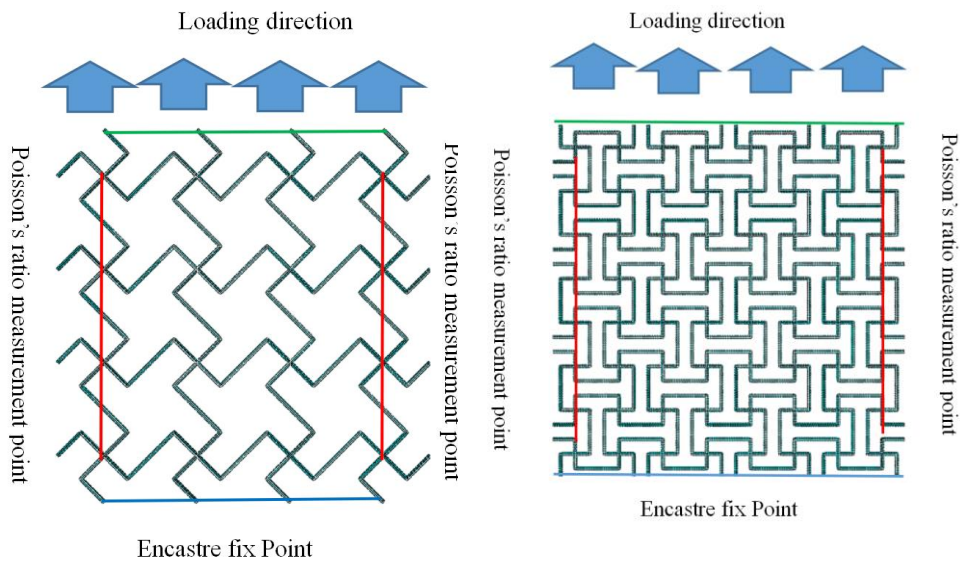
(d) Axisymmetric missing rib honeycomb. (lattice pattern:4-4).

**Figure 4.3.1** Centrosymmetric (a&c) and Axisymmetric (b&d) missing rib models used in the FE analysis.



(a) Mesh of a unit cell for Centrosymmetric model.

(b) Mesh of a unit cell of Axisymmetric model.



(c) Boundary and loading condition of a 4-4 Centrosymmetric model

(d) Boundary and loading condition of 4-4 Axisymmetric model.

**Figure 4.3.2** Mesh, boundary and loading conditions of FE models of missing rib models in tension.

The Poisson's ratio of the structures is determined by the ratio of the transverse strain and axial strain (loading direction) (Equations 4.3.1-4.3.3).

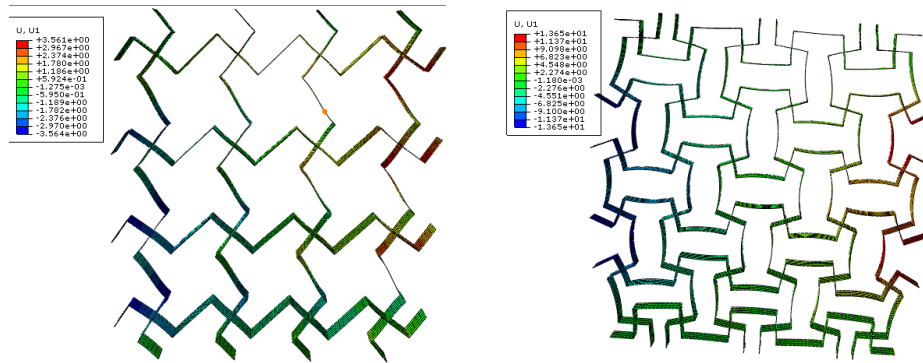
$$\epsilon_x = \frac{x_{load}}{x_0} \quad (4.3.1)$$

$$\epsilon_y = \frac{x_{right} - x_{left}}{y_0} \quad (4.3.2)$$

$$\nu = \frac{\epsilon_x}{\epsilon_y} \quad (4.3.2)$$

Where  $\nu$  is Poisson's ratio,  $\epsilon_x$  is transversal strain and  $\epsilon_y$  is axial strain,  $x_{load}$  is

displacement of loading points on axial direction,  $x_0$  is the original length on axial direction.  $x_{right}$  and  $x_{left}$  are displacement at traversal direction. Figure 4.3.3 a&b shows the deformation (displacement) of the auxetic samples in tension. The contour plots are for lateral displacement U1. As shown in the Figures, these two structures have different deformation patterns, but both show a clear lateral expansion under tension, exhibiting auxetic behaviours.

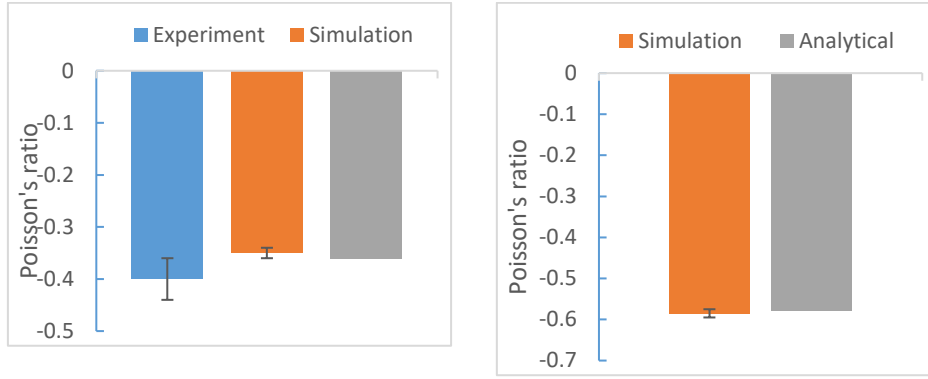


(a) Deformed shape of a 4-4 Centrosymmetric model. ( $E=22\text{MPa}$ ,  $\nu=0.3$ , beam wall thickness,  $t=1$ ). U1 is the lateral displacement.

(b) Deformed shape of a 4-4 Axisymmetric model. ( $E=22\text{MPa}$ ,  $\nu=0.3$ , beam wall thickness,  $t=1$ ). U1 is the lateral displacement.

Figure 4.3.3 Deformed shape and lateral displacement field of the auxetic samples in tension. (a) 4-4 Centrosymmetric model; (b) 4-4 Axisymmetric model.

Figures 4.3.4 shows the comparison between the Poisson's ratio obtained from FE modelling, analytical and experiments. Figures 4.3.4a is for the centrosymmetric missing rib structure, Figures 4.3.4b is for the Axisymmetric model. As shown by the bar chart, the FE data of Poisson's ratio are in a reasonable agreement with the analytical result and the experimental data. The analytical procedure was adapted from [Gaspar and Ren et al \(2005\)](#), which calculates the axial and transverse strain and the Poisson's ratio based on the key geometrical features including the beam length ( $r$ ) and the beam angles ( $\xi$  and  $\phi$ ) and the angles were labelled in Figure 4.3.1a.



(a) Comparison between the Poisson's ratio from FE modelling, analytical data (Gaspar et al., 2005) and experiments of the centrosymmetric model. (b) Comparison between the Poisson's ratio from FE modelling and analytical data (Gaspar et al., 2005) of the Axisymmetric model.

**Figure 4.3.4** Comparison between the Poisson's ratio from FE modelling, analytical and experiments of the two missing rib models.

For the centrosymmetric missing rib structure, the calculation was carried out using the following equations:

$$x = 4r \left( \frac{\cos(\xi_n - \phi_n + \Delta\phi(k-1))}{\cos(\xi_0 - \phi_0)} - 1 \right) \quad (4.3.4)$$

$$y = 4r \left( \frac{\sin \phi_n}{\sin \phi_0} - 1 \right) \quad (4.3.5)$$

$$v_{yx}^{ratio} = \frac{(\cos(\xi_n - \phi_n + \Delta\phi(k-1)) - \cos(\xi_0 - \phi_0)) - \sin \phi_0}{(\sin \phi_n - \sin \phi_0) \cos(\xi_0 - \phi_0)} \quad (4.3.6)$$

For Axisymmetric model, the calculation of the strains and the Poisson's ratio is based on the following equations:

$$x = 2r \left( \frac{3}{2} + \frac{\cos(\xi_n - \phi_n + \Delta\phi(k-1))}{\cos(\xi_0 - \phi_0)} \right) \quad (4.3.7)$$

$$y = 2r \left( \frac{3}{2} + \frac{\sin \phi_n}{\sin \phi_0} \right) \quad (4.3.8)$$

---


$$v_{yx}^{ratio} = \frac{(\cos(\xi_n - \phi_n + \Delta\phi(k-1)) - \cos(\xi_0 - \phi_0))(\frac{3}{2} + \sin\phi_0)}{(\sin(\phi + \Delta\phi) - \sin\phi_0)(\frac{3}{2} + \cos(\xi_0 - \phi_0))} \quad (4.3.9)$$

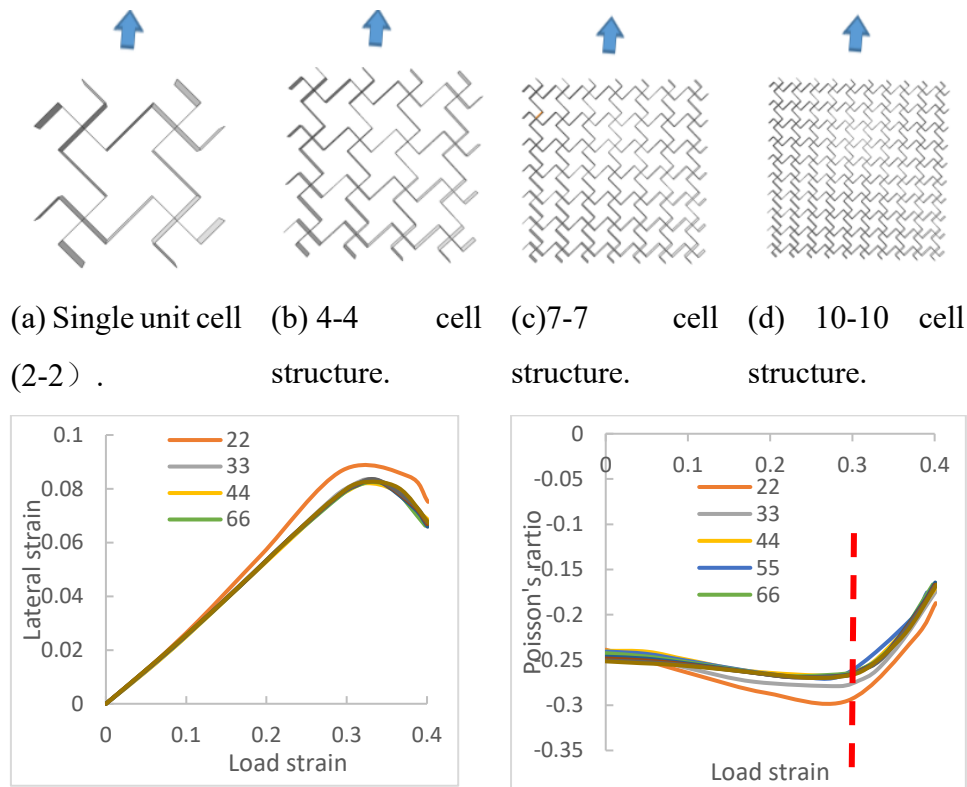
In formula,  $x$  and  $y$  are traversal displacement and axial displacement,  $r$  is length of single beam,  $\nu$  is Poisson's ratio and  $k = \frac{\Delta\xi}{\Delta\phi}$  is relative deformation. These equations are based on beam mechanics (considering bending and rotation deformation), they are valid for relatively small deformations (Gaspar and Ren et al., 2005). The experimental data in Figure 4.3.4 is based on samples of different materials, including EVA foams, injection moulded plastics (Gaspar and Ren et al., 2005) and silicone rubber (Li, 2018). The error bar represented the values scatter from different sources. As shown in the figure, the FE result shows a good agreement with the analytical prediction. The average experimental data is slightly higher than the analytical solution and the FE model, but in general these are in reasonable agreement. The close agreement suggests that the FE model is sufficiently accurate.

---

### 4.3.2 Effect of sample size effect on the Poisson's ratio and stability of auxeticity

To analyse the effect of cell numbers on the modelling results, especially in Poisson's ratios and the stability of the auxeticity (i.e., the Poisson's ratio remains negative stably over a range of strain level), it is important for practical design applications. If the Poisson's ratio changes, it will affect the materials selection and design. A Python program is developed to automatically generate the structures. Some typical structures are shown in Figure 4.3.5 (a-d). The material properties used are: Young's modulus ( $E$ ) is set as 22 MPa and Poisson's ratio of the material is set as 0.3. And beam length is 10mm. That series of models with different unit cell numbers are used to establish the effect of cell number on the simulation results. For convenience, the different lattice pattern is designated based on the number of repeating units (in both in-plane horizontal and vertical directions). For example, a missing rib model with 7 repeating units is named as MR-7-7. Mesh size effect was analysed by changing the mesh size until the modelling results showed limited changes with a further increase of the mesh density on the force and the Poisson's ratio. As the repeating unit/cell number is increased, the number of elements increased significantly. The study of the cell number effect is important as the number of cells may affect the effective deformation mechanism for cells at different positions. For a model with smaller cell numbers, the boundary effects will be more significant. In the model, a tension displacement load is applied from the top end and the bottom line is fixed for all degrees of freedom ( $U_1=U_2=U_3=0$ ,  $UR_1=UR_2=UR_3=0$ ). Some typical results are shown in Figure 4.3.5e&f. Figure 4.3.5e shows the lateral strain vs. the axial strain (loading direction). Figure 4.3.5f shows the Poisson's ratio v. the axial strain. As shown in Figure 4.3.5e, in all the cases, the lateral strain followed the axial strain close to a linear relation up a strain of about 25%. The effect of the cell numbers is shown in Figure 4.3.5f more clearly, when the cell number is over 4-4, there is no significant difference in the Poisson's ratio (Figure 4.3.5e), in other words, when the cell number is over 4-4, the boundary effect on the predicted Poisson's ratio is limited/negligible. Figure 4.3.5f also shows that the sample has a relatively

stable negative Poisson's ratio up to a strain level of about 35% (as indicated by the dotted line), beyond which, the Poisson's ratio is increased quickly towards the positive domains. This strain level is termed as the critical strain for stability of the auxeticity. This is important data for auxetic materials, as a stable auxeticity over a larger strain range is essential for applications with controlled properties. As shown by the dotted line, there is a slight difference in the critical strain for stable auxeticity among the models with different cell numbers, but difference is not significant.



(e) Lateral strain vs axial strain (load strain). (f) Poisson's ratio vs axial strain (load strain). The dotted line indicates the critical strain for stable auxeticity.

**Figure 4.3.5** Structures with different cell numbers used to study the sample size effect. The models are designated based on the number of repeating rows and columns. (Shell thickness=1mm, Material properties:  $E=22\text{MPa}$ ,  $\nu=0.3$ )

---

### **4.3.3 Effect of beam angles and the beam length ratio on the Poisson's ratio and auxeticity**

#### **Effect of the beam angles**

Figure 4.3.6 shows structures with different beam angles. The angle was automatically changed in the Python programs and number of cells can also be changed in the program. The beam length was kept the same ( $l=10\text{mm}$ ). Models with varying beam angles between  $60^\circ$  and  $120^\circ$  were developed and analysed, as shown in the figure. For each angle, the images show the original model of the undeformed model (top row), deformed model (second row) and enlarged view (third row) of a deformed cell taken from the corresponding large sample. As the beam angle increases, the overall sample size gets smaller. The deformed shapes at 20% load strain of the cells of different angles (70, 80, 90, 100, 110 degrees) are shown in the Figure. Under tension, all the samples showed clear expansion in the lateral direction showing clear negative Poisson's ratio behaviour. Figure 4.3.7a shows the lateral strain vs. axial strain (loading direction). All the data followed a similar trend, each curve consists of a stable/close-to-linear relationship, then lost the linearity at a certain strain point. The data shows that the structure with a lower beam angle undergoes much higher strain before losing the linear relationship between axial and lateral strain, which indicates the stability of the Poisson's ratio and reflects the critical strain for auxeticity. For example, the model with an angle of 60 degrees can maintain its stable Poisson's ratio up to a strain over 50%, while the model with an angle of 120 degrees has a critical strain for auxeticity just about 10%. Detailed data of Poisson's ratio over axial strain is shown in Figure 4.3.7b. For all the models, the Poisson's ratio is relatively stable over different strain levels, indicating a clear difference in the stability of the auxeticity. Figure 4.3.8a shows the effect of the beam angles on the initial Poisson's ratio of the structures. All the models have a negative Poisson's ratio, and the absolute values are increased with the beam angle. Figure 4.3.8b shows the critical strain for auxeticity, i.e., the strain level at which the Poisson's ratio lost its stability. The data shows a significant effect of the beam angles on the critical strains. These data are important for

---

understanding the behaviour of the structure as well as offering a potential way to control/design the Poisson's ratio through changing the angles.

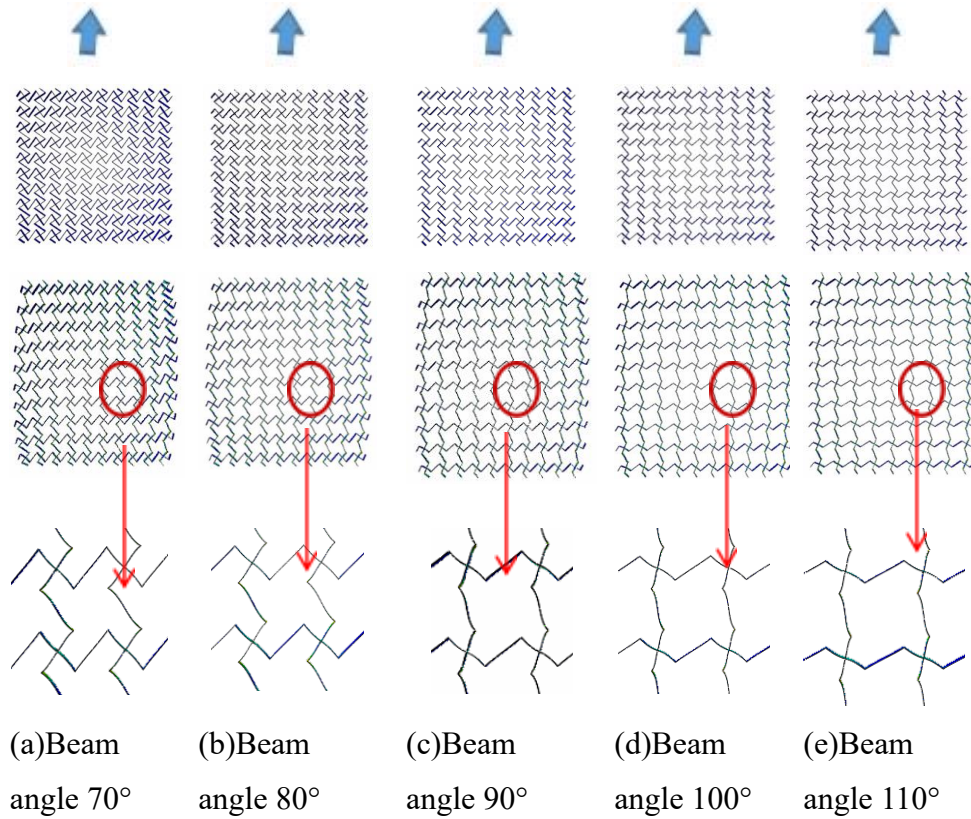
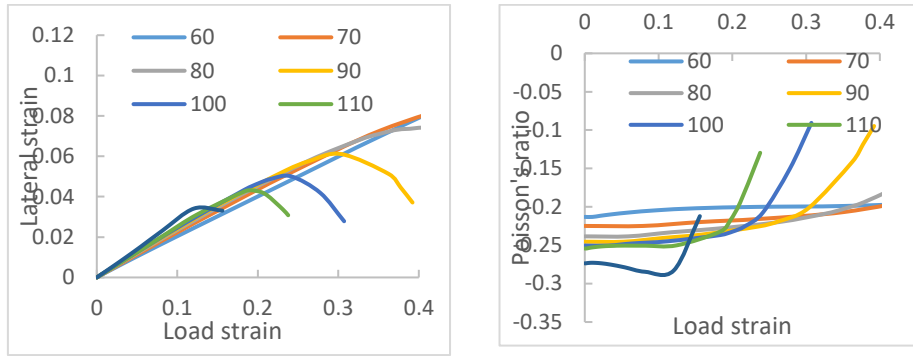
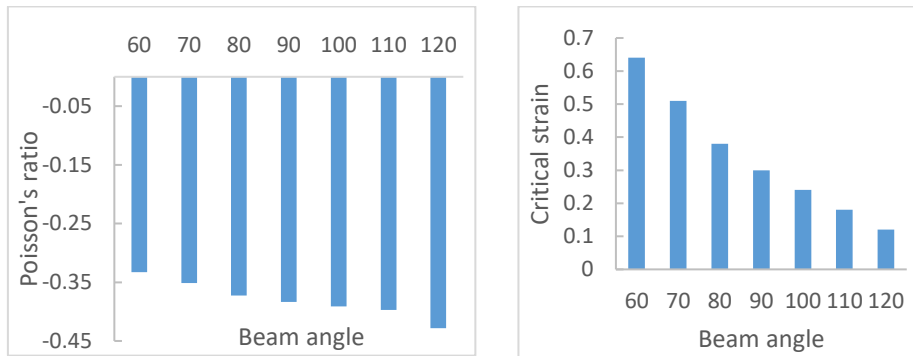


**Figure 4.3.6** Models and deformed patterns of auxetic structures at 20% load strain with different beam angles.



(a) Lateral strain vs. Axial strain for missing rib structures with different beam angles (60°-120°) (b)Poisson's ratio vs. axial strain for missing rib structures with different beam angles (60°-120°)

**Figure 4.3.7** Poisson's ratio and its stability over different strain level for missing rib auxetic structures with different beam angles.



(a)Initial Poisson's ratio for structures with different beam angles (60° to 120°) (b) Critical strain for stable auxeticity for structures with different beam angles (60° to 120°). The data was taken from Figure 4.3.7(b).

**Figure 4.3.8** Data showing the effect of the beam angles on the Poisson's ratio and critical strain for auxeticity.

---

### Effect of the beam length Ratio on the Poisson's ratio and auxeticity

Beam length ratio is a ratio connecting beam length divided by rotating beams length. The beam length ratio refers to the ratio between  $L_1/L_2$ . (as explained in Figure 4.3.1). Figure 4.3.9 shows some example of MR structures with beam length ratio of  $1/3$ ,  $1/2$ ,  $1$ ,  $2$ ,  $3$ , respectively. All these models of this study were set to the same overall size ( $200\text{mm} \times 200\text{mm}$ ) and width ( $7\text{mm}$ ).

Figure. 4.3.10 shows the models and deformed shapes of 10-10-unit models. As shown in the model, all the structures show lateral expansion under an axial tension load, indicating negative Poisson's ratio. From the deformed shapes, there is a significant difference between the structures as the beam length ratio is increased from  $1/3$  to  $1$ , then to  $3$ .

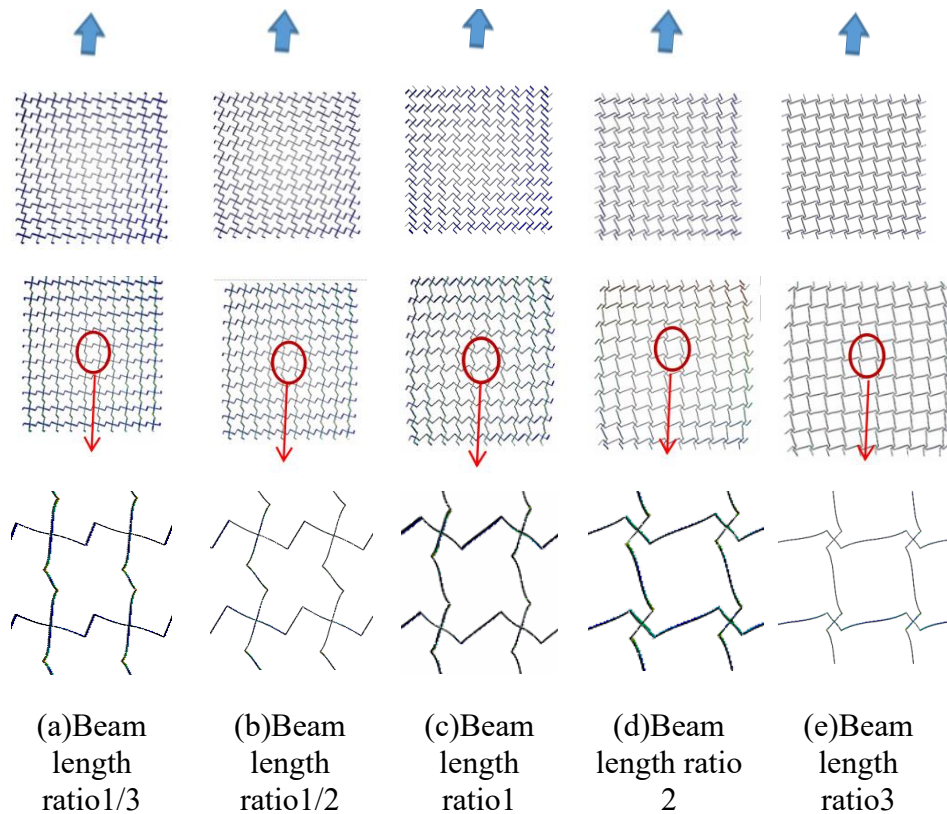
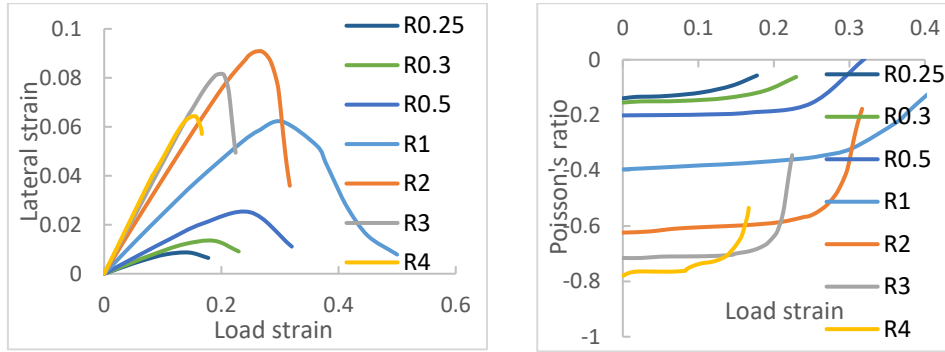


**Figure 4.3.10** Figures showing the effect of the beam length ratio on deformation patterns of missing rib structures.

As shown in Figure 4.3.11a, all the lateral strain vs. axial strain data showed linear trend stages, then the lateral strain decreases significantly. As shown in

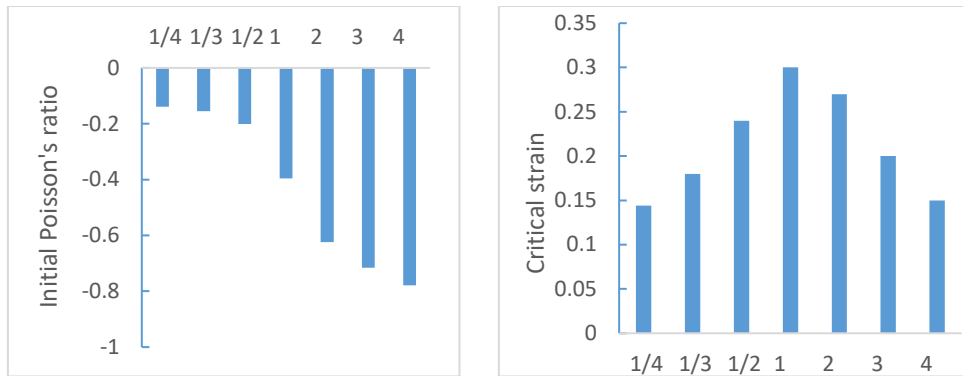
Figure 4.3.11b, the beam length ratio showed significant effect on the value of the Poisson's ratios as well as the critical strain for auxeticity.



(a) Lateral strain vs. Load strain of structures with different beam length ratio. (b) Poisson's ratio vs. load strain data for structures with different beam length ratio.

**Figure 4.3.11** Data showing the effect of beam length ratio on the Poisson's ratio and its stability. (See Figure 4.3.9 for details of the models).

Figure 4.3.12 shows the initial Poisson's ratio (at small strain) of the structures of different beam length ratios. The Poisson's ratio changes from -0.14 to -0.83 when the beam length ratio changes from 1/4 to 4. The data for the critical strain for Auxeticity is increased from beam length ratio of 1/4 to a beam length ratio of 1, then decreased when the beam length ratio is further increased. The data suggests a structure beam-length ratio of 1 (i.e., the regular missing rib model) has the best stability, in other words, a wider strain range for maintaining auxeticity. Another parameter for Poisson's ratio is the Poisson's ratio stability ( $\Delta\nu$ ) (Zhang et al., 2016) which is also analysed. It represents the variation of the Poisson's ratio. A low value of the Poisson's ratio stability indicates a more constant Poisson's ratio value. It is solved by using the LINEST function to solve the Poisson's ratio curve by a one-variable quadratic equation, and then deriving the equation twice to obtain the Poisson's ratio stability coefficient. The LINEST function uses the least squares method to perform a best straight line fit on known data and returns a function describing this line. The data is shown in Figure 4.3.12. The data shows that structures with a beam length ratio of 1 also has the best stability of the Poisson's ratio.



(a) Initial Poisson's ratio for structures with different beam length ratio (R1/4 – R4) (b) Critical strain for stable auxeticity of structures with different beam length ratio (R1/4 – R4).

**Figure 4.3.12** The effect of the beam length ratio on the Poisson's ratio and critical strain for stable auxeticity.

---

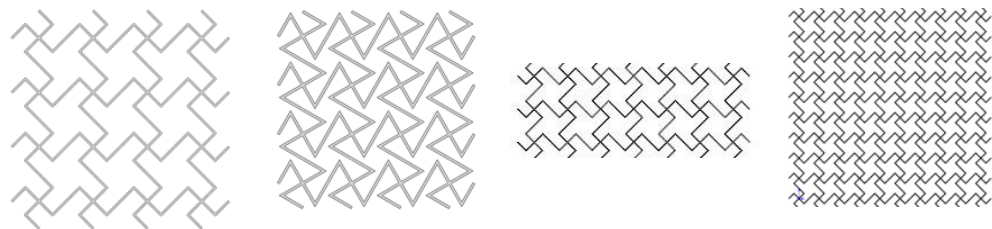
## 4.4 Deformation mechanism of missing rib models under compression

In this section, the deformation of missing rib auxetic structures and mixed structures are studied experimentally and numerically. The first part of the work is focused on experimental and numerical modelling of missing rib structures of 3D printed Thermoplastic Elastomers (TPE) samples. Parametric numerical models have been developed and correlated to testing data on structures of different beam angles, sample sizes/aspect ratios. The modelling results are also compared to other published experimental data of a different material. The key edge-wall contact stages in samples of different sizes and its effects on the structure deformation were investigated and analysed. The deformation of auxetic structures with different beam angles is established with a particular focus on the corner edge-wall contact and the deformed shapes at the full contact stage under compression. The deformation of mix structures with alternating columns of different directions are studied experimentally and numerically; the Poisson's ratio and its stability are established. The influence of corner-edge and beam wall contacts on the overall structural deformation, critical strain range for auxeticity and stability of the structures is discussed.

### 4.4.1 Structures, Experimental and Modelling Approaches

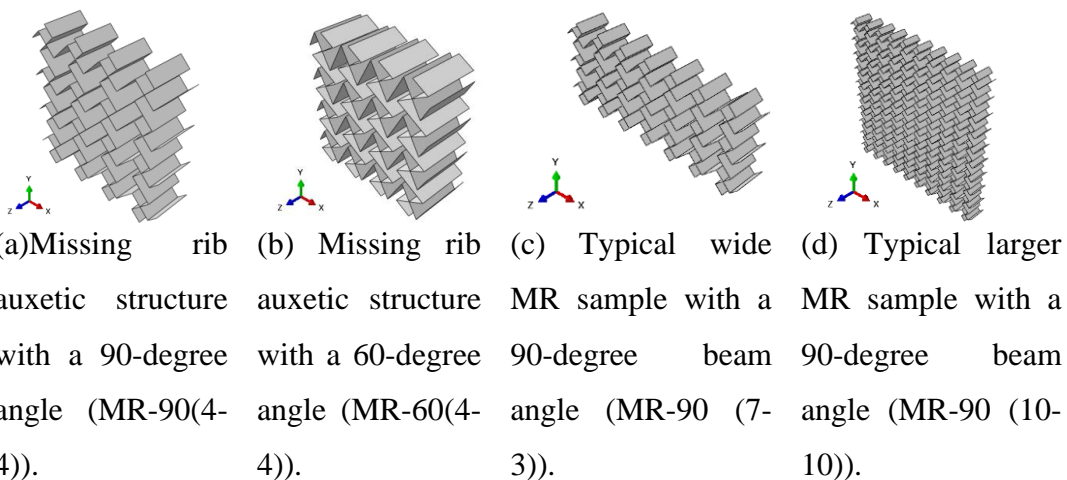
Figure 4.4.1 shows some typical structures studied experimentally and numerically. Figure 4.4.1a is a normal missing rib auxetic structure with a beam angle of 90 degrees. Figure 4.4.1b is a typical missing rib auxetic structure with a beam angle of 60 degrees. In the work, models with different beam angles have been studied (e.g., 60, 70, 80 and 90 degrees). Samples of different sizes including much larger samples are systemically studied in order to establish the deformation mechanisms, and the effective stable Poisson's ratios with a particular focus on the cell wall/edge contact, localised deformation and structure/shape stability. Figure 4.4.1c is a typical example

structure of wider samples. The example shown in Figure 4.4.1d is with a 10-10 lattice pattern. In the finite element model, a Python program is developed which is able to automatically vary the key parameters including the beam length ( $l$ ), thickness ( $t$ ), sample size and depth (out-of-plane sample dimension) as well as studying the effect of mesh size, friction and material models). Use of the Python program allows the mapping of potential effects of sample dimensions and sizes on the deformation process, deformed patterns, key properties, such as stress-strain data, Poisson's ratio and their stabilities. Figure 4.4.2 shows the models of the structures in Oblique side 3D view.



(a)Missing rib auxetic structure with a 90-degree angle (MR-90(4-4)). (b) Missing rib auxetic structure with a 60-degree angle (MR-60(4-4)). (c) Typical wide MR sample with a 90-degree angle (MR-90 (7-3)). (d) Typical larger MR sample with a 90-degree angle (MR-90(10-10)).

**Figure 4.4.1** Typical structures studied.



(a)Missing rib auxetic structure with a 90-degree angle (MR-90(4-4)). (b) Missing rib auxetic structure with a 60-degree angle (MR-60(4-4)). (c) Typical wide MR sample with a 90-degree angle (MR-90 (7-3)). (d) Typical larger MR sample with a 90-degree angle (MR-90 (10-10)).

**Figure 4.4.2** Typical models of studied in Oblique side 3D view.

---

Most of the numerical modelling is based on the FE model with as-testing full boundary conditions of a uniaxial compression test (Figure 4.3.3), while additional representative volume element (RVE) approach-based analysis has also been performed on selected samples as a comparison. The boundary and loading condition for the FE model with a full boundary condition is schematically shown in Figure 4.4.3. In the model, a uniaxial velocity ( $V_2$ ) load (1mm/s, same as the test) is applied on the top loading surface and an encastre fix condition ( $U_1=U_2=U_3=UR_1=UR_2=UR_3=0$ , all degrees of freedom are fixed) is applied on the bottom surface.  $U_1$  is lateral in-plane displacement,  $U_2$  is vertical displacement, and  $U_3$  is the out of plane displacement.  $UR_1-3$  are the rotational degrees of freedom). Figure 4.4.3 also shows the close-up view of the typical meshing scheme used in the finite element analysis. The element type used in the simulation is S4R which is a 4 node, quadrilateral, stress/displacement shell element. Detailed mesh sensitivity tests have been conducted. For compression tests with a particular focus on the contact and deformation pattern, the mesh sensitivity is crucial in particular for the post-contact stage. In the mesh sensitivity tests, the convergence of the simulation is depicted through the reaction force, and the deformed shape of the beams. The final mesh size selected is 1 mm, which give a ratio of element size of 1 and sufficiently accurate results within the strain range and contacting stage studied. Similar meshing conditions have been used in other published works of cellular structures ([Imbalzano et al., 2018](#); [Liu et al., 2015](#)). Self-contact is defined with a fitted plastic-plastic friction coefficient of 0.35 being used in the model. In the simulation, force-displacement is recorded, the deformation of the structures under compression is analysed, and the central points of the outermost left-right columns are recorded for calculating the Poisson's ratio from the captured images. The process excluded the two points immediately next to the fixed and loading end to reduce the uncertainty with the boundary effect. This gives the overall Poisson's ratio of the structure studied and provides a mean for studying the sample size (cell number) effects on Poisson's ratio.

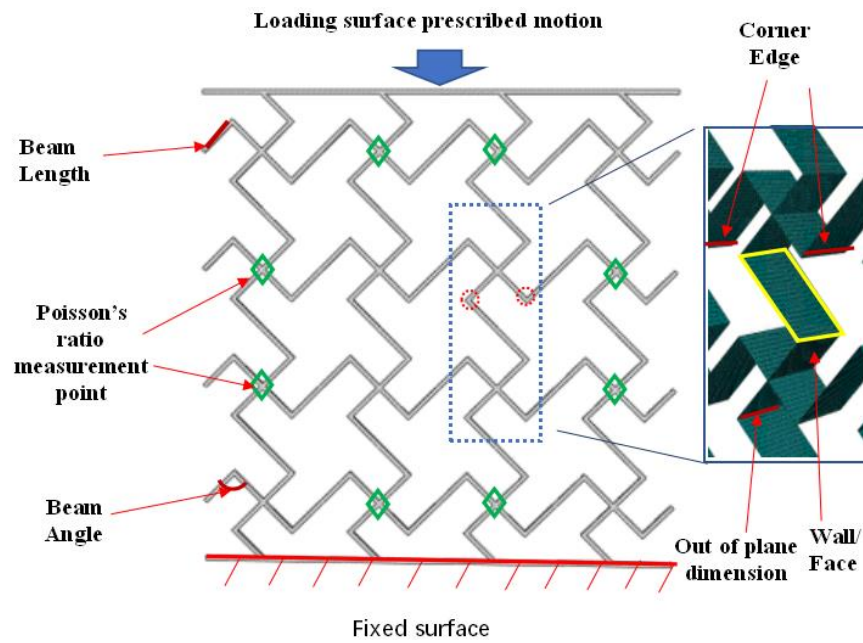
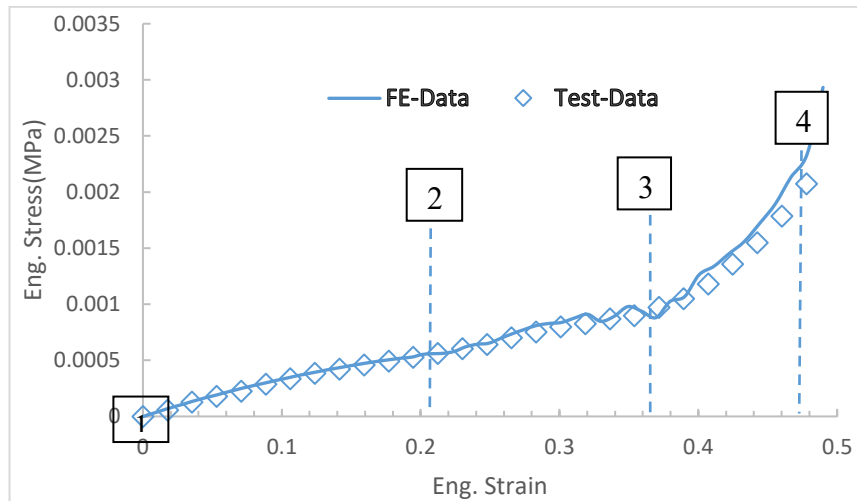


**Figure 4.4.3** The load and boundary conditions in the finite element model and RVE model using a regular missing model MR-90 (4-4) as an example.

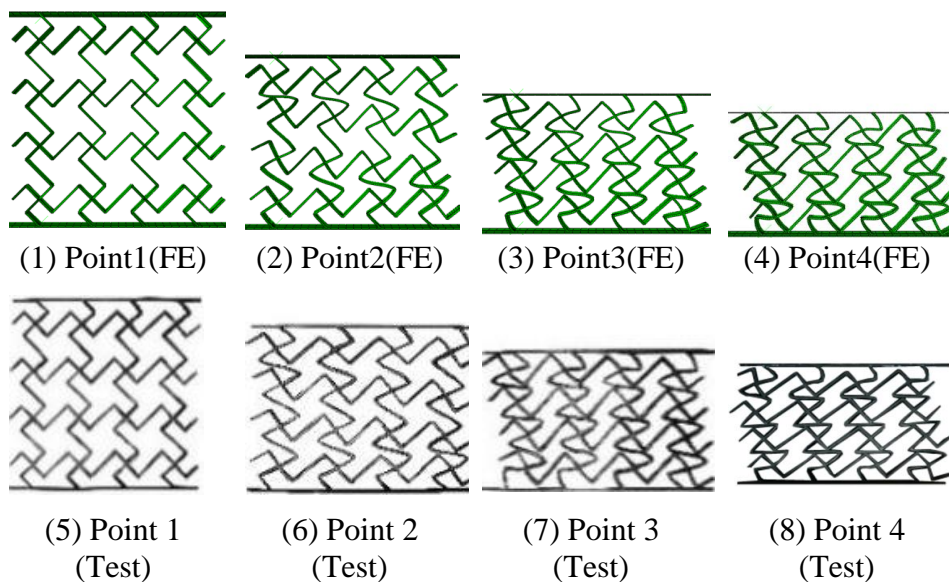
---

#### 4.4.2 Deformation of normal missing rib structures with a beam angle of 90 (MS-90).

Figures 4.4.4a compared the stress strain data of a normal missing rib model with a beam angle of 90 degrees (MR-90) from the experiments and numerical modelling. The stress is the overall force divided by the effect area of the sample; the strain is calculated by the overall displacement divided by the original height of the sample. The deformed structures at different stages are presented in Figure 4.4.4b. As shown in Figure 4.4.4a, the numerical data showed a good agreement with the experimental stress-strain curve. The experimental data is based on the average of three test data. There is some scattering of the data at high strains, but in general, the numerical result followed the trend of the testing data well. Point 1 is the initial unreformed stage, point 2 represents the initial corner edge-cell wall contact stage, point 3 represents the point when all the corner edges are in contact with the cell walls in the sample. Point 4 is the further deformation of the locked/contacted structure. As shown in Figure 4.4.4b, the simulated deformation patterns resemble the images from the test for all the key stages including the initial corner edge-wall contact ((2) and (5)), the location of the contact is highlighted in the red dotted circle. The structure when full contact is formed ((3) and (6)) also showed a reasonable resemblance. The stage shows the full corner edge-wall contact also shows a reasonable agreement between the modelling and the test, but this is not the focus of this report as it is subject to more complex modelling and testing with different materials. The results show that the relatively small sample size with a 4-4 lattice pattern is effective in capturing the key deformation stages. The simulation and testing also shows a skewing from left to right in this case. This is probably a specific feature for the missing rib type of structures. To study the potential effect of the sample size, both numerical and experiments have been conducted on a wider and shorter sample with a lattice pattern of 7-3. The lattice structure of the model is shown in Figure 4.4.1e, the results are presented in Figure 4.4.5.



(a) Numerical (solid line) and experimental (open symbols) Eng. stress-strain data of MR-90 (4-4) sample. The stress is calculated by the force divided by the overall area. The strain is calculated by the displacement by the original sample height.

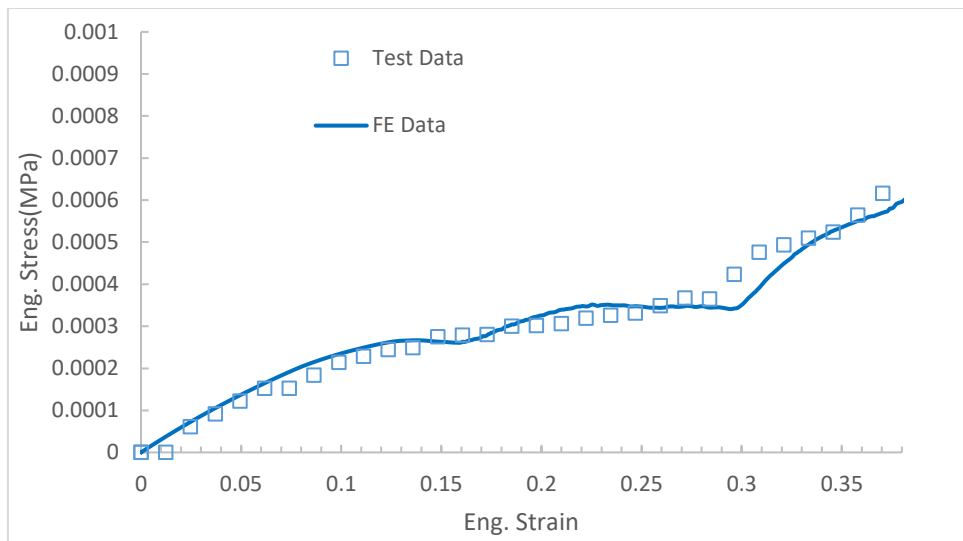


(b) Deformation and contact in the structure at different stages.

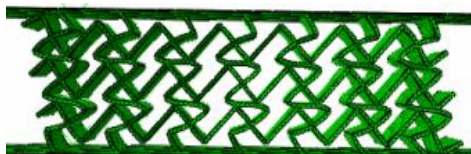
**Figure 4.4.4** Numerical and experiment stress-strain data and deformation of MR-90(4-4)

Figure 4.4.5a shows the Eng. stress strain for the wider sample processed with the same material and processing method in this work. The sample consists of 7-3 cells; the beam length is  $\sim 9.57$ mm, the wall thickness of 1.5 mm, the thickness of the sample is 30mm and the overall height of the sample is 82.5mm. The dimension is selected in order to assess the potential effect of the sample aspect ratio on the beam-wall contact and change of the stress-strain due to the contacts. As shown in the Figure 4.4.5a, the testing data and

the numerical results show a reasonable agreement. Figure 4.4.5b shows the comparison between numerical modelling results with published force-displacement data of a different material. The beam wall thickness is 1.5mm, the out-of-plane sample thickness is 50 mm (Remennikov et al., 2019). The overall sample height is the same as in Figure 4.4.5a of 82.5mm. The material used is Nylon with a Young's Modulus of 597MPa, Poisson's ratio is 0.33, and density of 1140 kg/m<sup>3</sup>. Both elastic and elastic plastic models have been evaluated based on the stress-strain data provided, there is no significant difference in the modelling results within the strain range studied. Only the results with an elastic model are shown in Figure 4.4.6.



(a) Comparison between numerical and testing data (MR-90 (7-3)) (Beam length: 9.57mm, wall thickness: 1mm, sample depth: 30, overall sample height: 82.5mm. Material: TPE).



(b) Full contact at point 3 (FE).



(c) Full contact at point 3 (Experimental)

**Figure 4.4.5** Comparison between numerical and testing data (MR-90 (7-3)) (Beam length: 9.57mm, wall thickness: 1mm, sample depth: 30, overall sample height: 82.5mm. Material: TPE).

As shown in the Figure 4.4.6, the FE modelling data is in a reasonable

agreement with the published data in terms of the key stages. For a wider sample, as shown in both Figure 4.4.5 and Figure 4.4.6, the overall sample deformation and key stages of the stress strain curves are similar to the key stages of the smaller square 4-4 structure presented in Figure 4.4.4. The wider model showed more significant plateau stages (circled in Figure 4.4.6) than the 4-4 model in Figure 4.4.4b. The deformation at the later stage showed certain diversion between the testing and modelling data, but the overall trend of the stress-strain curve over the contact stages is similar among these three set of data (Figures 4.4.4a, 4.4.5a and 4.4.6). Figure 4.4.6 used force-displacement data to preserve the feature of the original published experimental data (Remennikov et al., 2019). A key point of focus, the strain for reaching the first slope increase point on the stress-strain curves among these samples is similar, which is observed to be correlated to the first corner edge-wall contact in all the cases. The association of this with the overall Poisson's ratio and its stability is to be analysed based on data of different structures and sizes and is to be discussed in later sections in comparison with other structures (structures with different beam angles and mixed structures).

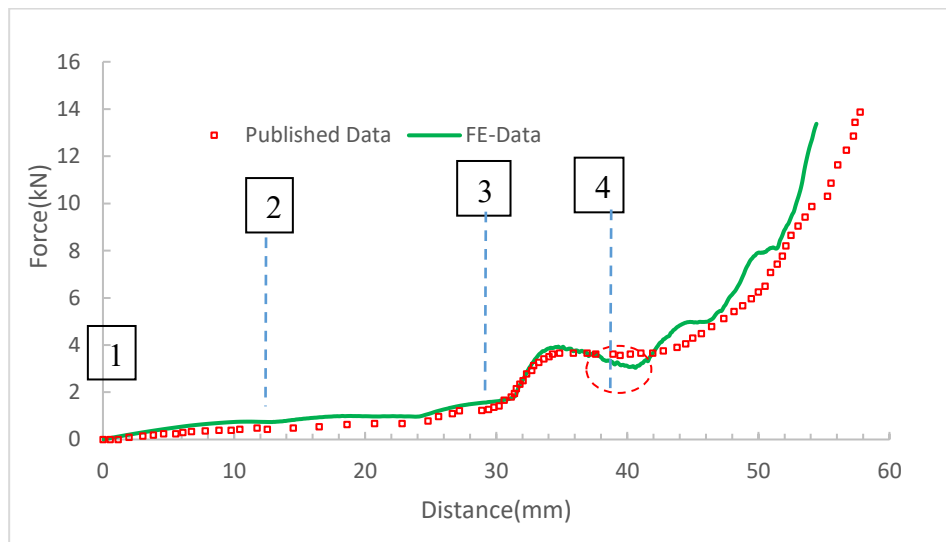
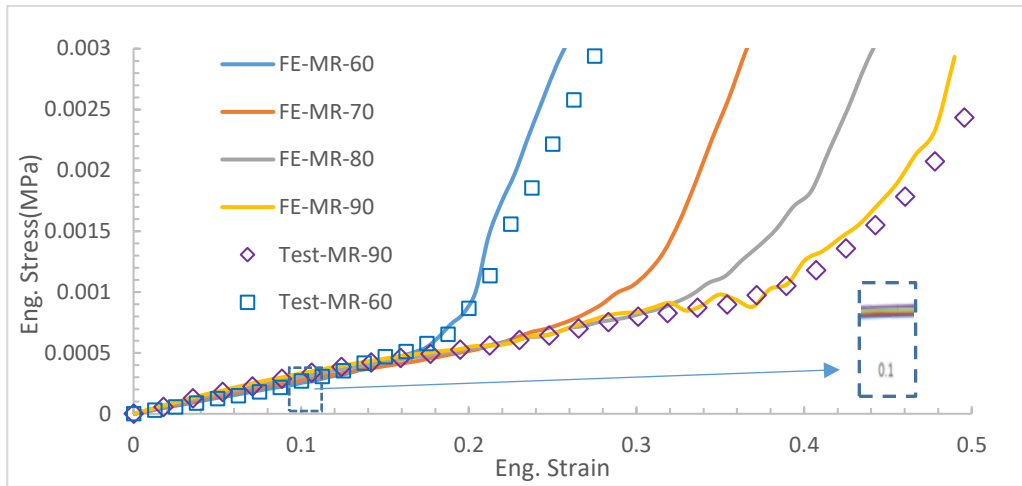


**Figure 4.4.6** Comparison between numerical and published force-displacement data (MR-90 (7-3) sample) (Remennikov et al., 2019).

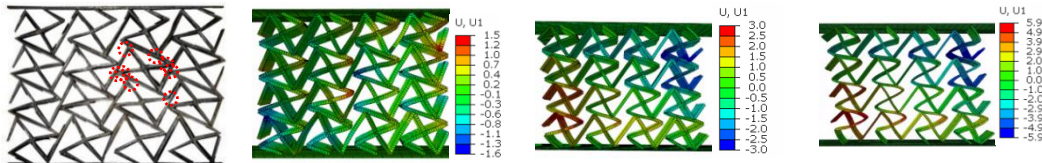
---

#### 4.4.3 Deformation of missing rib structures with different beam angles.

Figure 4.4.7 shows typical simulation and test data of missing rib auxetic structures with different beam angles. For each model, the beam length is the same ( $l=10\text{mm}$ ), so the sample size is reduced as the angle is changed from 90 to 60 degrees. From geometry analysis, when the angle changes, the distance between the corner edge and the opposite wall is changed accordingly for a fixed beam length and thickness, this directly affects the contacting situations. Experimental tests have been performed on the sample with an angle of 60 degrees, which is presented together with the testing data of the normal missing rib model with an angle of 90 degrees (open symbols). In general, the FE modelling and experimental data show a good agreement. As shown in the close-up view (dotted box), in the initial stage, the stress for the model with a higher beam angle is higher, the slope of the stress-strain data decreases as the angle is varied from 90 to 60 degrees. This is because the beam is tilting more in the structure with a smaller beam angle, the beam is much easier for the wall to bend. The data shows clearly that the critical strain for reaching the corner edge-wall contacting point for lower angled structure (for example the 60-degree model) is much lower due to the geometrical effect, and the stress increased significantly once the full corner edge-wall contact stage is formed. The typical deformed structure captured from the test and FE simulation is shown in Figure 4.4.7b&c. Comparing this with features for the 90-degree model (Figure 4.4.5&4.4.6), there is less bending of the beam wall for the 60-degree structure at the full corner edge-wall contact stage. The results (Figure 4.4.7b&c) also show that the full contact (or locked) structure has more corner edge-wall contacting points than the 90-degree structure (Figure 4.4.5&4.4.6). This is probably the main reason for the much stiffer stress-strain data for the 60-degree structure after contact. As shown in Figures 4.4.7b-e, the shape of the cells and the number of contacting points changes as the beam angle is increased and fewer contact points are formed, which would directly affect the stiffness of the structure.



(a) Eng. stress-strain data of missing rib auxetic structures with different beam angles (4-4 model). The symbols are experimental data, the solid lines are FE data. (Beam length=10mm, wall thickness=1mm, Out-of-Plane sample thickness =30mm).



(b) Deformed structure with the corner beam in full contact with the opposing wall. (Beam Angle=60) (Experimental)

(c) Deformed structure with the corner beam in full contact with the opposing wall. (Beam Angle=60) (FE model)

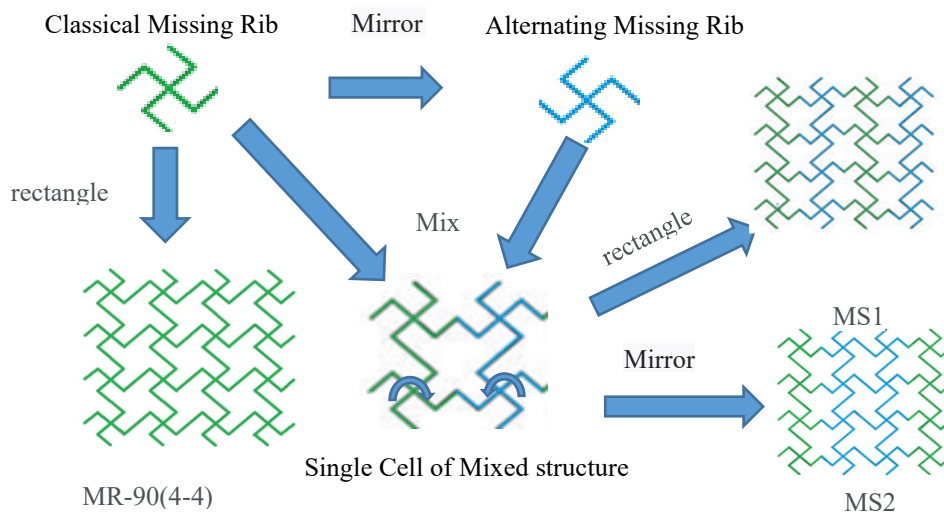
(d) Deformed structure of model (70-degree beam angle).

(e) Deformed structure of model (80-degree beam angle).

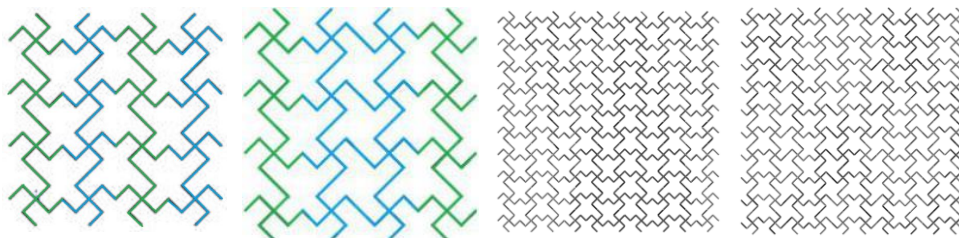
**Figure 4.4.7** Simulation and experiment results of structures with different beam angles.

#### 4.4.4 Deformation of the mixed structures and Poisson's ratio under compression

Figure 4.4.8 shows two typical mixed structures studied. The main idea is changing the pattern of the column to control the rotation of the beam (Figure 4.4.8a). Figure 4.4.8b shows mixed structure-1 which consists of alternating single column of normal missing rib model in opposite directions. As shown in the figure, cell columns in green are regular normal missing rib cells, and columns in blue are opposite normal missing rib cell. Figure 4.4.8e designated as mixed structure 2, contains two columns of normal missing rib model in opposite directions. Samples of different sizes, including much larger samples, are systematically studied to establish the deformation mechanisms, and the effective stable Poisson's ratios with a particular focus on the cell wall/edge contact, localized deformation, and structure/shape stability.



(a) Diagram illustrating the concept of designing mixed structures by control the rotation.



(b) Mixed structure 1 (MS-1) (4-4 model).

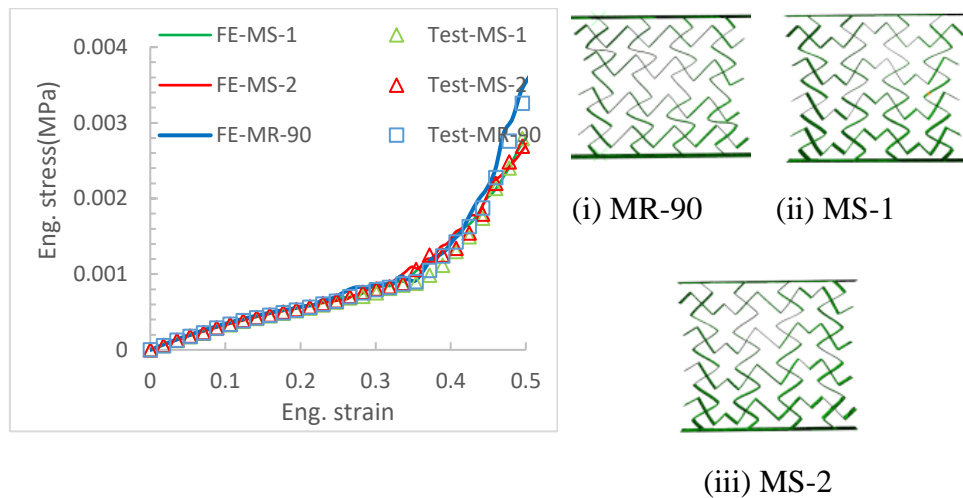
(c) Mixed structure 2 (MS-2) (4-4 model).

(d) Mixed structure 1 (MS-1) (10-10 model).

(e) Mixed structure 2 (MS-2) (10-10 model).

**Figure 4.4.8** Typical mixed structures studied.

Figure 4.4.9 compared the Eng. stress strain for the mixed structures (MS-1 and MS-2) with the normal missing rib structure (MR-90). As shown in data, the slopes of the initial stages are similar between these structures up to a strain level. However, the localised contact situation is much different. As shown in Figure 4.4.9b(i-iii), at a strain of  $\sim 20\%$ , the corner beam-wall contact starts to form for the normal missing rib model Figure 4.4.9b(i), however, no contact is formed for the mixed structure at this stage for the mixed structures (Figure 4.4.9b(ii&iii)). The connecting point between the columns with different angles restrains the rotation of the unit, which changes the strain to reach the corner edge-wall contact, as well as the formation of the contact. Another significant difference is the in-plane deformation between the three structures. The mixed structure-1 and mixed structure-2 structures are much more stable than the normal missing rib model. Both mixed structure-1 and mixed structure-2 exhibit clear inward lateral displacement under compression, suggesting that the structure has maintained the auxeticity of the missing rib model.



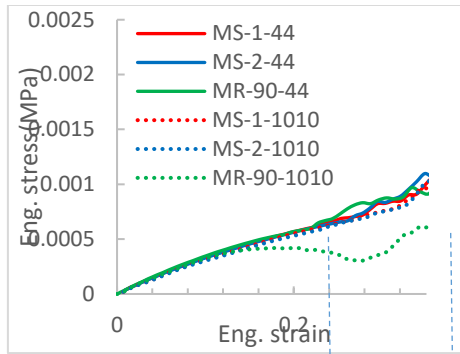
(a) Engineering stress-strain of mixed structures. (b) Typical deformed shape at strain 20%.

**Figure 4.4.9** Numerical and experimental data of normal missing rib (i) and mixed missing rib structures: MS-1(ii)&MS-2(iii).

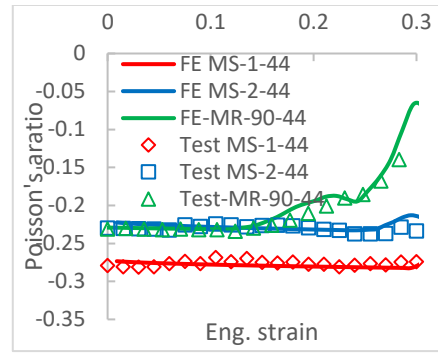
A series of FE models have been developed with much larger sample sizes to further establish the effect of the mixed structure on the Poisson's ratio and the stability of the sample shapes. Some typical examples are shown in Figure

---

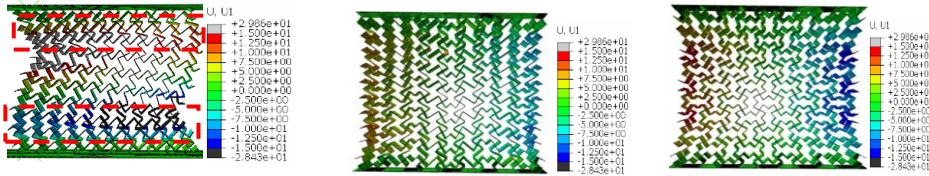
4.4.10. As shown in Figures 4.4.10a, the critical strain range for a stable Poisson's ratio corresponds to the corner beam-wall contact point (as marked by the dotted line in Figure 4.4.10a). The stress-strain curves for mixed structure-1 and mixed structure-2 are similar between the 4-4 and 10-10 models, but there is a clear difference between the 4-4 and 10-10 for the normal missing rib models (MR-90). Figure 4.4.10(b) plots the Poisson's ratio of the structures. Also plotted (open symbols) on the Figure 4.4.10b are the experimentally measured Poisson's ratio. As shown in Figure 4.4.10b, there is a slight difference in the value of the Poisson's ratio, but all structures are in the negative Poisson's ratio domain at small strains. The effective Poisson's ratio of the mixed structure-1 is similar/identical to the value for the normal missing rib model (MR-90), but the critical strain within which the Poisson's ratio is stable is much higher. The Poisson's ratio of mixed structure-2 is even lower indicating a stronger auxeticity, the stability range of the Poisson's ratio for mixed structure-2 is like that for mixed structure-1, much higher than the normal missing rib model. Figure 4.4.10c compared the deformed shape of the mixed structure and normal missing rib structures (10-10 structure) at a strain level of ~20%. At this strain level, the normal missing rib model has lost its stability of the auxeticity, the normal missing rib model shows a clear unstable deformation, and the Poisson's ratio becomes unstable. While both mixed structure-1 and mixed structure-2 have maintained a relatively stable structure, the contour of the lateral displacement ( $U_1$ ) is indicative of clear auxeticity. This may also have contributed to the difference in data from sample sizes. The image also shows that the large sample (10-10) could not form a fully contacted structure. The top and bottom sections formed a full contact pattern (box in dash line). This may have contributed to the difference in stress-strain data between the 4-4 and 10-10 normal missing-rib structures. This suggests that the mixed structure offers similar Poisson's ratio/auxeticity level with better shape stability and less sensitivity to the cell numbers under compression.



(a) Eng. Stress strains of different structures simulated with different cell numbers (4-4, 6-6, 10-10).



(b) Comparison of Poisson's ratio mixed structures and normal missing rib auxetic structures.



(i) Deformation of MR-90. (ii) Deformation of MS-1. (iii) Deformation of MS-2.

(c) Deformed shape of the mixed structure and normal missing rib structures at 20% strain. (the color band for U1 is applicable to all the figures (i-iii))

**Figure 4.4.10** Stress-strain, Poisson's ratio and deformed shape of the mixed structures.

#### 4.4.5 Effect of the sample size on the initial contact and Poisson' ratio

The experimental and corresponding numerical data showed that the contact between the corner edge and the opposite wall in the missing rib model played a significant role in the deformation mode of the structure and the Eng. Stress-Strain curve. Models with a larger beam length to thickness ratio ( $l/10$ ) and a relatively soft material provided an effective experimental set-up to study the deformation mechanism in detail. The work on samples of different sizes reveals that once the corner edge-wall contact is initialised, the stress is increased slightly, once a full contact position is formed, the structure becomes much stiffer. Figure 4.4.11 presents the initial corner edge-wall contact for different structures and sample sizes (4-4 and 10-10 lattice pattern). There is a clear difference between the three structures. For the normal missing rib models, the corner edge-wall contact starts at a diagonal corner. This is due to the shear point and the intrinsic angle of the structure. While for the mixed structures of different sizes as shown in Figure 4.4.11b&e for mixed structure-1 and Figure 4.4.11c&f for Mixed structure-2, the position of the initial contact is different, and the contact was at different orientations due to the rotation of the cells. This has probably contributed to improvement of the shape stability.

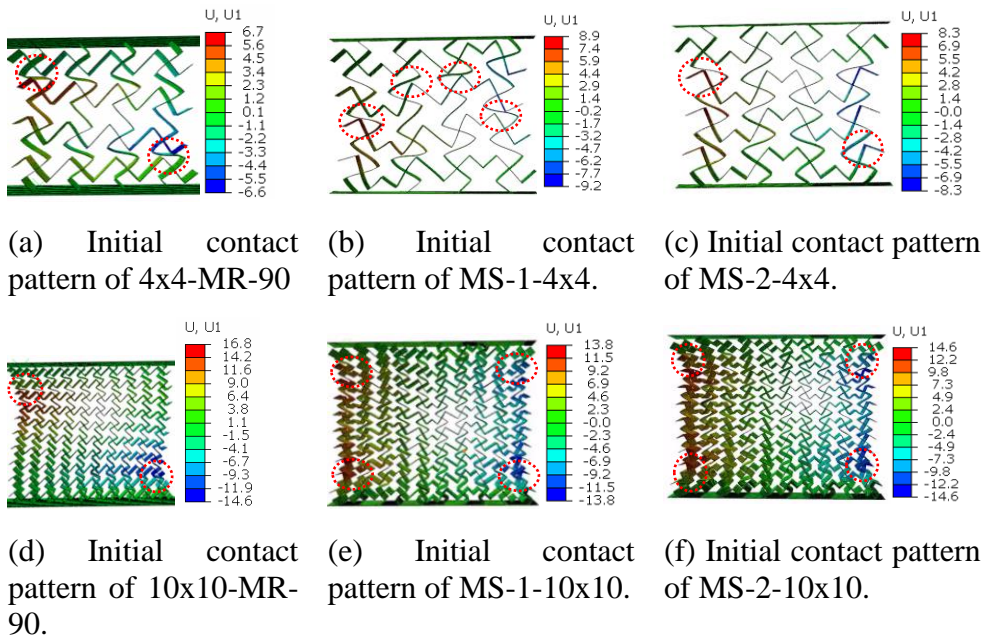
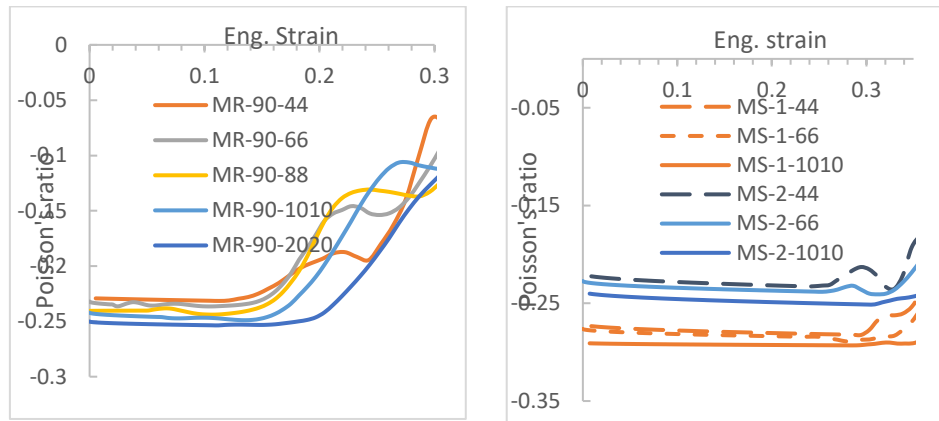


**Figure 4.4.11** Initial corner edge-wall contact position and deformed shapes (U1: Lateral displacement).

---

For auxetic structures, the stability of the Poisson's ratio and the auxeticity is also very important. The work shows that the critical strain for a stable Poisson's ratio is associated with the starting of the corner edge-wall contacting points. Figure 4.4.12a shows the Poisson's ratio of the normal missing rib model with different cell numbers. In all the cases, the Poisson's ratio at lower strain levels is negative reflecting an auxetic behaviour. In general, the value of the Poisson's ratio is close, but there are still differences in the values. When a small number of cells is used, the absolute value is relatively low. The Poisson's ratio is like other reported values (Jiang et al., 2019). Despite the difference in the Poisson's ratio values, the critical strain for stable Poisson's ratio among the samples of different sizes is only slightly increased as the number of cells is increased. The effect of the cell number agrees with the observations by others (Dong et al., 2019; Jiang et al., 2019; Mizzi et al., 2018; Mizzi et al., 2020). The influence of the edge might be associated with constraints of the edge on the operative deformation modes including potential shear induced deformation. In simulation and experimental studies on the tensile behaviour of tetrachiral honeycombs (Mizzi et al., 2018; Mizzi et al., 2020), it was found that the auxeticity of the system decreases upon increasing the number of repeating units in the system. This behaviour was found to be associated with the tendency of the tetrachiral systems to undergo shear deformation upon uniaxial loading, which is blocked by the edge effects at the regions where the geometry is being fixed. Similar process on the shear deformation can be observed under compression load as well. Further work will try to quantify the contribution of such a mechanism on the auxeticity of missing rib models under uniaxial compression. Figure 4.4.12b shows the Poisson's ratio of the mixed structures of different sizes. The Poisson's ratio values are all in a similar range. The Poisson's ratio for mixed structure-1 is similar to the normal missing rib model, while the Poisson's ratio for mixed structure-2 is lower and there is limited effect from the sample sizes (cell numbers). In every case, the critical strains for a stable Poisson's ratio of the mixed structures are higher than the normal missing rib model (Figure 4.4.11a). For compression loading, out of

shape in-plane deformation has also been observed by other experimental and numerical works in compression tests of missing rib and other auxetic structures (Cui et al., 2018; Dong et al., 2019; Jiang et al., 2019; Zhao et al., 2019; Wu et al., 2018), which may have an adverse effect on the design uncertainty and shape control processes. So, the improvement in the stability of the structures mixed structure-1 and mixed structure-2 could be a beneficial advantage to the structure design and development depending on the application. Also plotted on Figure 4.4.12b are the Poisson's ratios calculated by the RVE approach. The decreasing trend of the Poisson's ratio is similar to that from the FE models of the full boundary model for both mixed structure-1 and mixed structure-2. This has probably benefited from the stability of the two mixed structures.



(a) Poisson's ratio of normal missing ribs structure (MR-90) determined from different sample sizes.

(b) Poisson's ratio of mixed missing rib models (MS-1 and MS-2) determined from different sample sizes.

**Figure 4.4.12** Poisson's ratio vs Engineer strain of normal missing rib structure and mixed structures.

---

## 4.5 FE modelling of self-similar hierarchical honeycombs

### 4.5.1 Self-similar hierarchical structures.

This section presented the parametric program for modelling self-similar hierarchical honeycombs and typical results, including the deformation of self-similar honeycombs with different orders, effect of cell numbers and the ratio between the edge length of different ordered structures. As shown in Figure 4.5.1, self-similar hierarchical honeycomb structures are formed by replacing the vertices of a regular hexagonal lattice with smaller hexagons. (Mousanezhad et al., 2015; Sun and Pugno, 2013; Haghpanah et al., 2013). Higher order self-similar structure can be designed by repeating the operation of replacing the varieties and forming hierarchy for different orders (e.g., 1st, 2nd... nth). A typical example is shown in Figure 4.5.2 in 2D and 3D view. Typical target applications include vibration damping, crush resistance, etc. (Mousanezhad et al., 2015; Zhang et al., 2016). The focus of the work is to develop a parametric program to build a model of different structures for studying the deformation of structure of different levels of order and the effect of dimensional parameters on the Poisson's ratio.

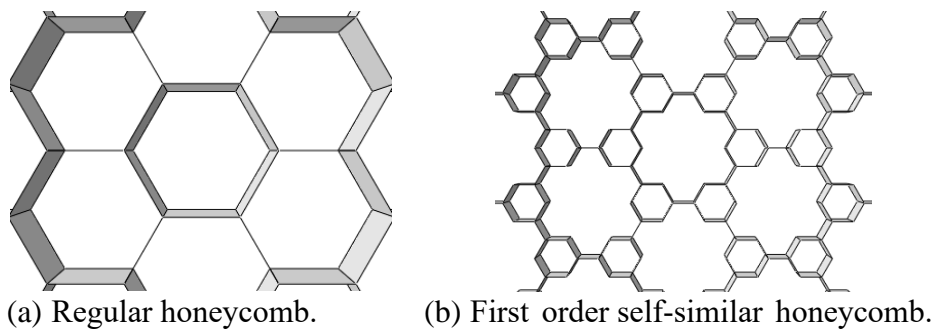
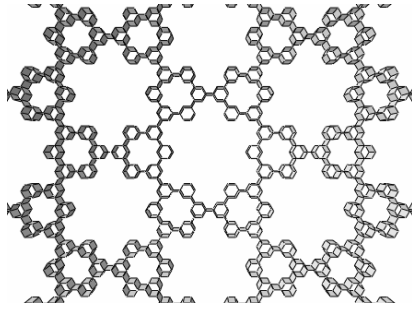
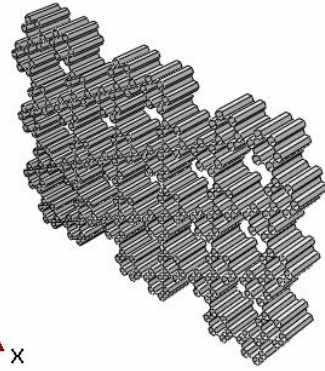


**Figure 4.5.1** FE model of Regular honeycomb and 1<sup>st</sup> order self-similar hierarchical honeycomb structures.



(a) front view of second order self-similar hierarchical honeycomb



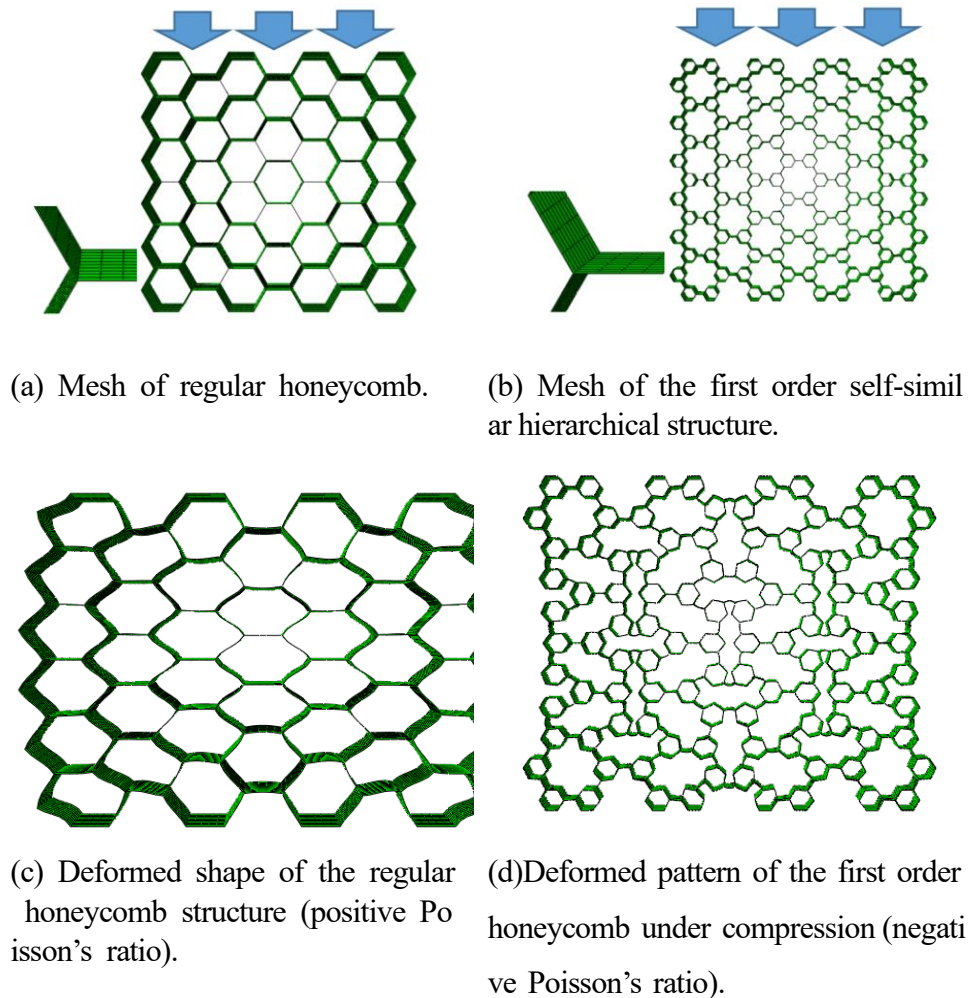
(b) Oblique side 3D view of second order self-similar hierarchical honeycomb

**Figure 4.5.2** Second order self-similar hierarchical honeycomb.

---

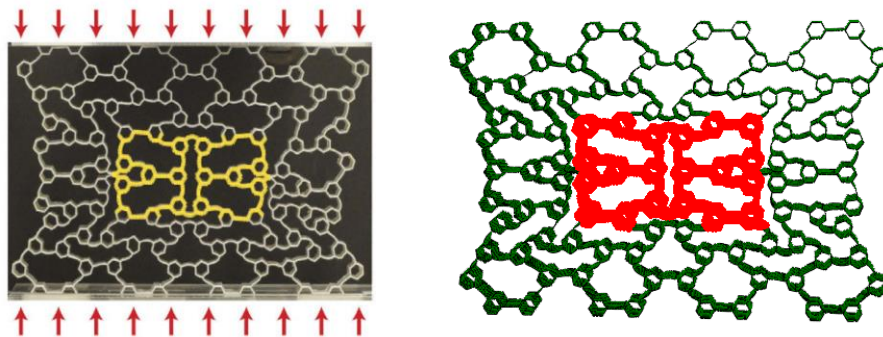
#### 4.5.2 Deformation of self-similar hierarchical honeycomb and FE model validation.

Figure 4.5.3a&b shows the FE models and meshes of a 1<sup>st</sup> order model in comparison with a normal honeycomb model for validating the modelling approaches. The effective Poisson's ratio was calculated based on the average lateral displacement over the edge. The dimensions were adapted from published works (Mousanezhad et al., 2015) for validation purposes. The material property is 5MPa Young's Modulus and Poisson's ratio for the solid material is 0.3. The meshed element is controlled to 10 elements per beam. As comparatively shown in Figure 4.5.3c&d, the regular honeycomb shows expansion upon the compression load (c), the self-similar model shows a clear inward deformation (d), indicating a negative Poisson's ratio behaviour.



**Figure 4.5.3** FE models of regular and self-similar hierarchical honeycomb structure under compression and deformation patterns.

Figure 4.5.4a&b compares the deformation of the first order hierarchical structure between published experimental image and deformed pattern of the FE model. The FE prediction showed a good agreement with the experimental data. The deformation of the regular honeycomb is uniform among the cells, but the deformation of the hierarchical honeycomb shows a quite different deformation pattern among the cells. The deformation of the cell in the middle section, as indicated by the box with the dashed lines, shows significant lateral deformation. The bending of the vertical beams is much more significant than the horizontal beams. This indicates a strong negative Poisson's ratio behaviour for the self-similar hierarchical structure. Compared to regular honeycomb and missing rib models, given the difference in the edge size of different ordered unit, a mesh control is critical. In each case, a detailed mesh sensitivity was performed by changing the mesh size then monitoring the force and Poisson's ratio using a parametric program. The approach used in the work is to control the element number for each unit to ensure consistency. In the model, each edge is a model with 5 elements.



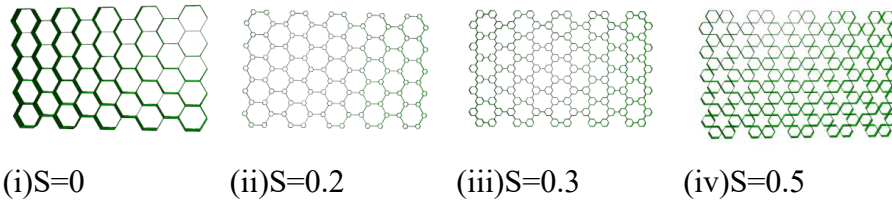
(a) Deformed shape of first order Hierarchical honeycomb at engineering strain of 0.266. (width, height, depth and beam thickness of the sample are 254, 229 and 20mm, 1mm respectively. (Mousanezhad et al., 2015). (b) FE simulated deformed shape of 1st order Hierarchical honeycomb (this work). The FE model has identical dimensional and properties as the published work (Mousanezhad et al., 2015).

**Figure 4.5.4** Comparison between FE model predicted deformation pattern and published data

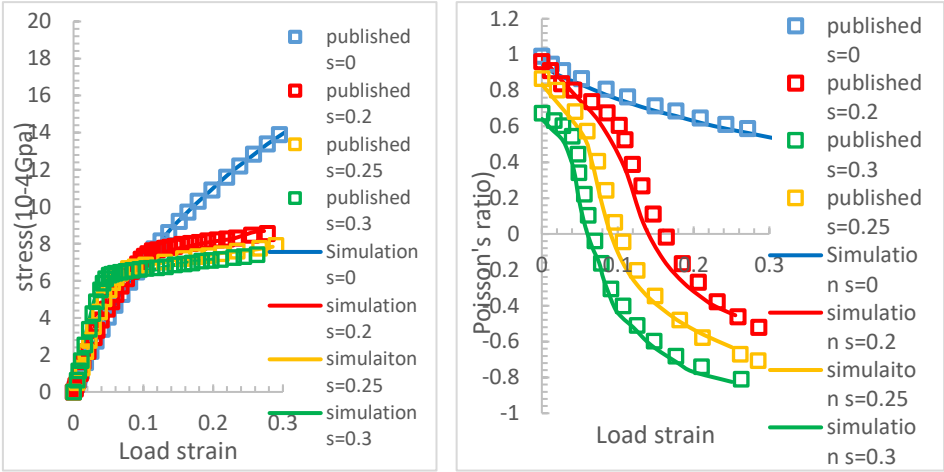
---

The parametric is used to generate structures with different length ratios. Figure 4.5.5a shows structures with different ratios between the edge length of the first order hexagon and beam length of the original hexagon structure. As the size of the first order hexagon increases, the overall shape of the structure changes significantly. Figure 4.5.5b compares the stress vs. strain data from the published experimental works and FE predicted data. It is shown that the FE prediction showed a good agreement with the experimental data. The data shows that the self-similar hierarchical structure reaches the plateau stage much early than the regular honeycomb because of the cell at the corners. Figure 4.5.5c plots the Poisson's ratio of the FE data and published experimental and numerical data. The Poisson's ratio was calculated based on the average values of the transverse displacement of the external edge points. As shown in the Figure, the trend of the FE data is in a reasonable agreement with that of the published data. The Poisson's ratio value for the regular honeycomb also agrees with other published data ([Papka and Kyriakiudes, 1994](#)). As shown in the figure 4.5.5, the Poisson's ratio for all the structures showed a decreasing trend with increasing strains from a positive value, the data for the normal honeycomb remains at positive range within the strain level studied, while the Poisson's ratio of self-similar hierarchical honeycombs entered negative Poisson's ratio domain at a strain level around 0.1. Samples with different material have been made in this work including PU resin, silicone rubber and 3D printing with Thermoplastic elastomer (TPE) materials. A typical example is shown in Figure 4.5.6a. The properties of the TPE materials are Young's modulus  $E=22\text{MPa}$ , Poisson's ratio of the plastic  $\nu=0.3$ . The deformed shape of the FE model is shown in Figure 4.5.6b. In both cases, the overall deformation mode is comparable to the experimental image. The materials show a clear inward deformation under compression.

The test was conducted on a MT2000 micro bending test (Deben Vertical 3/4 Point Bending Stage). The loading rate is 1mm/min. The force is recorded through a load cell as shown in the deformed image.



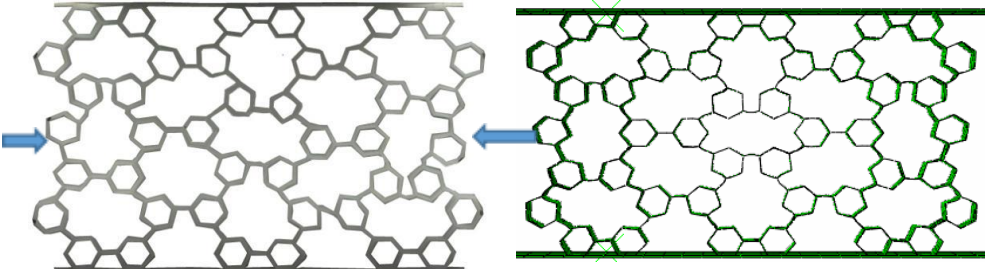
(a) Cells of different ratio between the newly added hexagonal edge length and length of the regular honeycomb.



(b) Comparison between the FE modelling results and the published stress-strain data. (c) Comparison between the FE modelling and experimental Poisson's ratio vs. axial strain data.

(Mousanezhad et al., 2015) for different structures.

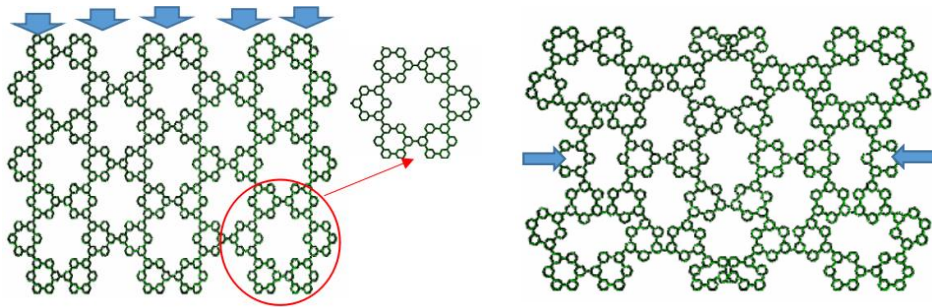
**Figure 4.5.5** Comparison between FE model predicted deformation pattern and Poisson's ratio of self-similar hierarchical structures with published data.



(a) Deformed shape of 3D printed wider sample. (b) Deformed shape at 0.15 Engineer strain (FE simulation).

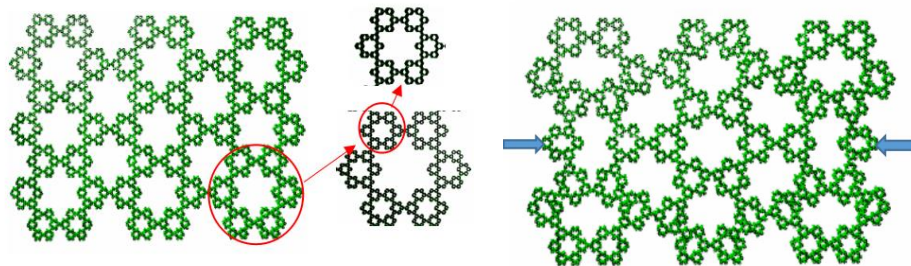
**Figure 4.5.6** Result with a 3D printed sample showing negative Poisson's ratio behaviour.

Figure 4.5.7 shows FE models of higher order (2<sup>nd</sup> and 3<sup>rd</sup>) self-similar hierarchical honeycomb and typical deformed shapes. Figure 4.5.7a shows the FE model of a 2<sup>nd</sup> order model and the deformed shape under compression is shown in Figure 4.5.7b. As shown in the Figure, the sample showed clear inward deformation indicating a negative Poisson's ratio. A similar trend can be observed from the third-order structure as shown in Figures 4.5.7c&d.



(a) Second order self-similar hierarchical honeycomb structure.

(b) FE deformed shape of (a) showing the shrinking of the sample indicating negative Poisson's ratio.



(c) Third order self-similar hierarchical honeycomb structure.

(d) FE Deformed shape of third order self-similar showing the shrinking of the sample indicating negative Poisson's ratio.

**Figure 4.5.7** FE result showing deformation of higher order self-similar Hierarchical honeycomb structures showing negative Poisson's ratio behaviour.

Figure 4.5.8 plots the Poisson's ratio vs. the axial strain for regular honeycomb and self-similar hierarchical structures (1<sup>st</sup>, 2<sup>nd</sup> and 3<sup>rd</sup> orders). A clear difference can be observed in the value and trend of the Poisson's ratios between different structures. The regular honeycomb has a positive Poisson's ratio while the self-similar hierarchical structures started with a positive value, then turned into a negative Poisson's ratio. The higher orders (2<sup>nd</sup> and 3<sup>rd</sup>)

start to undergo significant drops in Poisson's ratio at a relative smaller strain level (in this case, around 0,03), than the 1<sup>st</sup> order self-similar structure.

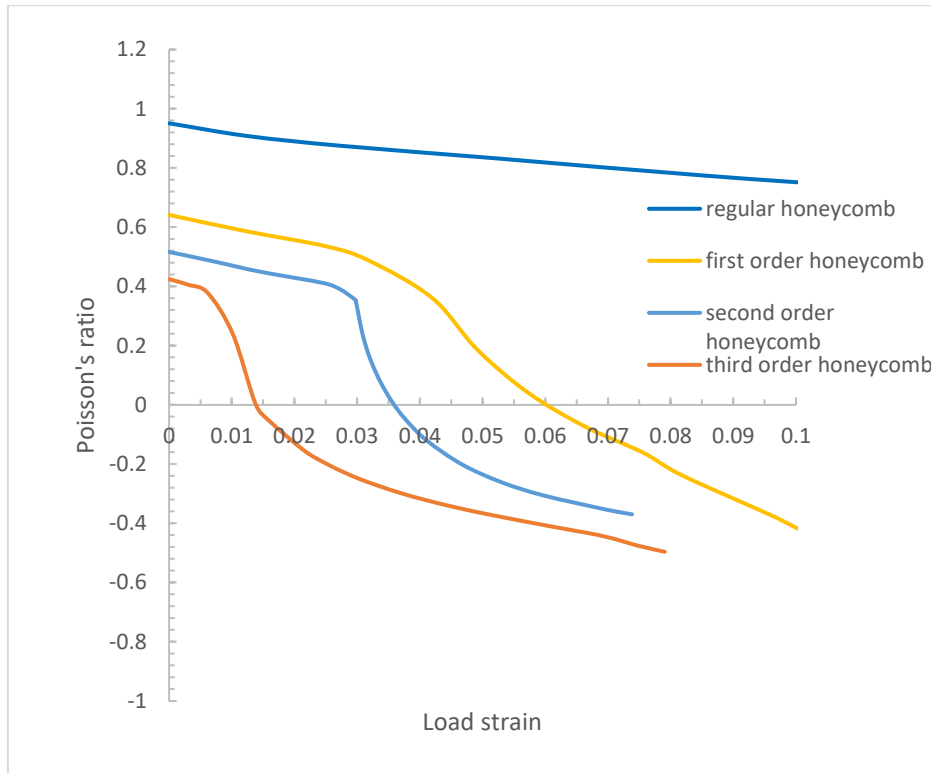
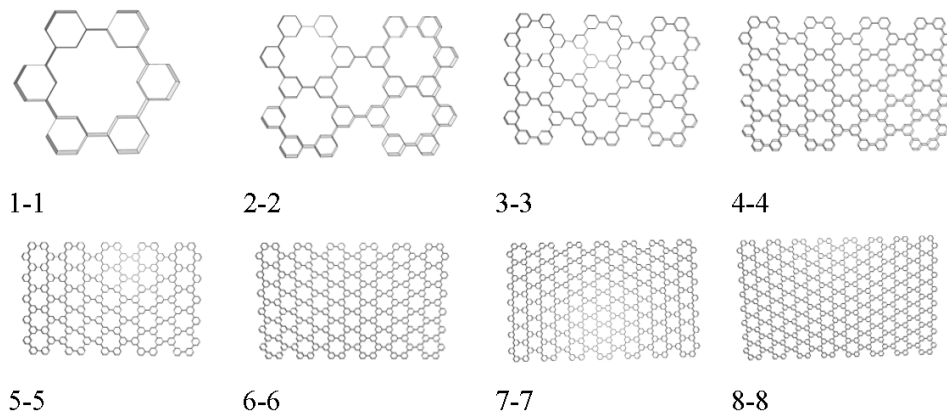


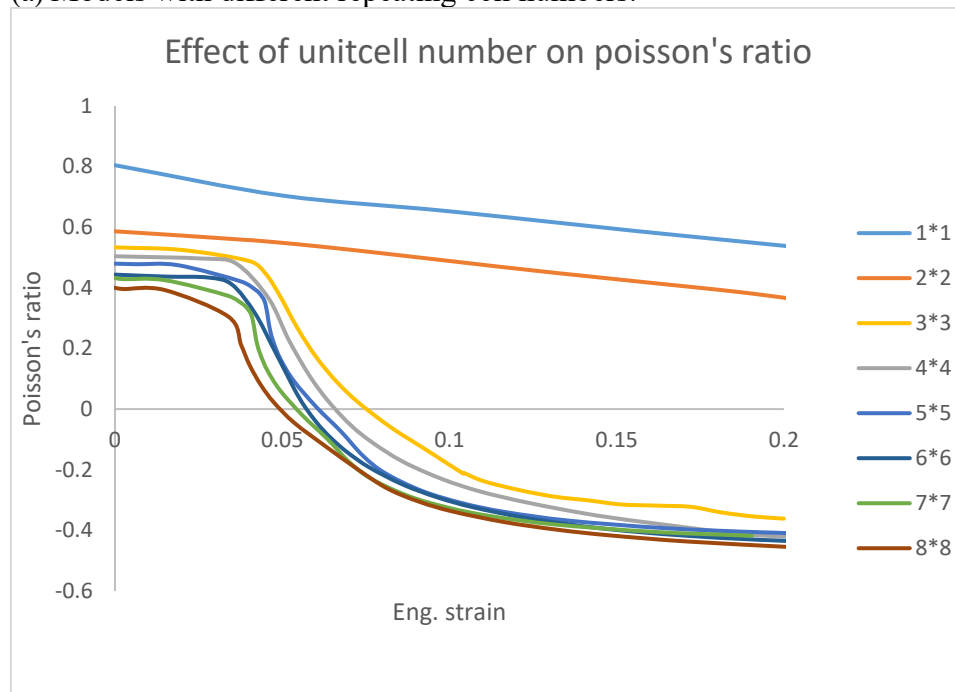
**Figure 4.5.8** FE Poisson's ratio vs. axial strain for different order hierarchical honeycomb (S=0.3 L=10)

The parametric program is also used to study the effect of cell numbers on the Poisson's ratio. Figure 4.5.9a shows models with different cell numbers for 1<sup>st</sup> order self-similar structures. The Poisson's ratio data is shown in Figure 4.5.9b. As shown in the Figure, there is a clear sample size effect when the repeating cell number is 1 or 2, further increase in the cell numbers showed relatively limited influence on the trend of the Poisson's ratio. Compare to the missing rib models, the effect of the cell numbers is much more significant for the self-similar model. This may be associated with the different mechanism of auxeticity. The origin of auxetic behaviour of the self-similar hierarchical structure is linked to the added hexagonal features within the hierarchical structure which make the instabilities occur at smaller compressive strains compared to the original non-hierarchical structure, this behaviour could lead to auxetic behaviour (Mousanezhad et al., 2015). Future work will use the program to establish systematic data considering both

structure and materials issues.



(a) Models with different repeating cell numbers.



(b) Poisson's ratio vs. Axial strain curves for self-similar hierarchical structures.

**Figure 4.5.9** Effect of repeating cell number on and Poisson's ratios of self-similar hierarchical honeycomb. ( $S=0.3$   $L=10$ )

---

## **4.6 Modelling and analysis of cell area changes of regular, missing ribs and self-similar hierarchical honeycomb structure under compression and tension.**

This section presents work on developing a program integrated with finite element modelling to calculate the areas of cells in different cellular structures under tension or compression loads. Different approaches of calculating the areas of the cells are compared including point-in-polygon (PIP), Heron's formula (HF) and the shoelace method (Ochilbek, 2018). A program based on the OpenCV (Open-source computer Vision Library) (<http://OpenCVopencv.org>) and Image processing software ImageJ (ImageJimagej.net) is also assessed to cross check the python program for area calculation. The area calculation program-based HF approach and the calculation is presented in the section. The key features and approaches implemented in the Python program including mathematical operations and key functional parts of the program are introduced. Some typical data of cell area changes in regular and auxetics honeycomb structures (missing rib structure and self-similar hierarchical structures) in comparison with the data for regular honeycomb is presented and analysed. The key features of area changes are correlated to the influence of the negative Poisson's ratio. The advantages and disadvantages, including the limitations of different approaches (*point-in-polygon* (PIP), HF, shoelace, open CV and Image J) are presented in the discussion section (4.7), together with cases showing the use of the area calculation program integrated with finite element modelling.

### **4.6.1 Area calculation program development and structures**

From the work presented in the last two sections, foams/cellular structures particularly auxetic structures undergoing complex in-plane shape changes and the deformation for the cells are different depending on the cell shape and location/position of the cells in the samples, detailed data of area changes

---

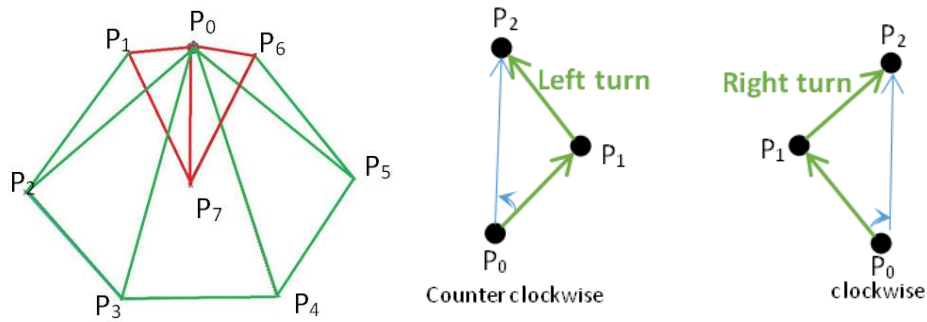
could offer important information for understanding the deformation mechanism of the cells at strain levels and identify weaker/sensitive cells within the structures of either a regular pattern or a random pattern. The data of area changes will add to the conventional data which can be obtained from finite element modelling (such as force, displacement, stress, strains). Calculation of the area is also important for parameters such as overall sample volume/area changes, reflecting the compressibility of the structure.

In this section a Python program has been developed to capture the area changes when a cellular structure is under in-plane tension/compression loads. The data is used to analyse the trend of area change of some typical cellular structures (regular honeycomb, missing rib and self-similar hierarchical honeycomb). It is firstly used to compare the area changes based on FE analysis of single cell models of regular honeycomb and missing rib models under tension and compression, then it is used to track the cell shape/area changes when a larger sample with multiple cells is being deformed.

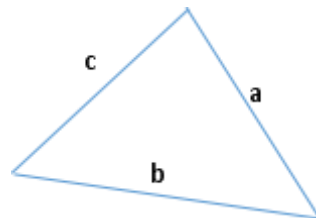
#### **4.6.2 Area calculation approach**

A range of area calculation approaches have been assessed including Heron's formula method, the Shoelace Method (SM), Open CV and Image J programs. Some simple approaches such as Paint shop are also analysed in the initial program concept evaluation stage. These approaches are used in various applications ([Huang and Shih, 1997](#); [Braden, 1986](#)). The Shoelace Method (SM) is a method calculating the polygon area based on point coordinates in the Cartesian coordinate system. But there are some limitations when it is being used with deformed shapes in Abaqus. Preliminary work shows that there are circumstances where the algorithm will produce wrong or unexpected results, when dealing with data of situations such as self-intersecting, overlapping or twisting of the lines. Further details will be presented in the discussion section (4.7) of the chapter. This section focuses on presenting briefly the PIP method for the calculation area or polygon of random shapes and Heron's formula for the area of triangles. The PIP-HF approach is integrated with some internal operation functions in Abaqus to calculate the cell area changes of cellular structures under in-plane tension and compression.

Point-in-polygon (PIP) is one of the fundamental operations of Geographic Information Systems. Yet nowadays this concept is also getting big attention in graphical programming, mobile game programming, and other fields. The PIP concept can be applied to any size of polygon (Huang and Shih, 1997). The basic concept of the approach is illustrated in Figure 4.6.1 and Figure 4.6.2.



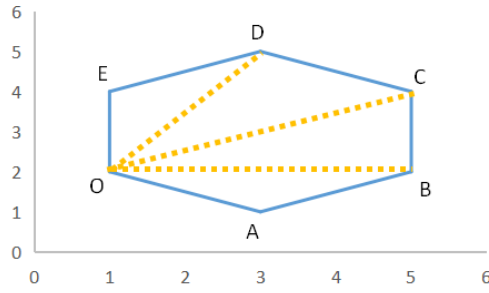
- (a) The Positive area (Green triangle) and Negative area (red triangle) in polygon area calculation
- (b) The convention for positive or negative signs for the area to calculate the overall area. The Counter clockwise is positive and clockwise direction is negative.



$$A_H = \sqrt{p(p-a)(p-b)(p-c)}$$

- (c) Calculation of the area of a triangle

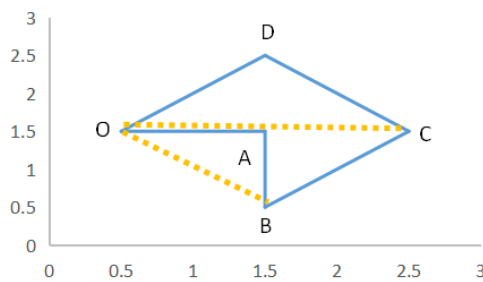
**Figure 4.6.1** point-in-polygon (PIP) algorithm to calculate the area of an enclosed P1-P7. p is random point.



Convex polygon: All the areas are positive.

$$A_{ODCBA} = A_{OED} + A_{ODC} + A_{OCB} + A_{OBA} + A_{OAO}$$

(a) Calculation of a Convex polygon with starting point on the curve.



Positive area: ODC, OCB:

Negative area: OAB

$$A_{ODCBA} = A_{ODC} + A_{OCB} - A_{OAB}$$

(b) Calculation of a Concave polygon with starting point on the curve.

**Figure 4.6.2** Diagram showing the point-in-polygon (PIP) approach to calculate the area of an enclosed polygon (Convex and Concave).

The overall area of polygon is calculated through a *point-in-polygon* (PIP) problem (Huang and Shih, 1997). In this process, many triangles are formed between a main/pivoting point and two points on the perimeter of the polygon. This pivoting point can be a separate point as in the case shown in Figure 4.6.1 or on the perimeter line as shown in cases in Figure 4.6.2. The area of polygon can be calculated as (Huang and Shih, 1997):

$$S_{Polygon} = ABS(\sum_1^n sign * S_n) \tag{4.6.1}$$

Where n is the number of points in polygon, S is area of every single triangle, Sign is Positive and negative area of triangle.

Figure 4.6.2(b) illustrates the determine the positive or negative signs of triangles. When calculating the total area of the polygon, the positive one will be added to the sum and the negative one will be deducted from the sum. Mathematically, the sign can be determined by the vector based on the

---

coordinates of the three points (Equation 4.6.2),

$$\text{vector} = (x_{p1} - x_{p0}) * (x_{p2} - x_{p1}) - (y_{p1} - y_{p0}) - (y_{p2} - y_{p1}) \quad (4.6.2)$$

The  $X_{p1}$  is the x coordinate of point 1 and  $Y_{p1}$  is y coordinate of point 1 and so on. When the vector value is negative, the Sign is -1, Conversely Sign is +1.

The area of the triangles can be calculated based on the Heron's formula (Figure 4.6.1(c)), using the lengths of the three sides of the triangle, Heron's formula can be written as:

$$A_H = \sqrt{p(p - a)(p - b)(p - c)} \quad (4.6.3)$$

Where a, b, c is the length of side a, b and c of a triangles. p is the half perimeter of the triangle:

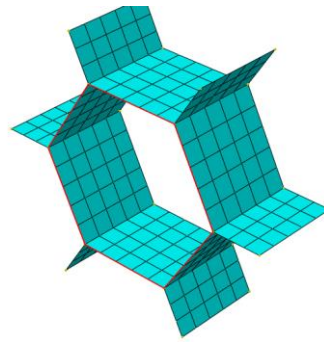
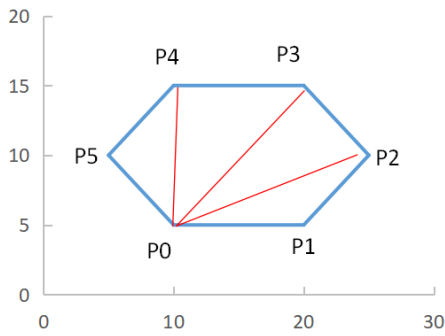
$$p = \frac{1}{2}(a + b + c) \quad (4.6.4)$$

Figure 4.6.2 shows the case when the main point for drawing the triangles is on the Polygon. This is a more convenient approach for calculating the areas of cellular structures based on the FE modelling, as the edges are all partitioned into nodes. Figure 4.6.2(a) is a convex shape, which is partitioned into four areas, then the total area is the sum of the four triangles. The polygon in Figure 4.6.1(b) can be calculated by adding  $A_{ODC}$  and  $A_{OCB}$  then remove the area for  $A_{OAB}$ .

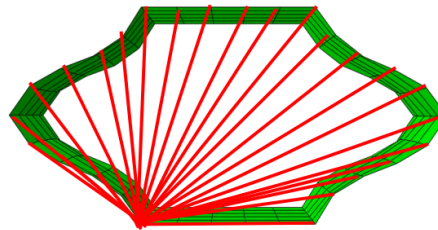
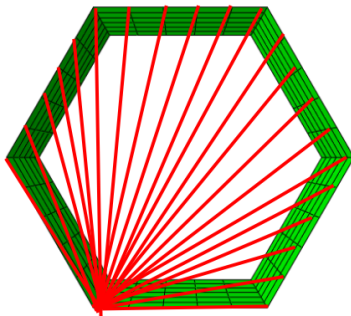
This calculation is coded in python and combined with some internal operation in pre- and post-processing of Abaqus. The details and key coding are presented in the next section.

### 4.6.3 Area calculation in finite element modelling and python program

In finite element modelling (FEM), the model is meshed into several elements with 3 nodes (Tri) or 4 nodes (Quad) per element. To tracking the node coordinate easily, an area for meshed node set is created which is illustrated in Figure 4.6.3. The node set record the node ID which can be read the undeformed and deformed coordinate from Abaqus result file(.ODB).



(a) Schematic to show the area partition of a hexagonal polygon. (b) A typical meshed hexagon for a regular honeycomb model.



(c) Area partition of undeformed hexagonal cell showing how the nodes on a meshed model are used to calculate the area. (c) Area partition of deformed hexagonal cell under compressions showing how the nodes on a meshed model are used to calculate the area.

**Figure 4.6.3** The area partition of undeformed and deformed hexagonal cells of regular honeycomb model based on the nodes on the edge.

The beam length of triangle can be calculated from the node coordinate:

$$l_{12} = \text{sqrt}((x_1 - x_2)^2 + (y_1 - y_2)^2) \quad (4.6.5)$$

Where  $x_1$  is the x coordinate of point1 and  $y_1$  is the y coordinate of point1.

The area partition of undeformed and deformed model shows on Figure 4.6.3.

**Table 4.6.1** Key stages/section/operation of the program for calculating the area of cellular structures under in-plane tension of compression.

Step	Step description
i	Identify all the closed geometry from Abaqus part partition, Calculate the partitioned area for each partitioned face.
ii	Obtain the nodes coordinates from the partitioned part to original model. Create a node set of each close geometry
iii	Run the model, then use the Python program to read the coordinate data from the deformed model at every simulation increment.
iv	Sorting the data in order to calculate the area for each closed geometry, through a loop operation.
v	Start a loop to go through calculating the area from each face, then store the data. Calculate the area for all the triangles (based on the number of nodes on the line) from each area node set and store the data into a Python parameter, make judgement about if it is negative or positive, then add the area together, then export to external .csv file. This process is repeated until all the faces has been calculated.
vi	Start loop to go through every increment time. Output the area data and identification (face id) information (such increment time, etc) to a data file (.csv) for analysis. The data is also available for viewing in Abaqus view

The area calculation is coded in python and combined with some internal operation in pre- and post-processing of Abaqus. The overall process is listed in Table 4.6.1. The key operation and coding are explained briefly below. As listed in Table 4.6.1, the work started by defining the geometry-based data sets in the part section (in Abaqus), then the nodes set is developed/defined based on the geometry set of lines, then the area for each set is calculated, their positive/or negative sign is given for each area, then the overall area is calculated by summing all the areas together. Some key operations and the coding approach are presented below.

The Step i of area calculation is to identify all the closed geometry from Abaqus part partition, then define the geometry-based set for each area and

---

calculate the original area for each face. To define all the close geometry, a new 2D part with same size as the original model is built. The size of 2D part is found by Abaqus command 'getboundarybox'. The new 2D part is partition by calculated model. Then the closed geometry form 2D part is automatic defined by Abaqus. A node set which found closed geometry is created by Abaqus command 'face.getEdges()'. Then a Abaqus command 'face.getSize()' is used to calculate area of undeformed geometry. The Step ii of area calculation is obtaining the nodes coordinates from the partitioned part to original model. Create a node set of each close geometry. A new parameter is created to record all the 2D node coordinates (x,y) from every edge of close geometry. And the out-of-plane direction coordinate will be added into this parameter. The Abaqus command 'edge.findAt(edge.pointon)' is used to find closed geometry node from original model.

One key operation is the node sorting Table 4.6.1(iii). As shown in Figure 4.6.1&2, the total area is calculated by adding all the areas of individual triangles with a positive or negative sign which can be determined through equation3 and executed in the code segment presented above. We used the starting point following the numbering from Abaqus. Node sorting: Area calculation of Heron's formula requires coordinate points to be arranged sequentially. However, the point export form Abaqus may not be arranged sequentially. The function of NodeSort is used to sort the nodes to be arranged sequentially based on their position (coordinates). The starting point is the one with the lowest coordinates number (x, y) for the polygon. The code is presented below Nodelabels to sortLabel.

---

```

#sort node
model = mdb.models[modelName]
part = model.parts.values()[0]
nodeSet = part.sets[nodeSetName].nodes
nodeLabels = {}
for i in nodeSet:
    nodeLabels[i.label] = i
firstNodeLabel= nodeLabels.keys()[0]
firstNode = nodeLabels[firstNodeLabel]
sortLabel = [firstNodeLabel]
findNext = 1
while findNext:
    findNext = 0
    vEdges = firstNode.getElemEdges()
    for ve in vEdges:
        vv = ve.getNodes()
        if vv[0].label == firstNodeLabel:
            nextV = vv[1]
        elif vv[1].label == firstNodeLabel:
            nextV = vv[0]
        if nextV.label not in sortLabel and nextV.label in nodeLabels.keys():
            firstNodeLabel = nextV.label
            firstNode = nextV
            sortLabel.append(firstNodeLabel)
            findNext = 1
            break
    if len(nodeLabels.keys()) != len(sortLabel):
        print nodeLabels.keys()
        print sortLabel
        getWarningReply(message='node set is not close',buttons=(CANCEL,))
        return None
    print "node sort successful"

```

In step (iii), once the data are sorted and coordinates obtained and stored, the area for each triangle formed between two adjunct nodes and the pivoting point (like P in the *point-in-polygon* (PIP)) through a Python code designated as “getAreaOfPolyGon”. To obtain the line segment vector for:  $\text{vecp1p2} = [p2[0] - p1[0], p2[1] - p1[1]]$ , determine the area calculation is positive or negative:  $\text{vecMult} = \text{vecp1p2}[0] * \text{vecp2p3}[1] - \text{vecp1p2}[1] * \text{vecp2p3}[0]$ , if  $\text{vecMult}$  is greater than 0, the area is positive, if it is less than 0, it is negative. As shown in the code, this operation Uses the loop nesting of  $i$  at the number of points -1. Each triangle counts as  $\text{triArea} = \text{getAreaOfTriangle}(p1, p2, p3) * \text{sign}$ , and the polygon area is  $\text{area} += \text{triArea}$ .

---

```

def getAreaOfPolyGon(points):
    area = 0
    if(len(points)<3):
        raise Exception("error")
    p1 = points[0]
    for i in range(1,len(points)-1):
        p2 = points[i]
        p3 = points[i+1]
        #Vector calculation
        vecp1p2 = [p2[0]-p1[0],p2[1]-p1[1]]
        vecp2p3 = [p3[0]-p2[0],p3[1]-p2[1]]
        #Negative Area and Positive Area judgment
        vecMult = vecp1p2[0]*vecp2p3[1] - vecp1p2[1]*vecp2p3[0]
        if(vecMult>0):
            sign = 1
        elif(vecMult<0):
            sign = -1
        triArea = getAreaOfTriangle(p1,p2,p3)*sign
        area += triArea
    return abs(area)

```

Most of the operation was done within the internal system and all the data can be output into external sources. The accuracy of the program was checked by comparing with regular shapes (Sphere, square, etc.) and irregular shapes with known areas (based on other imaging programs and the built-in functions (area/mass, etc.). The accuracy is also cross compared between shoelace and heron model. The accuracy and calculation efficiency are affected by the number of points on the lines, and in FE modelling, this corresponds to the mesh density. With the mesh used (detailed in Sections 4.3, 4.4 and 4.5) sensitivity tests, each beam/edge is meshed with small segments, which give sufficient accuracy to calculate the area for both undeformed and deformed beams. The preliminary result was not presented to preserve clarity. Some of the issues will be discussed in section 4.7.

#### 4.6.4 Typical area changes of different cellular structures under tension or compression

Figure 4.6.4 shows the typical structures studied in the area change of different lattice structures. Figure 4.6.4a is a normal honeycomb; the beam length is 5mm and the beam thickness is 1mm; the depth of the sample is 10mm. Figure 4.6.4b is multiple cell models of the regular honeycomb. Figure 4.6.4c&d is single cell or multiple cells models of missing rib structure, respectively. The loading conditions are like that presented in sections 4.3-5. The bottom side is fixed, and top side is loaded in compression or tension.

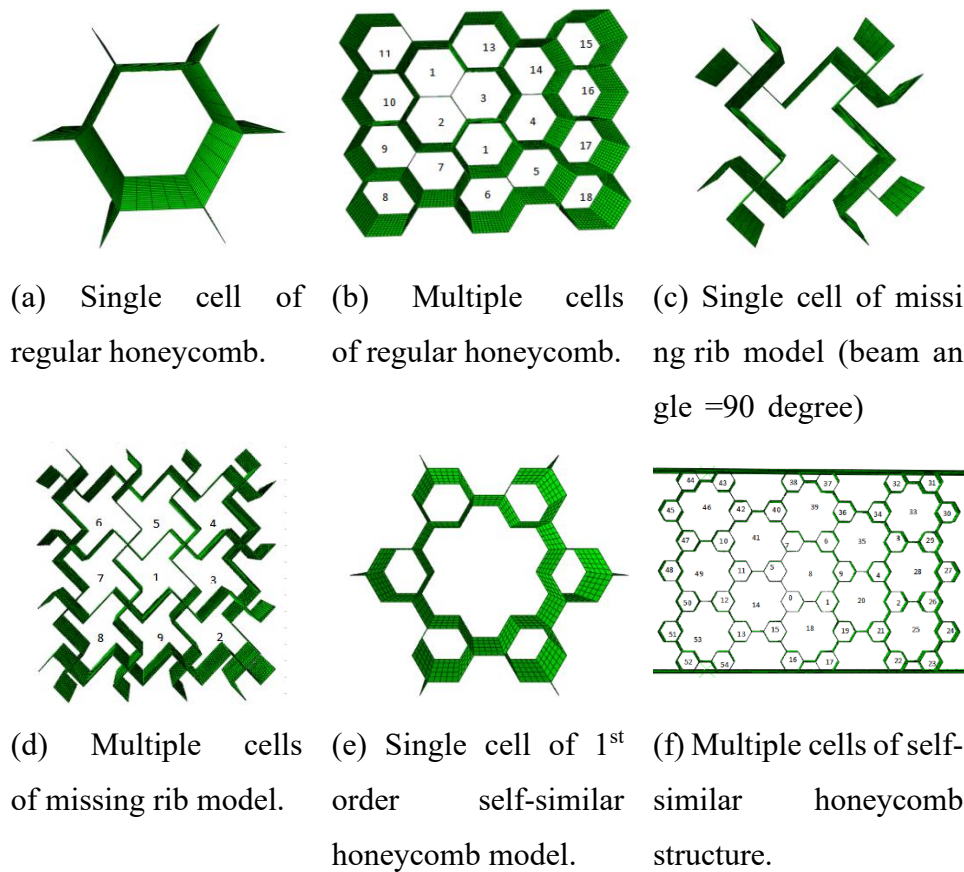
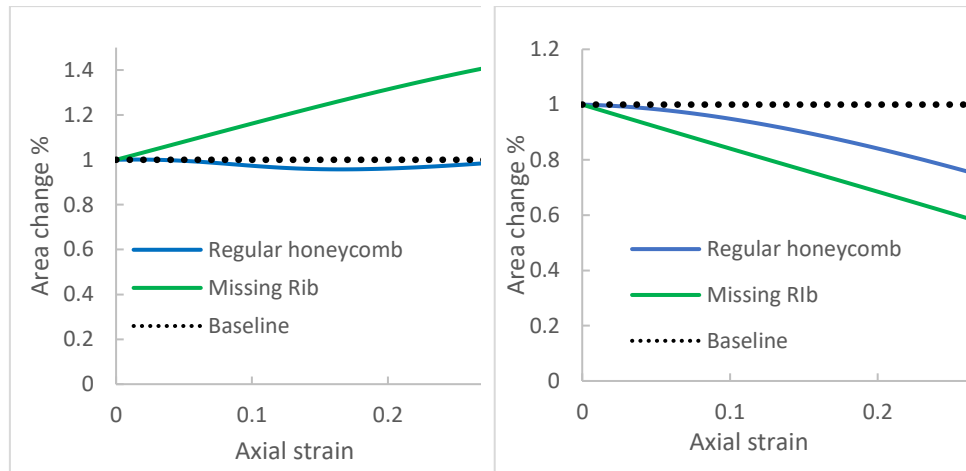


**Figure 4.6.4** Typical structure used in the deformation and area changes analysis under load.

Figure 4.6.5a&b shows the area changes of the single cell models of different structures under tension and compression. All the areas are normalized against the original area, which shows that the program is able to capture the area change. The data shows that there is a clear difference in area changes

between the tension and compressions loads for different structures. The area for the regular honeycomb decreased slightly due to its positive Poisson's ratio, then started to increase slightly. The missing rib model shows clear area increase due to the expansion of structure; this agrees with the negative Poisson's ratio. Under compression the area is reducing, and the Missing rib structure shows a more significant drop than the regular honeycomb structure.

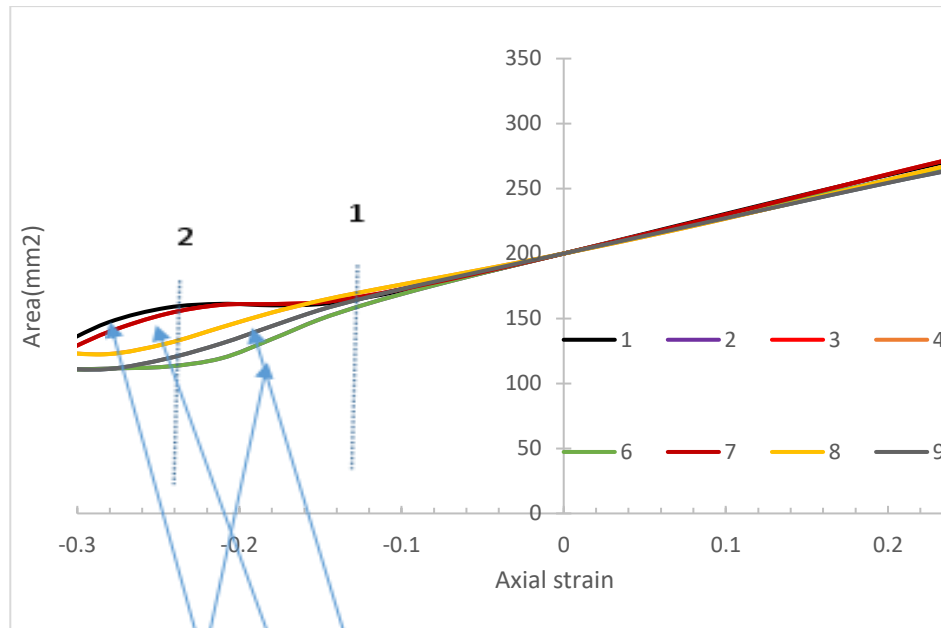


(a) Area change of single cells in tension. (b) Area change of single cells in compression.

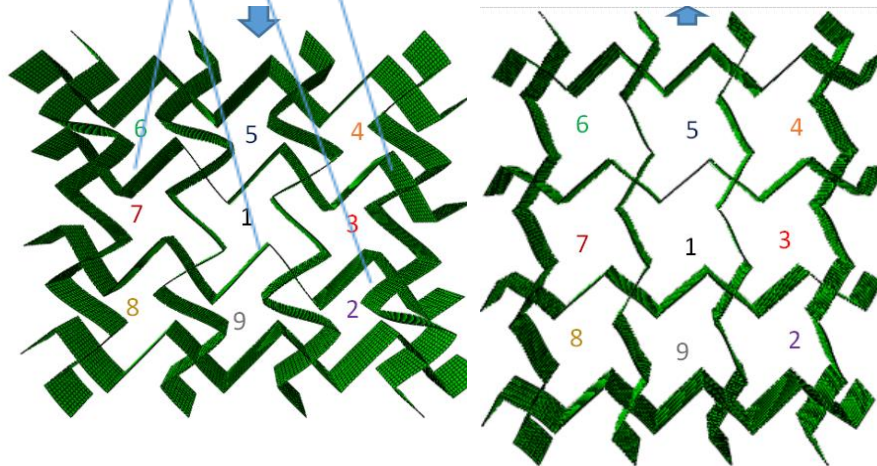
**Figure 4.6.5** Area changes of single cell models of the different structures (regular honeycomb and missing rib model) in tension and under compression. The area values are normalised against the original area of the cell (1).

Figure 4.6.6a shows the area change of the multi-cell missing rib models. There is a clear difference between the trend of cell area changes in tension and compression. Under tension load, every single cell shows a similar area change. The area increases with tension; this agrees with the negative Poisson's ratio. As it being stretched, it is expanding laterally. The trend of area changes in compression is quite different from that in tension. The area in general is decreasing and the trend is different between the cells. For example, cells 1, 3, 7 show far fewer area changes than other cells. The curve can be described by three stages which are separated by two dotted lines. Every single cell shows a similar area change before dotted line 1, and after dotted line 1, the area changing of cell 2 and 6 drop faster. These two cells are

at the same position where the initial corner edge-cell wall contact is formed as shown in section 4.4. There is more intensive deformation in the diagonal line as illustrated by a red dotted line. The area changing of cell 2 and 6 drop smoothly after dotted line 2(Figure 4.6.6a) due to the contact changing the deformation behaviour. The result of the area changing shows a reasonable trend with deformation stages reported in Section 4.3 and 4.4.

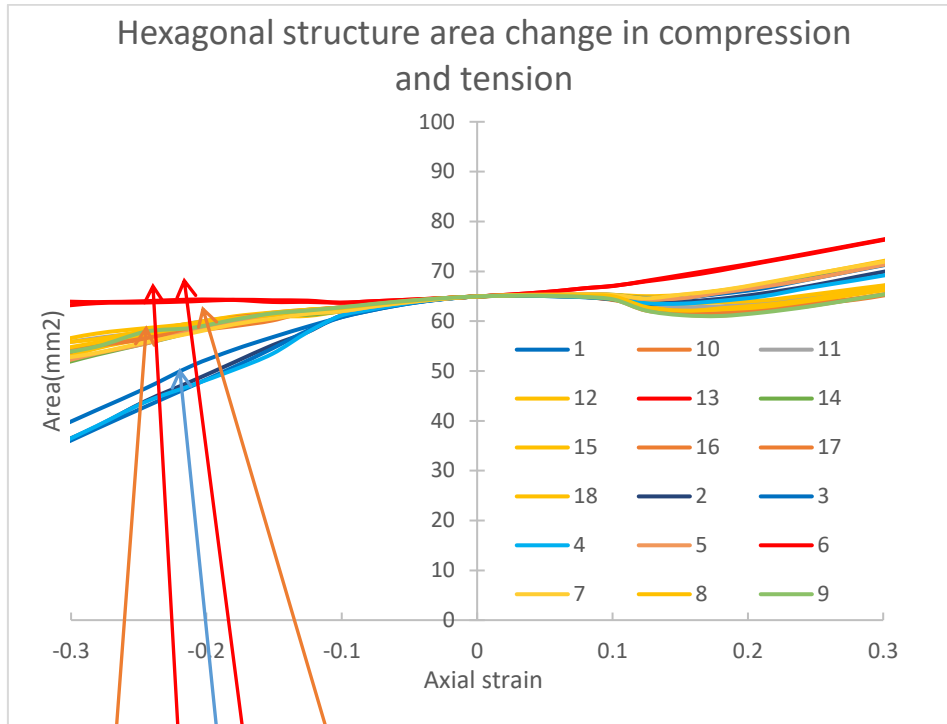


(a) Area change of different cells in missing rib models.

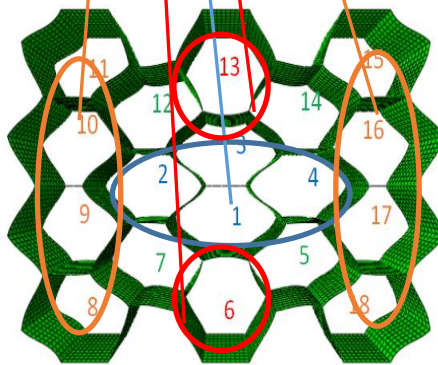


(b) Deformed shapes of the cells under compression at 0.2 engineering strain. (MR 44-90-T1). (c) Deformed shapes of the cells in tension at 0.2 engineering strain (MR 44-90 T1).

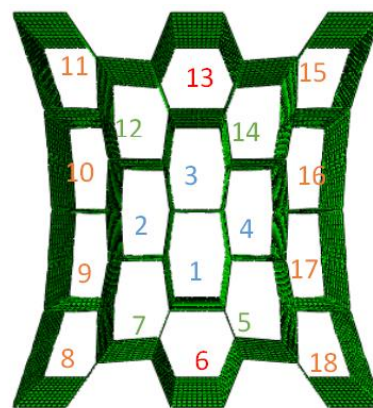
**Figure 4.6.6** Area changes of the cells in missing rib model under compression/tension. (MRS 44-90 t1).



(a) Area change vs. axial strain of regular honeycomb cells in tension and compression.



(b) Deformed shapes of the cells in a regular honeycomb model under compression at 0.2 engineering strain.



(c) Deformed shapes of cells in a regular honeycomb model in tension. at 0.2 engineering strain.

**Figure 4.6.7** Area changes of the cells in regular honeycomb model under compression and tension.

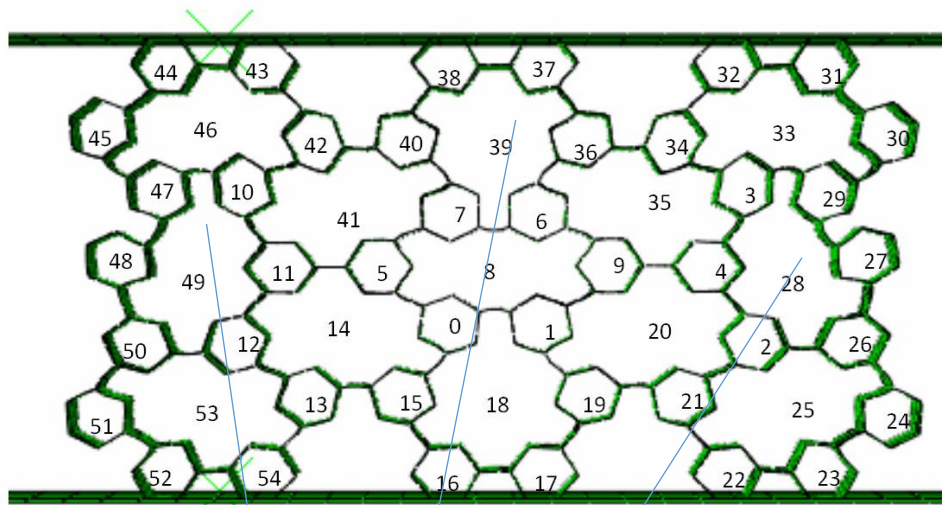
Figure 4.6.7 shows the cell area changes of a multi-cell regular honeycomb model. The deformation of the cells exhibits a different trend as indicated by

---

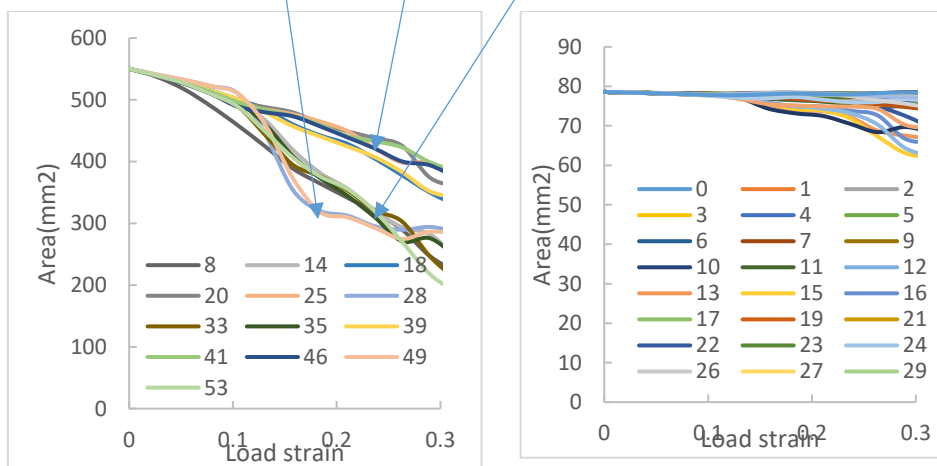
the arrows. As shown by the tension data, the deformation of the regular honeycomb is different from the missing rib model. There is significant difference between the cells for the regular honeycomb model. Some cells show increase in the area (e.g., cell 13, 16), while the areas of other cells are reducing slightly due to shrinking of the cells (Positive Poisson's ratio). Similar difference can be observed among the cells in compression. As indicated by the arrows, some cells show limited area changes (e.g., cells 13, 6), the cell to the side shows significant area increase (e.g., cells 8-11, 15-18). The most significant area changes could be observed with the cells in the middle section (e.g., cells 1-4). There are detailed reasons for the different area changes, but these data illustrate that the program is able to record the area changes.

Figure 4.6.8 shows the deformation of a 1<sup>st</sup> order Self-similar hierarchical honeycomb model Figure 4.6.8a and the area change in compression. Figure 4.6.8a shows the area changes of the base cells (i.e., cells in the original hexagon, while the area changes are plotted in 1<sup>st</sup> order cells are plotted in Figure 4.6.8b. The data shows that the areas of the cells all decrease at high strain levels, but the cells of the original hexagon start to change earlier than the 1<sup>st</sup> order cells. The cells of the original hexagon show a different trend in area changes. For example, cells 28 and 49 shows the most area reduction. These two cells are in the region where the sample showed clear shrinking, thus negative Poisson's behaviour. Cells showing smaller area reductions are the cells at the centre of the sample (e.g., cells 18 and 39), these are affected by the auxetic behaviours.

From representative data shown in the three structures, the area data reflects the deformation of the cells and it reflects the auxetic behaviour well, correlating well with the FE modelling reported in section 4.3 (missing rib model in tension), 4.4 (Missing rib in compression) and 4.5 (self-similar hierarchical models in compression). The turning point of the area also linked to the contact behaviours. The program could be used in future to provide more quantitative means to map the deformation of cellular structures.



(a) Deformed model showing the deformation of the base cells (cells in the original Hexagonal (e.g. 25, 28, 33, etc), and the 1<sup>st</sup> order cells (cells replacing the Vertices, e.g. 22, 23, etc).



(b) Area changes vs. Strain of the base cells in a 1<sup>st</sup> order self-similar hierarchical hexagonal structure

(c) Area changes vs. Strain of the base cells in a 1<sup>st</sup> order self-similar hierarchical hexagonal structure.

Figure 4.6.8 Cell area change of self-similar hierarchical honeycomb under compression.

---

## 4.7 Discussion

### 4.7.1 Effect of modelling approach and sample size/stiffness ratio/Poisson's ratio on auxeticity of missing rib structure

The work presented in section 4.2 -4.6 has covered key aspects of modelling and testing of cellular structures under in-plane loading with a particular focus on Poisson's ratio and auxeticity. The development of the Python programs has made it easier to study the effect of key process and parameters related to auxetic structures and applications (Gapser, 2005; Aw, 2017; Li, 2018; Khaled, etc.). The program is also being used in other current projects related to materials used in medical and orthotics (Zevallos Herencia, 2020; current PhD project). The selected cases and typical results show that the parametric FE program is effective in studying the deformation of structures, the Poisson's ratio, the stability of the auxeticity and related properties. Sections 4.3 and 4.4 have been focused on the missing ribs model, which is the subject of many recent works (Farrugia et al., 2018) both in tension and compression loads. Based on the three cases presented, the parametric program developed allows systematic studies on the effect of beam angles, sample size, beam length ratios and the effect of the size ratio of structure at different levels on the deformation behaviours of missing ribs and self-similar hierarchical honeycomb structures, which are important for their design and applications. The results have shown a good agreement with experimental and analytical data including cross comparison with other published data. The works show that Python based parametric modelling is an effective way for modelling, data analysis of these auxetic structures and future development. The new development of integrating the area calculation in FE modelling for quantifying the change of areas has laid a good effective framework for further data development. The data shows that the changes of areas under tension and compression load is different for the missing rib models (Figure 4.3.3 and Figure 4.4.4). The program is also able to identify difference of the area changes for cells at different positions, reflecting different deformation modes. The strain levels reflecting significant area changes of the missing rib

---

model correlate with the deformation stages established for missing rib model under compression. For example, the initial contact of missing rib structures also can be reflected by the area changes which show on Figure 4.6.4 (the dotted line 1). The detailed understanding on the deformation process of samples of different sizes (as shown in Figure 4.3.5, 4.4.11 and 4.5.9) could be important for structure design and application. The key results in section 4.4 clearly show that the contact between the corner edges and cell walls at high strains for normal MR and MS directly influence the mechanical behaviours, the Poisson's ratio, and stability of the auxeticity. The main data presented in this chapter is to demonstrate the use of the modelling approaches and Python-based data processing in research auxetic structures under in-plane loading. The three main cases (i.e., regular Honeycomb, missing ribs, and self-similar hierarchical models) are representative to general structures. So, the program can be transferred to other systems (such as re-entrant, etc.) and more complex loading conditions to build up systematic data for auxetic structures. Several recent works have been focused on extending the missing rib models to more complex shapes including replacing the vertices with complex shapes such as square, star (Farrugia et al., 2018; Jiang et al., 2019; Zhu et al., 2020). The work from the missing rib model and self-similar hierarchical honeycomb will naturally support the development.

The FE modelling of compression loading has covered regular missing rib models, missing rib structures with different angles and mixed structures. In all cases, the FE modelling data showed a good agreement with the testing data of 3D printed samples as well as other published data with known dimensions and material properties (Figure 4.3.4, Figure 4.4.4 and 4.5.5). The effect of angles showed a clear effect on the deformation modes and the Poisson's ratio in both tension and compression. The work for the first time established the key stages of deformation of missing rib models under compression. The key deformation stages include linear elastic deformation, corner edge–cell wall contact stage, full edge corner-wall contact stages and further deformation. This deformation process is much more complicated than the deformation process of a regular honeycomb, which consists of cell

---

bending, buckling and densification process (Figure 4.4.4) (Pakpka and Kyriakides, 1994). The data also shows clearly that the stability of the Poisson's ratio and the critical strain for stable auxeticity is directly linked to the initial contact. Once the contact is formed, the structure of the material changes and the system loses its auxeticity. The effects of the contact situation were also found to be influenced by sample size, beam angles as well as the deformation of mixed structures. One of the main advantages with automatic structure generation (Section 4.2) and FE modelling (Section 4.3-4.4) is to analyse the effect of cell size and numbers under different loading conditions. Sample size effect (different in effective stress-strain) is an important issue. For porous materials, the effective stress is determined by the overall force divided by the overall load bearing area. This value reflects the load resistance of the materials used in a design or material selection process. The difference in the stress-strain data and Poisson's ratio observed in a modelling may come from different causes, for example the boundary may affect the deformation. In the FE modelling and test, the boundary is fixed, and this may affect the deformation in the region close to the fixed end. For a smaller sample, this will have more significant effects than larger samples. In addition, as the sample size changes, the deformation pattern between connected cells may also change. This could be an important issue and it varies between different structures and loading modes. The boundary effect of structure deformation may vary between structures. The parametric program is able to effectively study the effect of cell/lattice numbers. As shown in Figure 4.3.5 and Figure 4.4.12, the sample size effect of missing rib model is different between tension and compression load. The cell number has less effect for tension and the results follow the analytical solution well. The area analysis also shows that the cells change their shape and area in a more uniform way, but for compression, the area change between the cells is different. The sample size effect is particularly important as missing rib honeycomb used in compression normally has far fewer layers, so a parametric FE modelling is important for simulating the overall deformation rather than just using a simple stress-strain data. The FE modelling is able to establish data for the stability of the auxeticity, the data (Figure 4.3.8) shows that the critical strain with stable

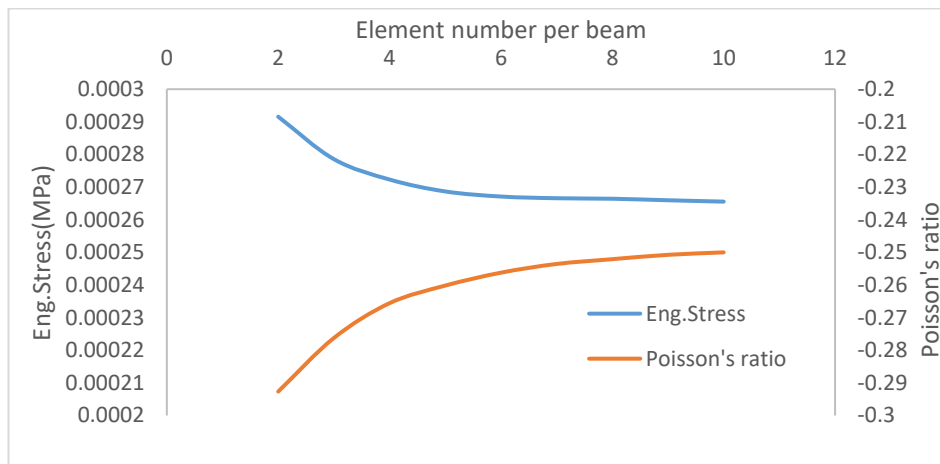
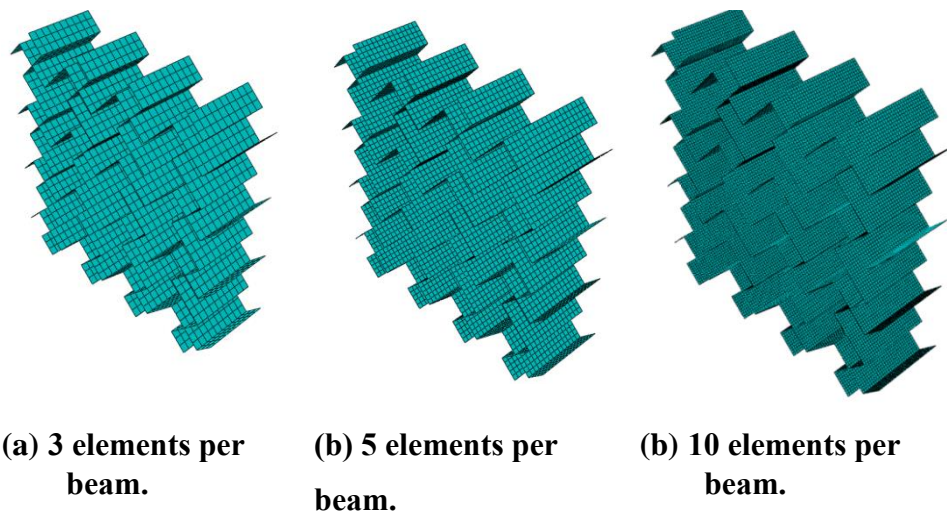
---

authenticity is affected by the beam angles and mixed structures. The stability data could provide design with more detailed information when using auxetic materials. The program could also provide an effective tool for developing structures with tunable auxeticity, through mixing either regular structures with different Poisson's ratios or random structures, which is an important research direction for material development ([Zhu et al., 2020](#)).

---

#### 4.7.2 Effect of different modelling approaches and mesh sensitivity

The FE model used shell elements which are widely used in modelling cellular materials (Schaedler and Carter, 2016). The model was validated through various approaches including analytical solution where applicable, selected experimental tests and published modelling or test data. The work of missing ribs in tension showed a good agreement with the analytical solution data. The FE compression model was validated against experimental data on 3D printed samples in the work and published experimental data on an elastic-plastic material (Figure 4.4.5). Some preliminary modelling work has also been conducted based on published data on regular honeycombs (Pakpka and Kyriakides, 1994), as the structure is well understood and well researched, so it can provide data for assessing the accuracy and effectiveness of the modelling approach in studying the deformation modes and Poisson's ratio. The work on self-similar hierarchical honeycombs showed a good agreement with published data (Figure 4.5.5). In preliminary work and previous work, the simulation is performed mainly with the ABAQUS explicit analysis. In the preliminary work, other modelling approaches have also been evaluated, including using 2D solid model with the out-of-plane depth controlled through a plane-strain thickness condition (Abaqus User 's Manual 2017); Full 3D solid model of some cases are also evaluated in both Abaqus and Solidworks. The results of these approaches were comparable. The shell model used is effective in producing accurate results, and in the meantime, more efficient in using computation resource in terms of computational time. The project is aiming to develop and evaluate a modelling approach with a long-term purpose to search for or design new structures with targeted Poisson's ratio, which may result in running a large number of models. For example, the random structure of Voronoi model is normally combined with progress such as Monte Carlo simulation to assess a large number of structures (Chu et al., 2018). So, a computationally fast modelling method is important. The shell element approach also makes simulating and tracking the area changes much easier as well as the structure design and discovery.



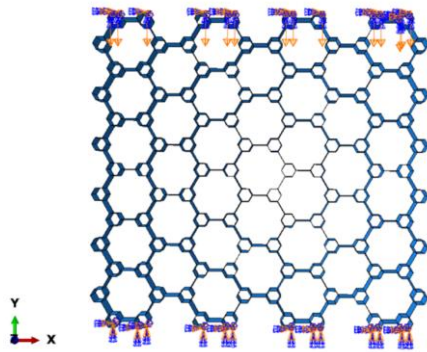
(d) Data showing the effect of element mesh size (no. of elements per beam) on the effective stress at 10% strain and Poisson's ratio.

**Figure 4.7.1** Effect of element number per beam on Engineer stress and Poisson's ratio at 10% Engineer strain. (beam length = 10 mm, the beam angle = 90-degree, E=22MPa)

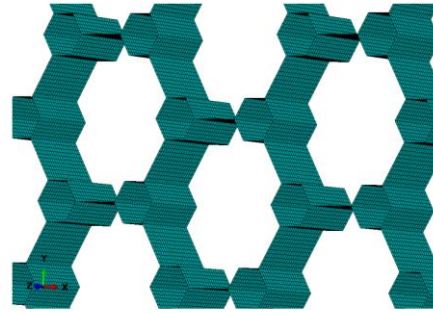
Mesh sensitivity is another important issue for the parametric FE model (<https://enterfea.com/correct-mesh-size-quick-guide/>). The parametric program has been used to assess the mesh sensitivities in which the mesh size is continuously reduced until the result is not affected by further mesh size reduction. The work could monitor the force and the Poisson's ratio. A typical case for the missing ribs model is shown in Figure 4.7.1a. In order to establish

---

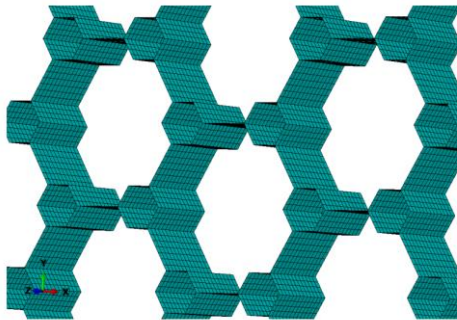
a suitable mesh size, two main approaches have been evaluated in the mesh sensitivity studies in the parametric models. One is to control the actual size; another is to control the number of elements per edge. Figure 4.7.1a shows some typical models with different mesh densities (element sizes). The size is controlled in the parametric model and the force/stress and Poisson's ratio is monitored. The effective stress is the overall force divided by the overall same area in the transverse direction (perpendicular to the loading direction). As shown in the figure, when the element per beam reaches 5, there is limited effect from the element numbers on both the effective stress and the ratio. So, the mesh size is selected as 5 elements per beam as the balance of accuracy and efficiency. Another set of typical data of mesh sensitivity study is shown in Figure 4.7.2b for a 1<sup>st</sup> order self-similar hierarchical model. The beam length of the corner hexagon is 5.5mm, the edge length of the small hexagon to the original hexagon is 1/4 (S value=0.25. the same as in Figure 4.5.5). The element size was changed from 1, 1.5, 1.75 and 2mm. It is shown in the data that the overall trend of the Poisson's ratio is similar, the data for 1 and 1.5mm element size has no difference but the value for element size of 2.5 is different. So, the mesh size is selected as 1mm as the balance of accuracy and efficiency. One advantage of the parametric program and data analysis is that the mesh size sensitivity studies can be processed systematically either through controlling the actual size or the number of elements per beam. Some trials have been conducted to further improve the mesh by controlling the regional mesh through modifying bias of the size, but it is not a major issue for the structures studied, but the parametric program could be modified to incorporate more complex meshing strategy for large quantity automatic modelling.



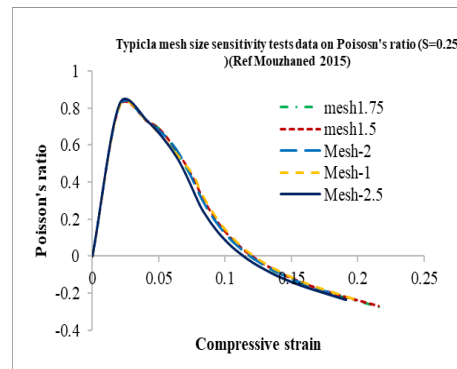
(a) FE model (Self similar hierarchical honeycomb)



(b) Mesh element size =1mm (enlarged view)



(c) Mesh element size=2mm (enlarged view)



(d) Effect of the mesh size on the Poisson' ratio.

**Figure 4.7.2** Effect of mesh size of on the Poisson's ratio of a 1<sup>st</sup> order self-similar hierarchical model. Overall sample size: W256-H240-Depth20.

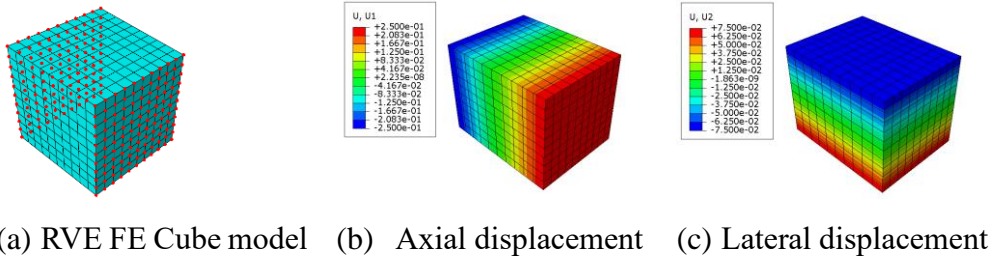
Beam Length of the small hexagon is 5.5. The hierarchical cell beam length ratio,  $S=1/4$ , beam thickness=1mm.

---

## **Comparison between full boundary and modelling with periodic boundary conditions**

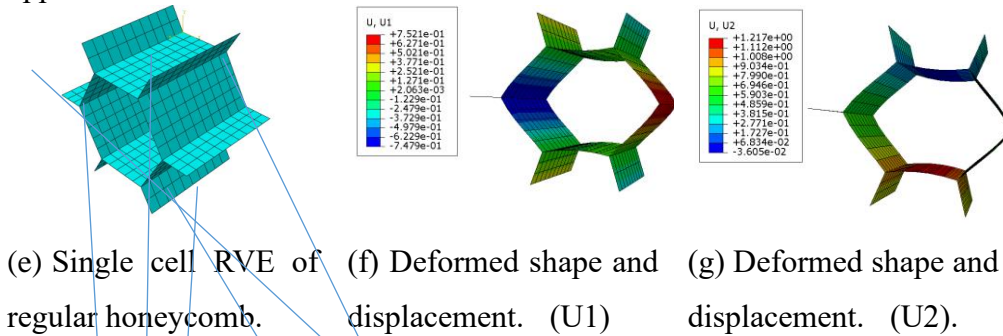
Most of the numerical modelling is based on the FE model with as-testing full boundary conditions of a uniaxial compression/tension test. Representative volume element (RVE) approach-based analysis has also been performed on selected samples as a comparison. The boundary conditions were applied using Micromechanics (Abaqus Micromechanics Plugin). After evaluating different approaches including EasyPBC, Matlab, etc., the main work was conducted with Abaqus Micromechanics Plug-in ([Obbink-Huizer, 2020](#)). Some typical models used and main equations for the boundary conditions are shown in Figure 4.7.3. These models are for evaluation purposes to assess the accuracy of the approach in analysing Poisson's ratios. Figure 4.7.3a is a simple isotropic 3D cube model, the material has a known Poisson's ratio, so it can be used to assess the prediction accuracy/effectiveness of the representative element volume and periodical boundary conditions. Figure 4.7.3b is a model for the regular honeycomb model; the regular honeycomb has an established known Poisson's ratio, so it could provide a means to validate the RVE approach for Poisson's ratio. The size of the cube is 5mm \*5mm \*5mm for the solid cube, the material property used is 22 MPa for Young's Modulus and 0.3 for Poisson's ratio. The size of regular honeycomb is 4.18 mm beam length, 0.145 mm beam thickness and 15.9 mm of out of plane depth. This dimension is adapted from [Papka and Kyriakides. \(1994\)](#) in order to compare the prediction with the experimental data. The Micromechanics Plug-in will collect all the nodes on the periodic boundary and separate the node to 6 node set (front, back, left, right, top, bottom). The deformation will be controlled by the RVE equation which is applied on Abaqus Keyword dialog by matching node set to node set. The equations applied are listed in Figures 4.7.3d&h for the cubic and the regular honeycomb model, respectively. In each case, there are 9 equations, for the solid cube model, the node set consists of all RVE\_AG\_PosX\_RVE\_AGSORT and RVE\_AG\_NegX\_RVE\_AGSORT consists of the nodes on the opposite surface as highlighted in Figure 4.7.3(a)

and the first equation (highlighted by the dashed underline). This equation forces these two surfaces to have the same displacement, this can be seen in Figure 4.7.3b.



```
*EQUATION
3
RVE_AG_PosX_RVE_AGSORT, 1, -1.000000e+00, RVE_AG_NegX_RVE_AGSORT, 1, 1.000000e+00, RP-Normal, 1, 5.000000e+00
3
RVE_AG_PosX_RVE_AGSORT, 2, -1.000000e+00, RVE_AG_NegX_RVE_AGSORT, 2, 1.000000e+00, RP-Shear, 1, 5.000000e+00
3
RVE_AG_PosX_RVE_AGSORT, 3, -1.000000e+00, RVE_AG_NegX_RVE_AGSORT, 3, 1.000000e+00, RP-Shear, 2, 5.000000e+00
3
RVE_AG_PosY_RVE_AGSORT, 1, -1.000000e+00, RVE_AG_NegY_RVE_AGSORT, 1, 1.000000e+00, RP-Shear, 1, 5.000000e+00
3
RVE_AG_PosY_RVE_AGSORT, 2, -1.000000e+00, RVE_AG_NegY_RVE_AGSORT, 2, 1.000000e+00, RP-Normal, 2, 5.000000e+00
3
RVE_AG_PosY_RVE_AGSORT, 3, -1.000000e+00, RVE_AG_NegY_RVE_AGSORT, 3, 1.000000e+00, RP-Shear, 3, 5.000000e+00
3
RVE_AG_PosZ_RVE_AGSORT, 1, -1.000000e+00, RVE_AG_NegZ_RVE_AGSORT, 1, 1.000000e+00, RP-Shear, 2, 5.000000e+00
3
RVE_AG_PosZ_RVE_AGSORT, 2, -1.000000e+00, RVE_AG_NegZ_RVE_AGSORT, 2, 1.000000e+00, RP-Shear, 3, 5.000000e+00
3
RVE_AG_PosZ_RVE_AGSORT, 3, -1.000000e+00, RVE_AG_NegZ_RVE_AGSORT, 3, 1.000000e+00, RP-Normal, 3, 5.000000e+00
```

(d) Applied equation in Abaqus used to control the displacement of the opposite faces/node sets.



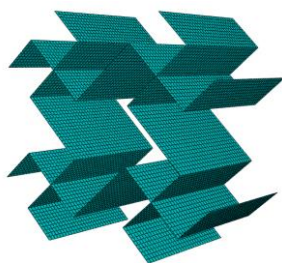
```
*EQUATION
3
RVE_AG_PosX_RVE_AGSORT, 1, -1.000000e+00, RVE_AG_NegX_RVE_AGSORT, 1, 1.000000e+00, RP-Normal, 1, 1.500000e+01
3
RVE_AG_PosX_RVE_AGSORT, 2, -1.000000e+00, RVE_AG_NegX_RVE_AGSORT, 2, 1.000000e+00, RP-Shear, 1, 1.500000e+01
3
RVE_AG_PosX_RVE_AGSORT, 3, -1.000000e+00, RVE_AG_NegX_RVE_AGSORT, 3, 1.000000e+00, RP-Shear, 2, 1.500000e+01
3
RVE_AG_PosY_RVE_AGSORT, 1, -1.000000e+00, RVE_AG_NegY_RVE_AGSORT, 1, 1.000000e+00, RP-Shear, 1, 1.299038e+01
3
RVE_AG_PosY_RVE_AGSORT, 2, -1.000000e+00, RVE_AG_NegY_RVE_AGSORT, 2, 1.000000e+00, RP-Normal, 2, 1.299038e+01
3
RVE_AG_PosY_RVE_AGSORT, 3, -1.000000e+00, RVE_AG_NegY_RVE_AGSORT, 3, 1.000000e+00, RP-Shear, 3, 1.299038e+01
3
RVE_AG_PosZ_RVE_AGSORT, 1, -1.000000e+00, RVE_AG_NegZ_RVE_AGSORT, 1, 1.000000e+00, RP-Shear, 2, 1.000000e+01
3
RVE_AG_PosZ_RVE_AGSORT, 2, -1.000000e+00, RVE_AG_NegZ_RVE_AGSORT, 2, 1.000000e+00, RP-Shear, 3, 1.000000e+01
3
RVE_AG_PosZ_RVE_AGSORT, 3, -1.000000e+00, RVE_AG_NegZ_RVE_AGSORT, 3, 1.000000e+00, RP-Normal, 3, 1.000000e+01
```

(h) Applied equation in Abaqus used to control the displacement of the opposite faces/node sets.

**Figure 4.7.3** Solid cube model and regular honeycomb model used to evaluate the effectiveness of REV approach with periodical boundary conditions in predicting the Poisson's ratio.

As shown in Figure 4.7.3b, the overall deformation is 0.5 in the U1 direction, 0.15 in the U2 direction, which gives a Poisson's ratio of 0.3, which matches the original material property used. A range of Poisson's ratio has been used with both negative and positive values, in all the cases tested, the RVE model is able to produce Poisson's ratio which matches target value within 1% error. In the case of the honeycomb (Figure 4.7.3e), the node set consists of the nodes on the edges, RVE\_AG\_PosX\_RVE\_AGSORT for the edge to the right, RVE\_AG\_NegX\_RVE\_AGSORT refers to the edge to left. RVE\_AG\_PosY\_RVE\_AGSORT refers to the top two edges and RVE\_AG\_NegY\_RVE\_AGSORT refers to the bottom two edges. RVE\_AG\_PosZ\_RVE\_AGSORT and RVE\_AG\_NegZ\_RVE\_AGSORT refers to the all the nodes on the size at the extrusion directions. The deformed shape of the models is shown in Figure 4.7.3f&g. The Poisson's ratio of a regular honeycomb is known to be close to a value of 1 (Papka and kyriakides, 1994). As shown in Figure 4.7.3f&g, the overall displacement at U1 direction is 1.54mm, the overall displacement at the U2 direction is 1.59mm, this gives a Poisson's ratio close to 1. These evaluation data show that the REV approach is accurate for evaluating the Poisson's ratios of both homogeneous material and cellular structures.

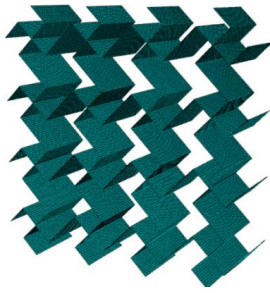
Figure 4.7.4 shows the REV for the auxetic missing rib models: Figure 4.7.4a is a single cell model, Figure 4.7.4b is a 4 cells models. In the mode all the edges on one side are grouped into one node set and then the equation is applied to the three directions (1,2,3). The beam length is the same as those for the model in Figure 4.4.4 (the beam length is 10mm, the beam thickness is 1mm). The mesh size is 1mm).



(a) Missing rib model (single cell model)

```
*EQUATION
3
RVE_AG_PosX_RVE_AGSORT, 1, -1.000000e+00, RVE_AG_NegX_RVE_AGSORT, 1, 1.000000e+00, RP-Normal, 1, 5.656854e+01
3
RVE_AG_PosX_RVE_AGSORT, 2, -1.000000e+00, RVE_AG_NegX_RVE_AGSORT, 2, 1.000000e+00, RP-Shear, 1, 5.656854e+01
3
RVE_AG_PosX_RVE_AGSORT, 3, 1.000000e+00, RVE_AG_NegX_RVE_AGSORT, 3, 1.000000e+00, RP-Shear, 2, 5.656854e+01
3
RVE_AG_PosY_RVE_AGSORT, 1, 1.000000e+00, RVE_AG_NegY_RVE_AGSORT, 1, 1.000000e+00, RP-Shear, 1, 5.656854e+01
3
RVE_AG_PosY_RVE_AGSORT, 2, 1.000000e+00, RVE_AG_NegY_RVE_AGSORT, 2, 1.000000e+00, RP-Normal, 2, 5.656854e+01
3
RVE_AG_PosY_RVE_AGSORT, 3, 1.000000e+00, RVE_AG_NegY_RVE_AGSORT, 3, 1.000000e+00, RP-Shear, 3, 5.656854e+01
3
RVE_AG_PosZ_RVE_AGSORT, 1, -1.000000e+00, RVE_AG_NegZ_RVE_AGSORT, 1, 1.000000e+00, RP-Shear, 2, 3.000000e+01
3
RVE_AG_PosZ_RVE_AGSORT, 2, -1.000000e+00, RVE_AG_NegZ_RVE_AGSORT, 2, 1.000000e+00, RP-Shear, 3, 3.000000e+01
3
RVE_AG_PosZ_RVE_AGSORT, 3, -1.000000e+00, RVE_AG_NegZ_RVE_AGSORT, 3, 1.000000e+00, RP-Normal, 3, 3.000000e+01
```

(b) Applied equation in Abaqus used to control the displacement of the opposite faces/node sets.



```

*EQUATION
3
RVE_AG_PosX_RVE_AGSORT, 1, -1.000000e+00, RVE_AG_NegX_RVE_AGSORT, 1, 1.000000e+00, RP-Normal, 1, 1.1
3
RVE_AG_PosX_RVE_AGSORT, 2, -1.000000e+00, RVE_AG_NegX_RVE_AGSORT, 2, 1.000000e+00, RP-Shear, 1, 1.13
3
RVE_AG_PosX_RVE_AGSORT, 3, -1.000000e+00, RVE_AG_NegX_RVE_AGSORT, 3, 1.000000e+00, RP-Shear, 2, 1.13
3
RVE_AG_PosY_RVE_AGSORT, 1, -1.000000e+00, RVE_AG_NegY_RVE_AGSORT, 1, 1.000000e+00, RP-Shear, 1, 1.13
3
RVE_AG_PosY_RVE_AGSORT, 2, -1.000000e+00, RVE_AG_NegY_RVE_AGSORT, 2, 1.000000e+00, RP-Normal, 2, 1.1
3
RVE_AG_PosY_RVE_AGSORT, 3, -1.000000e+00, RVE_AG_NegY_RVE_AGSORT, 3, 1.000000e+00, RP-Shear, 3, 1.13
3
RVE_AG_PosZ_RVE_AGSORT, 1, -1.000000e+00, RVE_AG_NegZ_RVE_AGSORT, 1, 1.000000e+00, RP-Shear, 2, 3.00
3
RVE_AG_PosZ_RVE_AGSORT, 2, -1.000000e+00, RVE_AG_NegZ_RVE_AGSORT, 2, 1.000000e+00, RP-Shear, 3, 3.00
3
RVE_AG_PosZ_RVE_AGSORT, 3, -1.000000e+00, RVE_AG_NegZ_RVE_AGSORT, 3, 1.000000e+00, RP-Normal, 3, 3.0

```

(c) Missing rib model (d) Applied equation in Abaqus used to control the displacement of the opposite faces/node sets.

**Figure 4.7.4** RVE models with periodical boundary conditions (PBC) of normal missing rib structure of different sizes.

Figure 4.7.5 compares the Poisson's ratio value predicted from the RVE models. It is shown that the two RVE models with different sizes have identical Poisson's ratios. The value is close to the data from large models with full boundary conditions. The data also shows that the RVE model with a periodical boundary condition is not able to predict the turning point of the Poisson's ratio. So, it is only feasible for very small deformation.

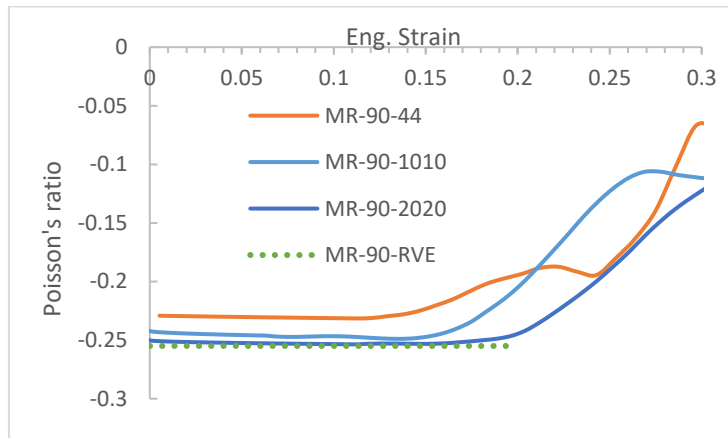


**Figure 4.7.5** Comparison of the Poisson's ratio of normal missing ribs structure (beam angle 90 degree) from the RVE modelling with periodical boundary conditions and different sample sizes (4-4, 10-10, 20-20) with full load conditions.

---

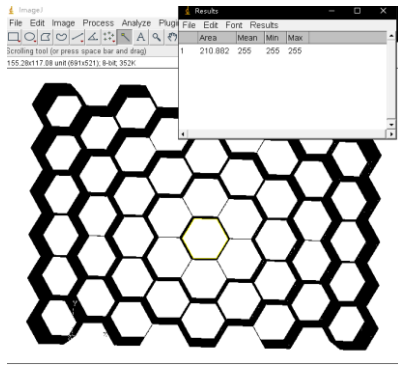
### **4.7.3 Factors affecting the area analysis with different approaches and use of the program in random structures generation**

As presented in section 4.6, the program for area calculation is effective in establishing the area changes of the cells of in-plane deformation of cellular structures. The area changes reflect the localised deformation patterns and the key deformation stages well. These will provide useful additional data for understanding the deformation of the structures. The program is able to study different deformation modes and quantify the trend and value of the cell area changes between regular honeycomb, missing rib models and self-similar hierarchical models. Work has also been done in other honeycomb structures, such as re-entrant, etc. (result not shown). As shown in Figure 4.6.6 and Figure 4.6.7, the program is able to show more uniform cell deformation in tension for the regular honeycomb and the missing rib models, it can also show the non-uniform deformation under compression. The uniform cell area changes of the missing rib model could be a beneficial material behaviour for applications such as filters, etc. The area data is also useful for another project on applying auxetic materials in foot orthotics, for which the size of the pore of the material affects the breathability of the materials ([Zevallos Herencia, 2020; current PhD project](#)).

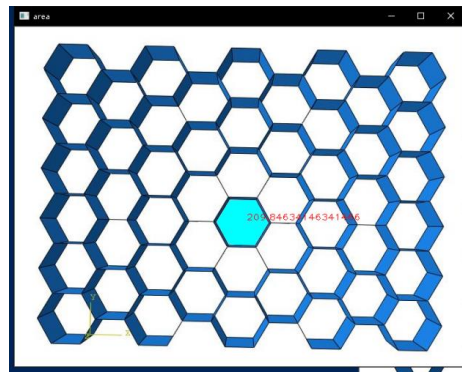
### **Comparison of different approaches for evaluating the accuracy and feasibility**

Area measurements and applications is a very active research area. In the preliminary works, many approaches are evaluated to assess their suitability for studying the area changes in cellular structures. Some other approaches also provide useful data to assess the accuracy of the python program developed in this work, such as ImageJ and OpenCV program (<https://opencv.org/>). It can display, edit, analyse, process, save and print 8-bit, 16-bit and 32-bit images. It can calculate area and pixel value statistics of user-defined selections. It can measure distances and angles. It can create density histograms and line profile plots. It supports standard image processing functions such as contrast manipulation, sharpening, smoothing, edge detection and median filtering

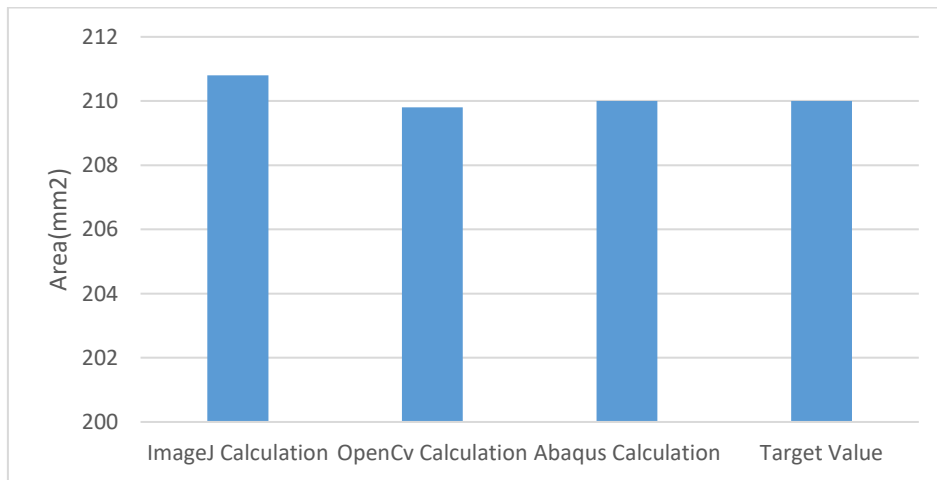
(<https://imagej.nih.gov/ij/docs/intro.html>). It is widely used in analysing images (Dutta et al., 2019). OpenCV (Open-Source Computer Vision Library) is an open-source computer vision and machine learning software library. OpenCV was built to provide a common infrastructure for computer vision applications and to accelerate the use of machine perception (OpenCVopencv.org). Some typical data are shown in Figure 4.7.6.



(a) Area calculation by Image-J.



(b) Area calculation python program from experiment picture base on Intel Open CV.



(d) Area validation of different method. (details of the Abaqus calculation can be found in section 4.6)

**Figure 4.7.6** Area calculation of different method and validation based on a cell with known area.

Figure 4.7.6a shows the image used to compare the ImageJ, Open CV and the approach reported in section 4.6. The area determined from the ImageJ, OpenCV and the Python program integrated in Abaqus has a comparable

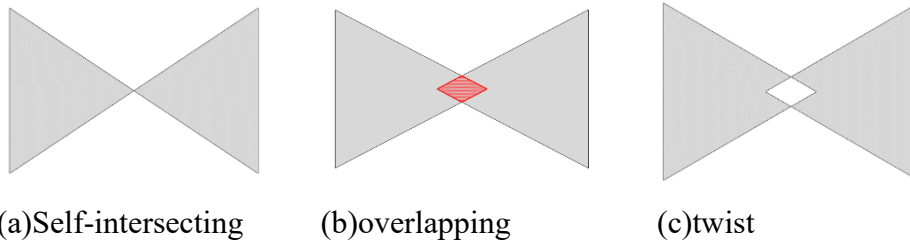
---

accuracy in comparison with the real area value. Similar tests have been conducted on other images; similar accuracy can be achieved with the Python program integrated with Abaqus. Both ImageJ and OpenCV will require operating on individual images, while the Python program developed is integrated in Abaqus, which can record details data of each calculation increment or step in Abaqus.

The area calculation of the program presented in section 4.6 is mainly based on the point-in-polygon (PIP) approach, which involves generating triangles then working out the sum of the area considering the positive or negative signs of the triangles based on Heron's formula (HF) (as detailed in section 4.6). Another commonly used approach directly using the coordinates of the polygon is the shoelace Method. The Shoelace Method can be calculated based on point coordinates in the Cartesian coordinate system  $A = \frac{1}{2} (\sum_{i=1}^{n-1} x_i y_{i+1} + x_n y_1 - \sum_{i=1}^{n-1} x_{i+1} y_i - x_1 y_n)$ , Where A is the area of polygon and n is the number of sides (or number of vertex) of the polygon. (x, y) are the coordinates of the points on the Polygon. The points need to be in sequential order based on their position on the Polygon (Ochilbek, 2018). In this work, a Python program was developed to calculate polygon area based on SM. This method is easier to use and achieve through computation as only the coordinates are required while the point-in-polygon requires more complex partitioning, point order sorting, etc. But there are some limitations for the shoelace approach, which affected the use of this method in calculating the area of deformed shapes or complex shapes in Abaqus. There are circumstances where the algorithm produces wrong or inaccurate results, such as Self-intersecting, overlapping or twist (Figure 4.7.7). If the geometry has self-intersection and twist, not a closed curve, the shoelace will end up giving a wrong value. In a computerised process, the program will exit with a wrong number. The geometry overlapping shows on the red zone of figure(b), The shoelace method would calculate the overlapping zone twice, which would not be as easy to correct as the point-on-polygon method (section 4.6). As detailed in section 4.6, a positive or negative sign was given to the triangles

---

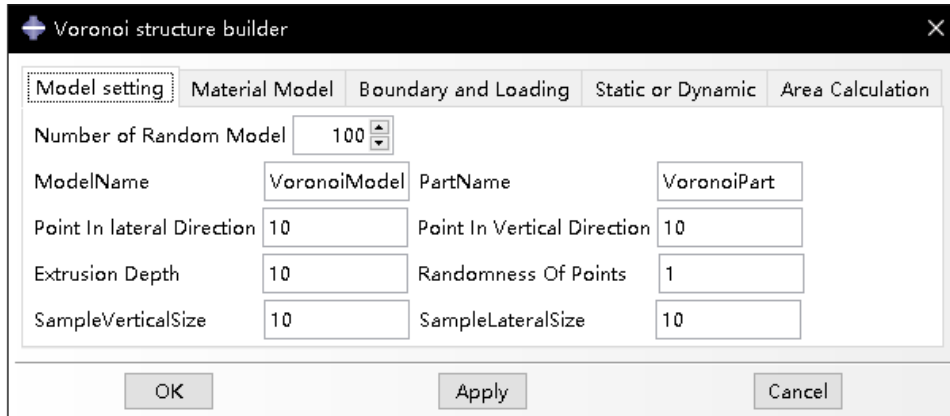
with the Point-on-Polygon approach, which will automatically remove the area being counted twice in the calculation.



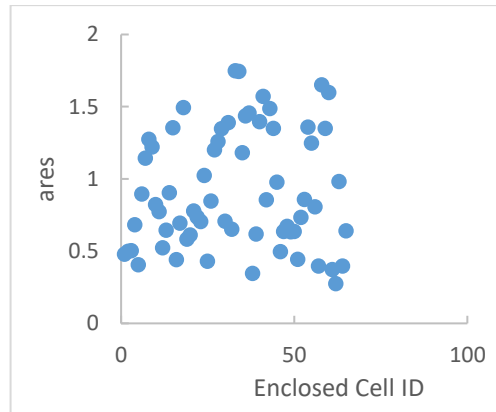
(a)Self-intersecting      (b)overlapping      (c)twist  
**Figure 4.7.7** Simulation/cases for which the Shoelace Method has limitation to deal with when calculate polygon area.

**Use of the program for cell size control of random Voronoi structure**

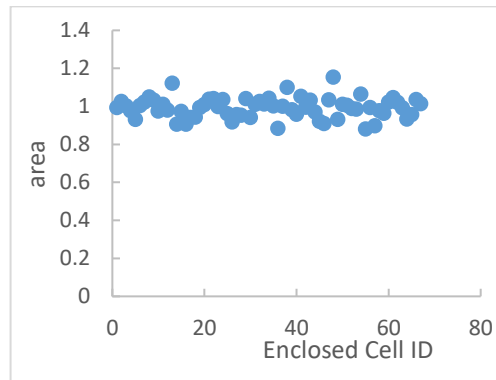
The area is also used in analysing random models in generating random cells when combined with the Voronoi structure generation Plug-in. Figures 4.7.8 shows the Abaqus GUI for generating Voronoi cells and the area distributions. Details of the Voronoi structure generation process was presented in section 4.2. In this program, the area calculation program is linked with the Voronoi structure generation and the area for each cell is automatically calculated. Both figures 4.7.8a&c have the same number of cells, the area of the cells is obtained through the area calculation program (details in section 4.6), the distribution of the area values for all the cells generated are plotted in Figure 4.7.8b&d. The vertical axis is for area values ( $\text{mm}^2$ ), the horizontal axis is the id of the cells generated. In Figure 4.7.8b the structures are not uniform; this is reflected in the high randomness of the cell area values plotted in Figure4.7.8c. The structure shown in Figure Figure4.7.8d is much more regular, this is reflected by the more uniform area values (Figure4.7.8e). This shows that the area calculation program is a useful tool for structure selection and modelling. Other detailed data such as the beam length, wall angle can also be produced and stored as data for further analysis.



(a) Graphic User Input for Voronoi cells generation and cell area calculation.



(b) A typical random structure produced based the Voronoi method. (c) cell area distribution showing the irregular sizes.



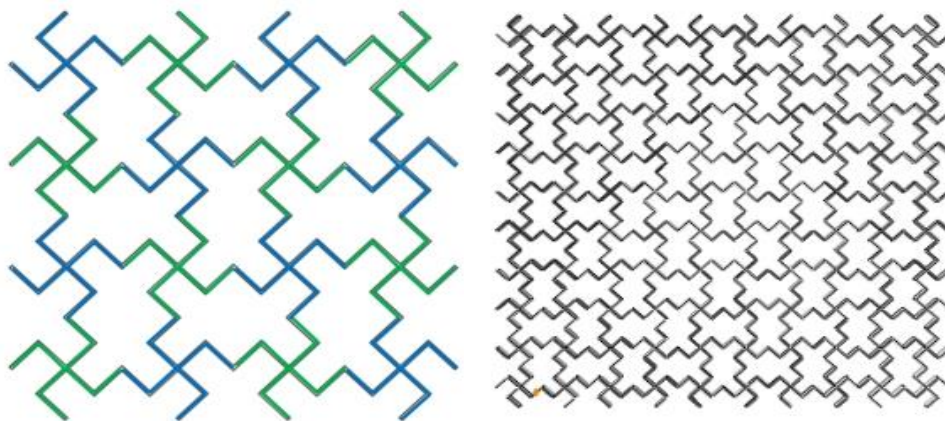
(d) A structure with regular cell area/size controlled by area rules (e) cell area distribution showing the regular sizes.

**Figure 4.7.8** Typical random structures produced by the Voronoi method and the area

---

#### 4.7.4 Development of mixed structures of regular shapes/patterns with targeted Poisson's ratios and other targeted properties.

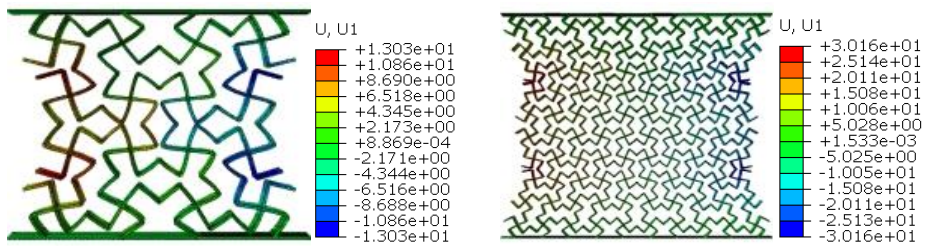
The FE modelling is an effective way to develop mixed structures with tunable Poisson's ratio and auxetic behaviours. Mix structure can change/disrupt the deformation mechanism or pattern, thus influence the material deformation. For auxetic structures, apart from research on single mechanism structures, several works have been reported exploring the use of mixed structures which combined auxetics materials with different mechanisms (Cabras and Brun, 2014; Fozdar et al., 2011; Hedayati et al., 2018; Hu et al., 2019; Meena et al., 2019; Nika and Constantinescu, 2018; Strek et al., 2017; Yang et al., 2015). All these have opened opportunities in design materials with auxetic structures. As shown in section 4.4, the mixed structure designed through altering the orientations of the missing rib columns could change the deformation process and the stability of the auxeticity. The mixed structure increased the stability of Poisson's' ratio and auxeticity of the structures. It also makes the model more stable and maintain its shape better. Other more complex mixed structures of missing rib models are also explored by alternating both the columns and the rows. A typical example is shown in Figure 4.7.9. The colour of Blue and green shows the different pattern of the structure. Figure (a) is a 4-4 model and Figure 4.7.9b is a larger 10-10 model.



(a) Mixed structure 3 (MS-3) (4-4 model). (b) Mixed structure 3 (MS-3) (10-10 model).

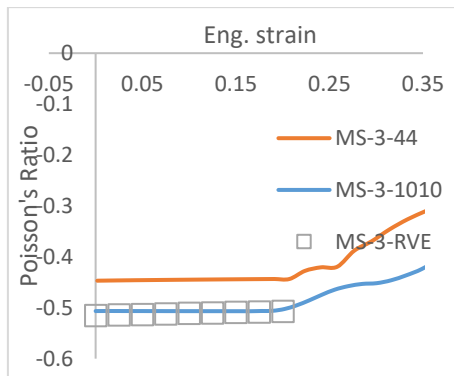
**Figure 4.7.9** Finite element model of mixed structure with alternating cell angles in the rows and columns.

Figure 4.7.10a&b shows the deformed shape of the mixed structure under compression, which shows clearly that the sample shrinks in the transverse direction indicating a negative Poisson's ratio. Figure 4.7.10c shows the Poisson's ratio vs. axial strain data, which suggests that mixed structure (MS-3) has a very stable Poisson's ratio up to a strain level of about 20%, which is lower than that for MS-1 and MS-2 (mixed structures with alternating column angles only). As shown in Figure 4.7.10d, the values of the Poisson's ratio values for the new mixed structure are much higher than the regular missing rib and the column based mixed structures (MS-1 and MS-2).

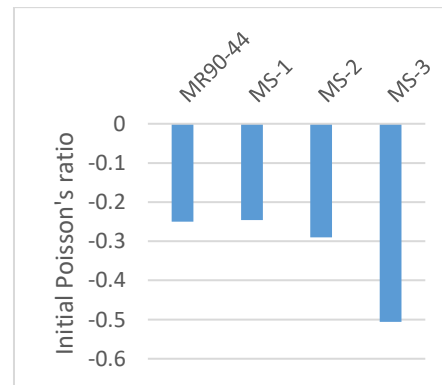


(a)The deformation of Mixed structure 3(MS-3) (4-4 model) at 0.2 load strain

(b)The deformation of Mixed structure 3(MS-3) (10-10 model) at 0.2 load strain



(c)Poisson's ratio vs. axial strain data of Ms-3



(d)Figure comparison the initial Poisson's ratio with different mixed structure

**Figure 4.7.10** The deformation of Mixed structure with different unit cell Poisson's ratio of mixed missing rib models (MR-3) determined from different sample sizes and RVE models.

---

#### 4.7.5 Development of random auxetic structures.

Mixed auxetic structures presented in section 4.4 and 4.7.4 are based on changing the pattern of regular structures, the variables that can be altered are relatively limited by the angles and beam lengths. As explained in earlier sections (section 4.2 and section 4.7.3), The Voronoi method is able to produce random structures but in Voronoi structure generation, not all the structures are applicable, i.e., some structures with intersections have to be removed ([Alsayednoor and Harrison, 2016](#)). In addition, Voronoi structures are limited to producing random structures with convex polygons, this reduces the possibility of generating negative Poisson's ratio structures as auxetic structures are often associated with concave polygons such as re-entrant structures, and self-similar hierarchical honeycombs.

A new random approach is explored involving generating a random point based on a predefined grid, the point is generated randomly occupying a different grid. The structure is then converted into an FE model (compression) to assess its Poisson's ratio and the new auxetic structure is then selected. The main program structure is shown in Figure 4.7.11. The model builder program is developed to generate random points in 2D grids with controlled densities. The lines are generated from these points. The cells formed by the lines will be extruded into a shell model and converted into a finite element model. The material properties and the boundary conditions are automatically applied in the FE model. One key operation integrated with the FE modelling process is to judge the Poisson's ratio of each newly generated structure by tracking the lateral deformation. If the Poisson's ratio is negative, the structure and the FE file will be stored for further analysis. If the Poisson's ratio is positive, no data will be kept, then the program will go back to the next structure generation directly.

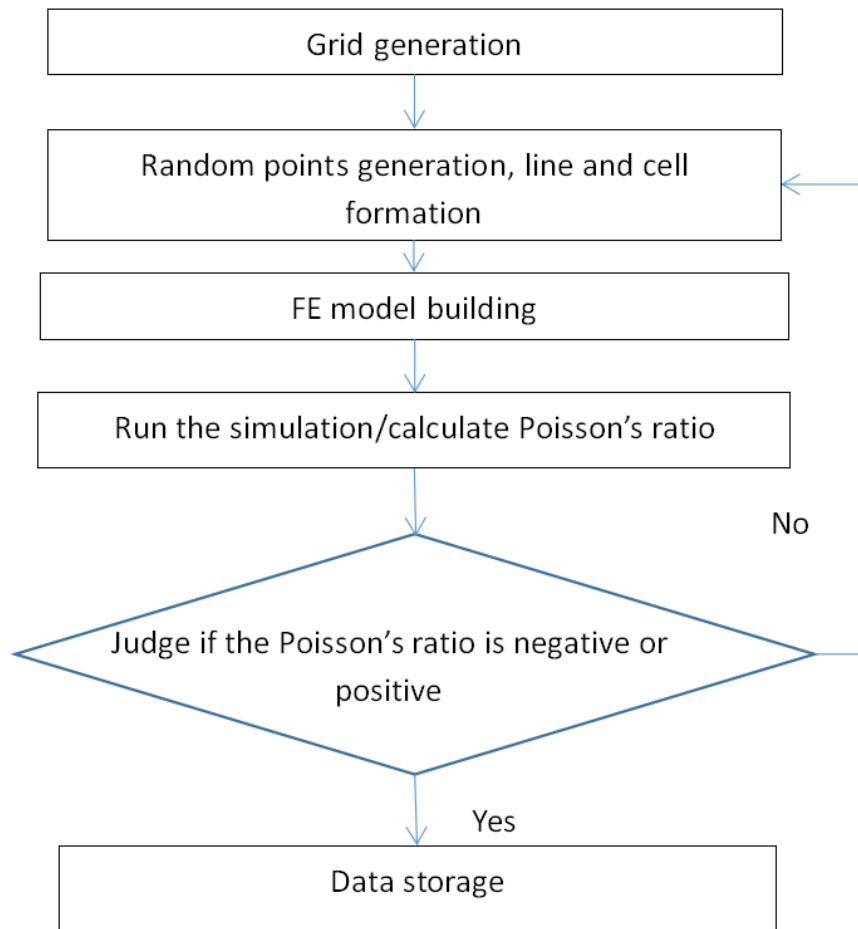


**Figure 4.7.11** Flow chart showing the overall structure of the program for identifying structures with a negative Poisson's a ratio over different strains.

The first part is generating random structure-based grid density and number of random points. Table 4.7.1 list the main steps and operations. Figure 4.7.12 is GUI of random model builder. The input parameter is used to define the calculation detail include number of models, overall grid size, grid density, number of random points on edge, number of random points on grid, maximum connect number, connect rate and number lattice pattern. The number of models is the number of generated random model, and this parameter is used to control the loop time of the program to ensure the number of generated random model. The overall grid size is controlled by Lateral grid size and Vertical grid size. Grid density is controlled by number of lateral grid layer and number of vertical grid layer. The number of random points on the edges is used to define how many random points to the structure edge, and

the edge points of top line and bottom line, left line and right line. The number of random points is the random point on the grid area except points on the edges. Maxima connect number is the maximum times that a point can be connected to another point. The program will start at creating a grid zone which the random point can be selected from the point on grid. Then a random module from import python module library is used to randomly select the point from grid point (Step 2). Then lines are formed by connect the points following connection rules (Step 3) to form a unit cell. Finally, the point connected sketch is extruded to form models for finite element simulation (Step 4&5). The unit cell can be copied and repeated following the lateralLatticeNum. and the verticalLatticeNum, as shown in Figure 4.7.13. Some of the typical example of auxetic structure automatically identified shows on figure 4.7.14

**Table 4.7.1** Main steps and key operation of the program for generating and searching random structures with auxetic behaviours.

Random structure generation	Generate Random Points, Generate Grids, Link points Random Points,
FE model development based on the random structure automatically formed.	Extrude, assign materials properties, mesh, boundary conditions,
Run the simulation	Run the simulation, obtain the displacement data, then convert to strain, calculate the Poisson's ratio by axial strain /lateral strain/transverse. Produce Poisson's ratio vs. Axial Strain data. Controlled increment/steps
Judge	If the Poisson's ratio is smaller than 0 at any strain point, keep the model and store the FE model/data, Poisson's ratio vs. axial strain data.

Move to the next cycle	If the structure has a positive Poisson's ratio, move to the next loop in searching for new auxetic structures.
Data storage	Selected data can be stored for future evaluation and analysis.

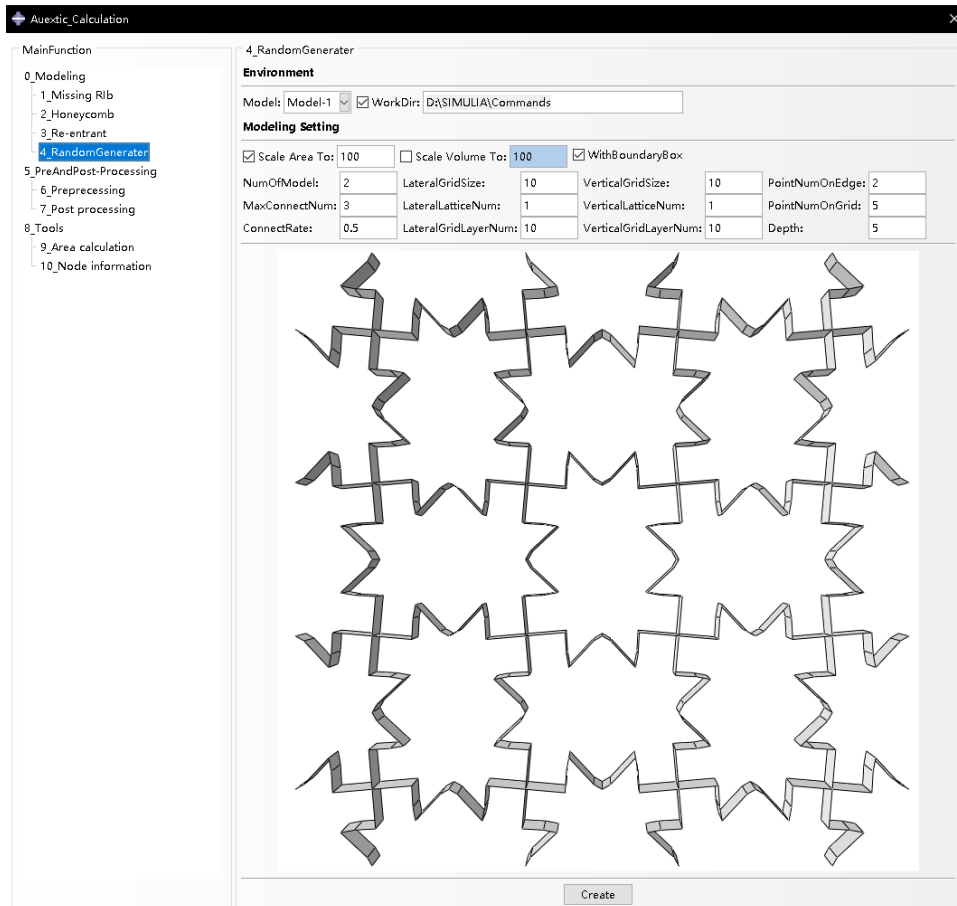
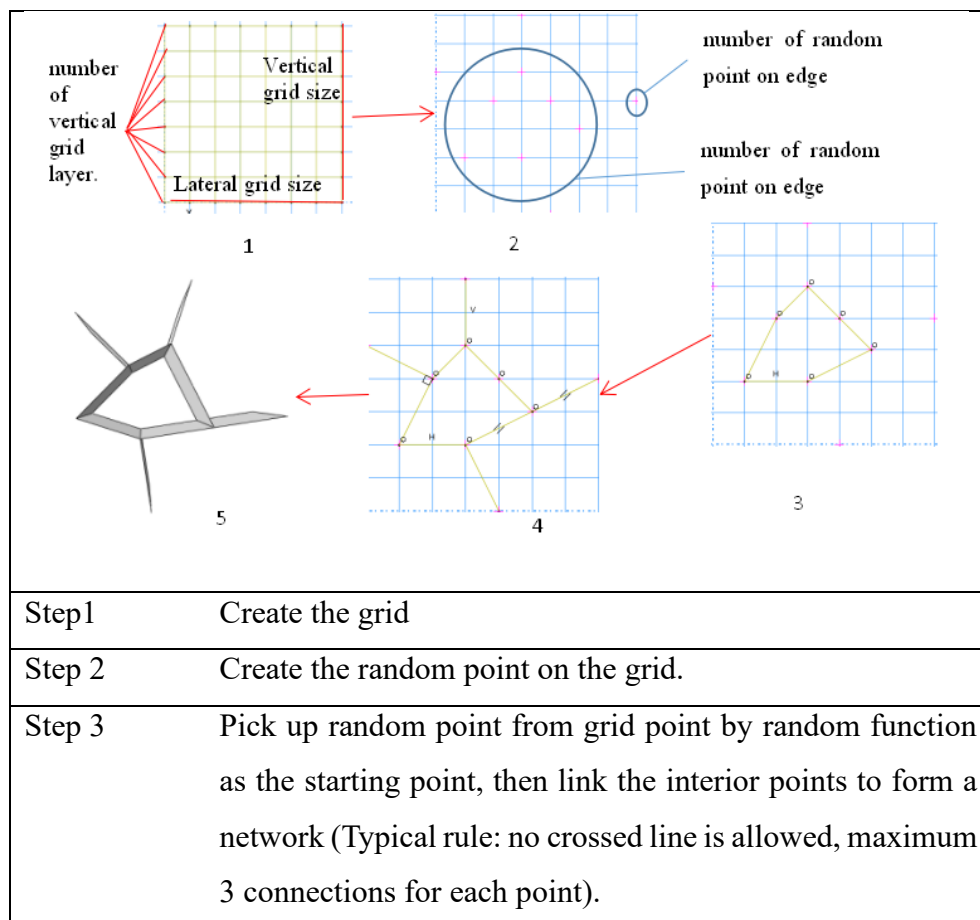


**Figure 4.7.12** Abaqus GUI for producing random structures.

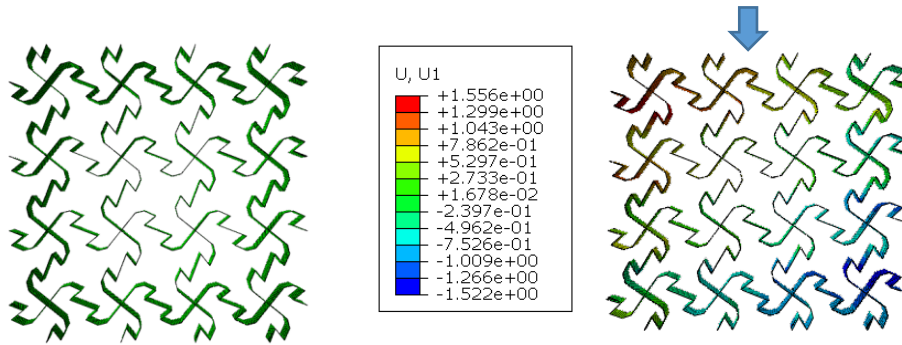
The first part is generating random structure-based grid density and number of random points. Table 4.7.1 lists the main steps and operations. Figure 4.7.12 is the GUI of random model builder. The input parameter is used to define the calculation detail including number of models, overall grid size, grid density, number of random points on edge, number of random points on grid, maximum connect number, connect rate and number lattice pattern. The number of models is the number of generated random models, and this parameter is used to control the loop time of the program to ensure the number of generated random models. The overall grid size is controlled by the Lateral

grid size and Vertical grid size. Grid density is controlled by the number of lateral grid layers and number of vertical grid layers. The number of random points on the edges is used to define how many random points to the structure edge, and the edge points of top line and bottom line, left line and right line. The number of random points is the random point on the grid area except points on the edges. Maxima connect number is the maximum times that a point can be connected to another point. The program will start at creating a grid zone in which the random point can be selected from the point on grid. Then a random module from the imported Python module library is used to randomly select the point from grid point (Step 2). Then lines are formed by connect the points following connection rules (Step 3) to form a unit cell. Finally, the point connected sketch is extruded to form models for finite element simulation (Step 4&5). The unit cell can be copied and repeated following the lateralLatticeNum. and the verticalLatticeNum, as shown in Figure 4.7.15.



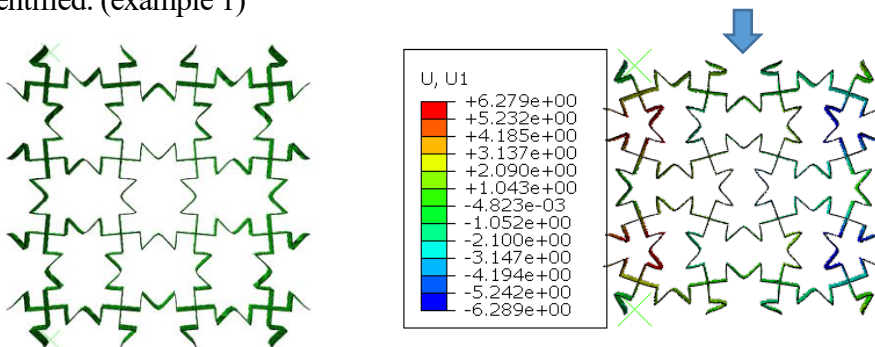
step4	Connect points on the side of the grid area and internal random points
Step 5	Extrude the sketch to form a honeycomb structure.

**Figure 4.7.13** Main steps in building the random structures.



(a) A typical example of auxetic structure automatically identified. (example 1)

(b) Typical deformed example of auxetic structure automatically identified (example 1)



(c) A typical example of auxetic structure automatically identified. (example 2)

(d) Typical deformed example of auxetic structure automatically identified (example 2)

**Figure 4.7.14** Typical auxetic structures predicted.

---

**CHAPTER FIVE**

**NUMERICAL STUDY ON**

**DIFFERENT CRYSTAL**

**STRUCTURES**

---

## 5.1 Introduction and main research works

This chapter is focused on developing a Python-based data system for analysing the data and link between crystal structures and key ground state properties of crystals based on first principle calculation with Materials Studio. A range of ground state properties including elastic constants ( $C_{ij}$ ), bulk modulus ( $K$ ), Young's modulus ( $E$ ), shear modulus ( $G$ ), Poisson's ratio ( $\nu$ ), etc. have been studied with a particular focus on Poisson's ratio, anisotropy. The correlation between the ground state elastic parameters and their link with other properties is analysed. Some compounds with low or negative Poisson's ratio were identified and detailed structures and properties data are given. In section 5.2, the basic procedure in first principle calculation with Materials Studio and the effect of key operation parameters (such as the cut-off energy, density of k-points, etc.) on the energy convergence and the accuracy of the calculated elastic constants ( $C_{ij}$ ) is explained. The main function of a Graphical User Interface for processing the data and properties is briefly explained. In section 5.3, some typical results on key engineering carbides including simple cubic systems ( $TiC$ ,  $VC$  and  $NbC$ ) are presented together with an explanation of the mathematical operation to calculate the  $K$ ,  $E$ ,  $G$ ,  $\nu$ , and function for 3D surface constructions of the ground state parameters incorporating anisotropic features. The bulk modulus, Young's Modulus, Shear Modulus, Poisson's ratio, and anisotropy in these parameters are presented and discussed. In section 5.4, the structure of a Python Graphical User Interface developed for systematic calculation and visualization of the key structures, properties and anisotropy features are explained in detail. The structure and properties of a range of carbides are analysed with a particular focus on Poisson's ratios and anisotropy coefficients. The key factors affecting the accuracy and efficiency of first principle calculation when dealing with data of different material systems is discussed. The uncertainty in Poisson's ratio and the link between property data is discussed. The structural data of a few compounds with negative Poisson's ratio is briefly presented, the correlation between the auxetic crystal

structure and some macro structures with auxetic behaviours are discussed. The procedure and use of materials studio in simulating other properties and processes is also briefly presented and discussed including surface energy, oxygen reduction reaction (ORR), structures with doping elements and the effect of temperatures. The overall use of the system and future work in data development is also discussed.

Table 5.1.1 Main research and development works

<p>Program development and applications</p> <ul style="list-style-type: none"> <li>➤ Python program to automatically generate file for sensitivity studies (Cut-off, k-points, etc.) on the energy convergence and simulation efficiency in crystal geometry optimization (Lattice constants) and property optimisation (elastic constants (Cij))</li> <li>➤ Python program to calculate the key elastic properties (K, E, G, <math>\nu</math>) from the (elastic constants (Cij)) and determine the key isotropic parameters (Universal and individual property isotropic parameters)</li> <li>➤ Integrate the calculation, 3D surface construction of key elastic properties and projection onto key planes</li> </ul>
<ul style="list-style-type: none"> <li>➤ Comparative study of the ground state elastic properties and anisotropy of simple carbides with first principle calculation.</li> <li>➤ Elastic property data and Poisson's ratio anisotropy in different carbides.</li> </ul>
<p>Discussion</p> <ul style="list-style-type: none"> <li>➤ Link between Poisson's ratio and other properties and the effect of anisotropy</li> <li>➤ Data and analysis of compounds with low or negative Poisson's ratios.</li> <li>➤ First principle calculation data for more complex cases: surface energy, energy, oxygen reduction reaction (ORR), structures with doping elements</li> <li>➤ Use of the program to study the effect of temperatures on the elastic properties and anisotropy.</li> </ul>

---

## 5.2 The main process and data in first principle calculation of ground state properties

Materials Studio is widely used in predicting material properties from atomic number and crystal structure, as atomic number and crystal structure being the input (Farhadizadeh et al., 2017). Materials Studio CASTEP is an ab initio quantum mechanical program that was developed based on density functional theory (DFT) to simulate the properties of solids as well as characteristics of interfaces and surfaces. First principle calculation is able to calculate physical properties directly from basic physical quantities (such as the mass and charge, Coulomb force of an electron, etc.) based on the principle of quantum mechanics.

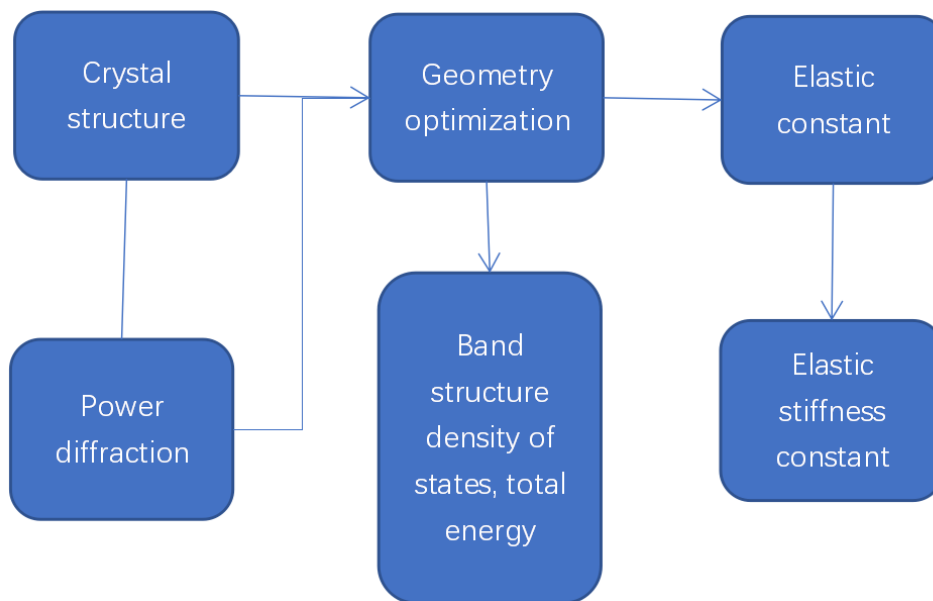


**Figure 5.2.1** Typical operation in Materials Studio process ground property simulation process.

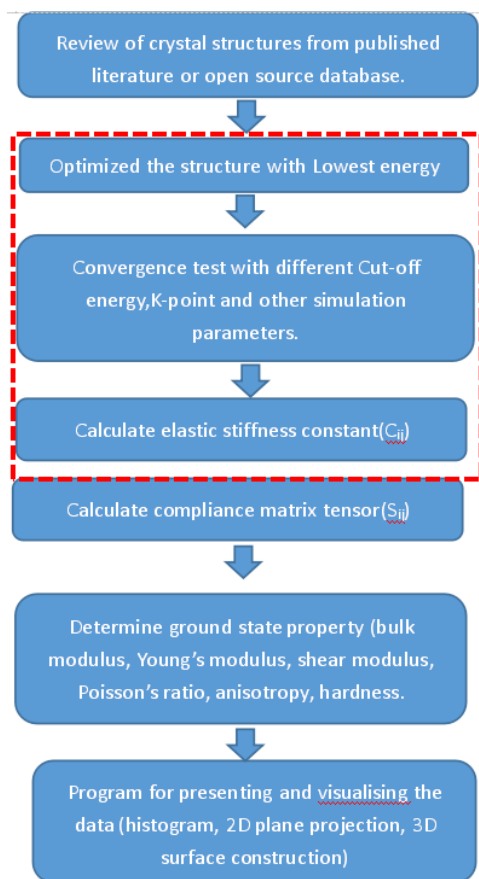
As shown in Figure 5.2.1, the main input is the crystal structure in the form of lattice parameter and the space group. One main step is determining the crystal geometry through energy convergence studies, i.e., identify the lattice parameter which gives the lowest energy. Based on the optimized geometry, the elastic constants can be calculated. Other structure parameters such as X-

---

Ray powder diffraction, electrical band structures, Density of state can also be determined. Other parameters can also be calculated with the geometry optimisation including band structure, core level spectroscopy, density of states, electron density difference, electron localization function, electronic excitations, Optical properties, phonons, polarizability, Raman spectra, population analysis. These are not the main research focus of this work, but the data could provide a means to cross check the results where data is available. As shown in Figure 5.2.1, the data starts from a crystal structure building, and then after optimisation, it can be stored in a crystallographic database. The optimised crystal geometry can be used to calculate elastic stiffness constant, which can then be used to calculate the ground state property of the crystal.

Figure 5.2.2 shows the key procedures of dynamic molecular simulation, property calculation and data analysis. The first key procedure is building a crystal structure. Building a crystal structure in Materials Studio (version 2017) requires lattice parameter (cell size (a,b,c), cell angle ( $\alpha$ ,  $\beta$ ,  $\gamma$ ), space group) and atom information (atom name, atom position, atom number). The second key procedure is geometry optimisation which can optimise the cell size (positions of the atoms) by first principle calculation to determine the structure with the lowest energy. Density functional theory (DFT) was used in calculation. The Generalized gradient approximation (GGA) with Perdew-Burke-Ernzerhof function (PBE) was applied by the CASTEP code package. There are a few simulation parameters which will affect the accuracy of results. The cut-off energy and k-point have the greatest impact on energy convergence and accuracy of simulation results. So, a convergence test is required in which, the value for the cut-off energy and the k-point is changed until the energy of the system becomes stable. The third main procedure is elastic constant ( $C_{ij}$ ) calculation by CASTEP. These steps are performed in Materials Studio CASTEP. A Python program has been developed to calculate elastic stiffness constant ( $S_{ij}$ ), and determine ground state properties (bulk modulus, Young's modulus, shear modulus, Poisson's ratio, anisotropy, hardness). Python program is also used to construct the surface plots of key

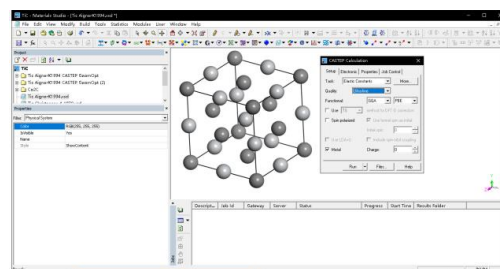
properties and the anisotropy parameter as shown in Figure 5.5.2. The details of the calculation and use of the program is to be presented in the sections 5.3-5.4 together with typical results.



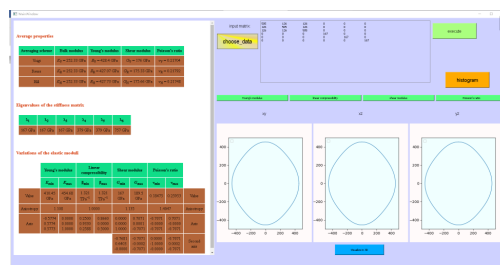
(a) Flow chart of ground state calculation



(b) Open sourced crystal database



(c) Materials Studio interface



(d) Interface of ground state property calculation and data Visualisation

**Figure 5.2.2** Flow chart show Data and key procedure of molecular dynamic simulation data analysis/ property calculation.

---

## 5.3 Calculation of anisotropic parameters and monocarbides

The ground state structural, mechanical property data of different carbides (e.g., TiC, VC and NbC) are important for material development and processing. Carbides are widely used in key engineering ceramics and manufacturing tools. Carbides also exist as secondary particles in steels, the structure, and properties of which may affect the stiffness, strength, hardness, toughness as well as the grain structures and manufacturability of the material. This is particularly relevant for materials with complex alloying systems such as stainless steels and welded structures (Guo et al., 2016). An in-depth understanding of the crystal structures, the mechanical and physical properties of these phases is important for the prediction of their deformation and performance in service. Detailed data of these high melting point phases are also relevant to other processes such as nucleation and growth of metallic phases as well as other complex carbides (e.g., Ferrite, Austenite, M7C3) (Montanari and Varone, 2019; Yu et al., 2016; Xiong et al., 2018).

In this section, first principle calculation is used to establish systematic data of three typical cubic binary monocarbides (TiC, VC and NbC). The key elastic constants are obtained from the first principle calculation. The bulk modulus, Young's modulus, shear modulus, and Poisson's ratio are determined from the Voigt-Reuss-Hill approximation method and compared with other published data. The micro-Vickers hardness is also predicted and compared to published data. The anisotropy in elastic properties of the carbides is studied through calculating the universal elastic anisotropic index, percentage anisotropy in compressibility and shear as well as the shear anisotropic factors on the specific crystal planes. A Python-based program is developed and used to integrate first principle calculation (using Materials Studio CASTEP) and data processing to establish the elastic properties in 3D space and projection on key crystal planes. The plane projection of the elastic

properties on the (001) plane based on the maximum, minimum and averaged values approaches is used to present and compare the anisotropy feature of the carbides. The data for E, G and Poisson's ratio is comparatively analysed and discussed, and future direction in developing systematic data through physical modelling is discussed.

### 5.3.1 Computational Method and data integration

Figure 5.3.1 shows the crystal structures of carbides TiC, VC and NbC. TiC is a binary carbide of group VI metal, while the VC and NbC are binary carbides of Group V metal. These carbides are widely used in making key engineering ceramics. In addition, as secondary phases, their structures and properties are also critical for high alloy steels and welded structures. It affects the strength, hardness, and thermal stability, as well as the microstructures (e.g., the nucleation of ferrite/austenite). These carbides were also reported to have refinement functions on other more complex multicomponent carbides systems such as  $M(\text{Fe,Cr})_7\text{C}_3$  carbides (Liu et al., 2017; Buytoz, 2006). All these three carbides follow a cubic structure. The carbide for Ti has only one main form (TiC) while Niobium and Vanadium may form carbide of different formulas and compositions (NBC and  $\text{Nb}_2\text{C}$  for Nb;  $\text{V}_8\text{C}_7$ ,  $\text{V}_6\text{C}_5$ ,  $\text{V}_4\text{C}_3$ ,  $\text{V}_5\text{C}_3$ ,  $\text{V}_2\text{C}$  for V) (Wu, 2013; Hamblyn and Reuben, 1975). The results presented in this paper are focused on data for the simple form of the carbides and anisotropy in the elastic properties analysed through the general anisotropy index and directional anisotropy through 3D surface configuration and plane projections.

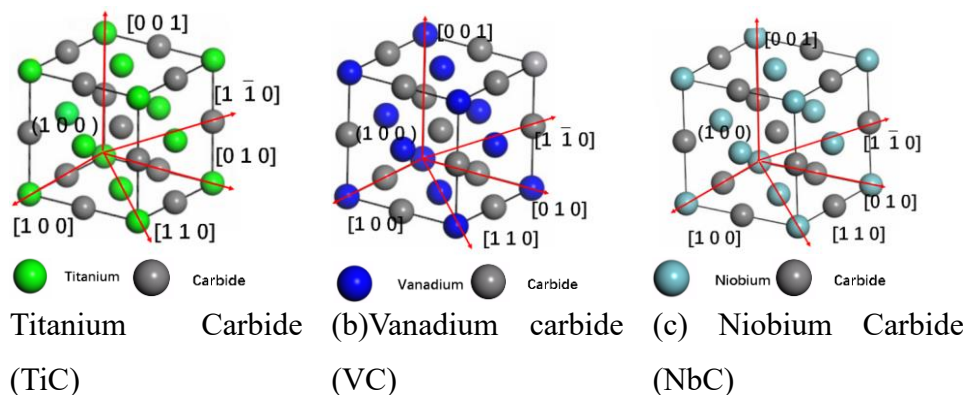
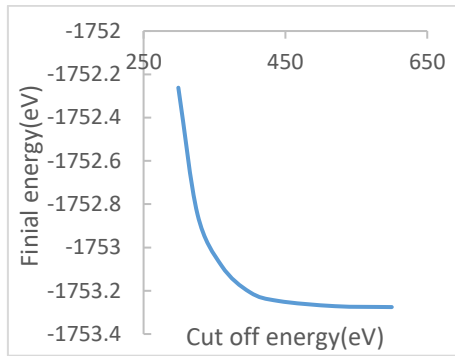
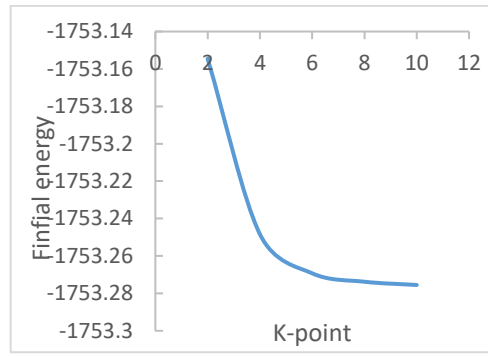


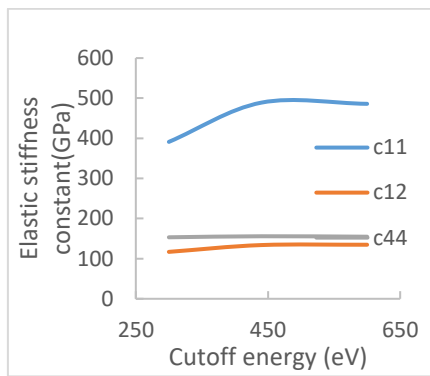
**Figure 5.3.1** The crystal structure of TiC, VC and NbC(Edstrom.D et al 2018; Cuppari and santos, 2016)



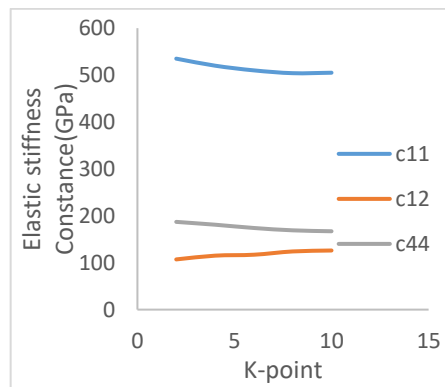
(a) Change of final energy with increasing cut-off energy.



(b) Change of final energy with increasing K point values.



(c) Change of elastic stiffness constant with increasing cut-off energy.



(d) Change of elastic stiffness constant with increasing K point values.

**Figure 5.3.2** Effects of the cut-off energy and K-point on final energy and elastic stiffness constants of Titanium carbide. (lattice parameter  $4.35 \times 4.35 \times 4.35$ , Space group: Fm-3m)

During the geometry optimisation process, the effect of the cut-off energy and the K-Monkhorst Pack grid (k-point) are important, which affects the accuracy and the calculation efficiency. The cut-off energy is the plane wave representing how much energy is taken after the plane wave is unfolded. The cut-off energy is the energy that separates the valence state electrons from the core (core state) electrons in the calculation of the pseudopotential. The purpose of the pseudopotential is to get a potential to best describe its behaviour on valence electrons, so the valence state and the core state has an essential effect on the pseudopotential behaviour. K-points control the Brillouin zone sampling directly. You can either specify a grid, or a desired

---

separation between k-points. Cut-off energy is an important parameter which affects the time to convergence (Basiuk et al., 2013; Bigelow, 2019; Hu et al., 2017; Kitchin, 2012;). Figure 5.3.2 shows the typical data for the sensitivity of TiC. Figure 5.3.2a&b shows the effect of cut-off energy and the k point, respectively. Figure 5.3.2c shows the cut-off energy on the  $C_{ij}$  values. The best parameters are decided by the point over which the energy is not affected significantly. In this case, cut-off is selected as 520eV, and the K-point value is selected  $10*10*10$ . The same convergence procedure has been applied to all the crystals studied.

Figure 5.3.3 shows the data flow and main works integrating the calculation in Materials Studio CASTEP, ground state property estimation and anisotropy analysis. As shown in Figure 5.2.1, the main functions in the Materials Studio for calculating the mechanical properties is the geometry optimisation and elastic constants prediction, this procedure can optimise the cell size (Lattice parameters) by identifying a stable structure with lower total energy. The Generalized gradient approximation (GGA) with Perdew-Burke-Ernzerhof function (PBE) was applied by the CASTEP code package. The main data output from the process is the lattice parameters including the lattice constants and the angles. Then the elastic stiffness constants are determined and output in a matrix form. As shown in Figure 5.3.3, in the second stage, a Python program is developed to calculate the compliance tensors ( $S_{ij}$ ), which is the derivative of strain with respect to stress. Then the ground state elastic properties are calculated based on the Voigt–Reuss–Hill (VRH) equations (Bao et al., 2019). The theoretical hardness of the carbides is also determined from the bulk and shear modulus. The general anisotropic index of the crystal is calculated, which represents the difference in the values of K, G and E. The data is a generalised property without considering the actual anisotropy at different directions. In the third part, a more complex program and data analysis is performed to plot the elastic properties in spherical coordinates to visualise the data of K, G, E and  $\nu$  in 3D, which provides a mean to analyse the directional anisotropy in E, G and Poisson’s ratio and their projections on key crystal planes. This provides a more detailed way to quantify and

---

visualise the anisotropy in different elastic properties.

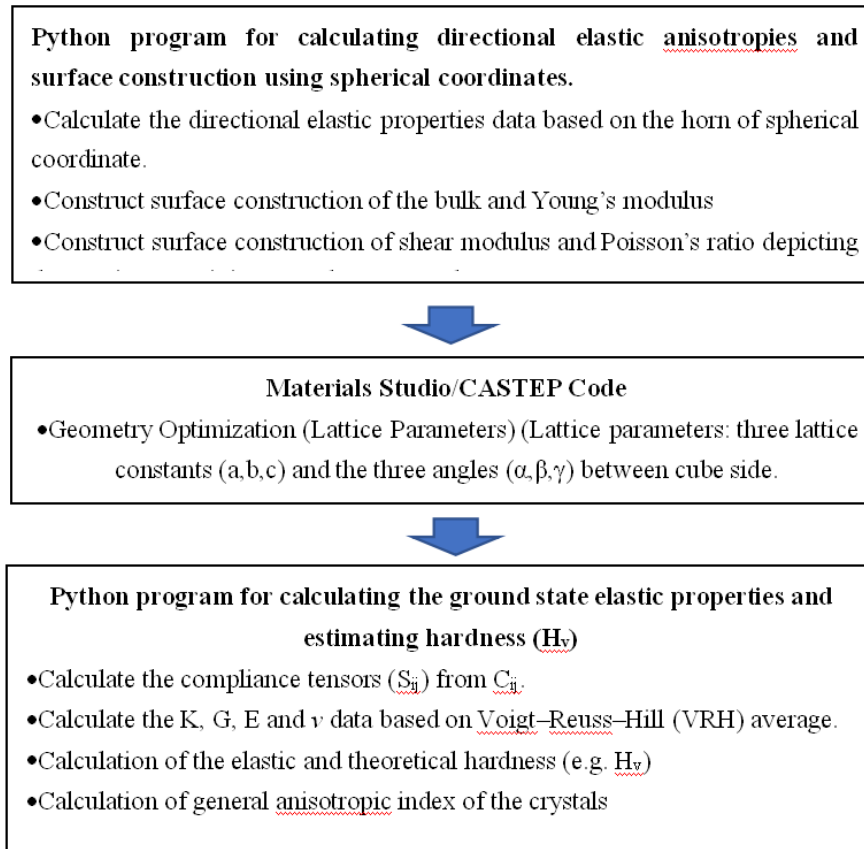


**Figure 5.3.3** Main programs integrating Materials Studio data, property and anisotropy analysis.

### 5.3.2 Elastic constants and ground elastic properties

The elastic constant and structures optimisation were performed in Materials Studio. The generalized gradient approximation (GGA) with Perdew-Burke-Ernzerhof function (PBE) was applied by the CASTEP code package (Bao et al., 2019; Wang et al., 2018; Liu et al., 2017). The key calculation parameters (e.g., the cut-off energy and the k-points) were selected based on systematic convergence analysis. In the test, the cut-off energy and the k-points values were systematically changed until the variation of the energy becomes negligible. The final cut-off energy used is 520V. The SCF tolerance was set as  $1e^{-6}$  eV/atom, and for the Brillouin-zone sampling, Monkhorst-Pack mesh was set as 10x10x10 k-points. One key output data used to calculate the ground state elastic properties are the elastic constants from CASTEP. It involves calculating stress strain response of the crystal under several different strain patterns based on Hooke's law. Due to symmetry of a cubic crystal, the related elastic constants can be expressed as in Equation (1)

$$\begin{pmatrix} \sigma_1 \\ \sigma_2 \\ \sigma_3 \\ \tau_4 \\ \tau_5 \\ \tau_6 \end{pmatrix} = \begin{pmatrix} C_{11} & C_{12} & C_{12} & & & \\ C_{11} & C_{11} & C_{12} & & & \\ C_{12} & C_{12} & C_{11} & & & \\ & & & C_{44} & & \\ & & & & C_{44} & \\ & & & & & C_{44} \end{pmatrix} \begin{pmatrix} \varepsilon_1 \\ \varepsilon_2 \\ \varepsilon_3 \\ \gamma_4 \\ \gamma_5 \\ \gamma_6 \end{pmatrix} \quad (5.1)$$

The relationship ( $\sigma_i = C_{ij} \varepsilon_j$ ) is for small stresses. Where  $\sigma$  is the normal stress,  $\tau$  is the shear stress,  $\varepsilon$  is the normal strain,  $\gamma$  is the shear strain. The elastic properties of solid material are calculated from stiffness constant  $C_{ij}$  (obtained from the first principle calculation) and elastic Compliance Constants  $S_{ij}$  (Nye, 1985). The compliance constants  $S_{ij}$  can be determined as the inverse matrix of the elastic stiffness matrix  $C_{ij}$  ( $[S_{ij}] = [C_{ij}]^{-1}$ ). As for simple cubic lattice symmetry, there are three independent variables in  $[C_{ij}]$  and  $[S_{ij}]$ , " $C_{11} C_{12}, C_{44}$ " and " $S_{11}, S_{12}, S_{44}$ ", respectively. The Voigt-Reuss-Hill (VRH) approximation is an effective way of converting anisotropic single-crystal elastic constants into effective isotropic (polycrystalline) elastic moduli (Chung et al., 1968). The Voigt approach sets the upper bound, the

---

Reuss approach sets the lower bound of the elastic properties while the Hill values takes the average between the Voigt and Reuss predictions (Voigt, 1928; Hill, 1952; Reuss, 1929). The approach provides a mean to calculate the average properties, the calculation also produces data showing potential difference in properties through comparing the upper and lower limit of the material's properties. Details of the theoretical background can be found in [7-9]. The bulk modulus can be calculated from the elastic constants  $C_{ij}$  as:

$$K_V = 2(C_{11} + C_{12} + \frac{C_{33}}{2} + 2C_{12})/9 \quad (5.2)$$

$$K_R = 1/[(S_{11} + S_{22} + S_{33}) - 2(S_{12} + S_{23} + S_{31})] \quad (5.3)$$

$$K_H = (K_V + K_R)/2 \quad (5.4)$$

The effective shear modulus can be written as:

$$G_V = [(C_{11} + C_{22} + C_{33}) - (C_{12} + C_{23} + C_{31}) + 3(C_{44} + C_{55} + C_{66})]/15 \quad (5.5)$$

$$G_R = 15/[4(S_{11} + S_{22} + S_{33}) - 4(S_{12} + S_{23} + S_{31}) + 3(S_{44} + S_{55} + S_{66})] \quad (5.6)$$

$$G_H = (G_V + G_R)/2 \quad (5.7)$$

The most common equation to estimate the Young's Modulus was based on the Hill bulk modulus (K) and shear modulus (G) with the following equation:

$$E_H = 9K_H G_H / (3K_H + G_H) \quad (5.8)$$

The effective Poisson's ratio of the crystal can be obtained from bulk modulus and shear modulus. When the Hill model is used, it can be written as:

$$\nu_H = (3K_H - 2G_H) / (6K_H + 2G_H) \quad (5.9)$$

The Vickers hardness can be calculated following the formula for theoretical hardness prediction from the bulk modulus (K) and shear modulus (G):

Tian's Model (Tian et al., 2012):

$$H_v = 0.92 \left(\frac{G}{K}\right)^{1.137} G^{0.708} \quad (5.10)$$

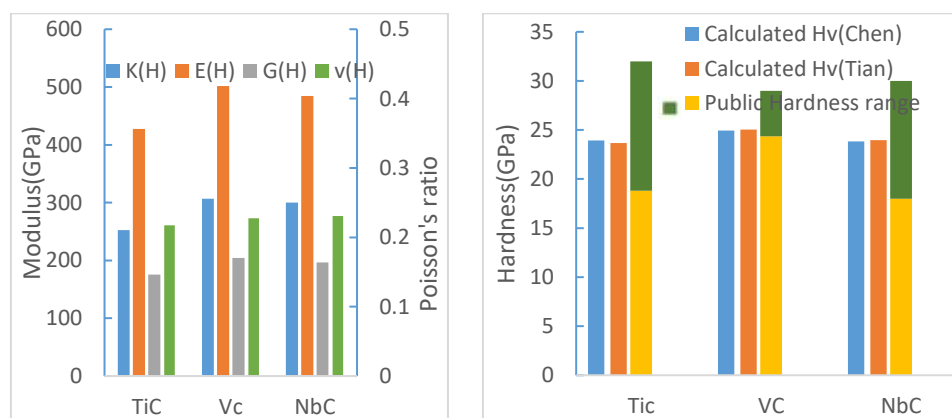
Chen's Model (Chen et al., 2011):

$$H_v = 2 \left(\frac{G^3}{K^2}\right)^{0.585} - 3 \quad (5.11)$$

Table 5.3.1 Calculated values of bulk modulus (K). Young's modulus (E), shear modulus(G), Poisson's ratio( $\nu$ ) based on the Reuss, Voigt and Hill models. (the Unit for K, E, G is GPa)

	K(H)	K(V)	K(R)	E(H)	E(V)	E(R)	G(H)	G(V)	G(R)	$\nu(H)$	$\nu(V)$	$\nu(R)$
TiC	252	252	252	427	428	427	175	176	175	0.217	0.217	0.217
VC	306	306	306	501	504	498	204	205	203	0.227	0.226	0.228
NbC	300	300	300	484	493	476	197	201	192	0.23	0.226	0.235

Table 5.3.1 lists the key values for K, G, E and Poisson's ratio( $\nu$ ) based on the Voigt–Reuss–Hill (VRH) models (Equations 5.2-5.9). The averaged values (Hill model) are comparable to published works (Gilman et al., 1961; Kim et al., 2012; Liu et al., 2008; Wang et al., 2013; Sun et al., 2010; Brown et al., 1966; Brenton et al., 1969; Gao et al., 2014). As shown in the data, the bulk modulus of the crystals determined by the Voigt, Reuss and Hill method are identical, the VC and NbC has much higher compressibility than TiC based on the values of K. The E(V) and E(R) is slightly different for TiC and VC, but there is a clear difference in the Young's modulus of NbC, the Voigt model gives a value of 493GPa and the Reuss model gives a much lower value of 476 GPa. There is limited difference between the data for the shear modulus between the upper (G(V)) and lower bounds (G(R)) for each of the carbides. The calculated values for the Poisson's ratio ( $\nu(V)$ ,  $\nu(R)$ ,  $\nu(H)$ ) are also similar for each material.



(a) Comparison between the predicted ground state elastic properties (B, E, G,  $\nu$ ) of the carbides. K, E, G uses the left axis and Poisson's ratio uses the right axis (b) Comparison between the predicted and published Vickers hardness data of the carbides. The minimum hardness shows on the yellow bar and the maximum hardness shows on green value.

**Figure 5.3.4** Predicted elastic properties and Vickers hardness of the carbides.

---

Figure 5.3.4a presents the calculated bulk modulus, Young's modulus, shear modulus and Poisson's ratio (average values based on the Hill model). The E and G values for VC are slightly higher than those for NbC and TiC. The bulk modulus of NbC is comparable to that of VC, both are higher than the K value of TiC. The Poisson's ratios for the carbides are all comparable between the model calculations with the  $\nu(H)$  being slightly higher. The predicted data of the modulus shows a good agreement with the published experimental and other theoretical data, for example, TiC (Gilman et al., 1961; Kim et al., 2012; Török et al., 1987); VC (Liu et al., 2008; Sun et al., 2010). NbC (Brown et al., 1966; Brenton et al., 1969; Gao et al 2014). Other data sources used included Matweb (<http://www.matweb.com/>) and CRC Materials Science and Engineering Handbook. The Reuss, Voigt and Hill data also provide a means to estimate the hardness (equations 5.10 & 5.11) from the bulk and shear moduli. The data for these carbides is shown in Figure 5.3.4b together with the range of published data. The different colour (yellow and green) represents the maximum and minimum among the reported values over different sources. It illustrates that, the predicted Vickers hardness values from both models are close to the average of published data based on a mix of reference including material data base (e.g., Yang et al., 2009; Edström et al., 2008).

### Anisotropy in the ground state elastic properties

For ceramics, the anisotropy in elastic properties can influence the formation and propagation of micro cracks and reduce the mechanical durability. The hardness and wear resistance are also related to the anisotropy of the crystal (Ren et al., 2002). The anisotropy in crystals is normally represented by anisotropy indexes such as the universal elastic anisotropic index ( $A_U$ ) (Ranganathan and Ostoja-Starzewski, 2008), percentage anisotropy in compressibility and shear ( $A_{comp}$  and  $A_{shear}$ ) (Chung et al., 1968), and the shear anisotropic factors on the (100), (010), and (001) planes ( $A_1$ ,  $A_2$  and  $A_3$ ) of cubic crystals (Ravindran et al., 1998; Liu et al., 2019). The equations are:

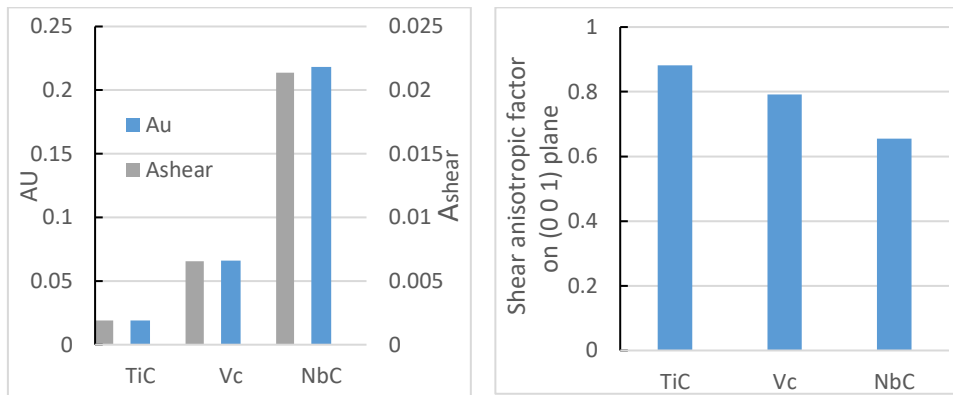
$$A_U = 5AG_V/G_R + K_V/K_R - 6 \quad (5.12)$$

$$A_{Comp} = (K_V - K_R)/(K_V + K_R) \quad (5.13)$$

$$A_{shear} = (G_V - G_R)/(G_V + G_R) \quad (5.14)$$

$$\text{For cubic structure, } A_1=A_2=A_3=A_1 = 4C_{44}/(C_{11} + C_{33} - 2C_{13}) \quad (5.15)$$

For an elastically isotropic solid,  $A_U=A_{Shear}=0$ ;  $A_1=1$ . Larger values for  $A_U$  and  $(1-A)$  indicates more elastic anisotropy.



(a) Universal elastic anisotropic index and percentage anisotropy in shear of the carbides. (b) Shear anisotropic factor on the (0 0 1) plane of the carbides

**Figure 5.3.5** Anisotropy index data of the carbides.

Figures 5.3.5a&b plot the universal elastic anisotropic index ( $A_U$ ), and percentage anisotropy in shear ( $A_{shear}$ ). It is clearly shown that the  $A_U$  for TiC and VC is relatively low with TiC (0.01) and VC (0.066), both are close to isotropic conditions, but NbC has a higher  $A_U$  value of 0.21. The values for

---

$A_{\text{Shear}}$  of the three carbides are all very low with TiC (0.001), VC (0.006) and NbC (0.021). The shear anisotropic factors on the (001) plane is represented by the  $A_1$  values (Figure 5.3.5d). The values are lower than 1 for all the carbides, indicating anisotropic characteristics on the (001) plane. The  $A_1$  value for TiC is closer to 1, suggesting low anisotropy, VC, NbC shows a much stronger anisotropy with  $A_1$  value of about 0.8 and 0.65, respectively. The data shows that the percentage anisotropy in shear ( $A_{\text{Shear}}$ ) seems to be a clearer indicator for anisotropy for the carbides. Both  $A_U$  and  $A_{\text{Shear}}$  are generalised values, data for directional anisotropy is required to establish more detailed data and present the anisotropy in a better visualisable way for both materials research, development, teaching and training.

---

### 5.3.3 Directional anisotropy data of elastic properties based on 3D surface construction and plane projection

In order to establish and visualise anisotropy of elastic properties in further details, a python program is developed to calculate the 3D directional distribution of the E, G and Poisson's ratio in spherical coordinate system. The process involves calculating the directional dependence of K, E, G and  $\nu$  in spherical coordinate to establish the 3D surface construction (Liu et al., 2017). Details of the theory can be found in [Luan et al \(2018\)](#) and details of the implementation in Python can be found in section 5.4.2

In order to establish and visualise anisotropy of elastic properties in further details, a python program is developed to calculate the 3D directional distribution of the E, G and Poisson's ratio. In 3D coordinate system (Cartesian coordinate system), The corresponding elastically distortion can be represented by a point on unit sphere with two angles. The buck modulus and young's modulus can be described by the first unit sphere 'a' which is defined by angle  $\theta$  (0 to  $\pi$ ) and  $\phi$  (0 to  $2\pi$ ) (Figure 5.3.6a). The shear modulus and Poisson's ratio need second unit sphere 'b' which is perpendicular to unit sphere 'a' and it is defined by an angle  $\chi$  (0 to  $2\pi$ ). ([Marmier et al., 2010](#))

The first unit sphere can be written as:

$$a = \begin{pmatrix} l1 \\ l2 \\ l3 \end{pmatrix} \quad (5.16)$$

Where ' $l1$ ,  $l2$ , and  $l3$ ' denote the direction cosines with respect to the a, b, and c directions of the lattice. And the equation can be written as:

$$l1 = \sin \theta \cos \phi \quad (5.17)$$

$$l2 = \sin \theta \sin \phi \quad (5.18)$$

$$l3 = \cos \theta \quad (5.19)$$

spherical coordinate system (Figure 5.3.6).

The process involves calculating the directional dependence of K and E to establish the surface plot cubic crystals based on the following equations:

$$\frac{1}{B} = (S_{11} + 2S_{12}) * (l_1^2 + l_2^2 + l_3^2) \quad (5.20)$$

$$\frac{1}{E} = S_{11} - 2(S_{11} - S_{12} - S_{44})(l_1^2 l_2^2 + l_2^2 l_3^2 + l_1^2 l_3^2) \quad (5.21)$$

The second unit sphere can be written as:

$$b = \begin{pmatrix} \cos \theta \cos \varphi \cos \chi - \sin \theta \sin \chi \\ \cos \theta \sin \varphi \cos \chi + \cos \theta \sin \chi \\ -\sin \theta \cos \chi \end{pmatrix} \quad (5.22)$$

The process involves calculating the directional dependence of G and  $\nu$  to establish the surface plot cubic crystals based on the following equations:

$$G(\theta, \varphi, X) = \frac{1}{4S'_{66}(\theta, \varphi, X)} \quad (5.23)$$

$$\nu(\theta, \varphi, X) = \frac{S'_{12}(\theta, \varphi, X)}{S'_{11}(\theta, \varphi)} = -\frac{a_i a_j b_k b_l S_{ijkl}}{a_i a_j a_k a_l S_{ijkl}} \quad (5.24)$$

Where  $s'_{11}$ ,  $S'_{12}$  and  $S'_{66}$  are fourth order Components in the sub vectorial space.

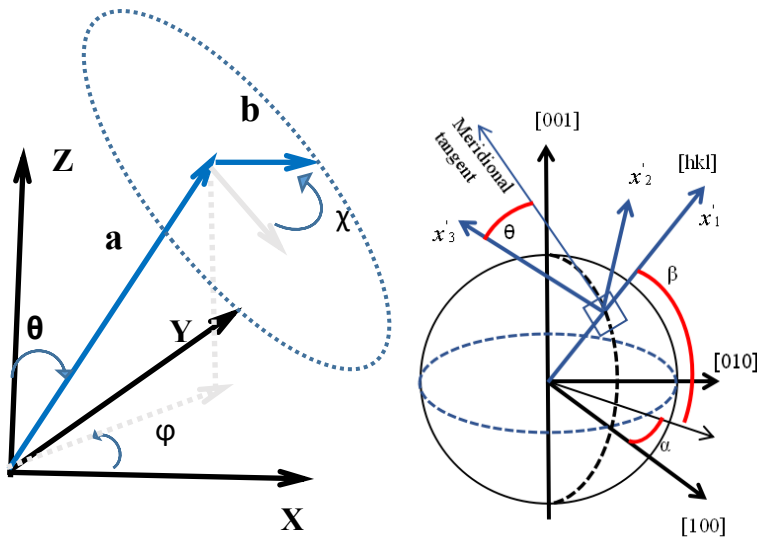
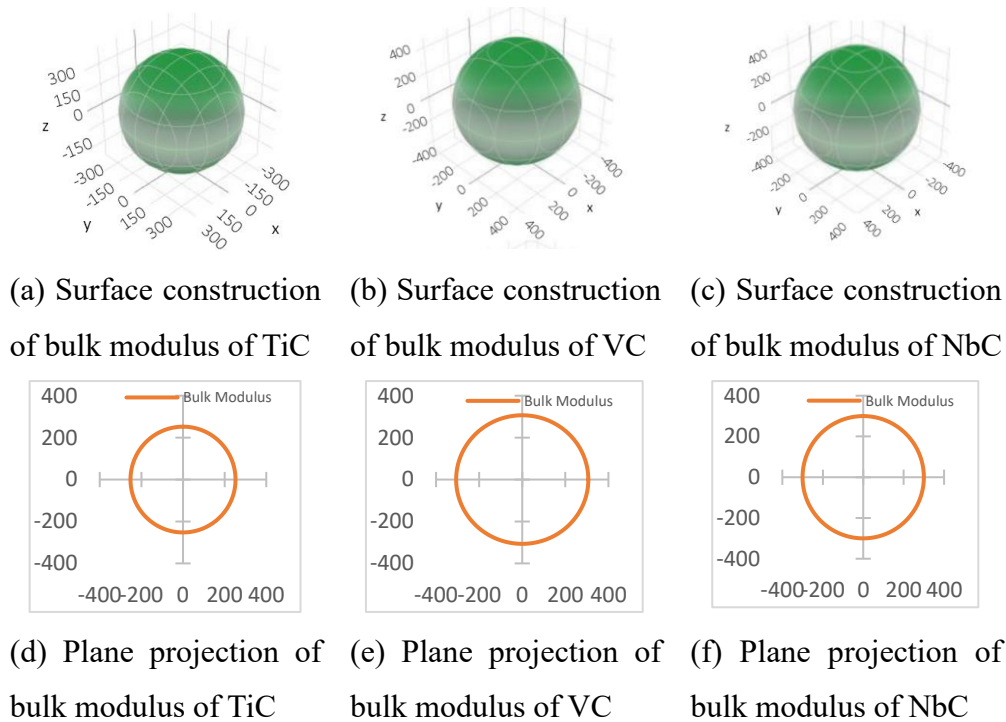


**Figure 5.3.6** Euler angles and geometrical reference frame. (adapted from Britton et al. 2016; Turley and Sines, 1971).

In general, an elastically isotropic solid has a spherical 3D surface construction of elastic parameter. A non-spherical 3D surface construction

indicates an elastically anisotropic solid. The more deviation the 3D surface construction from a sphere reflects a higher degree of elastic anisotropy is. (Bao et al, 2019). On a crystal plane (e.g. (001)), the degree of anisotropy can be represented by the closeness of the iso line to a circular shape. For cubic structure, the (001), (100) are identical anisotropy. So, the data on (001) is representative to the anisotropy feature including maximum and minimum values.

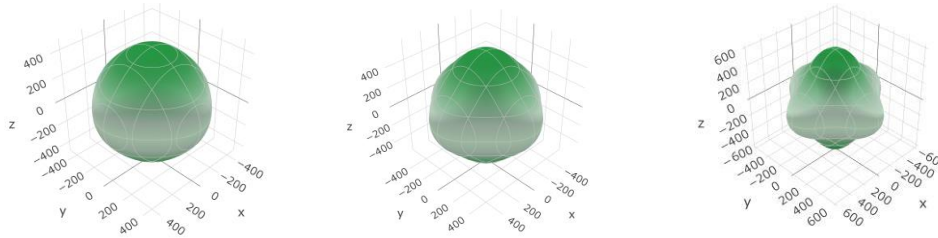
Figure 5.3.7 shows the surface construction and plane projection of the bulk moduli. For all the carbides, the surface plot of the bulk modulus is spherical, indicating isotropic distribution. This corresponds to the isotropic parameter of compression being '0' (Equation 5.13).



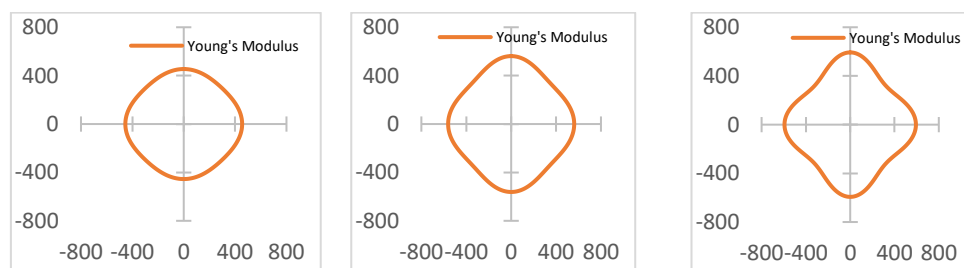
**Figure 5.3.7** Surface construction and plane projection of Bulk modulus of the carbides

Figure 5.3.8 shows 3D surface constructions of young's moduli for the carbides, which is the main indication of stiffness. The Young's Modulus of TiC has a near-spherical 3D graph, the projection on (100) is approximately circular indicating limited anisotropy. The Young's modulus for VC is deviated away more from near spherical, while the contour for NbC shows

significant anisotropy. The plane projection on (001) shows more clearly the directional anisotropy. The data indicate that TiC has limited anisotropy while NbC shows clear visible anisotropy with a high value at [110] direction.



(a) Surface construction of Young's modulus of TiC (b) Surface construction of Young's modulus of VC (c) Surface construction of Young's modulus of NbC

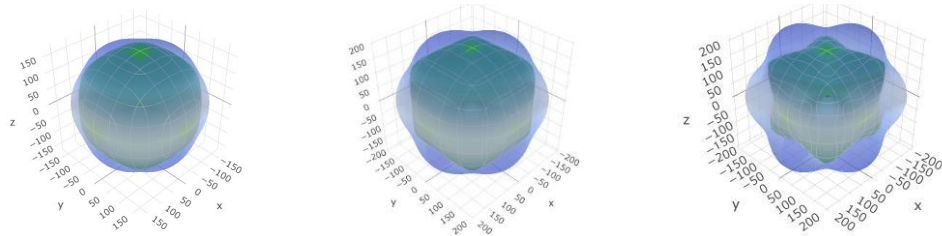


(d) Plane projection of Young's modulus of TiC (e) Plane projection of Young's modulus of VC (f) Plane projection of Young's modulus of NbC

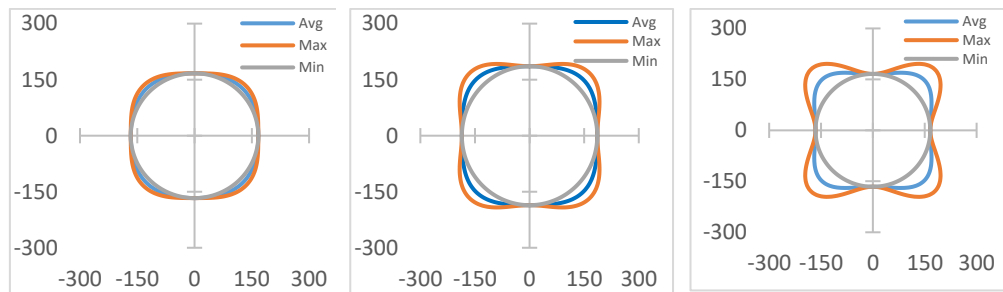
**Figure 5.3.8** Surface construction and plane projection of Young's modulus of the carbides

Figure 5.3.9 shows the 3D surface constructions and (100) plane projection of the shear moduli of TiC, VC and NbC. Different from the data for the Young's modulus in Figure 5.3.8, there are two surface plots (two sets of data), one is based on the maximum value (in Purple) and the other one is based on the minimum values (in green). This reflects the complex nature of the plane and direction of the shear modulus. The 3D construction of  $G$  for TiC is close to a spherical shape indicating isotropic, the surface for VC shows some increased anisotropy as the shape of the 3D surface has deviated from a perfect spherical shape. The shear modulus of NbC shows a stronger anisotropic, but the scale of anisotropic is not as significant as that for the Young's Modulus. The plane projections of shear modulus show the anisotropy more clearly as shown in Figures 5.3.9d&e&f based on the isolines

of the maximum values (in orange); minimum values (in grey line) and an iso line representing the average value (in blue). This approach could indicate more clearly the nature and scale of anisotropy. The iso lines on the plane projection show clearly that the higher G values are at the [110] direction.



(a)Surface construction of shear modulus of TiC (b)Surface construction of shear modulus of VC (c)Surface construction of shear modulus of NbC

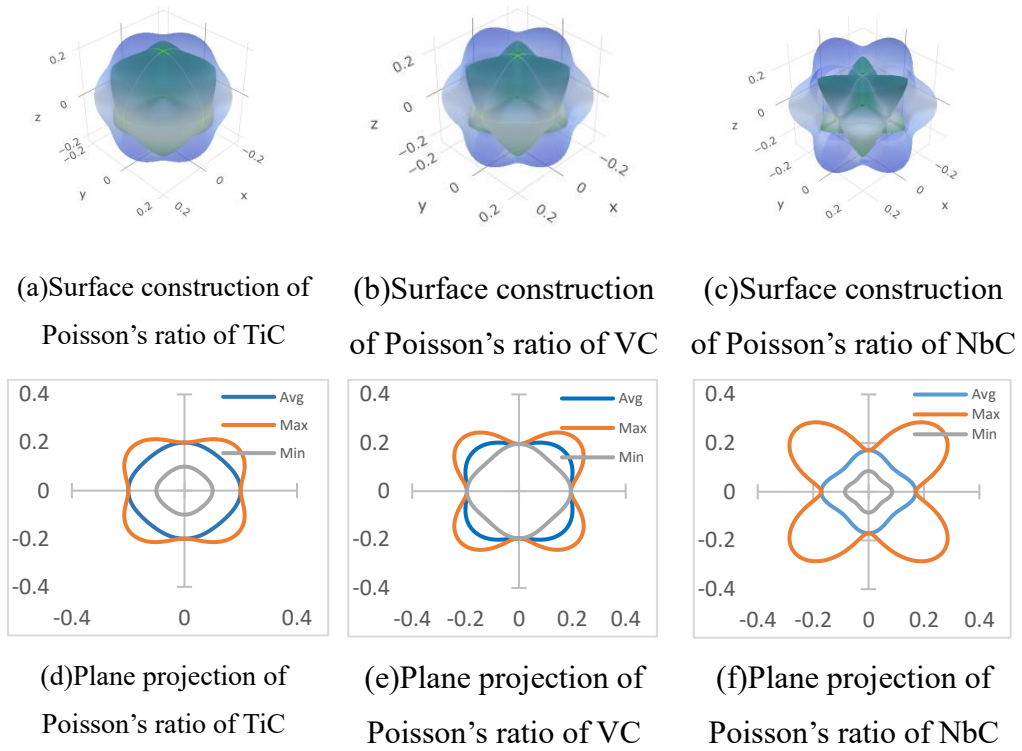


(d)Plane projection of shear modulus of TiC (e)Plane projection of shear modulus of VC (f)Plane projection of shear modulus of NbC

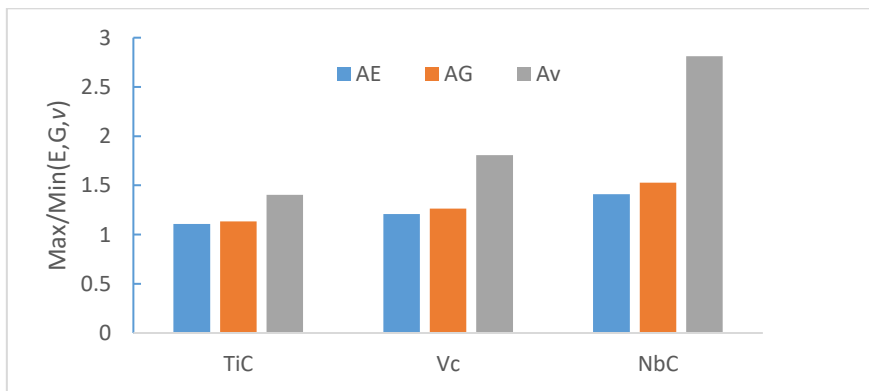
**Figure 5.3.9** Surface construction and plane projection of shear modulus of the carbides

Figure 5.3.10 shows 3D surface constructions and plane projection of Poisson’s ratio of TiC, VC and NbC. The same colour code and approach is used for presenting the anisotropy in the Poisson’s ratio. In general, all the three carbides showed clear anisotropy in the Poisson’s ratio, a much higher Poisson’s ratio exists in [110] direction.

Figure 5.3.11 shows the anisotropy of elastic property(E,G,v) based on the ratio between maximum and minimum property value. In TiC,VC and NbC, The anisotropy of Poisson’s ratio is greater than anisotropy of shear modulus and anisotropy of Young’s modulus. The Anisotropy of NbC is greater than is greater than VC and TiC.



**Figure 5.3.10** Surface construction and plane projection of Shear modulus of the carbides



**Figure 5.3.11** Anisotropy of elastic properties( $E, G, \nu$ ) based on the ratio between maximum and minimum property value (Max/Min).

---

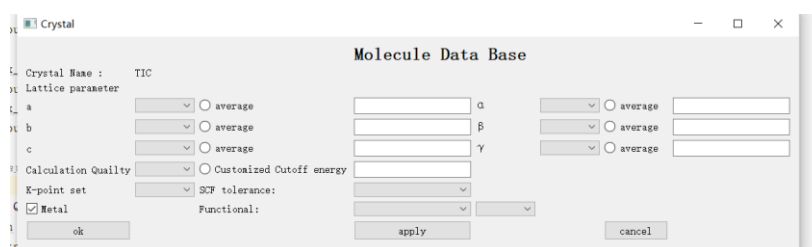
## 5.4 GUI for building crystal structure and systematic study of ground properties, anisotropy, Poisson's ratios of large number of carbides

### 5.4.1 Data for crystals structure

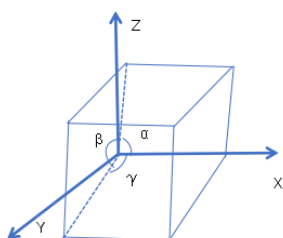
A GUI interface has been developed for processing the crystal structure input and analysing the data. This can be used as a tool to produce consistent crystal structures for visualisation and automatically generate files for Materials Studio studies. In addition, this also provides a tool to study large scale data through a consistent system. Data from different sources may have uncertainties, so it is important to process all the crystal data in the same procedure to avoid error when analysing the properties. For data from different sources, the program will run the energy optimisation, then store them in the database.

A visualisation of elastic anisotropy program combined with a visualized database (VAP) has been developed by Python. VAP has 2 modules: Database, and elastic anisotropy calculation. As shown in Figure 5.4.1, the database module can collect simulation files at working directory and displayed in Graphical User Interface. The crystal structure model builder allows the user to identify lattice parameters and generate a crystallographic Information File which can be used to submit in Materials Studio. The main data describing a crystal consists of the structural formula, each atom and its number and coordinates, space group coding, crystal system, cell angle (alpha, beta, gamma) (Figure 5.4.1b), number of atoms contained in the cell, cell size (a, b, c), cell volume (volume) and other information (Hall and McMahon, 2006). There are two standard crystallographic Information Files which are Cif and Xsd. .Cif file is composed of Crystal structure information, symmetry

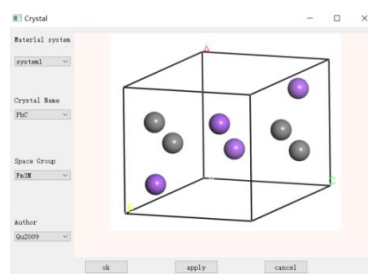
equation and Atomic parameter information. Symmetry equation is mainly describing the symmetrical position in the crystal and its coordinate information. The .xsd file is a Materials Studio standard file consisting of parameter type and crystal structure information. In this work, the input crystal data in the GUI was found from published data and open-source database (Crystallography Open Database, material project). In some cases, the lattice parameter may be slightly different between different sources. This crystal structure builder helped with generating consistent structure data through systematic geometry optimisation in the Materials Studio. This provided more reliable research data for establishing the link between properties.



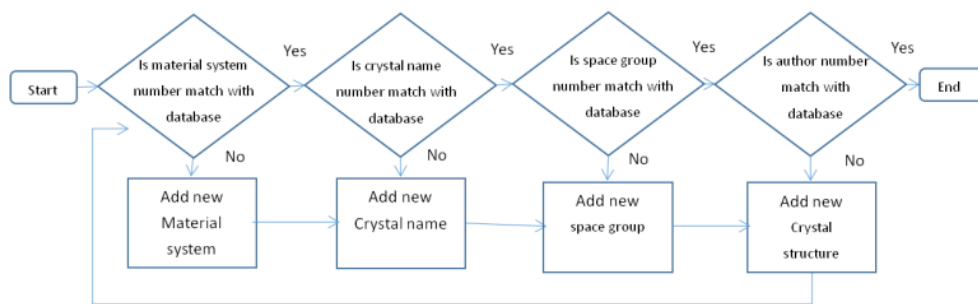
(a) GUI of Crystal structure model builder and optimisation (input: initial lattice parameter).



(b) Diagram showing the lattice parameters and the angles.



(c) Typical crystal structure data. (PbC)

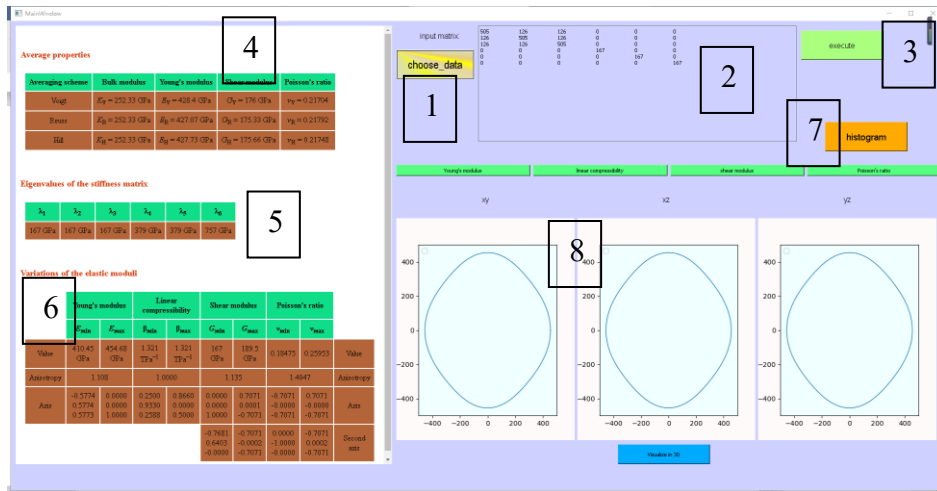


(d) Data flow of crystal structure Database.

Figure 5.4.1 GUI of crystallography and main data.

### 5.4.2 GUI for calculating ground state mechanical properties

Figure 5.4.2 shows the functions and structure of the main program for calculating /determining the K, E, G and Poisson's ratio and presentations in 3D surface and 2D plane projection.



(a) GUI of Elastic Anisotropy Calculation module



(b) GUI of Histogram

(c) 3D surface construction

Figure 5.4.2 GUI for property calculation and visualisation.

The program takes input, the elastic stiffness constants matrix ( $C_{ij}$ ) from Materials Studio through the input through a text file (1) or window (2). Then execute the calculations (3) (Equations 5.2 to 5.15). The program will automatically calculate the average properties (4), eigenvalues (5) and the key ground state material properties including maximum and minimum values for E, Linear compressibility, Shear modulus and Poisson's ratio including the anisotropy parameters. (6). The presentation includes histogram (7), 2D

---

plane projection (8) and 3D surface plot (9). The program is also able to present the 3D surface of the K, G, E and Poisson's ratio, in a similar way as shown in the previous section. In this section a Python GUI is developed to map the ground state properties of a larger number of carbides.

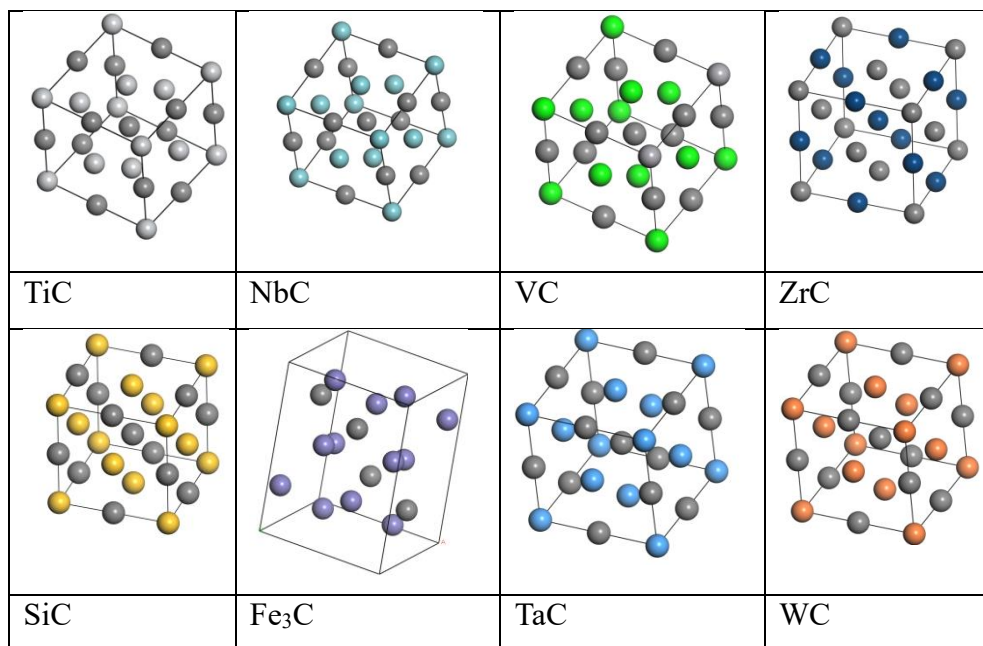
### 5.4.3 Typical materials (carbides) used, Poisson's ratio and anisotropy data analysis

Figure 5.4.3 shows typical crystal structures of selected carbides studied. These data have been cross compared with published data. Table 5.4.2 lists the space group of the crystals and the optimised lattice parameters. The data was compared to published data sources. All the structures have gone through energy convergence test in the same way as illustrated in the procedure for TiC (as previously illustrated in Figure 5.3.2). The lattice parameter was used as input in the first principle calculation to determine the  $C_{ij}$ , then the mechanical parameters (K, E, G and  $\nu$ ) were determined (following the same procedure as presented in section 5.3 for the monocarbides). The key analysis is focused on the Poisson's ratio and its anisotropy and correlation between the Poisson's ratio and other properties (e.g., G/K). The range of the Poisson's ratio is listed in Table 5.4.2. Figure 5.4.4 shows the variation in Poisson's ratio vs. universal anisotropy index ( $A_U$ ) of the carbide in comparison with Figure 5.4.4b which shows the published data of variation in Poisson's ratio versus  $A_U$  of other published data. The maximum and minimum Poisson's ratio data versus anisotropy shows a C shaped curve which has the same trend with published data. The data also identified a few compounds with negative Poisson's ratio value, which will be discussed in section 5.5 with reference to the mechanism of auxeticity.

**Table 5.4.2** Optimised lattice parameter used in the ground state property analysis.

Crystal Name	Space Group	a(Å)	b(Å)	c(Å)	$\nu$	$\nu$ range	Reference
TiC	Fm-3M	3.06	3.06	3.06	0.217	0.184 to 0.259	Edstrom.D et al 2018
NbC	Fm-3M	3.186	3.186	3.186	0.231	0.13 to 0.364	Cuppari and santos.2016

VC	Fm-3M	2.943	2.943	2.943	0.227	0.168 to 0.304	Edstrom.D et al 2018
ZrC	Fm-3M	3.341	3.341	3.341	0.209	0.171 to 0.258	Fu et al., 2009
TaC	Fm-3M	3.169	3.169	3.169	0.228	0.114 to 0.384	López-de-la-Torre et al.,2005
WC	Fm3m	3.105	3.105	3.105	0.315	0.126 to 0.559	Wereszcza 2007
Be <sub>2</sub> C	Fm-3M	4.33	4.33	4.33	0.085	0.027 to 0.179	Joshi KB H, 2016
SiC	Fm3M	2.87	2.87	2.87	0.206	0.154 to 0.263	Belgacem. B et al., 2014
Fe <sub>3</sub> C	Pmnn	4.49	5.03	6.73	0.338	-0.265 to 0.985	Jiang et al., 2008
Mo <sub>2</sub> C	P63/mmc	4.73	6.02	5.22	0.274	0.137 to 0.432	Liu et al., 2015
Ni <sub>3</sub> C	R <sub>3</sub> C	5.05	5.05	5.05	0.347	0.114 to 0.599	Kelling et al., 2017



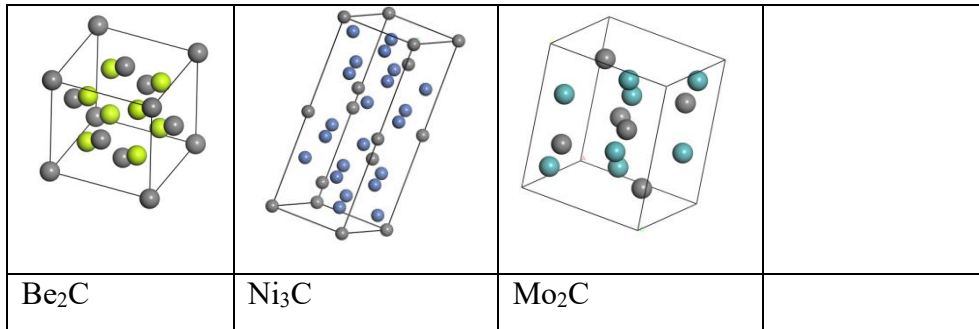
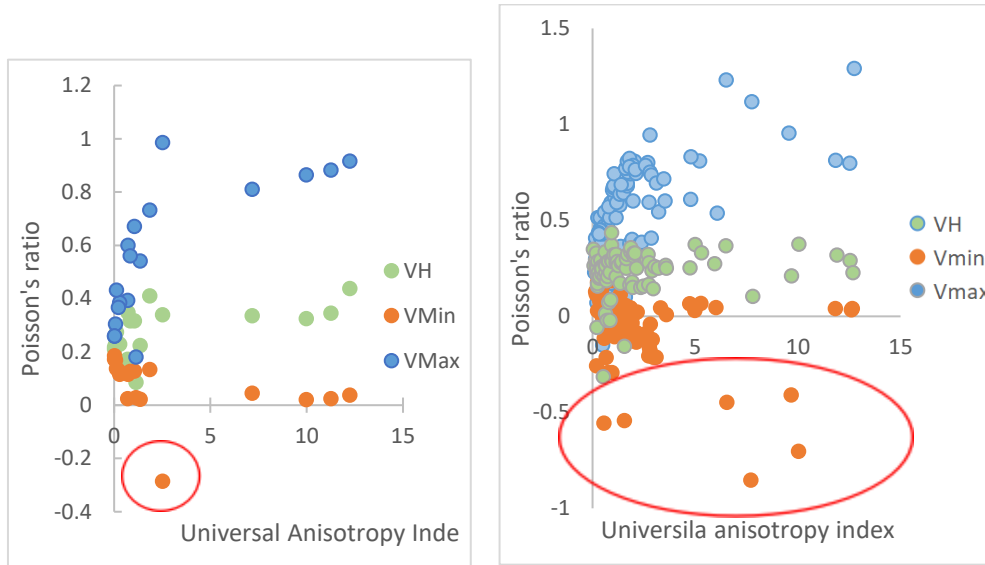


**Figure 5.4.3** Typical crystal structures of selected carbides studied.



(a) Poisson's ratio vs. Universal anisotropy index. (this work). green point is Hill's Poisson's ratio; orange point is minimum Poisson's ratio; blue point is maximum Poisson's ratio.

(b) Poisson's ratio vs. Universal anisotropy index. (Published data) (Healy et al., 2019).

**Figure 5.4.4** Variation in Poisson's ratio versus universal anisotropy index.

---

## 5.5 Discussion

### 5.5.1. Correlation between the Poisson's ratio and other properties.

This chapter is focusing on developing data for studying the relationship between crystal structures and key (ground state/theoretical) properties of crystals based on first principle calculation with Materials Studios. The properties predicted of TiC, NbC and VC showed a good agreement with other published data. The hardness predicted also agrees with some key references. The overall trend of the relationship between the maximum and minimum of the carbides exhibits a reasonable trend with another data-based research. This suggest that the framework used here is accurate and effective. The framework can be used in systematically developing data for materials systems such as stainless steels and weld hard facing to map out the key ground state properties of the carbides and other materials. It can also be used to analyse the effect of factors such as temperatures on the properties of carbides. Some typical results will be presented in the next section.

The Poisson's ratio of a crystal may be affected by many factors ([Ghosh, 2015](#)) which is more complicated for porous materials at macro scales. For cellular materials as shown in Chapter4, the Poisson's ratio is affected by the overall structure and the properties of the beams/cell walls. For crystals, the interaction between the atom is complicated. It is widely regarded that the average Poisson's ratio is correlated with the ratio between the bulk modulus and shear modulus.

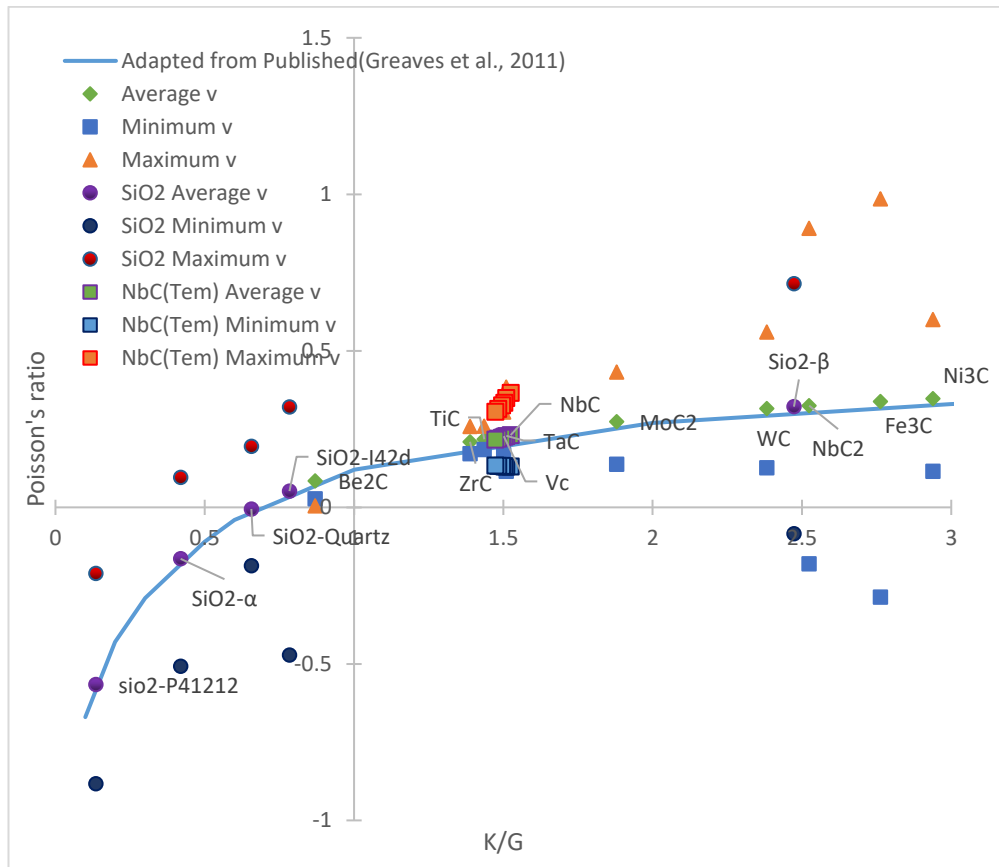


**Figure 5.5.1** Correlation between the Poisson's ratio and K/G and maximum and minimum Poisson's ratio. (Yeganeh-Haeri et al.,1992)

Figure 5.5.1 plots the Poisson's ratio of the carbides together with other compounds including SiO<sub>2</sub> of different space groups, which is known to have auxetic behaviours (Yeganeh-Haeri et al.,1992). Also plotted are the data for BaTiO<sub>3</sub>, which has also been reported to have auxetic behaviours at certain temperature ranges (Lake, 2017). Also plotted in the figure 5.5.1 is the Poisson's ratio vs K/G curve depicted from a published work (Greave, 2012), which is based on the generalised equation  $\nu_H = (3K_H - 2G_H)/(6K_H + 2G_H)$ . As shown in the figure 5.5.1, the average Poisson's ratio data followed the theoretical  $\nu$  vs /G curve in both the domain with Positive Poisson's ratio and the domain with negative Poisson's ratios curves. The Poisson's ratio gradually increases when the K/G is over 1. when the /G is less than one, the Poisson's ratio changes with K/G rapidly. In addition, when K/G is lower than 1, the minimum Poisson's ratio is either very low or in the negative range.

---

The average data of the Poisson's ratio reflects that the Poisson's ratio is associated with K/G ratio. However, when consider the maximum and minimum values, the correlation is less strong/clear. There is clear scatter when K/G is around 2.7. Future work is required to link these to the more detailed electronic and other properties. Several compounds have a positive Poisson's ratio overall, but the minimum values are in the negative range. This has been predicted by [Lake \(2017\)](#). The data for BaTiO<sub>3</sub> is also included, which is one of the most extensively studied ferroelectric materials. On cooling, it undergoes successive structural phase transitions with its symmetry changing from cubic (Pm3m) to tetragonal (P4mm), then to orthorhombic (Amm2) and finally to rhombohedral (R3m) ([Li et al., 1994](#)). The negative Poisson's has been reported including a recent materials discovery project ([Dagdelen et al., 2017](#)). The Poisson's ratio range of the compounds with negative Poisson's ratio is relative narrow such as SiO<sub>2</sub>. The Be<sub>2</sub>C also shown to have a potential structure with negative Poisson's ratio. The minimum value is clearly in the negative range. Interestingly, a recent work by [Qian et al \(2018\)](#) shows that Two-Dimensional Be<sub>2</sub>C has a negative Poisson's Ratio. These data suggest that the ratio between the K/G could be used to explore auxetic effect. The ground state of a quantum-mechanical system is its lowest-energy state; the energy of the ground state is known as the zero-point energy of the system. Most of the data are calculated at 0K which is a condition mostly used ([Haj Hassan and Akbarzadeh, 2006](#)). The data for TiC, VC and NbC at different temperatures (273K to 800K) also shows that the data at high temperatures also in general follow the general relationship between Poisson's ratio and the ratio between the bulk and shear modulus. The temperature effect is an important issue, and some detailed data from this work and some published experimental and simulation data are presented in the next section.

---

### 5.5.2 Effect of temperature on the Poisson's ratio and anisotropy data of simple monocarbides.

The effect of temperature on the ground state properties and the anisotropy is an important ([Hao et al., 2015](#)). The properties at different temperatures (273K-800K) were focused on three simple monocarbides: TiC, VC and NbC. The basic procedure by material studio CASTEP Module is similar to the procedure detailed in section 5.3. But the calculation was performed in the dynamic module in Materials Studio ([Material studio 2017 user manual](#)). The process is much more consuming on computation resources, about 10 times longer than ground state simulation at 0K. The main change of elastic property at different temperatures is caused by lattice parameter change (Volume change) ([Liu, 2018](#); [Wang et al., 2013](#)). The structures with different temperatures are to calculate the elastic stiffness constant ( $C_{ij}$ ) by Elastic constant calculation in CASTEP, then bulk Modulus, Young's Modulus, Shear Modulus, Poisson's ratio, and the anisotropy was calculated following the procedures in section 5.3. The details of the procedure are not repeated here, the key data presented and discussed in comparison with other published calculation and experimental data ([Muchiri, 2019](#)).

The data for high temperature for TiC and VC are available for comparison ([Chong et al., 2016](#); [Dang et al., 2014](#)). Only limited simulation is conducted. As evaluation of the procedure is one key part of the work, both the elastic constant and properties are compared between results from this work and published data where available.

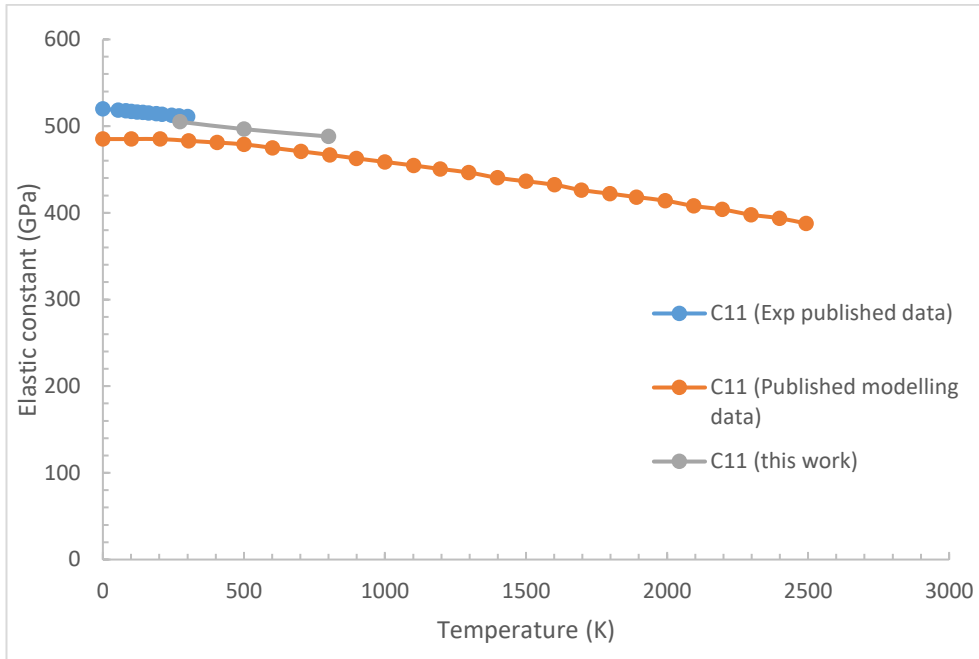
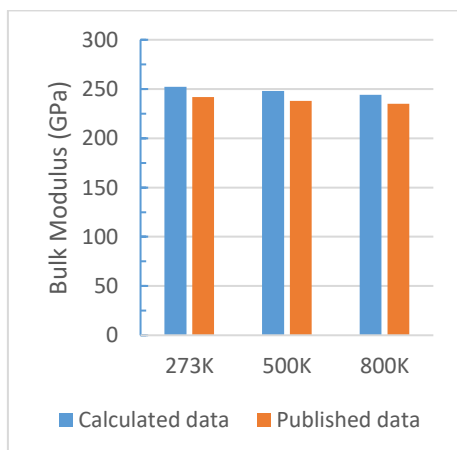


**Figure 5.5.2** Comparison of the elastic constant C11 of TiC from this work and published simulation data and experimental data.

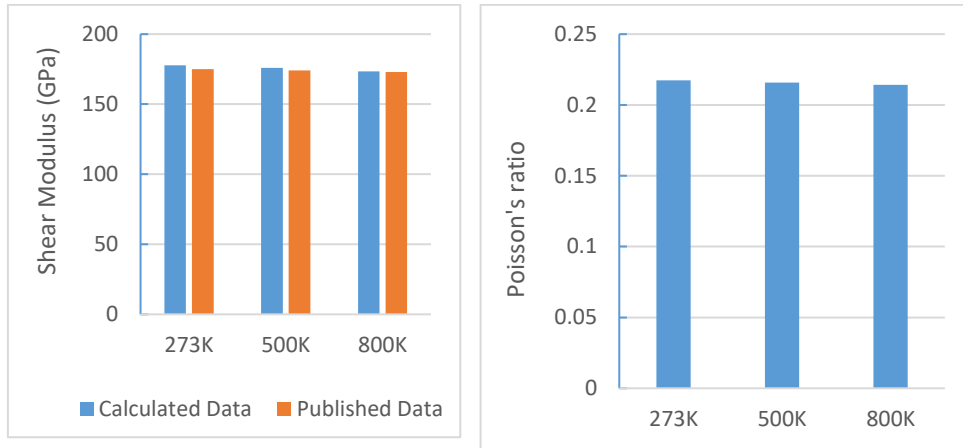
Figure 5.5.2 shows a typical example. As shown in the data, the C11 value from this work showed a good agreement with the published simulation data and experimental work (Dang et al., 2014). Only a few limited experimental data are available, and the trend is very good. The result from this work is almost identical to the published simulation data of TiC.



(a) Bulk modulus at different temperatures. (TiC)



(b) Young's modulus at different temperatures (TiC).

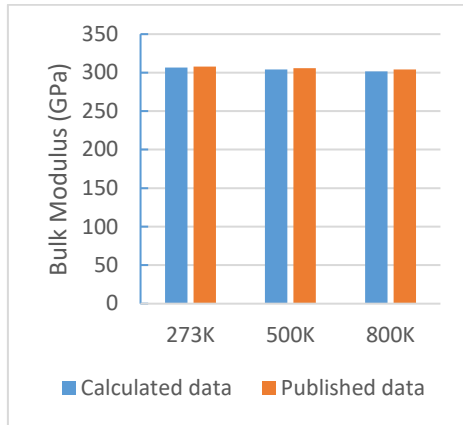


(c) Shear modulus at different temperatures (TiC).

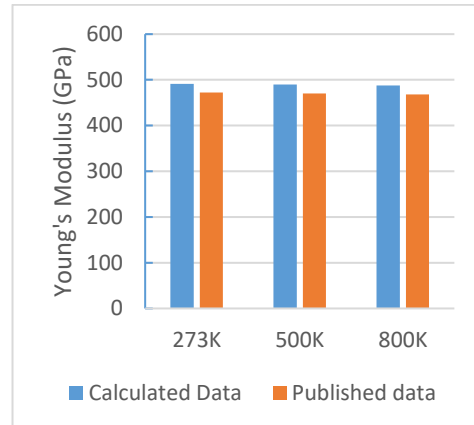
(d) Poisson's ratio at different temperatures. (TiC)

**Figure 5.5.3** Typical elastic property data of TiC at different temperatures in comparison with published data. (Dang et al., 2014)

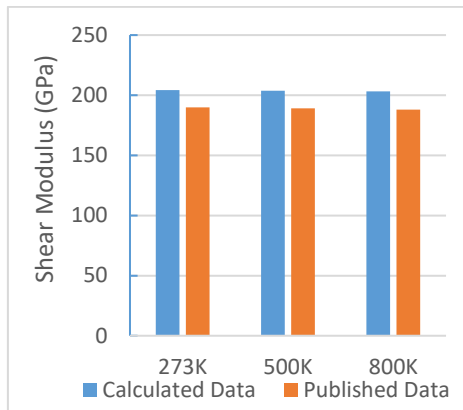
Figure 5.5.3 shows the comparison of the calculated  $K$ ,  $E$ ,  $G$  and Poisson's ratio values with published data of TiC. All data are in a good agreement. Similarly, the figure 5.5.4 predicted work for VC also resembles closely published data. These show that the procedure is sufficient to analyse the effect of temperatures. As this work is part of an effort to develop data for special applications, the presentation of comparison with published data is important. The properties of ceramics at these temperature ranges are important as it was reported that ceramics could start undergoing plastic deformation at 0.1-0.2 melting temperature ( $T_m$ ). For example, it is reported that the critical temperature for plastic deformation in Alumina is within 0.1-0.2 $T_m$ . The melting temperature is around 2072°C. (Zarudi et al., 1998). It was also important for future studies on the potential effect of impurity interactions and dislocation at critical temperatures as highlighted by Amodeo et al (2018). The good agreement from this work and published work at TiC and VC also give the confidence to use the procedure to study other less known material systems and the anisotropic features.



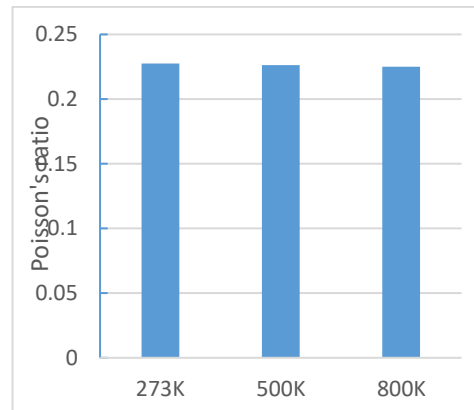
(a) Bulk modulus at different temperatures. (VC)



(b) Young's modulus values at different temperatures. (VC)



(c) Shear modulus values at different temperatures. (VC)



(d) Poisson's ratio at different temperatures. (VC)

**Figure 5.5.4** Typical elastic property data of VC at different temperatures in comparison with published data. (Chong et al., 2016)

As presented in section 5.3, the data for NbC showed more significant anisotropy than TiC and VC. Given the high anisotropic feature of NbC, more detailed data on NbC is conducted at different temperatures (273, 400, 500, 600, 700 and 800K). Typical data was illustrated in Figures 5.5.5 - 5.5.7. Figure 5.5.5 shows the temperature effect on cell volume of NbC. The cell volume increases from 91.4 Å<sup>3</sup> to 94.8 Å<sup>3</sup> while the temperature is increased from 293k to 800K in the simulation.

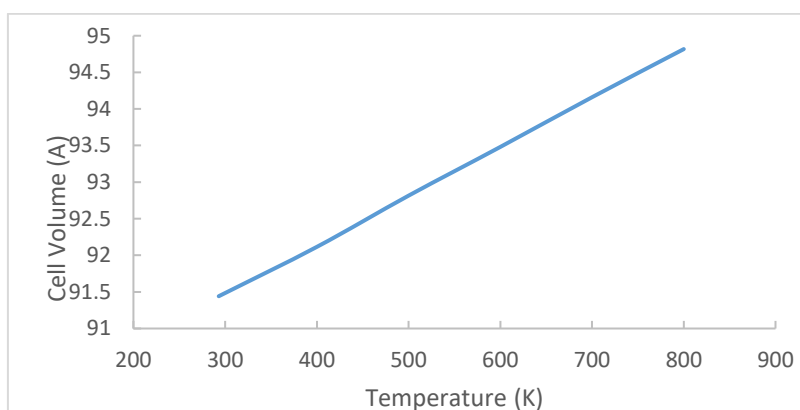
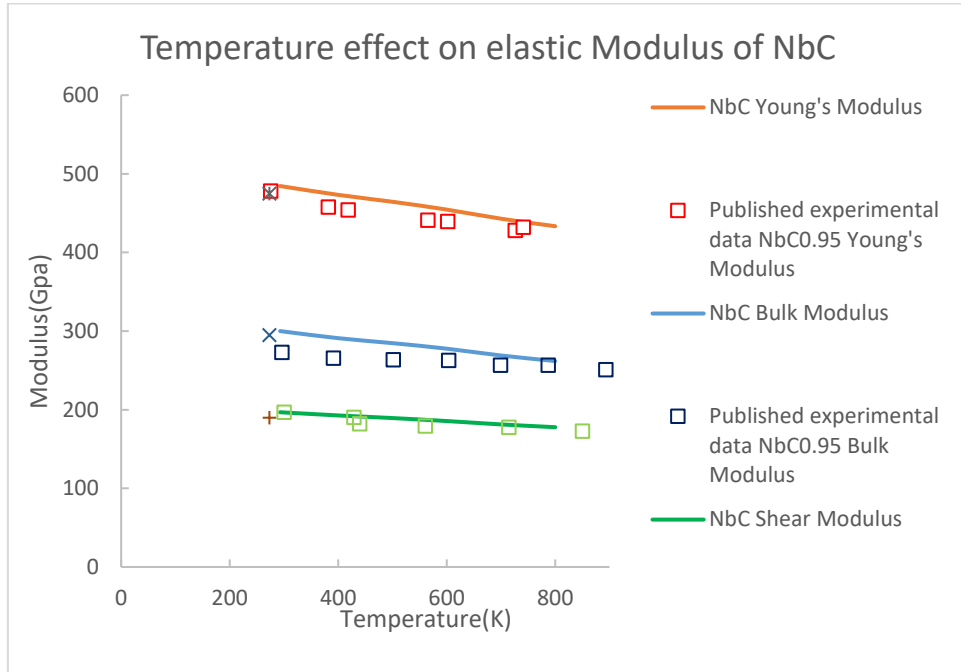


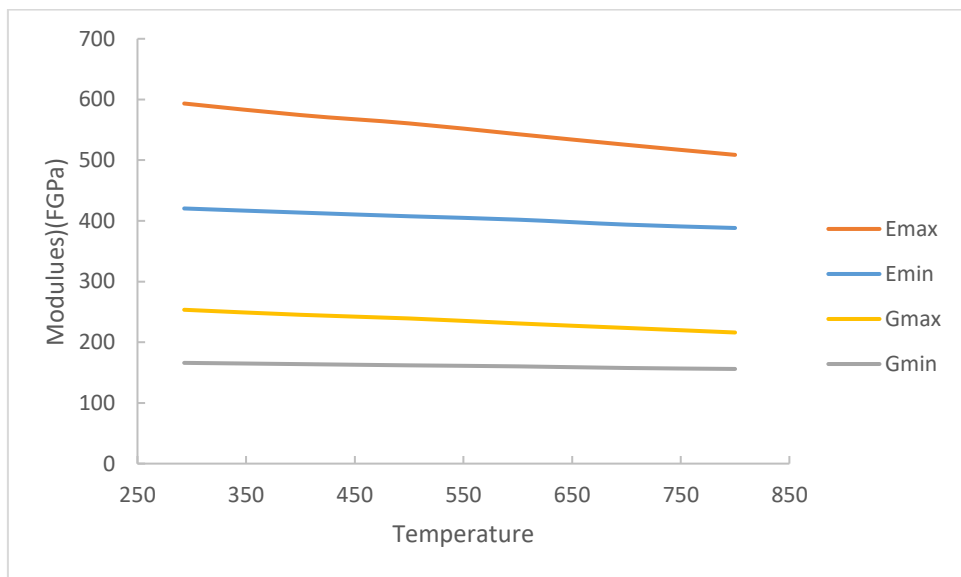
**Figure 5.5.5** The Cell volume change and elastic property change with different Temperature.

The effect of the temperature on the elastic properties is shown in Figure 5.5.6a. The solid lines are CASTEP calculation data, and the open symbols are published experiment data (Cuppari, 2016; Jun and Shaffer, 1971). Also, the data plotted on the figure 5.5.6(a) are some published modelling data of K, E, G of NbC at 273K (Hua and Li, 2015). In all the cases, the elastic modulus decreases with the temperature. The calculated data of bulk modulus is in a very good agreement with other modelling data at 273K. There is a slight difference between the simulation experiment data at lower temperature ranges, the data at higher range temperature showed a good agreement. Both Young's and shear modulus follows a similar trend as published experiment data, the shear modulus shows the better agreement with the testing data than of the bulk modulus and Young's modulus. Figure 5.5.6b shows the minimum and maximum value of Young's Modulus and shear Modulus ratio of NbC with different temperatures. It can be seen that all the min and max value of Young's Modulus and shear Modulus decrease while temperature is increased, and the max value of Young's Modulus and shear Modulus decrease more than the min value. Figure 5.5.7a shows the universal anisotropy index of NbC. The data for TiC and VC is also plotted as a comparison, both showed limited change in comparison with the data for NbC. Figure 5.5.7b plots the anisotropy data of E, G and Poisson's ratio of Nb. It shows that the change of anisotropy in the Poisson's ratio is much stronger than that for E and G as the temperature is increased from 273K to 800K. More detailed data of the

minimum and maximum Poisson's ratio is shown in Figure 5.5.7c&d. It is noticed that both the min value and maximum values of Poisson's are increased with the temperature. The main direction is [110].

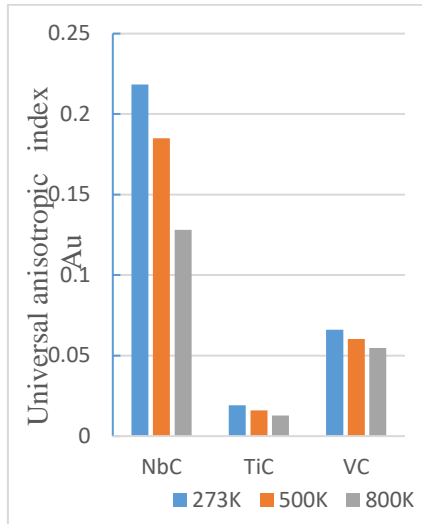


(a) Comparison elastic modulus with published experiment and modelling data at different temperature (Jun and Shaffer, 1971).

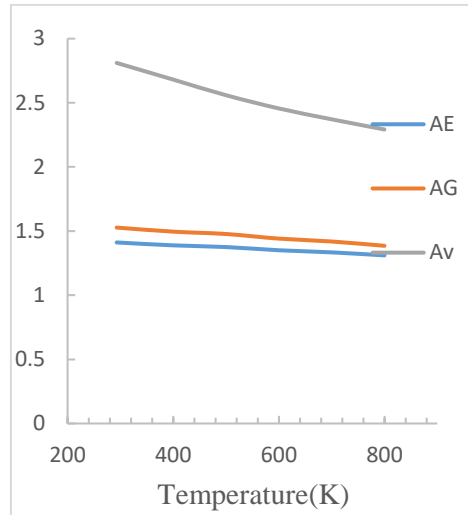


(b) Minimum and maximum value of Young's Modulus and shear Modulus ratio of NbC with different temperatures.

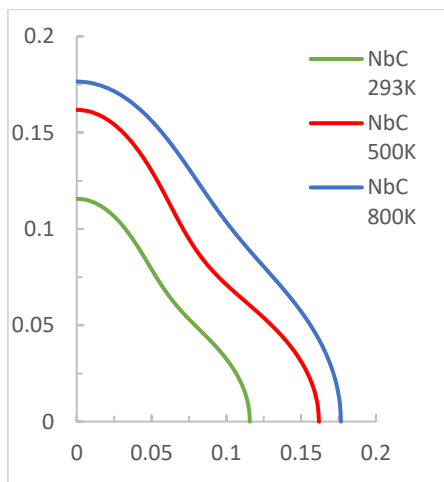
**Figure 5.5.6** Temperature effects on the elastic modulus of NbC



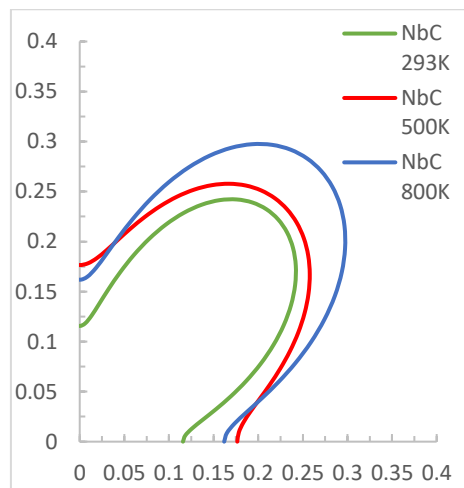
(a) Universal anisotropy index of NbC at different temperatures. The data for TiC and VC is plotted as a comparison.



(b) Anisotropy index of the E, G and  $\nu$  for NbC at different temperature showing more significant change in the anisotropy of  $\nu$ .



(c) 2D plane projection of Minimum value Poisson's ratio (NbC)



(d) 2D plane projection of maximum value Poisson's ratio (NbC).

**Figure 5.5.7** Temperature effect on the Anisotropy of NbC.

(Cuppari, 2016; Jun and Shaffer, 1971).

---

### 5.5.3 Use of Material Studio in studying other material properties and processes

Apart from the work with ground state properties, as explained in section 5.2, there are other important study has been evaluated including Surface energy, oxygen reduction reaction (ORR) and element doping effects. These are essential for developing complex data from the first principle calculating for different applications. Some procure, key result and validation is briefly presented below.

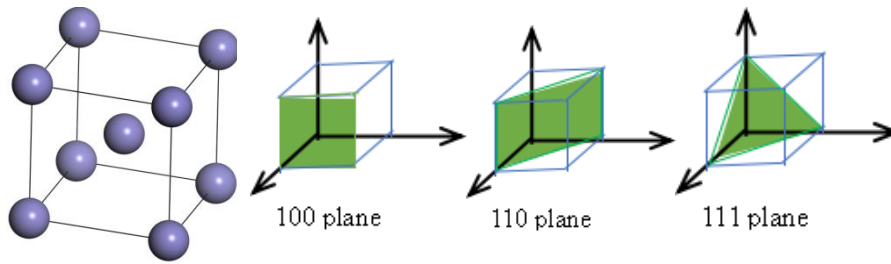
#### Surface Energy of metal crystals

Surface energy is an important parameter, which is the excess free energy per unit area of a particular crystal face which is one of the basic quantities in surface physics (Tran et al., 2016). The balanced shape of the microscopic crystal can be used to determine the surface energy. The data of surface energy are important for the understanding of roughening, crystal growth phenomena and surface segregation (Vitos et al., 1998). There is main situation between metal and ceramics where the surface energy of the material phase is essential (Zhao et al., 2018; Liu et al., 2018). The work in modelling the surface energy of Ferrite ( $\alpha$ -Fe, alpha iron) is briefly presented to illustrate the nature of the procedure and data. To calculate the surface energy of ferrite, a crystal structure of ferrite was built with  $2.8664\text{\AA} \times 2.8664\text{\AA} \times 2.8664\text{\AA}$  and Im-3M space group (Figure and optimized lattice parameter with lowest energy. The crystal structure is close with other published data. (Woodward et al., 2003). The first principle calculation of ferrite surface energy based on density function theory (DFT) by using CASTEP code in Material studio. OTFG Ultra-soft pseudopotential is based on generalized gradient approximation (GGA) - Perdew–Burke–Ernzerhof (PBE) exchange correlation approximation is used in the calculation. In the surface energy calculation of Ferrite, Plane wave truncation Cut off energy is 520 eV, convergence accuracy during iteration is  $5 \times 10^{-6}$  eV / atom. The max force is 0.01 eV/, max stress is 0.02 GPa, Max distance is  $5e-4\text{\AA}$ . The crystal structure was cleaved to three different surface which are (100), (110) and (111) plane (Figures 5.5.8b). To avoid the interaction between the two ends of the model, several models with

different vacuum thickness have been built and used to test surface energy convergence. After the convergence test, vacuum slab with distance of 10 Å was used in further calculation and the optimised structure for different planes are shown in Figures 5.5.8c&d. The surface energy ( $E_{surf}$ ) is calculated following Equation 5.1(Ji et al., 2016)

$$E_{surf} = (E_{totsuf} - NE_{slab})/2A \quad (5.5.1)$$

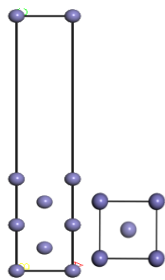
Where the  $E_{surf}$  is the surface energy;  $E_{totsuf}$  is the calculated Total energy of the slab;  $E_{slab}$  is the energy of one crystal;  $N$  is the number of crystals used in the slab;  $A$  is the surface area. The data of the surface energy calculated for (100), (110) and (111) of the is shown in Figure 5.5.8f. The result is in a good agreement with other published data (Guo et al., 2016). The surface energy of Ferrite is following the order:  $E_{surf100} > E_{surf111} > E_{surf110}$ .



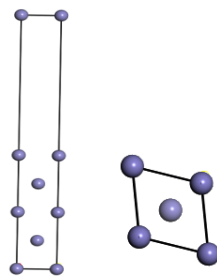
(a)Crystal

(b) Main calculated crystal planes

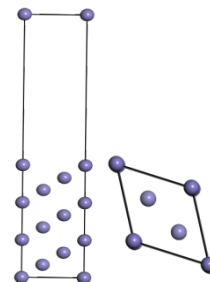
structure of ferrite



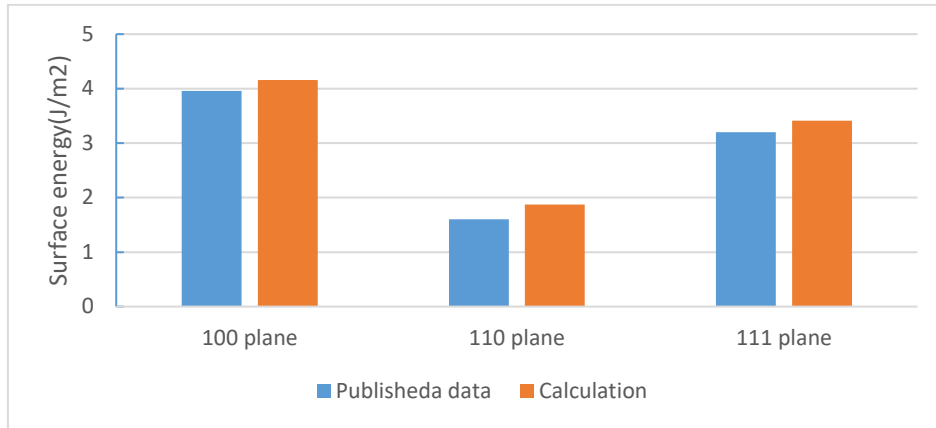
(c) 100 plane  
(front view and  
Top view)



(d) 110 plane (front view  
and Top view)



(e) 111 plane (front  
view and Top view)



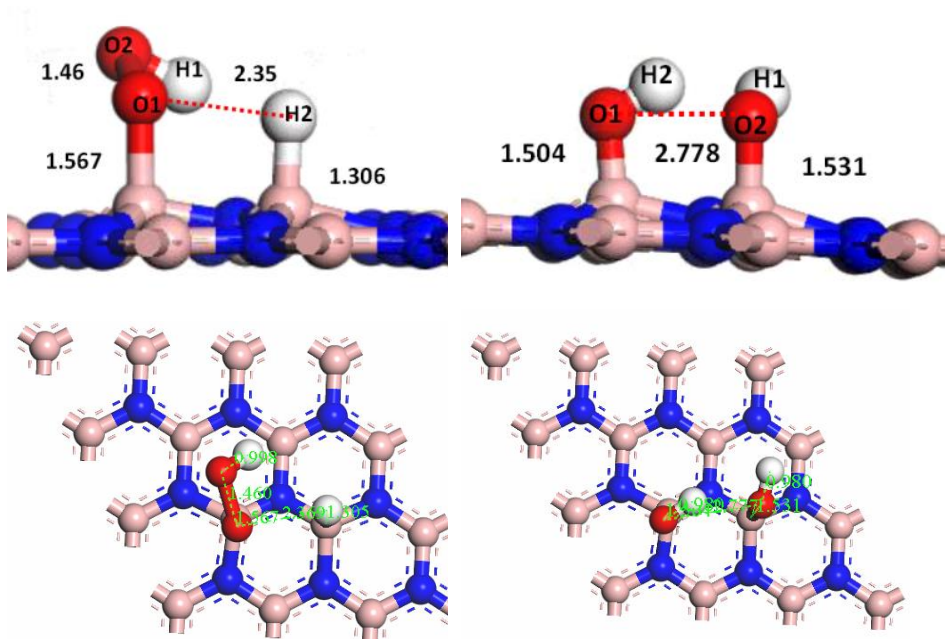
(f) The calculate Ferrite surface energy with (100),(110),(111) plane and other published data(Guo et al., 2016).

**Figure 5.5.8** The crystal structure of Ferrite with different plane and Calculation of the surface energy of Ferrite

---

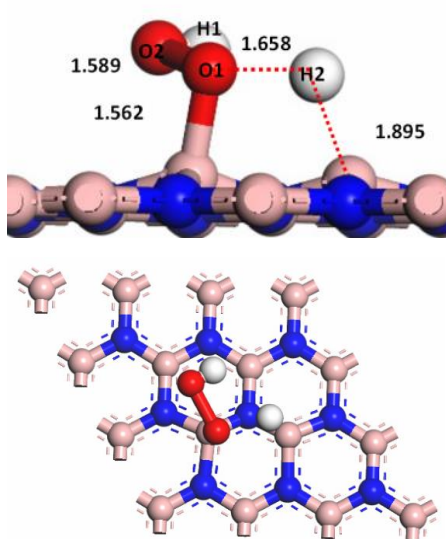
### **Oxygen reduction reaction (ORR)**

An oxygen reduction reaction (ORR) is another important area which can use Material studio density functional theory (DFT) computations. The procedure of the modelling oxygen reduction reaction is evaluated based on the typical data of an oxygen reduction reaction (ORR) of boron nitride nano-sheets. The calculation will be performed by Material studio DMol<sup>3</sup> Module, and a functional of Perdew–Burke–Ernzerh (PBE) is used to treat generalized gradient approximation. The basis set of calculation is DNP with 3.5 basis file. The reactant and product of ORR need optimize the geometry with lowest energy first. The global orbital cut-off is 4.1 Å and the K-points is 6\*6\*1 with actual spacing of 0.026077 1/Å, 0.026077 1/Å, 0.074627 1/Å. The transition state search protocol of ORR step is Complete LST/QST. The atom match between Reactant and Product of ORR is manually select from material studio reaction preview tools (Wen et al., 2018). Typical data and results are shown in Figure 5.5.9. The reactant and product of pathway ( $\text{OOH} + \text{H}^+ + \text{e}^- \rightarrow 2\text{OH}$ ) are built which shows on figure 5.5.9a&b. In reactant, the distance between O1 and B is 1.567Å and the distance of O-O bond is 1.46Å while the distance between O1 to H2 is 2.35Å. The figure 5.5.9b is the product of this ORR. The distance between O1, O2 and B is 1.504 Å and 1.531 Å. The transition state was found by TS search task of DMol<sup>3</sup> Module which show in Figure 5.5.9c. The energy barrier of reaction to transition state is 0.712 eV and the released energy is -3.669 eV. Those energies are matched with published data.

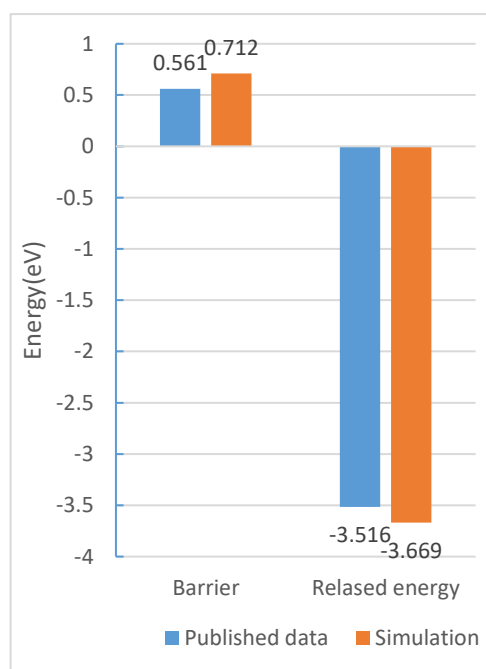


(a) Reactant

(b) Product



(c) Transition state



(d) Comparison between the released energy

**Figure 5.5.9** Crystal geometries of reactants, transition states, and products for oxygen reduction reaction (ORR) of boron nitride nano-sheets ( $\text{OOH} + \text{H}^+ + e^- \rightarrow 2\text{OH}$ ) (Wen et al., 2018)

---

#### **5.5.4 Link between properties at crystal and Poisson's ratio of materials at different scales**

As shown in the results section 5.4 and the cases discussed in section 5.5.3, the first principle calculation is an effective tool in predicting materials properties and characteristics in different conditions such as surface, chemical reaction etc. (Hua and Li, 2015; Wen et al., 2018). One potential use of the integrated data analysis program is for develop data of materials group. For example, in stainless steels, there can be many types of carbides, nitride. Systematic data including anisotropy of these secondary particles and their interface with other phases are important for understanding the mechanical, thermal, and manufacturing processes (Cuppari, 2016; Jun and Shaffer, 1971). One advantage of first principle calculation in establishing systematic data of the ground state properties lies in the fact that it is based on input data of the atoms and crystal structures. In addition, it can predict some detailed properties (e.g., full anisotropy data) that cannot be fully established by experimental methods. Many data sharing sources are being developed and becoming openly accessible recently, such as Materials projects (<https://materialsproject.org/>), chemical crystallography (<http://www.xtl.ox.ac.uk/crystals.1.html>), Crystallography Open Database (Gražulis et al., 2018). These data sources will provide support for data led research and development works for materials studies. The presentation and visualisation of the data are also important for knowledge sharing and training purposes. As shown by Graphical User Interface developed in this work and typical results presented in this thesis, Python based program could provide an effective frame for the data input, integration, cross-comparison, visualisation, and analysis. Apart from the elastic properties presented, other properties such as the sound velocity and Debye temperature can also be directly included which are linked to the elastic constants and anisotropy of the crystal.

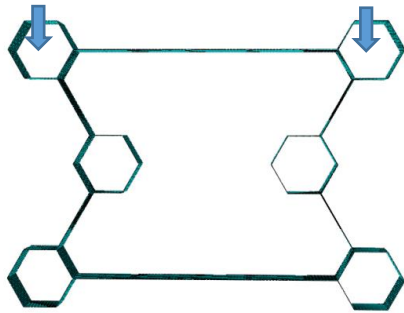
The work presented is focused data of simple carbides including the cross examination of the procedure and results, which is important for practical application of the data. Despite the wide applications of first principle

---

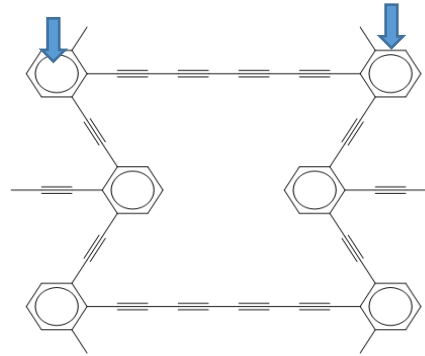
simulations, it is still important to understand the potential cause of error or uncertainty in the results due to variation of input lattice parameters and the calculation parameters (e.g., cutting off energy, K-point etc. as illustrated in section 5.3) (Gaudoin and Foulkes, 2002; Ahmad and Viswanathan, 2016). The development of the python program integrating all the calculations will make it easier to assess the results and cross-compare them with other sources including published data. Python program is very flexible, some simple practical operation such as taking average data for the lattice parameters, assess the effect of the cutting off energy, curve fitting, etc. are useful for practical applications of large-scale systematic data. The procedure of the work can be extended to other carbides, nitrides, including more complex systems such as multiple-elements carbides. For example, the work is being used to study the anisotropy of for  $M_7C_3$  carbides, where M can be a mixture of Fe, Cr, Mn, Mo, W element (Guo, 2020; EU IF project report, in process). The establish the anisotropy data at different temperature also offer than the potential new details for studying the function of TiC/VC/NbC as the nucleation agent for  $M_7C_3$  carbides and Ferrite.

Among the elastic properties, the data for Poisson's ratio, auxeticity and anisotropy are relatively less known previous than the data for K, E and G, but are gaining increased research attention (Kelkar et al., 2020). Some of the ground state properties determined by atomic simulation such as Young's modulus are directly linked to macro scale properties as the Young's modulus is mainly determined based on the inter-atomic forces (Greaves et al., 2013). The bulk modulus, shear modulus of the material studied also showed a good agreement with properties of single crystals. For polycrystalline materials, the overall properties may be affected by the grain structures and other parameters, but the ground state properties still offer guidance on the properties. As illustrated in section 5.4 and 5.5.1, the detailed anisotropy coefficients offer effective data to analyse the correlation data between the Poisson's ratio (including the maximum, minimum and average values) and the bulk modulus-shear modulus ratio. Even though the data fits the theoretical relation but the trend at negative Poisson's ratio range is different from the trend in the positive Poisson's ratio domain. At a negative Poisson's

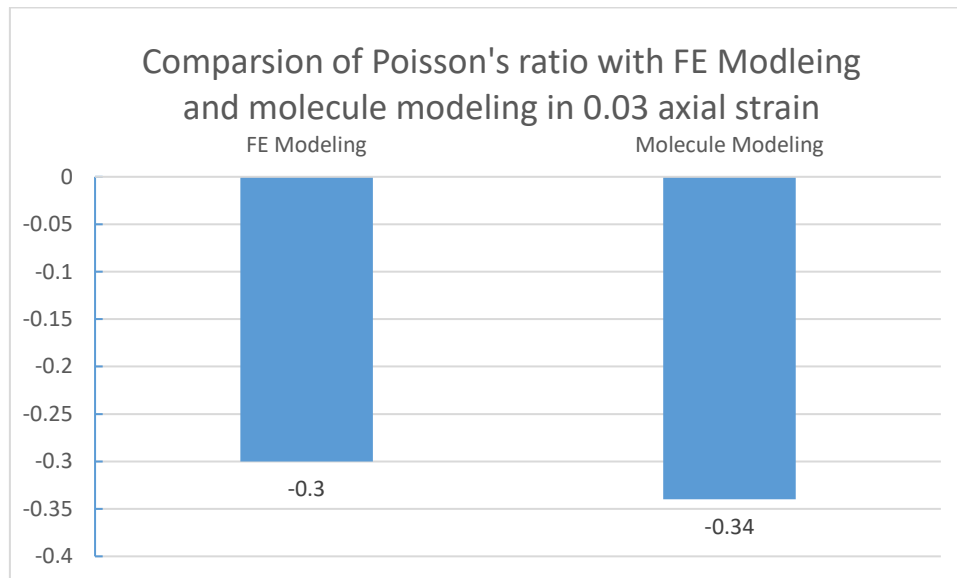
ratio, the slope of the curve showing much steeper variation of the Poisson's ratio with the K/G ratio. More detailed data at a larger scale need to be developed to explore the role between link of Poisson's ratio and K/G values. This may provide a mechanism for materials develop with targeted Poisson's ratios or K/G values.



(a) FE Modelling of a structure based on molecular structure in Abaqus



(b) Molecular simulation in Material studio.



(c) The Poisson's ratio from FE modelling and molecular modelling of a 1-4 (n-m) structure. The number 'n' is the number of acetylene links on the traversal direction branches and 'm' is the number of link on the axial direction branches.

**Figure 5.5.10** Comparison of Poisson's ratio with FE modelling and molecule modelling. (Hua and Li, 2015; Wen et al., 2018)

As covered in Chapter 2, negative Poisson's ratio could be caused by many mechanisms (Gibson et al., 1982; Grima et al., 2008; Gaspar et al., 2005;

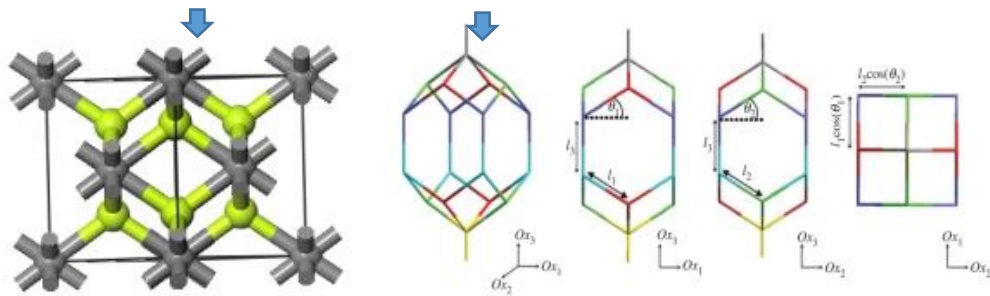
---

Mousanezhad et al., 2015; Lake, 2017). The parametric modelling of the auxetic behaviours at macro scales (Chapter 4) and Poisson's ratio/anisotropy at crystal structure level (Chapter 5) could contribute the understanding of the interlink between auxetic behaviours. Auxeticity is normally associated with high anisotropy (Gaspar et al., 2009; Lake, 2017). Preliminary works of this project on modelling 2D structure has found that the FE model built based on the scaled dimensions form an auxetic molecule in tension has a similar level of Poisson's ratio. A typical result is shown in Figure 5.5.10. Figure 5.5.10 compared the Poisson's ratio of a 1-4 (n-m) structure predicted by the Molecular simulation in Material studio. and an FE model (ABAQUS) based on the dimension and scale (aspect ratio) (a stable structure) from the Molecule model. The number 'n' is the number of acetylene links on the traversal direction branches and 'm' is the number of links on the axial direction branches. The molecular structure resembles a re-entrant honeycomb structure. As shown in figure 5.5.10c, the Poisson's ratio from these two approaches is in a similar range, which also close to published data. This is an interesting finding as the FE is used Young's Modulus while the Molecular simulation is based on electronic force between atoms. Further work could be performed to further explore the use of this approach to identify structures of auxetic behaviours, which will benefit from detailed property data in particular data in anisotropy and parametric FE modelling.

Linking molecular simulation at different scales supported by more powerful data analysis is a potentially useful approach in structure design (Dagdelen et al., 2017; Gaillac et al., 2020). Some of the data in this work also indicates the link between structures at different length scales. An interesting example is Be<sub>2</sub>C, the crystal showed a very low Poisson's ratio.

As shown in Figure 5.5.11a, the unit cell of Be<sub>2</sub>C consists of 12 tetragonums and forms a cage structure. The two-Dimensional Be<sub>2</sub>C with Octa coordinate Carbons has been reported to have a Negative Poisson's Ratio (Qian et al., 2018). It also interesting to compare the Be<sub>2</sub>C structure with some macro structure. The overall format of Be<sub>2</sub>C resemble the auxetic hexagonal dodecahedron reported previously by. (Grima et al., 2012). This clearly reflects the link between auxeticity at crystal levels and macro levels. These

interesting data supports the overall research effort to use data from molecular structure (in whole or partially in 3D or 2D) as a blueprint in the design, synthesis and/or manufacture of man-made multifunctional materials, which may be constructed at the macro-scale, micro-scale as well as at the nanoscale using, for example, micro-fabrication techniques such as 3D printing and additive manufacturing (Grima et al., 2012; Lake, 2017). It will also be interesting try to link FE modelling and first principle calculation to explore the detailed mechanisms. For a pure mechanical system (in finite element modelling), the energy is mainly associated strain energy, while with the molecular simulation the energy is a mixture of mechanical and magnetic-electrical forces. It is difficult to directly compare them quantitatively. Further work will explore the potential link through in-depth data analysis, which will benefit from the python program for parametric FE modelling and integrated data analysis for FE modelling and first principle simulation.



(a) Crystal structure of Be<sub>2</sub>C.

(b) The hexagonal dodecahedron and two-dimensional projections. (Grima et al., 2012)

**Figure 5.5.11** Crystal structure of Be<sub>2</sub>C and hexagonal dodecahedron

---

**CHAPTER SIX**

**CONCLUSIONS AND**

**FUTURE WORK**

---

## 6.1 Summary

This work focused on developing effective data-led simulation approaches for studying the behaviour and properties of auxetic structures and crystals with a particular focus on the Poisson's ratio and auxeticity. Several Python parametric programs were developed for structures and data processing integrated with Finite element modelling (Abaqus) and ab initio quantum mechanical program (Materials Studio CASTEP). The parametric FE modelling studies is concentrated on the development of Python based numerical models of typical auxetic structures. The program is integrated with the FE models to automatically build models of different structures and to calculate/analyse key parameters and results. The models are then used to investigate their deformation behaviours and establish the effect of key dimensional parameters on the deformation process, Poisson's ratio and stability of auxeticity. A range of auxetic structures has been studied including missing rib models in tension, missing rib and mixed cellular structures in compression, self-similar hierarchical structures in compression. A program is also developed for calculating and tracking of the area changes for cellular structures under compression and tension loads. The behaviours of mixed structures and use of Python program in developing Voronoi random structures and random structures with auxetic behaviours is also presented. The area analysis is effective in studying the cell shape and area changes and the data shows that that the areas of the missing rib and honeycomb show much more uniform cell deformation in tension than in compression. The area changes of the missing rib model under compression reflect the main deformation stages including the corner edge-cell wall contact. The work shows that deformation and instability auxeticity of missing rib structures are associated with the corner edge wall contact. The mixed model showed different beam-wall contact patterns, which contributes to the much higher critical strain of stable auxeticity and overall shape stability. The work with ab initio quantum mechanical program (Materials Studio CASTEP) is focused on developing a Python-based data system for analysing the data and

---

link between crystal structures and key ground state properties of crystals based on first principle calculation with Materials Studio. A range of ground state properties including elastic constants ( $C_{ij}$ ), bulk modulus (K), Young's modulus (E), shear modulus (G), Poisson's ratio ( $\nu$ ), etc. have been studied with a particular focus on Poisson's ratio, anisotropy. The correlation between the ground state elastic parameters and their link with other properties is analysed. Some compounds with low or negative Poisson's ratio were identified and detailed structures and properties data are given. Some typical results on key engineering carbides including simple cubic systems (TiC, VC and NbC) are presented together with the mathematical operation to calculate the K, E, G,  $\nu$  and functions for 3D surface constructions of the ground state parameters including anisotropic features. The Python Graphical User Interface developed is effective for systematic calculation and visualization of the key structures, properties, and anisotropy features. The structure and properties of a range of carbides showed a good agreement with the other published data mining programs. The data highlighted the source of uncertainty in Poisson's ratio and the link between link between property data. The Data for structures with Negative Poisson's ratio is briefly presented and analysed including the link between the atomic structure and a macro structure with auxetic behaviours. The procedure for modelling surface energy, oxygen reduction reaction (ORR), structures with doping elements and the effect of temperatures are also presented and showed a good agreement with published works. This laid a good foundation for future use of physical modelling in materials research.

---

## 6.2 Recommendations for further works

This work has established a framework for modelling auxetic structures and studying the anisotropy and auxeticity of materials. The work can be extended into the following areas.

Convert the model into an open-source program with parametric interfaces for studying auxetic structures. The framework established can incorporate other auxetic structures such as re-entrant. This will help the application of materials. As part of another project, the use of missing rib structures and other auxetic structures are being explored in orthotics. The parametric program will help to optimise the dimensions and materials used by students not from medical backgrounds. The work on mixed structures and random structure can be used in design structures for targeted properties. These are increasingly important areas, such as a parametric program that can help make the design process more efficient.

The work used a high beam length-to-wall thickness ratio, and this offered a case to study the initial contact patterns in detail and to evaluate the deformation, properties, and stability of missing rib structures and mixed structures. Future more quantitative work will systematically investigate the effect of angle and beam lengths on the deformation of different complex material systems at higher strains. The development of 3D additive printing and joining technologies has opened the path to produce complex structures with both plastics and metals stainless steels and titanium alloys and high entropy alloys

The work on ab initio quantum mechanical program (Materials Studio CASTEP) has established the modelling and data processing for the ground state properties and the anisotropy. The program is being used to map the compounds in stainless as part of another project. This will help the development of the database for materials groups. The effect of the temperature effect on the lattice parameters and properties of high temperature carbides will be used to study the nucleation of metallic phase or other complex carbides (such as  $M(Fe, Cr)_7C_3$ ) on precipitated carbides

---

## Reference:

Adorna, M., Falta, J., Fíla, T. and Zlámá, P. (2018). PREPROCESSING OF HOPKINSON BAR EXPERIMENT DATA: FILTER ANALYSIS. *Acta Polytechnica CTU Proceedings*, 18, p.77.

Ahmad, Z. and Viswanathan, V., 2016. Quantification of uncertainty in first principles predicted mechanical properties of solids: Application to solid ion conductors. *Physical Review B*, 94(6).

Ajdari, A., Nayeb-Hashemi, H. and Vaziri, A., 2011. Dynamic crushing and energy absorption of regular, irregular and functionally graded cellular structures. *International Journal of Solids and Structures*, 48(3-4), pp.506-516.

Al-Badani, 2020, PhD thesis; Experimental and Numerical Investigation of Droplet Formation and Material Interactions Under Different Conditions.

Alderson, A., Rasburn, J., Ameer-Beg, S., Mullarkey, P., Perrie, W. and Evans, K., 2000. An Auxetic Filter: A Tuneable Filter Displaying Enhanced Size Selectivity or Defouling Properties. *Industrial & Engineering Chemistry Research*, 39(3), pp.654-665.

Alsayednoor, J. and Harrison, P., 2016. Evaluating the performance of microstructure generation algorithms for 2-d foam-like representative volume elements. *Mechanics of Materials*, 98, pp.44-58.

Amodeo, J., Merkel, S., Tromas, C., Carrez, P., Korte-Kerzel, S., Cordier, P. and Chevalier, J., 2018. Dislocations and Plastic Deformation in MgO Crystals: A Review. *Crystals*, 8(6), p.240.

Aw, J., Zhao, H., Norbury, A., Li, L., Rothwell, G. and Ren, J., 2015. Effects of Poisson's ratio on the deformation of thin membrane structures under indentation. *physica status solidi (b)*, 252(7), pp.1526-1532.

Babae, S., Shim, J., Weaver, J., Chen, E., Patel, N. and Bertoldi, K. (2013). Metamaterials: 3D Soft Metamaterials with Negative Poisson's Ratio (Adv. Mater. 36/2013). *Advanced Materials*, 25(36), pp.5116-5116.

Baimova, J., Rysaeva, L., Dmitriev, S. and Lisovenko, D., 2017. AUXETIC BEHAVIOUR OF CARBON NANOSTRUCTURES. *Materials Physics and*

---

*Mechanics*, 33(1-11).

Bao, L., Qu, D., Kong, Z. and Duan, Y., 2019. Anisotropies in elastic properties and thermal conductivities of trigonal TM<sub>2</sub>C (TM = V, Nb, Ta) carbides. *Solid State Sciences*, 98, p.106027.

Barrett, T., Savage, D., Ardeljan, M. and Knezevic, M., 2018. An automated procedure for geometry creation and finite element mesh generation: Application to explicit grain structure models and machining distortion. *Computational Materials Science*, 141, pp.269-281.

Basiuk, V., Henao-Holguin, L., 2013. Effects of Orbital Cutoff in DMol3 DFT Calculations: A Case Study of meso-Tetraphenylporphine-C60 Complex. *Journal of Computational and Theoretical Nanoscience*, 10(5), pp.1266-1272

Baumgart, C., Halle, T., Weigelt, C., Krüger, L. and Aneziris, C., 2018. Effect of honeycomb cell geometry on compressive properties: Finite element analysis and experimental verification. *Science and Technology of Materials*, 30(1), pp.35-42.

Ben-Belgacem, M., Richet, V., Terrani, K., Katoh, Y. and Snead, L., 2014. Thermo-mechanical analysis of LWR SiC/SiC composite cladding. *Journal of Nuclear Materials*, 447(1-3), pp.125-142.

Bensoussan, A., Lions, J., Papanicolaou, G. and Caughey, T., 1979. Asymptotic Analysis of Periodic Structures. *Journal of Applied Mechanics*, 46(2), pp.477-477.

Benyelloul, K. and Aourag, H., 2013. Elastic constants of austenitic stainless steel: Investigation by the first-principles calculations and the artificial neural network approach. *Computational Materials Science*, 67, pp.353-358.

Bertoldi, K. (2018). Harnessing Instabilities to Design Tunable Architected Cellular Materials. *Annual Review of Materials Research*, 47(1), pp.51-61.

Bigelow, C., Kim, J., Barr, J., Ye, H. and Mckee, N., 2020. *1St Post 2019 | Density Functional Theory and Practice Course*. [online] Sites.psu.edu. Available at: <<https://sites.psu.edu/dftap/category/1stpost2019/>> [Accessed 6 July 2020].

Braden, B., 1986. The Surveyor's Area Formula. *The College Mathematics Journal*, 17(4), pp.326-337.

Brely, L., Bosia, F. and Pugno, N., 2015. A Hierarchical Lattice Spring Model

---

to Simulate the Mechanics of 2-D Materials-Based Composites. *Frontiers in Materials*, 2.

Brenton, R., Saunders, C. and Kempter, C., 1969. Elastic properties and thermal expansion of niobium mono-carbide to high temperatures. *Journal of the Less Common Metals*, 19(3), 273-278.

Brown, H., Armstrong, P. and Kempter, C., 1966. Elastic Properties of Some Polycrystalline Transition-Metal Monocarbides. *The Journal of Chemical Physics*, 45(2), 547-549.

Bultinck, P. and Carbó-Dorca, R., 2005. Molecular quantum similarity using conceptual DFT descriptors. *Journal of Chemical Sciences*, 117(5), pp.425-435.

Buytoz, S., 2006. Microstructural properties of M7C3 eutectic carbides in a Fe–Cr–C alloy. *Materials Letters*, 60(5), pp.605-608.

Cabras, L. and Brun, M. (2014). Auxetic two-dimensional lattices with Poisson's ratio arbitrarily close to  $-1$ . *Proceedings of the Royal Society A: Mathematical, Physical and Engineering Sciences*, 470(2172), p.20140538.

Chen, H., Muros-Cobos, J., Holgado-Terriza, J. and Amirfazli, A., 2017. Surface tension measurement with a smartphone using a pendant drop. *Colloids and Surfaces A: Physicochemical and Engineering Aspects*, 533, pp.213-217.

Chen, X., Niu, H., Li, D. and Li, Y., 2011. Modeling hardness of polycrystalline materials and bulk metallic glasses. *Intermetallics*, 19(9), 1275-1281.

Chenoweth, K., Cheung, S., van Duin, A., Goddard, W. and Kober, E., 2005. Simulations on the Thermal Decomposition of a Poly(dimethylsiloxane) Polymer Using the ReaxFF Reactive Force Field. *Journal of the American Chemical Society*, 127(19), pp.7192-7202.

Chong, X., Jiang, Y., Zhou, R. and Feng, J., 2016. The effects of ordered carbon vacancies on stability and thermo-mechanical properties of V8C7 compared with VC. *Scientific Reports*, 6(1).

Chong, X., Jiang, Y., Zhou, R. and Feng, J., 2017. Multialloying effect on thermophysical properties of Cr7C3-type carbides. *Journal of the American Ceramic Society*, 100(4), pp.1588-1597.

- 
- Chu, L., Shi, J., Souza de Cursi, E., Xu, X., Qin, Y. and Xiang, H., 2018. Monte Carlo-Based Finite Element Method for the Study of Randomly Distributed Vacancy Defects in Graphene Sheets. *Journal of Nanomaterials*, 2018, pp.1-12.
- Chung DH, Buessem WR, in F.W. Vahldiek, S.A. Mersol (Eds.), *Anisotropy in Single Crystal Refractory Compound*, Plenum, New York, 1968.
- Chung, D.H., 1969. Anisotropy in single-crystal refractory compounds. *Journal of the Less Common Metals*, 18(3), p.316.
- Clark, S., Segall, M., Pickard, C., Hasnip, P., Probert, M., Refson, K. and Payne, M., 2005. First principles methods using CASTEP. *Zeitschrift für Kristallographie - Crystalline Materials*, 220(5/6).
- Cui, S., Gong, B., Ding, Q., Sun, Y., Ren, F., Liu, X., Yan, Q., Yang, H., Wang, X. and Song, B. (2018). Mechanical Metamaterials Foams with Tunable Negative Poisson's Ratio for Enhanced Energy Absorption and Damage Resistance. *Materials*, 11(10), p.1869.
- Cuppari M and Santos S, 2016, Physical Properties of the NbC Carbide, *Metals*, 6(10):250.
- D'Alessandro, L., Zega, V., Ardito, R. and Corigliano, A., 2018. 3D auxetic single material periodic structure with ultra-wide tunable bandgap. *Scientific Reports*, 8(1).
- Dagdelen, J., Montoya, J., de Jong, M. and Persson, K., 2017. Computational prediction of new auxetic materials. *Nature Communications*, 8(1).
- Dang, D., Fan, J. and Gong, H., 2014. Thermodynamic and mechanical properties of TiC from ab initio calculation. *Journal of Applied Physics*, 116(3), p.033509.
- Darwish, S. and Aslam, M. (2014). Auxetic Cellular Structures for Custom Made Orthopedic Implants using Additive Manufacturing. *International Journal of Engineering and Advanced Technology (IJEAT)*, Volume-4(ISSN: 2249 – 8958), p. Issue-2.
- Das, S., Sneijders, S., Deen, N. and Kuipers, J., 2018. Drag and heat transfer closures for realistic numerically generated random open-cell solid foams using an immersed boundary method. *Chemical Engineering Science*, 183, pp.260-274.

- 
- Dong, Z., Li, Y., Zhao, T., Wu, W., Xiao, D. and Liang, J. (2019). Experimental and numerical studies on the compressive mechanical properties of the metallic auxetic reentrant honeycomb. *Materials & Design*, 182, p.108036.
- Duncan, O., Shepherd, T., Moroney, C., Foster, L., Venkatraman, P., Winwood, K., Allen, T. and Alderson, A., 2018. Review of Auxetic Materials for Sports Applications: Expanding Options in Comfort and Protection. *Applied Sciences*, 8(6), p.941.
- Dutta, S., Burman, S., Mazumdar, A. and Roy, N., 2019. Crowd Behavior Analysis and Alert System Using Image Processing. *Advances in Intelligent Systems and Computing*, pp.721-729.
- Edström, D., Sangiovanni, D., Hultman, L., Petrov, I., Greene, J. and Chirita, V., 2018. Elastic properties and plastic deformation of TiC- and VC-based pseudobinary alloys. *Acta Materialia*, 144, pp.376-385.
- Edström, D., Sangiovanni, D., Hultman, L., Petrov, I., Greene, J. and Chirita, V., 2018. Elastic properties and plastic deformation of TiC- and VC-based pseudobinary alloys. *Acta Materialia*, 144, pp.376-385.
- Evans KE (1991). Design of doubly-curved sandwich panels with honeycomb cores. *Compos. Struct*, 17: 95-111.
- Evans, K. and Alderson, A., 2000. Auxetic Materials: Functional Materials and Structures from Lateral Thinking. *Advanced Materials*, 12(9), pp.617-628.
- Farhadizadeh, A., Amadeh, A. and Ghomi, H., 2017. Structural and Mechanical Properties of TiN-TiC-TiO System: First Principle Study. *Communications in Theoretical Physics*, 68(5), p.678.
- Farrugia, P., Gatt, R., Zammit Lonardelli, E., Grima, J. and Evans, K. (2018). Different Deformation Mechanisms Leading to Auxetic Behavior Exhibited by Missing Rib Square Grid Structures. *physica status solidi (b)*, 256(1), p.1800186.
- Fozdar, D., Soman, P., Lee, J., Han, L. and Chen, S. (2011). Three-Dimensional Polymer Constructs Exhibiting a Tunable Negative Poisson's Ratio. *Advanced Functional Materials*, 21(14), pp.2712-2720.
- Fu, H., Peng, W. and Gao, T., 2009. Structural and elastic properties of ZrC

---

under high pressure. *Materials Chemistry and Physics*, 115(2-3), pp.789-794.

Gaillac, R., Chibani, S. and Coudert, F., 2020. Speeding Up Discovery of Auxetic Zeolite Frameworks by Machine Learning. *Chemistry of Materials*, 32(6), pp.2653-2663.

Gao, X., Jiang, Y., Liu, Y., Zhou, R. and Feng, J., 2014. Stability and elastic properties of Nb<sub>x</sub>C<sub>y</sub> compounds. *Chinese Physics B*, 23(9), 097704.

Gaspar, N., Ren, X., Smith, C., Grima, J. and Evans, K., 2005. Novel honeycombs with auxetic behaviour. *Acta Materialia*, 53(8), pp.2439-2445.

Gaspar, N., Smith, C. and Evans, K. (2003). Effect of heterogeneity on the elastic properties of auxetic materials. *Journal of Applied Physics*, 94(9), pp.6143-6149.

Gaspar, N., SMITH, C. and EVANS, K., 2009. Auxetic behaviour and anisotropic heterogeneity. *Acta Materialia*, 57(3), pp.875-880.

Gaudoin, R. and Foulkes, W., 2002. Ab initio calculations of bulk moduli and comparison with experiment. *Physical Review B*, 66(5).

Ghosh, G., 2015. A first-principles study of cementite (Fe<sub>3</sub>C) and its alloyed counterparts: Elastic constants, elastic anisotropies, and isotropic elastic moduli. *AIP Advances*, 5(8), p.087102.

Gibson, L., Ashby, M., Schajer, G. and Robertson, C., 1982. The Mechanics of Two-Dimensional Cellular Solids. *Proceedings of the Royal Society of London*, (A 382), pp.25-42.

Gilman, J. and Roberts, B., 1961. Elastic Constants of TiC and TiB<sub>2</sub>. *Journal of Applied Physics*, 32(7), 1405-1405.

Gitman, I., Askes, H. and Sluys, L., 2007. Representative volume: Existence and size determination. *Engineering Fracture Mechanics*, 74(16), pp.2518-2534.

Gostick, J., Khan, Z., Tranter, T., Kok, M., Agnaou, M., Sadeghi, M. and Jervis, R., 2019. PoreSpy: A Python Toolkit for Quantitative Analysis of Porous Media Images. *Journal of Open Source Software*, 4(37), p.1296.

Gražulis, S., Merkys, A. and Vaitkus, A., 2018. Crystallography Open Database (COD). *Handbook of Materials Modeling*, pp.1-19.

Greaves, G., 2013. Poisson's ratio over two centuries: challenging hypotheses. *Notes and Records of the Royal Society*, 67(1), pp.37-58.

- 
- Grima, J., Caruana-Gauci, R., Attard, D. and Gatt, R., 2012. Three-dimensional cellular structures with negative Poisson's ratio and negative compressibility properties. *Proceedings of the Royal Society A: Mathematical, Physical and Engineering Sciences*, 468(2146), pp.3121-3138.
- Grima, J., Farrugia, P., Gatt, R. and Attard, D., 2008. On the auxetic properties of rotating rhombi and parallelograms: A preliminary investigation. *physica status solidi (b)*, 245(3), pp.521-529.
- Grima, J., Gatt, R., Ravirala, N., Alderson, A. and Evans, K., 2006. Negative Poisson's ratios in cellular foam materials. *Materials Science and Engineering: A*, 423(1-2), pp.214-218.
- Grima, J., Oliveri, L., Attard, D., Ellul, B., Gatt, R., Cicala, G. and Recca, G., 2010. Hexagonal Honeycombs with Zero Poisson's Ratios and Enhanced Stiffness. *Advanced Engineering Materials*, 12(9), pp.855-862.
- Guo, L., Hua, G., Yang, B., Lu, H., Qiao, L., Yan, X. and Li, D., 2016. Electron work functions of ferrite and austenite phases in a duplex stainless steel and their adhesive forces with AFM silicon probe. *Scientific Reports*, 6(1)
- Habib, F., Iovenitti, P., Masood, S. and Nikzad, M., 2017. Cell geometry effect on in-plane energy absorption of periodic honeycomb structures. *The International Journal of Advanced Manufacturing Technology*, 94(5-8), pp.2369-2380.
- Habib, F., Iovenitti, P., Masood, S. and Nikzad, M., 2017. In-plane energy absorption evaluation of 3D printed polymeric honeycombs. *Virtual and Physical Prototyping*, 12(2), pp.117-131.
- Haghpanah, B., Oftadeh, R., Papadopoulos, J. and Vaziri, A., 2013. Self-similar hierarchical honeycombs. *Proceedings of the Royal Society A: Mathematical, Physical and Engineering Sciences*, 469(2156), p.20130022.
- Haj Hassan, F. and Akbarzadeh, H., 2006. Ground state properties and structural phase transition of beryllium chalcogenides. *Computational Materials Science*, 35(4), pp.423-431.
- Hall, S. and McMahon, B., 2006. International Tables for Crystallography. *International Tables for Crystallography*,
- Hall, S., Hamerton, I., Howlin, B. and Mitchell, A., 2008. Validating software

---

and force fields for predicting the mechanical and physical properties of poly(bisbenzoxazine)s. *Molecular Simulation*, 34(10-15), pp.1259-1266.

Hamblyn and Reuben, 1975; Use of Radio-Frequency Plasma in Chemical Synthesis, *Advance in Orgnic Chemcistyr and Radio Chemistry/file Fundamental*, 17, 89-114.

Hanifpour, M., Petersen, C., Alava, M. and Zapperi, S. (2017). Mechanics of disordered auxetic metamaterials. *The European Physical Journal B*, 91(11).

Hao, R., Zhang, X., Qin, J., Ning, J., Zhang, S., Niu, Z., Ma, M. and Liu, R., 2015. Anisotropy in elasticity and thermodynamic properties of zirconium tetraboride under high pressure. *RSC Advances*, 5(94), pp.77399-77406.

He, Q., Zhou, F., Zhan, S., Huang, N. and Tian, Y., 2018. Photoassisted oxygen reduction reaction on mpg-C 3 N 4 : The effects of elements doping on the performance of ORR. *Applied Surface Science*, 430, pp.325-334.

Healy, D., Timms, N. and Pearce, M., 2019. The variation and visualisation of elastic anisotropy in rock forming minerals.

Hedayati, R., Mirzaali, M., Vergani, L. and Zadpoor, A. (2018). Action-at-a-distance metamaterials: Distributed local actuation through far-field global forces. *APL Materials*, 6(3), p.036101.

Hill.R., 1952, The elastic behaviour of a crystalline aggregate, *Proc. Phys. Soc.* 65, 349.

Ho, D., Kwon, S. and Kim, S. (2016). Metal [100] Nanowires with Negative Poisson's Ratio. *Scientific Reports*, 6(1).

Hoffman, G., 1958. Poisson's Ratio for Honeycomb Sandwich Cores. *Journal of the Aerospace Sciences*, 25(8), pp.534-535.

Hu, L., Luo, Z. and Yin, Q. (2019). Negative Poisson's ratio effect of re-entrant anti-trichiral honeycombs under large deformation. *Thin-Walled Structures*, 141, pp.283-292.

Hu, S., Gao, R., Ding, Y., Collins, L. and Kress, J., 2017. First-principles equation-of-state table of silicon and its effects on high-energy-density plasma simulations. *Physical Review E*, 95(4).

Hu, Z., Xu, T., Wang, X., Xie, Z., Luo, H., He, Y., Guo, L., Li, Y., Gan, R. and Lu, H., 2017. Fluorescent digital image correlation techniques in experimental mechanics. *Science China Technological Sciences*, 61(1),

---

pp.21-36.

Hua, G. and Li, D., 2015. A first-principles study on the mechanical and thermodynamic properties of  $(\text{Nb}_{1-x}\text{Ti}_x)\text{C}$  complex carbides based on virtual crystal approximation. *RSC Advances*, 5(125), pp.103686-103694.

Huang, C. and Shih, T., 1997. On the complexity of point-in-polygon algorithms. *Computers & Geosciences*, 23(1), pp.109-118.

Imbalzano, G., Linforth, S., Ngo, T., Lee, P. and Tran, P. (2018). Blast resistance of auxetic and honeycomb sandwich panels: Comparisons and parametric designs. *Composite Structures*, 183, pp.242-261.

James Ren, X. and Silberschmidt, V., 2008. Numerical modelling of low-density cellular materials. *Computational Materials Science*, 43(1), pp.65-74.

Ji, D., Zhu, Q. and Wang, S., 2016. Detailed first-principles studies on surface energy and work function of hexagonal metals. *Surface Science*, 651, pp.137-146.

Jiang, C., Srinivasan, S., Caro, A. and Maloy, S., 2008. Structural, elastic, and electronic properties of  $\text{Fe}_3\text{C}$  from first principles. *Journal of Applied Physics*, 103(4), p.043502.

Jiang, C., Srinivasan, S., Caro, A. and Maloy, S., 2008. Structural, elastic, and electronic properties of  $\text{Fe}_3\text{C}$  from first principles. *Journal of Applied Physics*, 103(4), p.043502.

Jiang, Y., Rudra, B., Shim, J. and Li, Y. (2019). Limiting strain for auxeticity under large compressive Deformation: Chiral vs. re-entrant cellular solids. *International Journal of Solids and Structures*, 162, pp.87-95.

Jun, C. and Shaffer, P., 1971. Elastic moduli of niobium carbide and tantalum carbide at high temperature. *Journal of the Less Common Metals*, 23(4), pp.367-373.

Kaman, M., Solmaz, M. and Turan, K., 2010. Experimental and Numerical Analysis of Critical Buckling Load of Honeycomb Sandwich Panels. *Journal of Composite Materials*, 44(24), pp.2819-2831.

Kelkar, P., Kim, H., Cho, K., Kwak, J., Kang, C. and Song, H., 2020. Cellular Auxetic Structures for Mechanical Metamaterials: A Review. *Sensors*, 20(11), p.3132.

- 
- Kelling, J., Zahn, P., Schuster, J. and Gemming, S., 2017. Elastic and piezoresistive properties of nickel carbides from first principles. *Physical Review B*, 95(2).
- Kim, J and Kang, S., 2012. Elastic and thermo-physical properties of TiC, TiN, and their intermediate composition alloys using ab initio calculations. *Journal of Alloys and Compounds*, 528, 20-27.
- Kitchin, J., 2012. *Modeling Materials Using Density Functional Theory*. [online] Kitchingroup.cheme.cmu.edu. Available at: <<http://kitchingroup.cheme.cmu.edu/dft-book/dft.html>> [Accessed 6 July 2020].
- Kolken, H. and Zadpoor, A., 2017. Auxetic mechanical metamaterials. *RSC Advances*, 7(9), pp.5111-5129.
- Kolpakov, A., 1985. Determination of the average characteristics of elastic frameworks. *Journal of Applied Mathematics and Mechanics*, 49(6), pp.739-745.
- Koudelka, P., Jiroušek, O., Fíla, T. and Doktor, T. (2016). Compressive properties of auxetic structures produced with direct 3D printing. *Materiali in tehnologije*, 50(3), pp.311-317.
- Kumpenza, C., Matz, P., Halbauer, P., Grabner, M., Steiner, G., Feist, F. and Müller, U., 2018. Measuring Poisson's ratio: mechanical characterization of spruce wood by means of non-contact optical gauging techniques. *Wood Science and Technology*, 52(6), pp.1451-1471.
- Lakes, R. (2017). Negative-Poisson's-Ratio Materials: Auxetic Solids. *Annual Review of Materials Research*, 47(1), pp.63-81.
- Lakes, R. and Witt, R. (2002). Making and Characterizing Negative Poisson's Ratio Materials. *International Journal of Mechanical Engineering Education*, 30(1), pp.50-58.
- Langrand, B., Casadei, F., Marcadon, V., Portemont, G. and Kruch, S., 2017. FE Modelling of Cellular Materials Under Compressive Load. *Procedia Engineering*, 173, pp.1951-1958.
- Lekesiz, H., Bhullar, S., Karaca, A. and Jun, M., 2017. Mechanical characterization of auxetic stainless steel thin sheets with reentrant structure. *Smart Materials and Structures*, 26(8), p.085022.

- 
- Li, K., Wang, P., Liu, G., Yuan, P. and Zhang, Q., 2018. Development of simulation system for large H-beam hot rolling based on ABAQUS. *The International Journal of Advanced Manufacturing Technology*, 85(5-8), pp.1649-1663.
- Li, S., Al-Badani, K., Gu, Y., Lake, M., Li, L., Rothwell, G. and Ren, J., 2017. The Effects of Poisson's Ratio on the Indentation Behavior of Materials with Embedded System in an Elastic Matrix. *physica status solidi (b)*, 254(12), p.1600832.
- Li, Z., Chan, S., Grimsditch, M. and Zouboulis, E., 1991. The elastic and electromechanical properties of tetragonal BaTiO<sub>3</sub> single crystals. *Journal of Applied Physics*, 70(12), pp.7327-7332.
- Lim, T., 2009. Out-of-plane modulus of semi-auxetic laminates. *European Journal of Mechanics - A/Solids*, 28(4), pp.752-756.
- Liu, H., Zhu, J., Liu, Y. and Lai, Z., 2008. First-principles study on the mechanical properties of vanadium carbides VC and V<sub>4</sub>C<sub>3</sub>. *Materials Letters*, 62(17-18), 3084-3086.
- Liu, S., Gao, Y., Wang, Z., Shi, Z., Zhou, Y., Ren, X. and Yang, Q., 2018. Refinement effect of TiC on ferrite by molecular statics/dynamics simulations and first-principles calculations. *Journal of Alloys and Compounds*, 731, pp.822-830.
- Liu, X., Feng, Q., Tang, B., et al., 2019. First-principles calculations of mechanical and thermodynamic properties of tetragonal Be<sub>12</sub>Ti. *RSC Advances*, 9(10), 5302-5312.
- Liu, Y. and Hu, H., 2010. A review on auxetic structures and polymeric materials. *Scientific research and essays*, 5(10), pp.1052-1063.
- Liu, Y., Chong, X., Jiang, Y. and Feng, J., 2017. Stability, electronic structures, and mechanical properties of Fe–Mn–Al system from first-principles calculations. *Chinese Physics B*, 26(3), p.037102.
- Liu, Y., Jiang, Y., Zhou, R., Liu, X. and Feng, J., 2015. Elastic and thermodynamic properties of Mo<sub>2</sub>C polymorphs from first principles calculations. *Ceramics International*, 41(4), pp.5239-5246.
- Liu, Y.Z., Jiang, Y.H., and Zhou, R., 2014. First-Principles Study on Stability and Mechanical Properties of Cr<sub>7</sub>C<sub>3</sub>. *Rare Metal Materials and Engineering*,

---

43(12), pp.2903-2907.

López-de-la-Torre, L., Winkler, B., Schreuer, J., Knorr, K. and Avalos-Borja, M., 2005. Elastic properties of tantalum carbide (TaC). *Solid State Communications*, 134(4), pp.245-250.

Luan X, Qin H, Liu F, Dai Z, Yi Y, and Li Q, 2018, The Mechanical Properties and Elastic Anisotropies of Cubic Ni<sub>3</sub>Al from First Principles Calculations, *Crystals* 2018, 8, 307.

Marmier, A., Lethbridge, Z., Walton, R., Smith, C., Parker, S. and Evans, K., 2010. ElAM: A computer program for the analysis and representation of anisotropic elastic properties. *Computer Physics Communications*, 181(12), pp.2102-2115

Malianis, G., Sarafis, I., Lazaridis, T., Varoutoglou, A. and Tsakataras, G., 2016. Random lattice structures. Modelling, manufacture and FEA of their mechanical response. *IOP Conference Series: Materials Science and Engineering*, 161, p.012045.

Meena, K. and Singamneni, S. (2019). A new auxetic structure with significantly reduced stress concentration effects. *Materials & Design*, 173, p.107779.

Meza, L., Philipot, G., Portela, C., Maggi, A., Montemayor, L., Comella, A., Kochmann, D. and Greer, J., 2017. Reexamining the mechanical property space of three-dimensional lattice architectures. *Acta Materialia*, 140, pp.424-432.

Milton, G., 1992. Composite materials with poisson's ratios close to — 1. *Journal of the Mechanics and Physics of Solids*, 40(5), pp.1105-1137.

Mir, M., Ali, M., Sami, J. and Ansari, U., 2014. Review of Mechanics and Applications of Auxetic Structures. *Advances in Materials Science and Engineering*, 2014, pp.1-17.

Mitschke, H., Schury, F., Mecke, K., Wein, F., Stingl, M. and Schröder-Turk, G., 2016. Geometry: The leading parameter for the Poisson's ratio of bending-dominated cellular solids. *International Journal of Solids and Structures*, 100-101, pp.1-10.

Mizzi, L., Mahdi, E., Titov, K., Gatt, R., Attard, D., Evans, K., Grima, J. and Tan, J., 2018. Mechanical metamaterials with star-shaped pores exhibiting

- 
- negative and zero Poisson's ratio. *Materials & Design*, 146, pp.28-37.
- Mizzi, L., Salvati, E., Spaggiari, A., Tan, J. and Korsunsky, A., 2020. Highly stretchable two-dimensional auxetic metamaterial sheets fabricated via direct-laser cutting. *International Journal of Mechanical Sciences*, 167, p.105242.
- Montanari, R. and Varone, A., 2019. Processing–Structure–Property Relationships in Metals. *Metals*, 9(8), p.907.
- Mousanezhad, D., Babae, S., Ebrahimi, H., Ghosh, R., Hamouda, A., Bertoldi, K. and Vaziri, A., 2015. Hierarchical honeycomb auxetic metamaterials. *Scientific Reports*, 5(1).
- Muchiri, P., Mwalukuku, V., Korir, K., Amolo, G. and Makau, N., 2019. Hardness characterization parameters of Niobium Carbide and Niobium Nitride: A first principles study. *Materials Chemistry and Physics*, 229, pp.489-494.
- Nesládek, M., Španiel, M., Kuželka, J., Jurenka, J. and Doubrava, K., 2016. A fretting damage correction factor applicable to the McDiarmid criterion of plain high-cycle fatigue. *Fatigue & Fracture of Engineering Materials & Structures*, 40(1), pp.27-44.
- Nguyen, K., Fookes, C., Ross, A. and Sridharan, S., 2017. Iris Recognition with Off-the-Shelf CNN Features: A Deep Learning Perspective. *IEEE Access*, 6, pp.18848-18855.
- Nguyen, K., Nasouri, R., Bennett, C., Matamoros, A., Li, J. and Montoya, A., 2017. Sensitivity of Predicted Temperature in a Fillet Weld T-Joint to Parameters Used in Welding Simulation with Prescribed Temperature Approach.
- Nika, G. and Constantinescu, A. (2018). Design of multi-layer materials using inverse homogenization and a level set method. *Computer Methods in Applied Mechanics and Engineering*, 346, pp.388-409.
- Norbury, A., 2017. Parametric Studies Based Mechanical and Thermal Modelling of Spot-Welded Joints. Doctoral thesis, Liverpool John Moores University.
- Nye, J. F.: Physical properties of crystals: their representation by tensors and matrices, Oxford University Press, 1985.

- 
- Obbink-Huizer, C., 2020. Use Abaqus To Simulate Additive Manufacturing – Printing A Hip Implant. [online] Info.simuleon.com. Available at: <<https://info.simuleon.com/blog/using-abaqus-to-simulate-additive-manufacturing-printing-an-optimized-hip-implant#comments-listing>> [Accessed 31 July 2020].
- Ochilbek, R., 2018. A New Approach (Extra Vertex) and Generalization of Shoelace Algorithm Usage in Convex Polygon (Point-in-Polygon). 2018 14th International Conference on Electronics Computer and Computation (ICECCO).
- Ogden, R., Saccomandi, G. and Sgura, I., 2004. Fitting hyperelastic models to experimental data. *Computational Mechanics*, 34(6), pp.484-502.
- Omairey, S., Dunning, P. and Sriramula, S., 2018. Multiscale surrogate-based framework for reliability analysis of unidirectional FRP composites. *Composites Part B: Engineering*, 173, p.106925.
- Papka, S. and Kyriakides, S., 1994. In-plane compressive response and crushing of honeycomb. *Journal of the Mechanics and Physics of Solids*, 42(10), pp.1499-1532.
- Parmar, C., Gill, C., Pellereau, B. and Hurrell, P., 2016. Simulation of a Multi-Pass Dissimilar Metal Nozzle to Pipe Weld Using Abaqus 2D Weld GUI and Comparison with Measurements. *Volume 6B: Materials and Fabrication*,
- Prawoto, Y. and Alias, A., 2015. Stress Intensity Factor and Plastic Zone of Auxetic Materials: A Fracture Mechanics Approach to a Chiral Structure Having Negative Poisson's Ratio. *Mechanics of Advanced Materials and Structures*, 22(3), pp.213-223.
- Putanowicz, R., 2015. Implementation of Pore Microstructure Model Generator and Pore Space Analysis Tools. *Procedia Engineering*, 108, pp.355-362.
- Qian, S., Sheng, X., Zhou, Y., Yan, X., Chen, Y., Huang, Y., Huang, X., Feng, E. and Huang, W., 2018. Two-Dimensional Be<sub>2</sub>C with Octacoordinate Carbons and Negative Poisson's Ratio. *The Journal of Physical Chemistry C*, 122(14), pp.7959-7967.
- Rad, M.S, Prawoto, Y. and Ahmad, Z., 2014. Analytical solution and finite element approach to the 3D re-entrant structures of auxetic materials.

---

*Mechanics of Materials*, 74, pp.76-87.

Ranganathan, S. and Ostoja-Starzewski, M., 2008. Universal Elastic Anisotropy Index. *Physical Review Letters*, 101(5).

Ranganathan, S. and Ostoja-Starzewski, M., 2008. Universal Elastic Anisotropy Index. *Physical Review Letters*, 101(5).

Ravindran, P., Fast, L., Korzhavyi, P., Johansson, B., Wills, J. and Eriksson, O., 1998. Density functional theory for calculation of elastic properties of orthorhombic crystals: Application to TiSi<sub>2</sub>. *Journal of Applied Physics*, 84(9), pp.4891-4904.

Rebhi, L., Dinulovic, M., Andric, P., Dodic, M. and Krstic, B., 2016. On the effective shear modulus of composite honeycomb sandwich panels. *Scientific Technical Review*, 66(4), pp.59-65.

Remennikov, A., Kalubadanage, D., Ngo, T., Mendis, P., Alici, G. and Whittaker, A. (2019). Development and performance evaluation of large-scale auxetic protective systems for localised impulsive loads. *International Journal of Protective Structures*, 10(3), pp.390-417.

Ren XJ, Hooper R. M., Griffiths C., Henshall J. L., 2002, Indentation-size effects in single-crystal MgO, 2001. *Philosophical Magazine A*, 82, 10.

Ren, X., Das, R., Tran, P., Ngo, T. and Xie, Y. (2018). Auxetic metamaterials and structures: a review. *Smart Materials and Structures*, 27(2), p.023001.

Ren, X., Smith, C., Evans, K., Dooling, P., Burgess, A., Wiechers, J. and Zahlan, N., 2010. Elastic Deformation of Materials under Distributed Shear Loading. *Experimental Mechanics*, 50(5), pp.651-659.

Reuss, A., 1929, Calculation of the flow limits of mixed crystals on the basis of the plasticity of monocrystals, *Z. Angew. Math. Mech.* 9, 49–58.

Riaño, L. and Joliff, Y., 2019. An Abaqus™ plug-in for the geometry generation of Representative Volume Elements with randomly distributed fibers and interphases. *Composite Structures*, 209, pp.644-651.

Riccardi, B. and Montanari, R., 2004. Indentation of metals by a flat-ended cylindrical punch. *Materials Science and Engineering: A*, 381(1-2), pp.281-291.

Sanami, M., Ravirala, N., Alderson, K. and Alderson, A., 2014. Auxetic Materials for Sports Applications. *Procedia Engineering*, 72, pp.453-458.

- 
- Scarpa, F., Adhikari, S. and Wang, C., 2010. Nanocomposites with auxetic nanotubes. *International Journal of Smart and Nano Materials*, 1(2), pp.83-94.
- Scarpa, F., 2020. Decontamination of liquids using novel adsorbents and 3D porous composite structures – supersieving through auxetic technologies
- Selinger, P., 2003. Potrace: a polygon-based tracing algorithm.
- Selvadurai, A., 2009. Boussinesq indentation of an isotropic elastic halfspace reinforced with an inextensible membrane. *International Journal of Engineering Science*, 47(11-12), pp.1339-1345.
- Schaedler, T. and Carter, W., 2016. Architected Cellular Materials. *Annual Review of Materials Research*, 46(1), pp.187-210.
- Shariatmadari, M., English, R. and Rothwell, G., 2010. Finite Element Study into the effect of footwear temperature on the Forces transmitted to the foot during quasi- static compression loading. *IOP Conference Series: Materials Science and Engineering*, 10, p.012126.
- Sheffield, J., 2007. ImageJ, A Useful Tool for Biological Image Processing and Analysis. *Microscopy and Microanalysis*, 13(S02).
- Shi, L., Xu, C. and Yuan, H., 2011. A CASTEP study on magnetic properties of C-doped ZnO crystal. *Physica B: Condensed Matter*, 406(17), pp.3187-3191.
- Shim, J., Shan, S., Košmrlj, A., Kang, S., Chen, E., Weaver, J. and Bertoldi, K. (2013). Harnessing instabilities for design of soft reconfigurable auxetic/chiral materials. *Soft Matter*, 9(34), p.8198.
- Sissler, L., Jacques, A., Rao, G., Berton, E. and Gueguen, N., 2013. A 3-D finite element model of the foot-shoe structure during a walking cycle for shoe sole design. *Footwear Science*, 5(sup1), pp. S36-S37.
- Smith, C., Grima, J. and Evans, K. (2000). A novel mechanism for generating auxetic behaviour in reticulated foams: missing rib foam model. *Acta Materialia*, 48(17), pp.4349-4356.
- Soman, P. and Chen, S., 2013. Projection Printing of Three-Dimensional Tissue Scaffolds with Tunable Poisson's Ratio. *Biofabrication*, pp.47-57.
- Sorohan, Ş., Sandu, M., Sandu, A. and Constantinescu, D., 2016. Finite Element Models Used to Determine the Equivalent In-plane Properties of

- 
- Honeycombs. *Materials Today: Proceedings*, 3(4), pp.1161-1166.
- Spagnoli, A., Brighenti, R., Lanfranchi, M. and Soncini, F., 2015. On the Auxetic Behaviour of Metamaterials with Re-entrant Cell Structures. *Procedia Engineering*, 109, pp.410-417.
- Strek, T., Jopek, H., Idczak, E. and Wojciechowski, K. (2017). Computational Modelling of Structures with Non-Intuitive Behaviour. *Materials*, 10(12), p.1386.
- Sun, Y. and Pugno, N., 2013. Hierarchical Fibers with a Negative Poisson's Ratio for Tougher Composites. *Materials*, 6(2), pp.699-712.
- Sun, Z., Ahuja, R. and Lowther, J., 2010. Mechanical properties of vanadium carbide and a ternary vanadium tungsten carbide. *Solid State Communications*, 150(15-16), 697-700.
- Tanaka, H., Suga, K., Iwata, N. and Shibutani, Y. (2016). Orthotropic Laminated Open-cell Frameworks Retaining Strong Auxeticity under Large Uniaxial Loading. *Scientific Reports*, 7(1)
- Three-dimensional cellular structures with negative Poisson's ratio and negative compressibility properties
- Tian, B., 2012. *Numerical Simulation of Elastic Wave Propagation in Honeycomb Core Sandwich Plates*. PhD.
- Tian, Y., Xu, B. and Zhao, Z., 2012. Microscopic theory of hardness and design of novel superhard crystals. *International Journal of Refractory Metals and Hard Materials*, 33, pp.93-106.
- Tokmakova, S., 2005. Stereographic projections of Poisson's ratio in auxetic crystals. *physica status solidi (b)*, 242(3), pp.721-729.
- Tran, R., Xu, Z., Radhakrishnan, B., Winston, D., Sun, W., Persson, K. and Ong, S., 2016. Surface energies of elemental crystals. *Scientific Data*, 3(1).
- Tretiakov, K. and Wojciechowski, K., 2014. Partially auxetic behavior in fcc crystals of hard-core repulsive Yukawa particles. *physica status solidi (b)*, 251(2), pp.383-387.
- Ungureanu, B., Achaoui, Y., Enoch, S., Brûlé, S. and Guenneau, S., 2015. Auxetic-like metamaterials as novel earthquake protections. *EPJ Applied Metamaterials*, 2, p.17.
- Vitos, L., Ruban, A., Skriver, H. and Kollár, J., 1998. The surface energy of

- 
- metals. *Surface Science*, 411(1-2), pp.186-202.
- Voigt, W., 1928, *Handbook of Crystal Physics*, 1928. Leipzig, Taubner.
- Wafai, L., Zayegh, A., Woulfe, J., Aziz, S. and Begg, R., 2015. Identification of Foot Pathologies Based on Plantar Pressure Asymmetry. *Sensors*, 15(8), pp.20392-20408.
- Wang, B., Liu, Y. and Ye, J., 2013. Mechanical properties and electronic structures of VC, V<sub>4</sub>C<sub>3</sub> and V<sub>8</sub>C<sub>7</sub> from first principles. *Physica Scripta*, 88(1), p.015301.
- Wang, X., Chen, Y. and Ma, L. (2018). The manufacture and characterization of composite three-dimensional re-entrant auxetic cellular structures made from carbon fiber reinforced polymer. *Journal of Composite Materials*, 52(23), pp.3265-3273.
- Wen, X., Wang, Y. and Zhao, J., 2018. Negatively charged boron nitride nanosheets as a potential metal-free electrocatalyst for the oxygen reduction reaction: a computational study. *New Journal of Chemistry*, 42(15), pp.12838-12844.
- Wen, Y., Gao, E., Hu, Z., Xu, T., Lu, H., Xu, Z. and Li, C., 2019. Chemically modified graphene films with tunable negative Poisson's ratios. *Nature Communications*, 10(1).
- Wilbert, A., Jang, W., Kyriakides, S. and Floccari, J., 2011. Buckling and progressive crushing of laterally loaded honeycomb. *International Journal of Solids and Structures*, 48(5), pp.803-816.
- Winkler, C., Kirik, D. and Björklund, A., 2005. Cell transplantation in Parkinson's disease: how can we make it work? *Trends in Neurosciences*, 28(2), pp.86-92.
- Woodward, P., Suard, E. and Karen, P., 2003. Structural Tuning of Charge, Orbital, and Spin Ordering in Double-Cell Perovskite Series between NdBaFe<sub>2</sub>O<sub>5</sub> and HoBaFe<sub>2</sub>O<sub>5</sub>. *Journal of the American Chemical Society*, 125(29), pp.8889-8899.
- Wu, L., Yao, T., Wang, Y., et al., 2013. Understanding the mechanical properties of vanadium carbides: Nano-indentation measurement and first-principles calculations. *J. of Alloys and Com.*, 548, 60-64.
- Wu, W., Owino, J., Al-Ostaz, A. and Cai, L., 2014. Applying Periodic

---

Boundary Conditions in Finite Element Analysis. *SIMULIA Community Conference*, pp.707-719.

Wu, W., Qi, D., Liao, H., Qian, G., Geng, L., Niu, Y. and Liang, J., 2018. Deformation mechanism of innovative 3D chiral metamaterials. *Scientific Reports*, 8(1).

Xie, T., Liu, Z., Liu, Q. and Wang, G., 2015. Structural insight into the oxidation of sinapic acid by CotA laccase. *Journal of Structural Biology*, 190(2), pp.155-161.

Xiong, H., Zhang, H., Zhang, H. and Gan, L., 2018. First Principle Calculation of NbC Precipitation Competition between TiC Particle and Ferrite Matrix. *Journal of Wuhan University of Technology-Mater. Sci. Ed.*, 33(5), pp.1076-1081.

Yang, C., Vora, H. and Chang, Y. (2018). Behavior of auxetic structures under compression and impact forces. *Smart Materials and Structures*, 27(2), p.025012.

Yang, L., Harrysson, O., West, H. and Cormier, D. (2015). Shear properties of the re-entrant auxetic structure made via electron beam melting. pp.1394-1409.

Yang, Y., Lu, H., Yu, C. and Chen, J., 2009. First-principles calculations of mechanical properties of TiC and TiN. *Journal of Alloys and Compounds*, 485(1-2), 542-547.

Yao, Y., Alderson, K. and Alderson, A., 2016. Modeling of negative Poisson's ratio (auxetic) crystalline cellulose I $\beta$ . *Cellulose*, 23(6), pp.3429-3448.

Yeganeh-Haeri, A., Weidner, D. and Parise, J., 1992. Elasticity of agr-Cristobalite: A Silicon Dioxide with a Negative Poisson's Ratio. *Science*, 257(5070), pp.650-652.

Yelleswarapu, V., Buser, J., Haber, M., Baron, J., Inapuri, E. and Issadore, D., 2019. Mobile platform for rapid sub-picogram-per-milliliter, multiplexed, digital droplet detection of proteins. *Proceedings of the National Academy of Sciences*, 116(10), pp.4489-4495.

Yu, J., Cheung, J., Fan, Y., Zhang, Y., Leung, A. and Zhang, M., 2008. Development of a finite element model of female foot for high-heeled shoe design. *Clinical Biomechanics*, 23, pp. S31-S38.

- 
- Yu, W., Li, J., Shi, C. and Zhu, Q., 2016. Effect of Titanium on the Microstructure and Mechanical Properties of High-Carbon Martensitic Stainless Steel 8Cr13MoV. *Metals*, 6(8), p.193.
- Zarudi, I., Zhang, L. and Cockayne, D., 1998. subsurface structure of alumina associated with single-point scratching. *Journal of materials science*, 33, pp.1639-1945.
- Zhang, G., Lin, L., Hu, W., Yang, C. and Pask, J., 2017. Adaptive local basis set for Kohn–Sham density functional theory in a discontinuous Galerkin framework II: Force, vibration, and molecular dynamics calculations. *Journal of Computational Physics*, 335, pp.426-443.
- Zhang, M., Jiang, R. and Nie, H., 2016. A numerical study on the friction and wear predictions of finger lock chuck in landing gear. *Proceedings of the Institution of Mechanical Engineers, Part G: Journal of Aerospace Engineering*, 231(1), pp.109-123.
- Zhang, X., Ding, H., An, L. and Wang, X. (2015). Numerical Investigation on Dynamic Crushing Behavior of Auxetic Honeycombs with Various Cell-Wall Angles. *Advances in Mechanical Engineering*, 7(2), p.679678.
- Zhang, Y., Lu, M., Wang, C., Sun, G. and Li, G., 2016. Out-of-plane crashworthiness of bio-inspired self-similar regular hierarchical honeycombs. *Composite Structures*, 144, pp.1-13.
- Zhao, C., Zhou, Y., Xing, X., Liu, S., Ren, X. and Yang, Q., 2018. Investigation on the relationship between NbC and wear-resistance of Fe matrix composite coatings with different C contents. *Applied Surface Science*, 439, pp.468-474.
- Zhao, Z., Yuan, C., Lei, M., Yang, L., Zhang, Q., Chen, H., Qi, H. and Fang, D. (2019). Three-Dimensionally Printed Mechanical Metamaterials with Thermally Tunable Auxetic Behavior. *Physical Review Applied*, 11(4).
- Zhu, Y., Jiang, S., Poh, L., Shao, Y. and Wang, Q., 2020. Enhanced hexamissing rib auxetics for achieving targeted constant NPR and in-plane isotropy at finite deformation. *Smart Materials and Structures*, 29(4), p.045030.